Characterisation of Australian Opals

A thesis submitted for
the award of Ph.D.

by

Leslie Dean Brown, BSc. (Mat. Sci.) Hon 1

University of
Technology, Sydney
8 March, 2005.

STATUTORY DECLARATION

I hereby declare that this submission is my own work and that to the best of my knowledge and belief, it contains no material previously published or written by another person (nor material to which to a certain extent has been excepted for the award of any other degree or diploma of the university or other institute of higher learning), except where due acknowledgment is made.

Leslie Brown

ACKNOWLEDGMENTS

This is dedicated to...

Assoc. Prof. Abhi Ray; for your unwavering support and encouragement, I am eternally grateful. This single paragraph of appreciation remains inadequate, as the assistance you provided made the entire thesis possible.

and

Dr. Paul Thomas; I will forever appreciate your guidance and your devotion towards this research – especially in the last couple of years, for some much needed motivation and enthusiasm.

I sincerely thank you both for being so approachable and so considerate. By sharing your esteemed knowledge so willingly, you have nurtured my writing skills, enabling me to communicate my ideas effectively.

...if I had any other supervisors
I am sure I would have quit.

I would also like to thank the following people:

Ashwini Sharma and Norman Pearson at GEMOC, Macquarie University,
for their help with the Laser Ablation ICPMS.

Kathryn Prince and staff at SIMS microanalysis unit at ANSTO.

Gary Lee and Kamali Kannangara, NMR

Jean-Pierre Gerbois, for his assistance with
the thermal analysis instrumentation.

Richard Wuhrer and Matthew Phillips at the Microstructural Analysis Unit,
for assistance with SEM.

Chris McCrea at Particle and Surface Science Laboratories,
for the ultramicroporosity analyses.

Anthony Smallwood, for several helpful discussions
and supplying many of the opal samples investigated.

The opal miners at Lightning Ridge, who also graciously donated
many samples from their own personal collections.

Mum, Dad and Michelle; thanks for all the support.

TABLE OF CONTENTS

LIST OF FIGURES

LIST OF TABLES

LIST OF EQUATIONS

GLOSSARY OF TERMINOLOGY

Agglomeration	Collect into a mass; accumulate in a disorderly way.
Aggregation	A term used for all the ways in which colloidal particles are linked together. This includes gelling, coagulation and flocculation.
Aluminium silicate	Octahedrally coordinated aluminium within silica.
Aluminosilicate	Tetrahedrally coordinated aluminium within silica.
BCC	Body Centred Cubic stacking sequence.
Coacervate	Primary particles accreting around a nucleus to form a much larger secondary particle.
Coagel	Fully dehydrated precipitate of a sol or gel.
Coagulation	Particles that come together into relatively close-packed clumps as a result of the inability of a colloidal system to maintain its dispersed sate. This is usually an irreversible process.
Coagulum	An aggregate of colloidal particles having a relatively tight, dense structure. A coagulum cannot easily be distinguished from a floc.
Coalesce	The process of eliminating the negative radius of curvature at the point where spheres contact each other (similar to sintering, but at low temperatures).
Co-coagulation	See heterocoagulation.
Colloidal system	A system which contains a dispersed phase, which is finely divided and distributed evenly throughout a medium (the continuous phase). The particle size is just larger than that of a true molecular solution but less than a coarse suspension. Usually it is between 1nm and 1μm.
Common opal	A type of opal that is not associated with precious opal.
α-Cristobalite	A crystalline phase in which the silica tetrahedra of adjacent silicate sheets occur in the 'trans' structural arrangement.
Critical coagulant concentration (c.c.c.)	The specific concentration of coagulant required to initiate rapid coagulation of all colloids in a sol.
Cryptocrystalline	A crystalline substance that contains crystallites which are too small to be observable with the microscope.
CSA	Chemical Shift Anisotropy.
CTE	Coefficient of Thermal Expansion.
Decrepitation	When a mineral, such as opal, "breaks up" (fractures) on heating.

EDX	Energy Dispersive X-Ray Spectroscopy.
Electrical double layer	The variation in electrical potential that is generated at various distances from a charged surface.
EPS/ESR	Electron Paramagnetic Spectroscopy / Electron Spin Resonance.
FCC	Face Centred Cubic stacking sequence.
Floc	Particles linked together by bridges of the flocculating agent that are sufficiently long so that the aggregated structure remains relatively open and voluminous. A floc cannot easily be distinguished from a coagulate.
Flocculation	The process of forming flocs.
FWHM	Full Width of a peak at Half its Maximum height.
Gel	Particles which are linked together in branched chains that fill the whole volume of the original sol so that there is no increase in the concentration of the dispersed phase in any macroscopic region in the medium. A gel can easily be distinguished from a floc or a coagulate.
Gelling	Process of forming a gel.
Geminal silanol	Twin hydroxyls (Q^2 resonance).
HCP	Hexagonal close-packed stacking sequence.
Heterocoagulation	The simultaneous coagulation of two oppositely charged colloids.
Homodisperse	See monodisperse.
HRTEM	High-Resolution Transmission Electron Microscopy.
Hydrophilic	"water loving"
Isodisperse	See monodisperse.
Isoelectric point (IEP)	pH of zero ζ potential, interpreted as the point of zero charge at the shear plane. The IEP is not necessarily the ZPC.
LA-ICPMS	Laser Ablation Inductively-Coupled-Plasma Mass Spectrometry.
LDG	Libyan Desert Glass.
Lyogel	A type of gel where the colloids are sterically but not dynamically separated by layers of liquid.
Macropores	Pores with a diameter greater than 2000Å.
Mesopores	Pores with a diameter between 20 and 2000Å.
Metastable	To exist in a state which is not thermodynamically stable.
Microcrystalline	A crystalline substance in which the crystallites are

	resolvable in the standard optical petrographic microscope.
Micropores	Pores with a diameter less than 20Å.
Monodisperse	A colloidal system containing particles of uniform dimensions.
Monosilicic acid	$Si(OH)_4$
MRJ	Maximally Random Jammed structure; state that minimises disorder among all statistically homogeneous and isotropic jammed structures.
Network colloid	Systems that contain two inter-penetrating networks. Technically speaking, opal-AG is a network colloid.
NMR	Nuclear Magnetic Resonance spectroscopy.
Octahedral aluminium	Aluminium atoms in a six-fold co-ordination. Sometimes this is written as Al^o or ^{VI}Al.
Opal-A	Amorphous opal.
Opal-AG	Amorphous opal, with a colloidal microstructure.
Opal-AN	Amorphous opal with a glassy, network-like structure.
Opal-C	Paracrystalline opal with a predominantly cristobalite molecular structure.
Opal-CT	Paracrystalline opal containing both cristobalite and tridymite stacking sequences, but still predominantly amorphous.
Paracrystalline	A term which implies partial ordering in a disordered matrix, while still constituting a continuous network.
Poc	Play of colour.
Polydisperse	A colloidal system that contains particles of various sizes.
Polysilicic acid (oligomers)	SiO_2 polymers with molecular weights up to about 100,000.
Potch	Opal that lacks a play of colour.
Precious opal	Opal that displays a play of colour.
RCP	Random Close-packing; the maximum density that a large, random collection of spheres can attain = 0.64.
RF	Radio Frequency.
RMS	Root Mean Square, a statistical measure of the magnitude of a varying quantity. Also referred to as the quadratic mean.
SANS	Small Angle Neutron Scattering
Sedimentation	Natural process of microscopic solid particles (usually in a fluid phase) falling to the bottom of a container

	due to the force of gravity.
SEM	Scanning Electron Microscopy.
Shear plane	A very thin region just outside the stern layer, where the viscosity effects change rapidly.
Silanol	Si–OH bond
Silica	Silica occurs in a variety of polymorphs, such as: cristobalite, tridymite, chalcedony, amorphous silica, opal and quartz.
Siloxane	Si–O–Si bond
SIMS	Secondary Ion Mass Spectrometry.
Sol	A solid dispersion of small particles in a liquid medium. See "colloidal system".
SSA	Specific Surface Area
Stern layer	A small space separating the ionic atmosphere near an interface, the diffuse double layer, from the steric "wall" of the charged plane just adjacent to the interface. Ions in the stern layer remain with the surface.
Tectosilicate	Fully polymerised (or condensed) silica, where each of the four corners of the silica tetrahedra are connected to other tetrahedra (Silicon in the Q^4 configuration).
Tetrahedral aluminium	Aluminium atoms in a four-fold co-ordination. Sometimes this is written as Al^t or ^{IV}Al.
TGA	Thermogravimetric Analysis.
TMA	Thermomechanical Analysis.
Transition temperature	The temperature at which the opal changes from a positive to a negative thermal expansion coefficient (the point where the thermal expansion coefficient equals zero).
α-Tridymite	A crystalline phase in which the silica tetrahedra of adjacent silicate sheets occur in the 'cis' structural arrangement.
Vicinal silanol	Single hydroxyl (Q^3 resonance).
XAS	X-Ray Absorption Spectroscopy
Xerogel	A gel in which the micelles are in direct contact with each other.
XRD	X-Ray Diffraction.
Zeta (ζ) potential	Potential at the shear plane. Also referred to as the electrokinetic potential.
ZPC	Point of Zero Charge.

ABSTRACT

Australia is the world's largest producer of precious opals, contributing more than $1 billion per annum to the GDP. However, to date little fundamental research has been carried out on banded opals, which are potentially the most valuable of all opal varieties. Opal is also Australia's national gemstone; yet for such an important resource, it is surprising that the mechanisms of opal formation remain in dispute, in particular for banded opals. The focus of this study is to understand the formation of opal by investigating the chemistry and microstructure of banded and non-banded opals. Opals from several regions of Australia (Coober Pedy, Lightning Ridge, Andamooka and Tintenbar), in addition to opals from Mexico, were thus investigated in detail using a range of techniques.

Evaluation of the trace element chemistry of opals was carried out by employing a combination of experimental techniques, including Laser Ablation Inductively Coupled Mass Spectrometry (LA-ICPMS) and Secondary Ion Mass Spectrometry (SIMS). Darker-coloured bands contained significantly higher concentrations of certain transition elements (Ti, V, Co, Ni, Cu, Zn and Y) and rare-earth elements (La, Ce) than the lighter-coloured bands. The concentrations of other elements (Mg, Ca, Al, Fe and Mn) were in most cases found to be similar between bands. Some elements (Ti, Cr, Cu, Zn, Co and Zr) were found to be distributed more heterogeneously than others (Na, Ca, Mg, K, Al and Fe). Based on this evidence, a solution depletion model was proposed to explain the formation of banded opals, involving the charge-neutralisation of silica colloids by highly-charged transition metal cations.

The microstructural characteristics of several Australian opal-AG (amorphous, gel-like opal) specimens were studied using a number of experimental techniques such as porosity measurement, thermomechanical analysis (TMA) and thermogravimetric analysis (TGA). An initial expansion followed by contraction was observed in TMA. The temperature at which this 'transition' occurred ranged from 200 to 400°C and was found to be region dependent. TGA revealed that the temperature range, from 215 to 350°C,

over which the maximum rate of dehydration occurred, was again region dependent, consistent with the TMA data. A dehydroxylation–sintering mechanism was proposed to account for these results. Porosity measurement yielded a greater degree of porosity in the opaque white samples than the transparent ones; the additional voids consequently scatter light internally, rendering the opal opaque.

^{29}Si NMR and ^{27}Al NMR experiments were undertaken to characterise the relative disorder, silanol content and the coordination state of Al within opal-AG and opal-CT (cristobalite-tridymite opal). The comparison of ^{29}Si NMR spectra demonstrated that opal-CT samples contained a higher proportion of both geminal (Q^2) and vicinal silanol groups (Q^3) than opal-AG. This result was attributed to the large internal surface area of opal-CT compared to that of opal-AG. Since Al was found to exist in a tetrahedral coordination within the opal structure, incorporation of Al occurred through substitution of Si during the period of colloidal growth. As the concentration of Al in banded opals was similar, the colloids within each band are considered to have formed at similar times.

1. RATIONALE AND OBJECTIVES

"Great things are not done by impulse,
but by a series of small things brought together."
–Vincent Van Gogh, Impressionist painter

1.1. AUSTRALIAN OPAL RESEARCH

Considering Australia supplies 95% of the world's demand for opal, there is disproportionately less published research on opal from Australia than there is from other countries. To some extent this may be due to the difficulty in obtaining samples, although a lack of research incentives seems to be the main reason. Traditionally in Australia, there has been limited funding on the research of opal, particularly in relation to banded opal (potentially the most valuable), due to the fact that major mining companies are not involved in opal extraction. Hence, little fundamental research has been carried out on these types of opals. Nevertheless, a number of research groups in Australia have renewed interest towards the investigation of opals and their formation processes.

It is well known that on any particular opal field, potch opal is much more prevalent than precious opal (Darragh *et al.* 1976), but the reasons for this are not well understood. To form precious opal, the conditions required must inherently be very stable, whilst the precursor solutions must also be relatively uncontaminated (Deniskina *et al*. 1981). Precious opal is found at numerous locations around the world, therefore general mechanisms of formation must exist (falling within prescribed limits). However, the underlying processes which preferentially generate potch opal, while inhibiting or limiting the formation of precious opals, have not yet been established. Preliminary studies on the chemical composition of precious and potch opals have revealed that they contained similar amounts of minor elements (Bayliss and Males 1965), indicating similar, but subtly different conditions of formation. Given the intimate relationship between the formation of potch and precious opal, an understanding of the formation mechanisms and properties of precious opal should be based on an investigation of both precious and potch opal. This research, therefore, aims to generate data concerning the chemistry and structure of potch and precious Australian opals to gain a better understanding of their processes of formation.

Although a few studies have considered the elemental composition of opals (Graetsch *et al.* 1990; McOrist *et al.* 1994; McOrist and Smallwood

1997), one problem with analysing a variety of opal samples from a certain region is that opals which appear alike often contain significantly different quantities of trace elements. There exists a great deal of overlap in the trace element chemistry of numerous samples with an identical geological origin. It is therefore not possible to accurately attribute any particular elements directly to the formation of potch or precious opal. However, it is anticipated that the trace element investigation of banded opals could alleviate this problem, as these types of opal samples can contain adjacent layers of potch and precious opal. Thus, in the case of banded opals, any differences in elemental composition of each layer are likely to be due to differences in their respective mechanisms of formation. Hence, the subtle differences in environmental conditions that result in potch or precious opal can be identified in this manner. An investigation into the minor and trace element concentrations was therefore carried out on adjacent layers in banded opal.

1.2. Formation of Banded Opals

Australian opals are often banded; a single opal may be composed of several layers which are most easily distinguished by their different base colours (e.g. transparent, white, grey, black, etc). The finest gem-quality opals, which possess a black opaque band adjacent to a band with a play of colour, are the most valued. This is partly due to their exceptionally vivid play of colour, and partly to their rarity. The patterns observed in precious opals are also totally unique. To a researcher, it is somewhat disconcerting to learn that of all the types of opals, very little is known about the formation mechanisms of different opal bands within these gem-quality stones.

To date, the origin of the bands remains a mystery, and the generally accepted sphere-sedimentation model of opal-genesis (Darragh *et al.* 1966; Jones *et al.* 1966) appears inadequate to account for banded opal samples. Ordered packing sequences commonly occur within banded opal; in fact, at locations such as Lightning Ridge, precious opal rarely occurs in non-banded opal. The localised formation conditions at particular positions within a banded opal sample are still uncertain. One hypothesis suggested in this

thesis is that the elemental composition affects the ordering of spheres within sedimentary opals, as monodisperse sols (which can form ordered stacking sequences) require high-purity solutions to form. Hence, a solution containing a high level of impurities should form a more polydisperse sol, which cannot produce an ordered microstructure.

To test this hypothesis, the elemental composition of banded opals has been investigated, in order to determine whether any differences might identify the processes involved in the formation of different bands. Elemental analyses were therefore carried out on a number of banded opals from different regions of Australia, using Laser Ablation Inductively-Coupled-Plasma Mass Spectrometry (LA-ICPMS), to ascertain the trace element composition of each layer. Secondary Ion Mass Spectrometry (SIMS) was also used to provide elemental depth profiles within each layer as well as profiles across the interfacial regions of such samples, to assess the compositional homogeneity of the constituent bands.

1.3. WATER CONTENT AND MICROSTRUCTURE

The majority of opals found in Australia fall within the opal-AG category, although several opal-CT deposits have also been identified (e.g. Tintenbar). Opal-AG is initially thought to have formed from a colloidal silica solution, which slowly coagulates into a solid aggregate of silica particles (Darragh *et al.* 1966). Water is incorporated into the structure as molecular water (H_2O) and silanol (Si–OH) groups. In addition to vicinal (single) hydroxyl groups that are contained within natural opals, it is possible that geminal (double) hydroxyl groups may also arise (Segnit *et al.* 1965). They are most likely to occur at lattice imperfections caused by incomplete polycondensation of silica tetrahedra (Hockey and Pethica 1961), such as at the surfaces of the silica spheres where the continuous silica network is interrupted. However, uncertainty exists in the literature concerning the existence of these twin hydroxyl groups (Langer and Flörke 1974; Cong *et al.* 1993; Graetsch *et al.* 1994; Graetsch and Topalović-Dierdorf 1996). One aim of this research is to determine the proportion of single and twin hydroxyl groups in opal-AG and opal-CT. This study seeks to clarify the nature of the silanol bonds contained within opal-AG and opal-CT using

Nuclear Magnetic Resonance (NMR) spectroscopy. Furthermore, NMR provides information concerning the relative amorphous character of opal-AG and the 'crystallinity' of opal-CT. Thermal analysis is also used to investigate the dehydration behaviour and water content of opals; in conjunction with nitrogen adsorption analysis, details concerning the microstructure (micropores) of opal samples can therefore be inferred from these results. The ultimate objective of this thesis is to use the results generated in all sections to advance the level of understanding of the current chemical and physical structure of opal, and to subsequently use that new information to generate new models relevant to the formation of natural precious and potch opals (banded or otherwise).

1.4. THESIS STRUCTURE

Chapter 1 consists of the rationale, describes the primary research objectives, and also outlines the thesis structure. Chapters 2 and 3 essentially report on the current literature concerning natural opal. Specifically, chapter 2 provides a general overview of the microstructural differences and elemental composition of precious and potch opal. The classification schemes of the various types of opal are considered (opal-AG, opal-AN, opal-CT and opal-C); the nature of water (molecular and hydroxyl groups) in these respective categories is also discussed.

Chapter 3 presents a comprehensive review of the formation mechanisms of opal-AG and opal-CT that have been proposed in the literature. This includes SiO_2 solubility, nucleation, polymerisation and particle growth in the colloidal state. Fundamental concepts are discussed, such as Ostwald ripening, the silica diagenesis mechanism and the transport and deposition of aqueous silica ('mobility by metastability'). This chapter also reports on other pertinent opal-genesis models.

Chapters 4 to 7 represent the main body of research regarding this thesis. Each of these chapters contains separate introductions, which represent detailed opal-specific literature that is applicable to each particular chapter. The introductory sections in each case are followed by the experimental details, results, discussion and conclusion sections for every individual chapter.

The thermomechanical analysis (TMA), thermogravimetric analysis (TGA) and nitrogen adsorption investigations of opal are presented in chapter 4; this includes pore size distribution, total porosity and specific surface area (SSA), dehydration rates and temperatures, as well as thermal expansion and contraction data. Explanations of the observed thermal behaviour are then given with reference to the microstructures (and other factors) of the opal samples.

Chapter 5 includes the study of trace-element composition of opal-AG using LA-ICPMS. Various models are proposed for the formation of non-banded and banded opal-AG within this chapter, based on the results obtained.

Chapter 6 comprises the investigation of banded opals using SIMS. The experimental, results and discussions sections are further subdivided into 'individual spot analyses' and 'linescans'. Further concepts involving the formation of ordered and disordered opal phases are discussed later in this chapter. High-resolution SEM is also used in this chapter to speculate on the artefacts that may be brought about by HF acid etching.

Chapter 7 concerns the investigation of opal with ^{27}Al and ^{29}Si NMR. The experimental, results and discussions sections of this chapter concerning ^{29}Si NMR are subdivided into 'bloch decay' and 'cross-polarisation' experiments. The discussion elaborates on the differences between opal-CT and opal-AG spectra, with respect to their silanol content, crystallinity and internal surface area; this chapter also examines the incorporation of Al within the structure of opal-CT and opal-AG and its significance.

Chapter 8 summarises the general conclusions of the complete thesis. References for all chapters are listed at the end of the thesis. A glossary of terminology is provided at the beginning of the thesis.

2. INTRODUCTION

"The saddest aspect of life right now
is that science gathers knowledge
faster than society gathers wisdom."
–Isaac Asimov,
Science fiction writer and biochemist

2.1. THE HISTORY OF OPAL

Opal has long been admired for its unrivalled colour and uniqueness. Indeed, opal artefacts dating from as early as 4000 B.C. have been found in a cave in Kenya by the anthropologist Louis Leakly. The Romans first established opal as a gemstone when it was introduced to the Roman Empire around 100 B.C (Barnes and Townsend 1982). Opals are found at numerous deposits around the world, including: Slovakia (Rondeau *et al.* 2004), Mexico (Koivula *et al.* 1983; Spencer *et al.* 1992), Brazil (Bartoli *et al.* 1990), Honduras (Banerjee and Wenzel 1999), Japan (Yoshida 1987), Canary Islands (Graetsch and Topalović-Dierdorf 1996; Bustillo and Martínez-Fríaz 2003), Turkey (Esenli *et al.* 2001) and Zambia (Milisenda *et al.* 1994).

During the 18th and early 19th centuries, opal gained the reputation of being a stone of ill-fortune. Pestilence, famine and the fall of monarchs have been blamed on its powers. Through superstition, owning an opal was considered to bring bad luck. This was probably caused in part by the tendency of some types of opal to crack some time after mining (Shepherd 1971).

2.1.1. Australian opal

Individual occurrences of precious opal were discovered in South Australia in 1849, and again by gold panners in 1863 in north Victoria (Barnes and Townsend 1982). Commercial production commenced at White Cliffs in 1890. Organised mining started at Lightning Ridge in 1903. Coober Pedy and Andamooka were discovered in 1915 and 1930 respectively. Only then did opal reclaim some of its appeal.

Currently, Australia is by far the biggest producer of opals in the world and supplies over 95% of the world's opals; as such the export of Australian opal to overseas markets contributes more than one billion dollars annually towards the Australian economy (Olliver and Townsend 1993). In 1993, opal was declared the "national gemstone of Australia" by the Governor-General of the Commonwealth of Australia.

2.2. CHEMICAL COMPOSITION

It has been known for more than 70 years (Levin and Ott 1933; Dwyer and Mellor 1934) that opals consist primarily of silica (between 85% and 99%), with trace quantities of metal oxide impurities (Graetsch *et al.* 1987; Flörke *et al.* 1991). Water is also present within the structure of opal; generally between 1 and 20% in common opals, and usually between 6 and 10% in precious opals. Hence, the chemical formula for opal is generally expressed as $SiO_2.nH_20$, where n is a variable number (Section 2.6).

Very little research has been conducted on the minor constituents of opal; the research has instead focused on the unique crystal- and microstructure of opal. The secondary elements contained within most opals are: Al, Ca, Na, Mg, and Fe (Graetsch *et al.* 1987; Flörke *et al.* 1991; Bustillo and Martínez-Fríaz 2003). Table 2-1 lists the trace element composition of several black opals from NSW. The trace element chemistry of opal is further discussed elsewhere (5.1.3).

Element	Concentration Range (ppm)
Na	700 – 1800
Mg	170 – 320
Al	5900 – 10,200
K	920 – 4000
Ca	1300 – 2700
Ti	120 – 1900
V	1.7 – 15
Cr	1.1 – 7.0
Mn	16 – 38
Fe	810 – 2000
Co	7 – 120
Cu	36 – 1100
Zn	6 – 130
Ba	100 – 190
Ce	10 – 91

Table 2-1: Concentration ranges of various elements of nine black opals from NSW. From McOrist et al. (1994).

2.3. MICROSTRUCTURE OF OPAL-AG

2.3.1. Play of colour

The term "play of colour" (poc) is used when the colour of an opal appears to change colour as it is rotated. Over the ages, many researchers speculated on what might cause the observed poc, but their theories were unable to be substantiated. It was not until 1964, several years after the development of the electron microscope, that the microstructure of opal was finally revealed and an adequate theory was postulated for the origin of the poc (Jones *et al.* 1964; Pense 1964). Jones *et al.* (1964) found that precious opal consisted of a multitude of microscopic spheres of silica with a uniform diameter. The size of the spheres depended on the type of opal, and their diameter was usually between 150 and 300 nanometres[1]. For precious opals displaying a poc, the spheres within each colour domain were of almost identical size and arranged very regularly to form a close-packed array (Figure 2-1; Figure 2-2).

[1] In a few exceptional volcanic samples, Darragh *et al.* (1976) reported spheres up to 10μm in diameter. Sanders (1976) also reported spheres up to 700nm in diameter within a few opal samples.

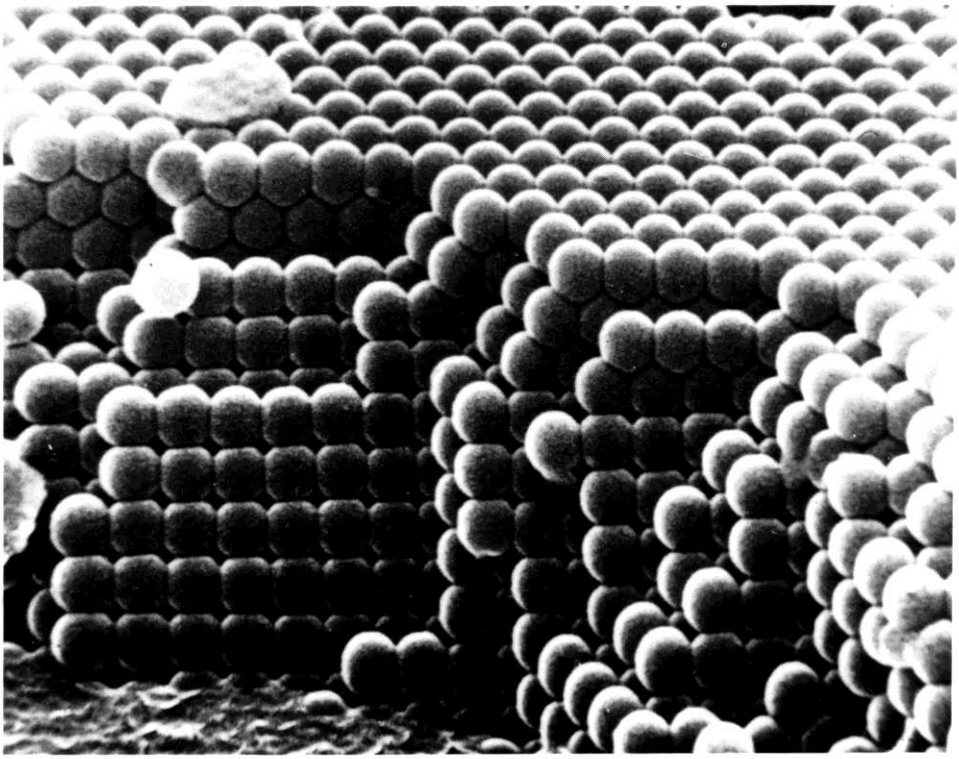

Figure 2-1: SEM micrograph of the ordered sphere arrangement of a synthetic opal-A structure containing monodisperse silica spheres. From Heaney et al. (1994).

The model proposed by Sanders (1964) was that the play of colours displayed by precious opals were caused by the diffraction of light within the opal from regions of high refractive index, such as the silica spheres, to regions of low refractive index such as the silica 'cement' or mesopores, which contain air and water. Thus, opal acts as a three-dimensional diffraction grating, producing spectrally pure colours from the incident white light. Further research revealed that opals with very few stacking faults in the sphere layering sequence showed rather uninteresting colour effects when compared to opals with a higher degree of stacking faults (Darragh *et al.* 1976).

The maximum wavelength of light observed is controlled by the size of the silica spheres (Sanders 1964). The limit to the range of colours that appear is also dependent on the type of sphere stacking. For hexagonal close-packed and face-centred cubic arrangements of spheres, equivalent to atomic-scale HCP and FCC stacking in crystalline matters, this relationship

can be expressed explicitly by the respective formulae, where λ_{max} is the longest wavelength of light seen in the play of colour, and d is the diameter of the uniform silica spheres:

$$\lambda_{max} = 2.51d \qquad \text{(HCP)}$$

$$\lambda_{max} = 2.37d \qquad \text{(FCC)}$$

Equation 2-1: Relationship between maximum wavelength of diffracted light observed vs. diameter of spheres. From Sanders (1968) and Darragh and Perdrix (1975).

According to the above formulae, opals with larger spheres should display colours of longer wavelengths, while opals with smaller spheres only diffract colours with shorter wavelengths. Other factors may also influence the range of colours observed. For example, the range of colours may be limited if the opal has a flat polished surface, as any light leaving the opal at an angle of incidence greater than about 45° will be totally internally reflected. This undesirable effect is greatly reduced by rounding the surface of the opal and is the reason why most opals are cut in a cabochon shape.

2.3.2. Potch and common opals

Opal that has no play of colour is given the generic name "potch" by Australian opal miners (Smallwood 1997). Potch is found (or mined) in association with precious opal in opal fields that produce precious opal. The term "common opal" is given to potch opal found in fields that do not produce precious opal (Ball 1982). Neither potch nor common opal show any play of colour because the silica spheres are not in ordered arrays. However, the spheres may either be randomly sized (i.e. they have a particular size distribution) and hence will be randomly packed, or they may be uniform in size yet randomly packed. These conditions result in a scattering of the incident light and hence no net diffraction effect.

Although potch opals do not display a poc, they exhibit various base colours; potch opals from Lightning Ridge may be transparent, translucent or opaque, and are typically colourless, honey, grey or black in colour.

Opals from Mexico characteristically have an orange base colour (Koivula *et al.* 1983; Spencer *et al.* 1992).

2.3.3. Stacking sequences of spheres

Ordering in domains does occur, and over 30 consecutive layers have been observed packed in an ordered manner (Sanders 1968). Usually, ordered microstructures contain regions with FCC or HCP stacking, so that overall, the sequence of FCC and HCP layers is random (Sanders 1964; Cole and Monroe 1967; Monroe *et al.* 1969). In general, there is evidence of a slight preference for the FCC sphere stacking sequence over HCP or simple cubic stacking (Cole and Monroe 1967; Rau and Amaral 1969; Míguez *et al.* 1997; Pusey *et al.* 1989; Cheng *et al.* 1999; Figure 2-2), although there is evidence towards the contrary. A small angle neutron scattering (SANS) study of opal revealed that opal-AG probably contained more than 50% HCP stacking; one opal-AG sample from Coober Pedy was estimated to contain about 75% HCP and 25% FCC stacking (Graetsch and Ibel 1997). One study involving the diffraction of light by opals declared that stacking was entirely hexagonal (Baier 1966).

Recently, it has been confirmed using computer simulations that there is indeed a slight preference to crystallise FCC packed spheres rather than the HCP sphere sequence (Woodcock 1997), although once formed, these close-packed structures possess identical entropies (Rintoul and Torquato 1996).

Other packing arrangements have also been reported, such as simple cubic packing (Cole and Monroe 1967; Rau and Amaral 1969). In some instances, the lattice was occasionally found to be faulted or twinned (Cole and Monroe 1967; Rau and Amaral 1969). Other stacking faults such as dislocations and point defects were also present (Monroe *et al.* 1969).

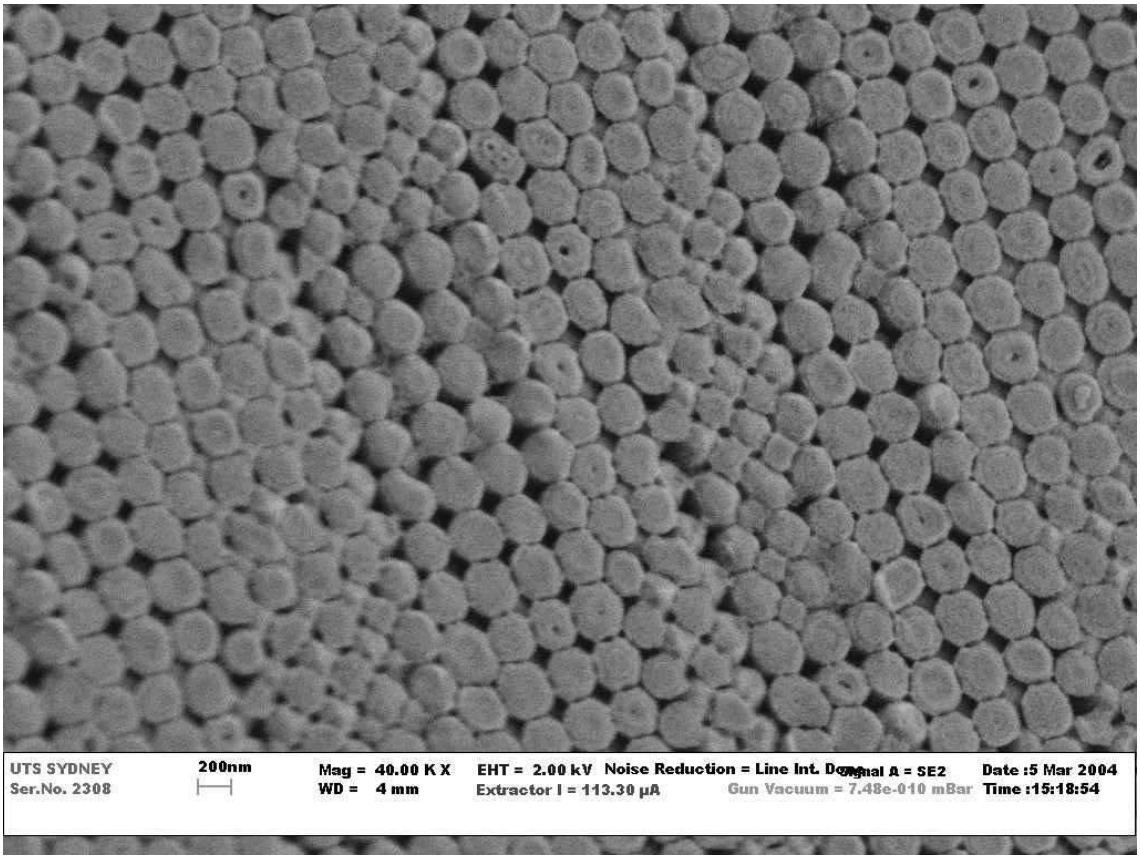

Figure 2-2: SEM microstructure of opal displaying spheres arranged in an ordered FCC manner. The fracture plane is oriented diagonally across the image and slopes down to the bottom right hand corner. A secondary electron detector was used for imaging.

2.3.4. Voids

Scanning Electron Microscopy (SEM) indicated that voids between spheres were not necessarily tetrahedral or octahedral as to be expected in a close-packed structure, but instead had non-ideal shapes (Sanders 1964). The sizes of the voids were smaller than expected for a close-packed FCC or HCP system; the smaller tetrahedral voids were also commonly missing. Since the colloids had an almost perfectly spherical shape, it was deduced that subterranean compression forces could not have reduced the size of the voids. An alternative suggestion was that the voids were filled with a second generation of 'silica cement', which in-filled the interconnected pores and hence rendered them different shapes (Sanders 1964). Sanders further proposed that the extent to which these void spaces were filled with 'silica cement' appeared to correlate with an opal's diaphaneity (opacity); i.e.

opals that appeared transparent were comprised of voids which were filled with silica to a greater degree than the voids of opaque opals.

2.3.5. Primary spheres

The structure of the spheres themselves has been investigated in a number of studies. In order to observe the structure, recently-fractured opal surfaces were carefully etched with hydrofluoric acid (HF). The resulting structure that was revealed was not the expected spherulitic structure consisting of radial lines, instead the silica spheres exhibited a series of concentric rings (from 1 to 3 rings, depending on the type of opal) and these were thought to consist of smaller sub-spheres (Darragh *et al.* 1966; Cole and Monroe 1967). Darragh *et al.* (1966) postulated that the silica spheres were composed of shells of smaller primary spheres with a diameter of approximately 20-50nm, the primary spheres of the outer layers accreting around a single primary sphere at the core of this larger sphere, and the whole assembly assumed to be in a close-packed configuration (Darragh *et al.* 1976). Monroe *et al.* (1969) observed a maximum of five strata. Figure 2-3 illustrates the fractal-like arrangement of three 'shells' contained within a secondary sphere, each 'shell' comprised of several close-packed primary spheres. For this reason, the original spheres between 100 and 350nm in diameter were described as secondary spheres, while the smaller spheres 20-50nm in diameter were denoted primary spheres. In some instances, they may also be termed primary particles because at this very small size the macromolecular silica network only approximates a sphere.

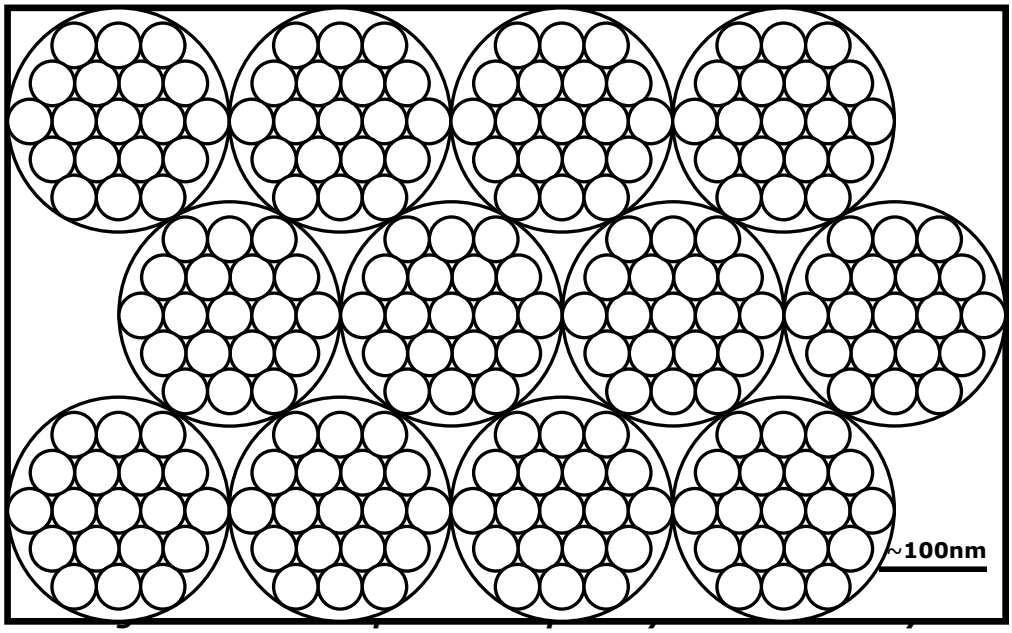

sphere arrangement of opal-AG, as proposed by Darragh et al. (1976).

2.4. MICROSTRUCTURE OF OPAL-CT

The microstructure of opal of volcanic origin is often difficult to resolve with SEM, because it contains very small-scale textures with little detail or relief (Jones *et al.* 1964). Darragh *et al.* (1966, 1976) reported that in some of the opals from volcanic deposits (opal-CT), the filling of voids by silica is often so complete that the discontinuities were no longer visible with SEM. However, a microstructure consisting of very small spheres (particles) about 100Å in diameter is frequently observed for opal-CT (Darragh and Sanders 1969; Sanders 1975).

The TEM study by Nagase and Akizuki (1997) has shown that the surface of one volcanic opal-CT sample examined was comprised of 'thin platy microcrystals' similar to the lepispheres found in opal-CT of organic origin (Figure 2-4). It is thought that one of the reasons for the imaging difficulties is that opal-A might be deposited in between these plate-like crystallites (Flörke *et al.* 1975).

Opal-CT commonly appears as lepispheres (1-10μm spheroids) and blades 10-100nm in thickness (Flörke *et al.* 1973, 1976; Scurfield and Segnit 1984; Williams *et al.* 1985; Figure 2-4; Figure 2-5). Blade sizes

commonly differ in size, and may be well-bladed or stubby in appearance, but have characteristically serrated edges (Flörke *et al.* 1976).

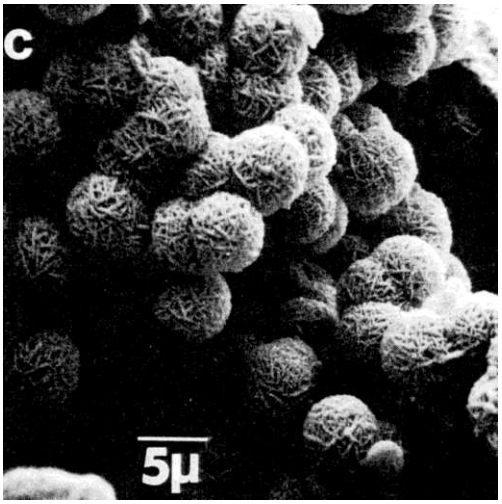

Figure 2-4: SEM micrograph of opal-CT lepispheres. From Hinman (1990).

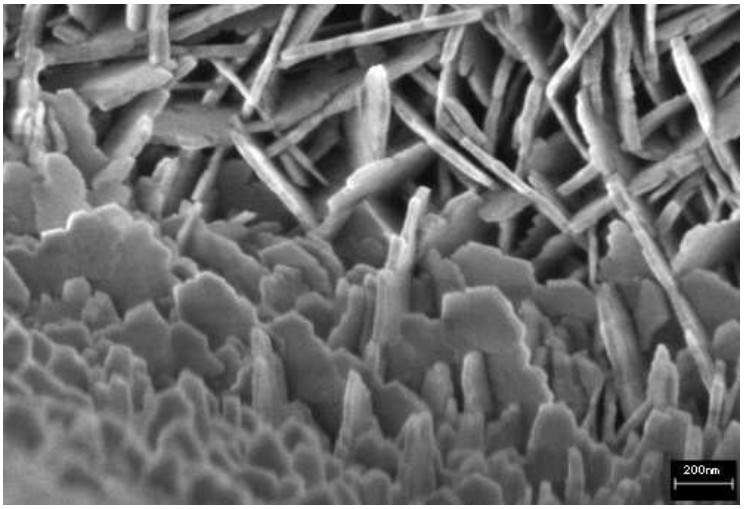

Figure 2-5: SEM micrograph of opal-CT blades. From Bermanec et al. (2004).

2.5. MORPHOLOGY OF OPAL

Before the study by Jones and Segnit (1971), opals were generally classified as either being X-Ray amorphous or partially crystalline. In that study, X-Ray Diffraction (XRD) analyses were reported on 300 opal samples from various locations around the world (Jones *et al.* 1964; Jones and Segnit 1971). These opals were shown to fall into one of three groups, each group showing a distinctly different XRD pattern. Opals that produced an

XRD pattern similar to α-cristobalite with minor evidence of tridymite were termed opal-C. This cannot be referred to as α-cristobalite because all diffraction patterns showed evidence of tridymitic stacking. Opals that showed signs of both cristobalite and tridymite XRD patterns were designated opal-CT. Opals that resulted in an amorphous silica XRD pattern consisting of a prominent but very diffuse band at a d-value of 4.1Å were called opal-A (Figure 2-6). Similar diffraction patterns are obtained from silica gel and silica glass. Prior to those studies, opals were only classified into two groups: amorphous and poorly crystalline.

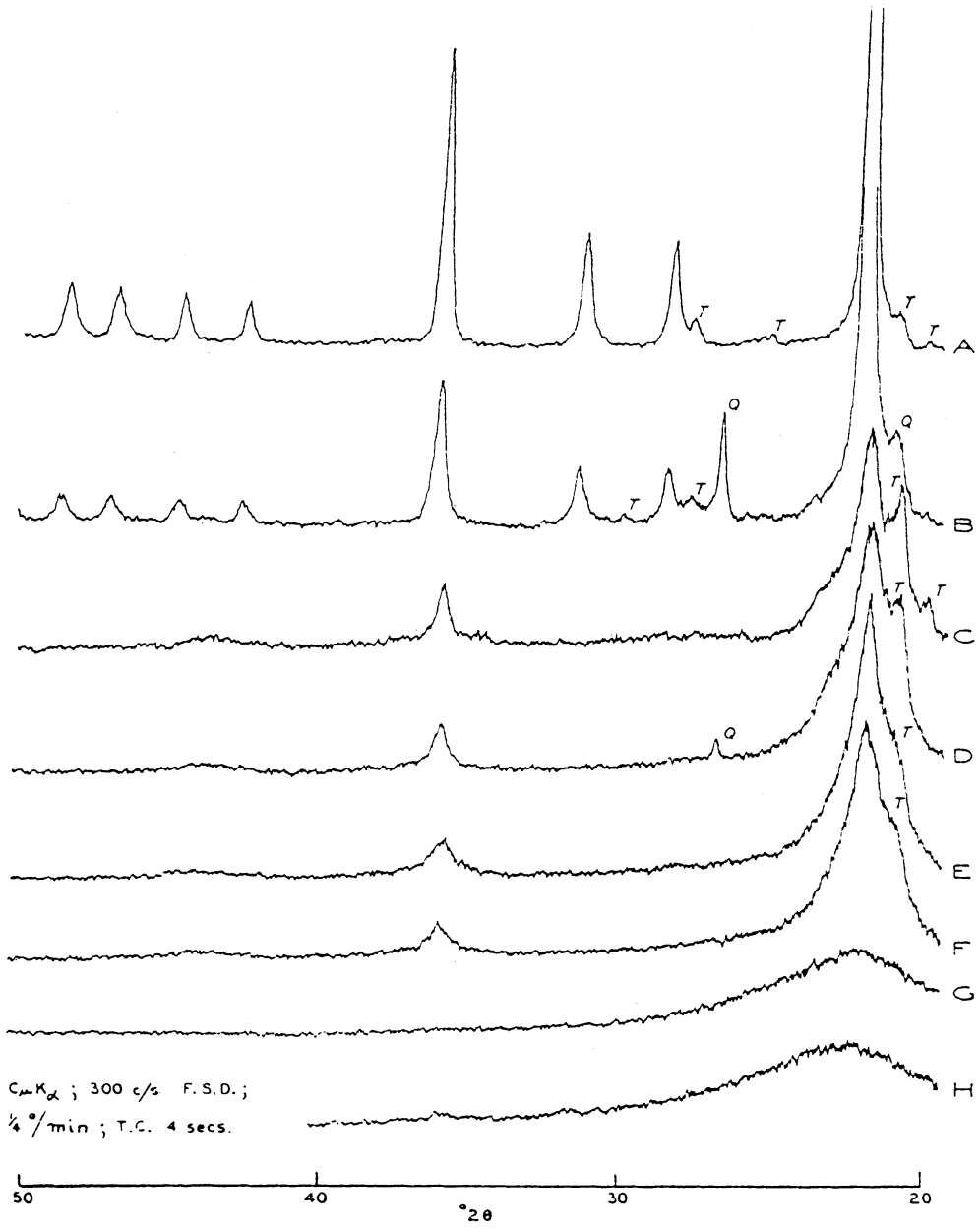

Figure 2-6: XRD of silica polymorphs and opals. Curve A: synthetic α-cristobalite. Curve B: Opal-C. Curves C to F: Opal-CT. Curves G and H: Opal-A. Peaks marked Q are due to quartz; those marked T are due to tridymitic stacking. From Jones and Segnit (1971).

2.5.1. Opal-A

From various XRD studies undertaken by Jones and Segnit (1971), opal-A was found to have a highly disordered near amorphous structure similar to glass (Figure 2-7). Nuclear Magnetic Resonance (NMR) studies show that opal-A is not quite as disordered as either synthetic opal (de Jong

et al. 1987; Graetsch *et al.* 1990; Adams *et al.* 1991; Brown *et al.* 2003), Libyan desert glass (LDG) or other synthetic silica glasses (Graetsch *et al.* 1990, 1994). However, IR and XAS data indicate that the structure of opal-A shows a resemblance to tridymite and cristobalite, respectively (Li *et al.* 1994; Elzea and Rice 1996). Opal-A is most commonly found as diatomite, a deep ocean sediment formed by the decomposition of marine life organisms (3.4.1). Opal-A can be further classified into two sub-categories: opal-AG (precious opal) and opal-AN (hyalite), which are further expanded upon below.

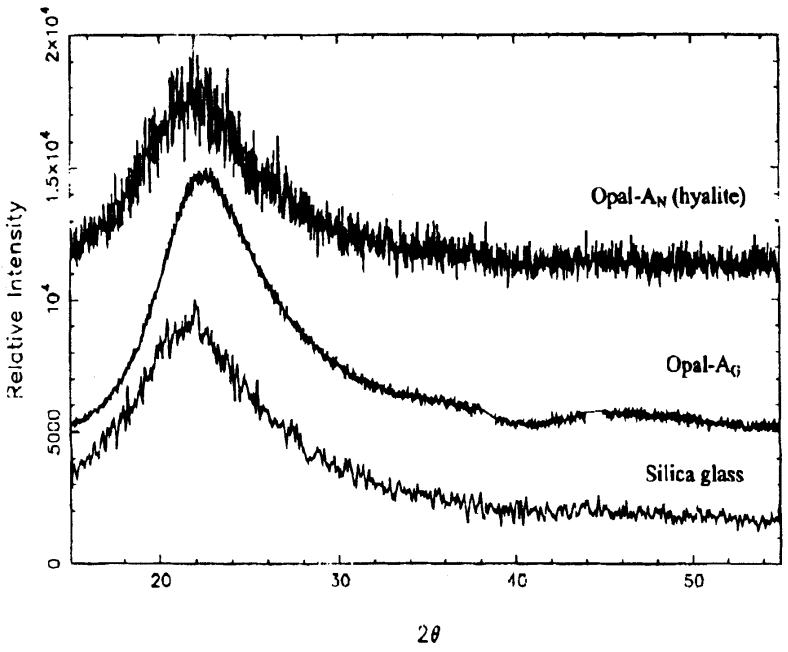

Figure 2-7: Top to bottom: XRD spectra of opal-AN, opal-AG and silica glas. From Smith (1998).

2.5.1.1. Opal-AG

Opal-AG refers to a "gel-like" structure (Flörke *et al.* 1991). These opals are commonly found as the sedimentary type of opals mined in the major Australian opal fields for gemmological purposes. The structure and formation processes of opal-AG will be discussed elsewhere in more detail (3.1), as most of the precious Australian opals investigated for this thesis belong to this classification. The microstructure of opal-AG consists of

spheres that are 100 to 300nm in diameter; this distinguishes it from opal-A of biogenic origin.

2.5.1.2. Opal-AN

Opal-AN is defined as having a "network amorphous" structure, which is characterised by a homogeneous microstructure when examined with SEM (Göttlicher *et al.* 1998). There is evidence that they form by a different process, possibly involving precipitation of silica from high temperature solutions onto cold substrates. Opal-AN is also known as hyalite, and does not display a poc. Flörke *et al.* (1973) hypothesised that opal-AN is formed through a different process to that of opal-AG, involving high temperatures and/or pressures (Flörke 1972; Flörke *et al.* 1973; Langer and Flörke 1974).

2.5.2. Opal-C and opal-CT

Opal-C and opal-CT can originate from biogenic silica (via silica diagenesis of marine diatoms in deep ocean sediments; 3.4.1), or they may be found in conventional terrestrial opal deposits that are normally associated with volcanic environments. Wood opal, caused by the replacement of the organic material in wood with opal, is also generally classified as opal-CT (Scurfield 1979; Scurfield and Segnit 1984). Several studies have closely examined the crystalline structure of opal-C and opal-CT using XRD (Flörke *et al.* 1975, 1976; Kastner *et al.* 1977; Kano and Taguchi 1982; Elzea *et al.* 1994; Rice *et al.* 1995; Nagase and Akizuki 1997). Other methods such as NMR (de Jong *et al.* 1987) and Transmission Electron Microscopy (Taijing *et al.* 1995; Cady *et al.* 1996) have also been utilised in an attempt to better understand their respective structures. Even though the designations opal-C and opal-CT refer to cristobalite and tridymite respectively, the corresponding structures of these opals only resemble the XRD patterns of cristobalite and tridymite; the actual opal structures are predominantly amorphous, as indicated by the broadening of the peaks in the XRD patterns (Jones and Segnit 1971; Figure 2-8).

It is the nature of this crystalline phase that has caused some difficulty in the categorisation of each class of opal (Jones and Segnit 1975; Elzea and Rice 1996; Nagase and Akizuki 1997). The complexity of the problem lies in the following issues.

1. The extent of the ordering contained within opal-C and opal-CT, and the size of these crystal domains is not accurately known. For example, the observed crystallinity may occur in small but very ordered domains in an otherwise amorphous matrix (cryptocrystalline); or, throughout the entire silica network, albeit in a more disordered state (paracrystalline).

2. The ratio of cristobalite to tridymite in opal-CT is also not accurately known, nor whether it exists as tridymite stacking faults in a predominantly cristobalite arrangement, or cristobalite stacking faults in a predominantly tridymite arrangement. The study of synthetic tridymite and cristobalite by Nukui and Flörke (1987) has also shown that up to eleven possible combinations of coexisting cristobalite and tridymite structural modifications can exist.

3. The cristobalite component of opal-CT exists as the high-temperature form, not the low-temperature form of cristobalite. Yet most opals are known to have formed through relatively low-temperature mechanisms, hence the high temperature polymorph of cristobalite should be absent in opal. (Greig 1932; Buerger and Shoemaker 1972; Jones and Segnit 1972). Moreover, opal-C cannot be defined as partially disordered α-cristobalite, as XRD patterns of opal-C also contain tridymite reflections (Elzea *et al.* 1994).

4. To further complicate the matter, samples of opal artificially crystallised (3 hours at 1200°C) were found to be composed of high-cristobalite (Sanders 1975). No evidence of intergrowth of cristobalite and tridymite were observed in the fragments of cristobalite or tridymite produced by this artificial crystallisation.

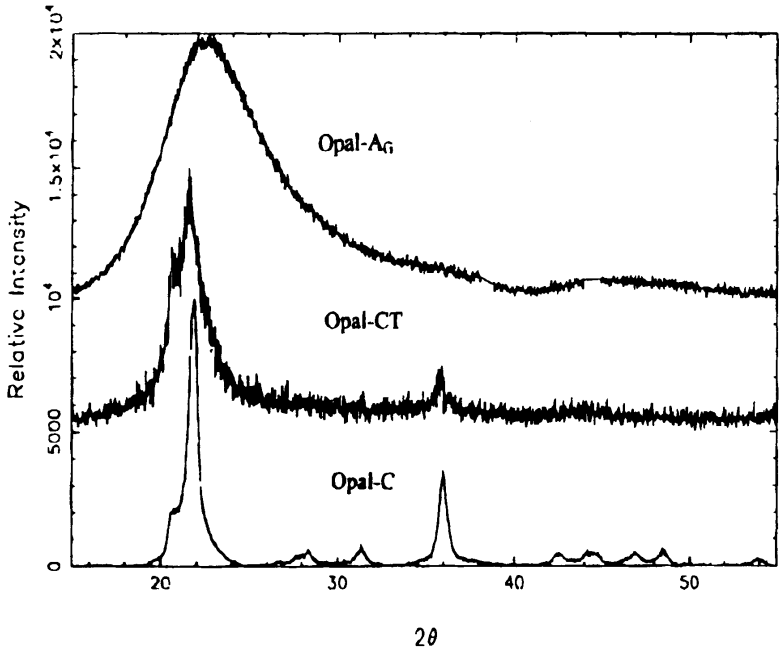

Figure 2-8: Top to bottom: XRD spectra of opal-AG, opal-CT and opal-C. From Smith (1998).

Using XRD and impedance spectroscopy, de Pablo-Galán *et al.* (1997) concluded that opal-CT was a crystalline stacked sequence of tridymite-M and high-cristobalite. However, IR spectra of opal-CT more closely resemble those of α-tridymite than α-cristobalite (Jones and Segnit 1971). Furthermore, NMR spectra of opal-CT resemble those of amorphous silica more than either tridymite or cristobalite (de Jong *et al.* 1987).

Based on Transmission Electron Microscopy (TEM) measurements (Elzea and Rice 1996), the opal component in all samples studied (which ranged from bentonite deposits of various localities, to diatomaceous Earth, porcellanites and zeolites) had mean crystallite sizes ranging from 120 to 320Å. The data also suggested that opal-CT had a cristobalite-like structure with varying degrees of stacking disorder leading to the appearance of tridymite reflections. This type of structure is more clearly depicted in Figure 2-9.

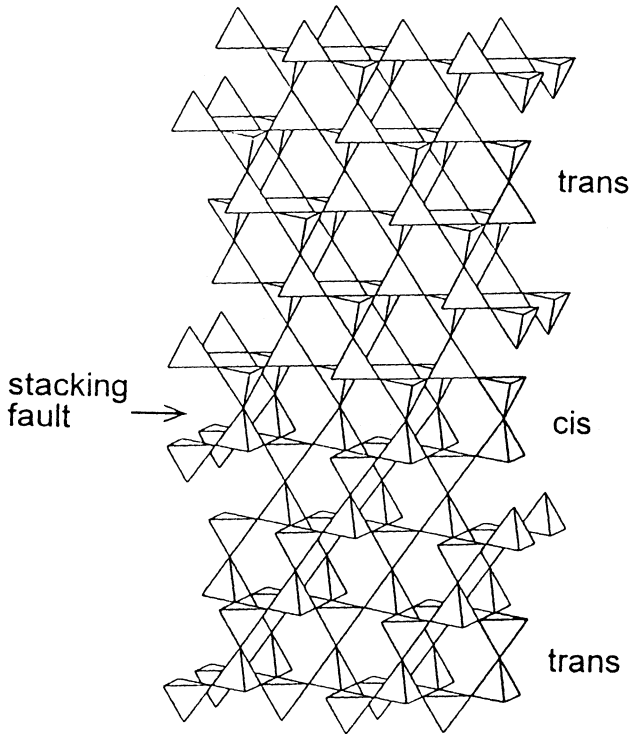

Figure 2-9: Tridymite stacking fault (cis) in a cristobalite sequence (trans). Each tetrahedron represents one SiO_4 group. From Graetsch et al. (1994).

There was also no precise distinction between opal-C and opal-CT samples investigated by Elzea and Rice (1996), meaning that the observed structures should be more accurately described as a continuous series extending from cristobalite to the tridymite phase (Plyusnina 1979; Williams and Crerar 1985; Williams *et al.* 1985; Elzea and Rice 1996). This result reflects the opal-A to opal-CT transformation that takes place during silica diagenesis (3.4.1).

The ordered regions of opal-CT occur in a matrix of disordered silica, although it is unknown whether the ordered domains are anhydrous and thus can be identified as cristobalite. Opal-C contains domains that are more ordered than those of opal-CT, as the corresponding XRD peaks of opal-C are sharper and more intense than those of opal-CT (Elzea and Rice 1996). Although the XRD patterns for opal-C are very similar to those of cristobalite, they are quite broad, meaning that there is insufficient long-range order for true crystallinity. The weak intensities observed for opal-CT,

imply that the volume (weight) fraction of ordered domains is small (probably not over 10%), or that the crystallite size is very small (X-Ray amorphous). The fraction of ordered domains in opal-C is more than that of opal-CT, but is probably considerably less than 50%. Opal-CT also contains considerable stacking disorder in the ordered domains, whereas opal-C has considerably fewer stacking faults.

Based on TEM observations, opal-CT can be classified into two types: columnar and massive (opal-CT_M). Both textures of opal-CT consist of thin and platy crystals attributed to the {101} faces of low cristobalite (Nagase and Akizuki 1997). The TEM images of opal-CT_M were similar to lepispheres described elsewhere (3.4.1; Figure 2-4).

High-Resolution Transmission Electron Microscopy (HRTEM) lattice-fringe images revealed that in some lussatite[1] fibres, the presence of different types of stacked lamellar domains resulted in the local distortion of silica tetrahedra at lamellar boundaries. Significant amounts of lattice strain were also identified in several lussatite and opal-C fibres, which occurred as isolated domains that separated ordered domains located along the direction of the fibre axes. These observations were interpreted as an indication of solid-state structural reordering (Cady *et al.* 1996).

2.5.2.1. Degree of crystallinity

Opals are commonly referred to as microcrystalline or cryptocrystalline throughout the literature. However, this is misleading as both terms should only be applied to samples with essentially 100% crystallinity. The term "microcrystalline" normally refers to samples that contain crystallites that are resolvable with the standard optical petrographic microscope (i.e. they have micron-sized dimensions). The term "cryptocrystalline" is reserved for samples with crystallites that are too small to be observable with the microscope (i.e. sub-micron size), which show sharp X-ray diffraction patterns. Although some degree of order is evident in opal-C and opal-CT on short length scales, opal-C and opal-CT do not readily fall into either of these categories due to the high degree of amorphous character. Therefore, opal-C and opal-CT are best described as "paracrystalline", a term which

[1] A fibrous variety of low-temperature cristobalite that occurs with opal and chalcedony near the surface of low-temperature hydrothermal deposits.

implies partial ordering in a predominantly disordered matrix, while still constituting a continuous network (Smith 1998).

2.5.2.2. Ratio of cristobalite and tridymite in opal-CT

X-ray diffraction patterns of opal-CT are consistent with models of interstratifications of cristobalite and tridymite (Guthrie *et al.* 1995). From calculated X-ray diagrams simulating disordered stacking of cristobalite and tridymite it can be estimated that in the most disordered opal-CT, the stacking is about 50% tridymitic and 50% cristobalitic (Graetsch *et al.* 1994). The 19.5 - 24.5° 2θ band is sensitive to the relative proportions of tridymite and cristobalite (35-55% tridymite). The band at 41 - 45° 2θ is very sensitive to ordering (a peak appears at 43° 2θ upon ordering of the structure towards a cristobalite stacking sequence). However, Guthrie *et al.* (1995) reported that water is probably not present on a specific crystallographic site within the opal-CT structure.

2.5.3. Infrared Spectroscopy

Almost all siloxane (Si–O–Si) compounds show at least one strong band in infrared spectroscopy, between λ = 1000 and 1110 cm^{-1}, arising from an asymmetric Si-O-Si stretch vibration. With an essentially infinite siloxane chain, the absorption occupies almost the entire interval between 1000 and 1110 cm^{-1} with peaks of maximum absorption at 1085 and 1020 wavenumbers (Smith 1960). Table 2-2 lists the common IR assignments of hydrous silicates.

XRD patterns of opal-CT reveal that its structure includes cristobalite stacking, but the expected IR absorptions at 385 and 620 cm^{-1} have not been observed (Figure 2-10). Instead, the IR spectra of opal-CT and opal-A are similar to that of tridymite (Jones and Segnit 1971). Spectra of various opal-CT specimens show only a broad absorption centred at 475 cm^{-1}, while spectra of opal-A show a broad absorption centred at 465 cm^{-1}, and its absorption at this frequency is rather less than that of opal-CT.

Absorption (cm^{-1})	Vibrational mode	Reference
300	Low-cristobalite (inter-tetrahedral vibration)	Graetsch *et al.* 1994 Etchepare *et al.* 1978
380	Low-cristobalite (inter-tetrahedral vibration)	Graetsch *et al.* 1994 Etchepare *et al.* 1978
480	Tetrahedral silicates	Graetsch *et al.* 1994 Plyusnina 1979
525		Plyusnina 1979
550–560	Presence of octahedrally coordinated aluminium	Webb and Finlayson 1987
620	Low-cristobalite (inter-tetrahedral vibration)	Graetsch *et al.* 1994 Etchepare *et al.* 1978
780–800	α-quartz doublet	Plyusnina 1979
790	Tetrahedral silicates	Graetsch *et al.* 1994 Plyusnina 1979
950	Si–OH deformation	Plyusnina 1979 Plyusnina *et al.* 1971 Webb and Finlayson 1987
1100	Tetrahedral silicates (antisymmetric Si–O–Si stretching vibration)	Graetsch *et al.* 1994 Webb and Finlayson 1987
1200	α-cristobalite	Plyusnina *et al.* 1971
1230	Si–O–Si vibration	Pechar 1985
1650 1630	OH symmetrical bending deformation (v_2)	Plyusnina 1979 Plyusnina *et al.* 1971 Langer and Flörke 1974
2340	(High temperature) Short H–bond of about 2.6Å	Graetsch *et al.* 1985
2359/2339	CO_2	Langer and Flörke 1974
2900–3700	Fundamental OH stretching of molecular water and Si–OH	Graetsch *et al.* 1985 Jones and Segnit 1969
3400–3440	Superposition of molecular water and strongly H–bonded surface silanol groups	Graetsch *et al.* 1985 Thompson 1965 Langer and Flörke 1974
3550	OH deformation	Jones and Segnit 1969
3650	OH symmetric stretching deformation (v_1) (Internal weakly interacting silanol groups not associated with impurities)	Graetsch *et al.* 1985 Plyusnina 1979 Langer and Flörke 1974
3740	OH antisymmetric stretching deformation (v_3) (surface silanol groups not associated in interactions)	Graetsch *et al.* 1985 Langer and Flörke 1974
4350	Bending and stretching vibrations of hydroxyl (free from superposition of H_2O molecules)	Graetsch *et al.* 1985 Graetsch *et al.* 1987
4500	Bending and stretching vibrations of hydroxyl (free from superposition of H_2O molecules) – the absence of high-energy component at 5250 in silica gel and amorphous opal indicates absence of monomeric water.	Graetsch *et al.* 1985 Graetsch *et al.* 1987 Langer and Flörke 1974 Langer *et al.* 1979
5100–5260	Combination of bending and stretching vibrations of molecular water	Langer and Flörke 1974 Graetsch *et al.* 1987 Langer *et al.* 1979
7000	OH stretching overtone	Langer and Flörke 1974

Table 2-2: IR absorption peak assignments.

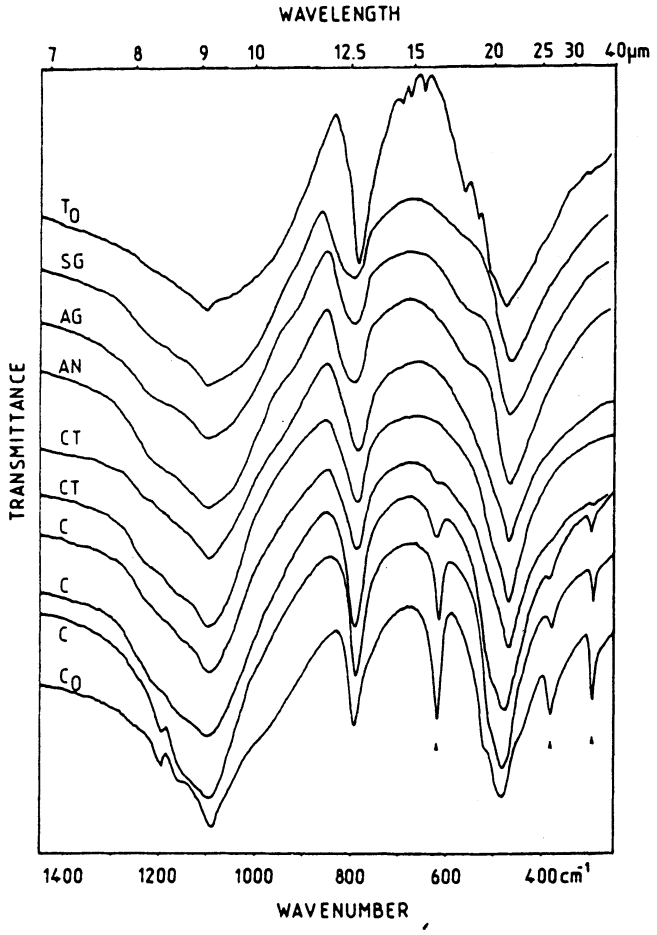

Figure 2-10: Infrared spectra of various silica polymorphs and opals. T_o = tridymite; SG = silica glass; AG = opal-AG; AN = opal-AN; CT = opal-CT; C = opal-C; and C_o = cristobalite. From Graetsch et al. (1994).

The opal component is revealed by the weak band at 1200 cm^{-1} (Hunt 1950) and a gradual broadening of the 1167 and 525 cm^{-1} bands. Opal-C produced spectra with three distinctive bands: two strong ones around 100 and 470 cm^{-1}; and a medium strength one at 790 cm^{-1}. This demonstrates that the main structural element in opal-C is α-cristobalite, but that this is extremely disordered, because the 620 cm^{-1} band specific for ordered cristobalite is absent (Plyusnina 1979).

Graetsch *et al.* (1994) also observed that as the silica network in opals became more disordered (opal-CT to opal-A) the infrared absorption bands pertaining to the silica framework (620, 380 and 300 cm^{-1}) broadened and shifted slightly to shorter wavelengths, which revealed differences in the local tetrahedral arrangements.

2.6. NATURE OF WATER

Before the water content of opals can be discussed in detail, a distinction must be made between silanol water, adsorbed molecular water, and free water. Silanol (chemical) water is a hydroxyl (OH) group covalently bonded to the silicon atom in the SiO_2 network. Adsorbed (molecular) molecular water is held in place by hydrogen bonding to the hydroxyl groups (McDonald 1958; Benesi and Jones 1959). Free (molecular) water is present in the microstructural voids and it is retained by capillary action.

Several IR spectroscopic studies of opals concluded that both molecular water (H_2O) and chemically bound water (–OH) were present in opal-AN, opal-AG, opal-CT and opal-C (Segnit *et al.* 1965; Langer and Flörke 1974; Webb and Finlayson 1987). The proportion of molecular and chemical water varies between each of these types of opal. The model discussed below was proposed by Langer and Flörke (1974) for the incorporation of water within opal-AG.

2.6.1. Molecular water

Two different types of molecular (physically bound) water have been isolated with near-infrared spectroscopy, A and B: Type A has almost no H-bonding and occurs as isolated water molecules trapped within "cages" in the network of SiO_2; type B has liquid-like H-bonded water occurring in larger voids or as a multi-molecular film on inner surfaces (Langer and Flörke 1974). The proportion of the B type molecular water increases from opal-AN to opal-AG and to opal-CT (Figure 2-11).

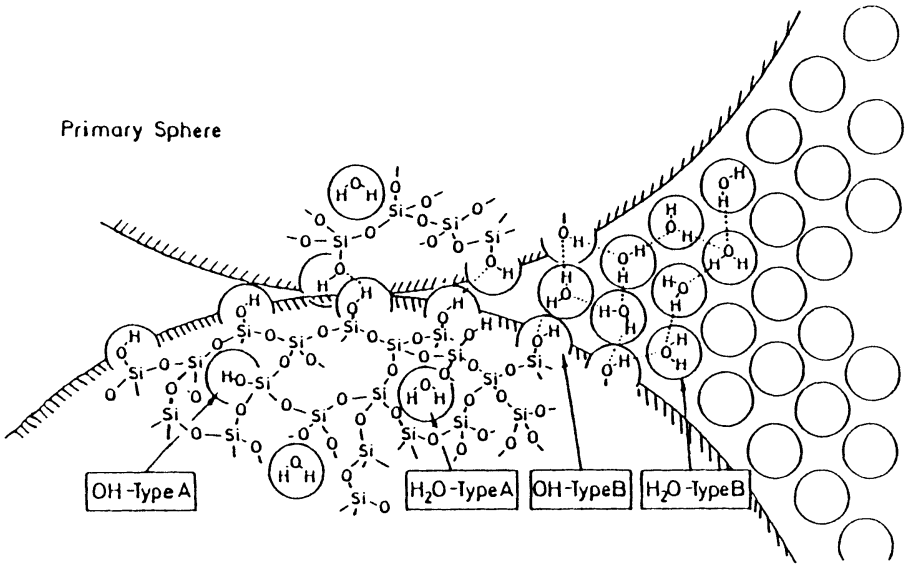

Figure 2-11: Model of water incorporation in opal-AG. From Langer and Flörke (1974).

With infrared spectroscopy, molecular water is generally observed as a broad absorption band at 5000-5300cm^{-1} (Anderson and Wickershiem 1964). Such absorption peaks have been observed in the IR spectra of opal indicating the presence of free water (Langer and Flörke 1974; Plyusnina 1979). Langer and Flörke (1974) found that molecular water was present in two different states, non-hydrogen bonded and hydrogen-bonded.

2.6.1.1. Non hydrogen-bonded

The high-energy component of the absorbance peak at 5260cm^{-1} was assigned to water molecules almost free of H-bonding (Figure 2-12). If the SiO_2 tetrahedra network is constructed with six-membered rings on average, it contains cages with an estimated diameter of 35Å. Thus, one isolated water molecule (diameter 28Å) can be accommodated in each of these cages. These water molecules are expected to be either non-hydrogen bonded or only weakly H-bonded, because the charge field within the cages is nearly symmetrical (Langer and Flörke 1974).

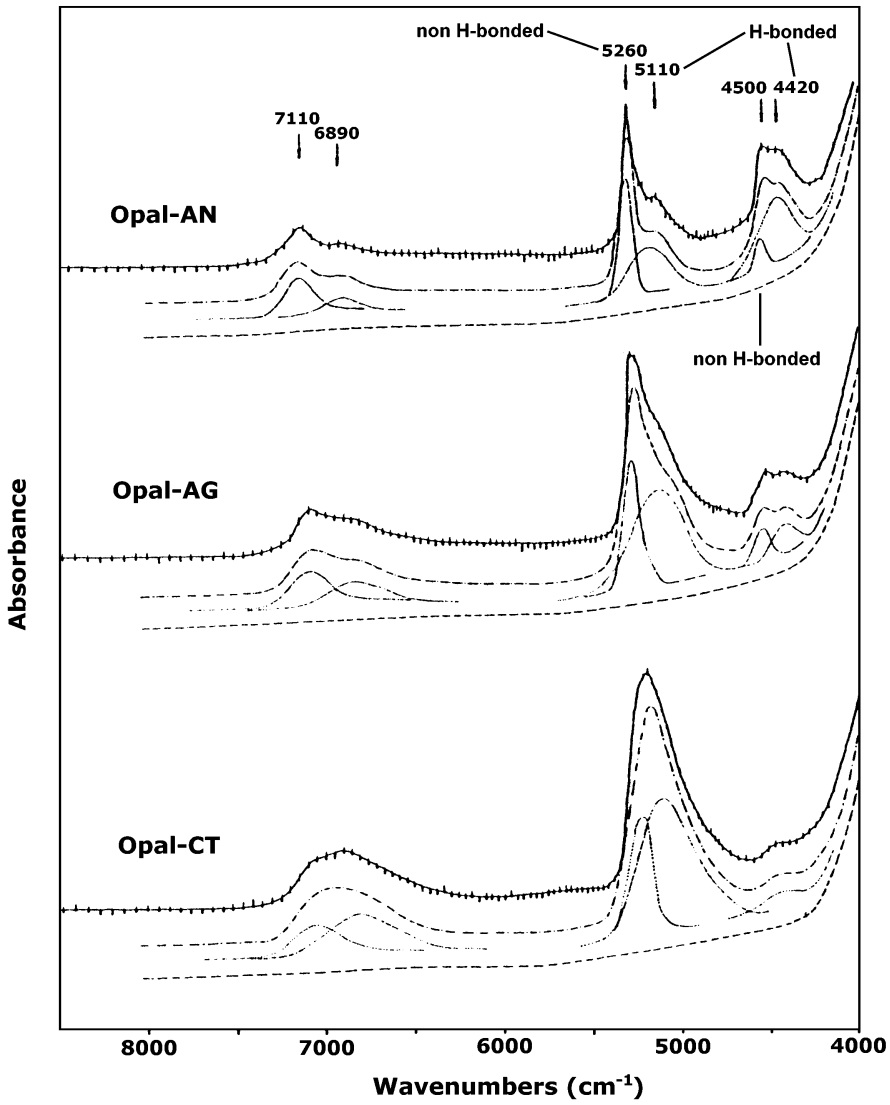

Figure 2-12: IR spectra showing H_2O and OH combination bands. From Langer and Flörke (1974).

2.6.1.2. Hydrogen-bonded

The position and large half-width of the other component of the absorption at 5100cm^{-1} compares very well with that of the corresponding vibrational mode observed in liquid water, in which the H_2O molecules are hydrogen bonded. This type of water is H-bonded and must occur in larger voids or as multi-molecular films on inner surfaces. Opal-CT contained the highest amount of the H-bonded molecular water, which is a consequence of its large inner surface and irregular microstructure; opal-AN had the lowest content, this result was ascribed to the higher density of the silica network of opal-AN.

2.6.2. Chemically bound silanol groups

Silanols (Si-OH) exhibit the usual OH stretching bands between 3333 and 3703 cm^{-1}, as found in organic alcohols. In addition, the asymmetric SiO stretching at 833 and 909cm^{-1} is also present for silanols (Smith 1960). From infrared spectroscopy, silanol groups are known to give an absorbance at roughly 4500cm^{-1} (Zarubin 2001). Opal-AG and opal-AN have two types of silanol (chemically bound) water: A and B; with B having stronger H-bonding than A. These were attributed by Langer and Flörke (1974) to internal silanols located at defects (A); and surface silanols interacting with water molecules (B). The fraction of silanol water varies as follows: 0.9% Si–OH in opal-AG; 1.5% in opal-AN; and 0.3% in volcanic opal-CT, from Mexico and Tintenbar (Table 2-3). Therefore water in opal-AN is 30-40% chemically bound; opal-AG 10-15%; and opal-CT 2%. This difference in the proportion of silanol and molecular water was attributed to the different formation times of the various opal types, rapid in the case of opal-AN, slower in opal-AG and slowest in opal-CT (Langer and Flörke 1974).

	Opal-AN	Opal-AG	Opal-CT	Opal-C
Si–OH	1.4 – 1.6%	0.8 – 0.9%	0.2 – 0.4%	0.1 – 0.3%
H_2O	3.5 – 4.6%	5.1 – 6.3%	widely varying	1.1 – 1.6%
Total	3.0 – 6.70%	4.88 – 15%	3.5 – 15.5%	1.0 – 7.4%

Table 2-3: Typical water content (%) of the various water fractions contained within opal. From Langer and Flörke (1974), Graetsch et al. (1987, 1985), Adams et al. (1991), Flörke et al. (1991), and Esenli et al. (2001).

2.6.2.1. Single and twin hydroxyl groups

Silanol groups may also occur either as single (vicinal) or double (geminal), and both types are shown in Figure 2-13 (Thompson 1965). However, with IR spectroscopy, no change in the OH–stretching energy occurs when more than one OH is bound to one Si, provided the protons are not involved in Hydrogen bonding. Hence, the more H-bonded hydroxyls may not necessarily be twin hydroxyl (or geminal) groups (Langer and Flörke 1974).

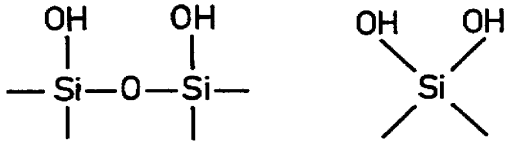

Figure 2-13: Left: single (or vicinal) hydroxyls. Right: twin (or geminal) hydroxyl groups. From Thompson (1965).

2.6.2.2. Inferences concerning the genesis of opal

The ratio of Si–OH to the total water content is significantly different for opals of different types, reflecting their different microstructure and formation conditions (Langer and Flörke 1974). Opal-AN showed the highest Si–OH water fraction, indicating an origin from SiO_2–H_2O fluid phases containing $Si(OH)_4$ or $Si_2O(OH)_6$, or higher associated species $Si_nO_{n-1}(OH)_{2n+2}$ (Flörke *et al.* 1973; Langer and Flörke 1974; Langer *et al.* 1979). Although the nature of the silica species and the equilibria between them in supercritical fluids are not yet clear, these fluid phases contain hydrous silica species with small molecular weights at high concentrations, i.e. in close contact (Langer and Flörke 1974). It is conceivable that during the rapid solidification on a cold substrate, numerous OH groups were retained (Langer and Flörke 1974). Opal-AG is assumed to form rapidly from super-saturated solutions (or sols) at low temperatures in sediments 10 to 100 metres below the Earth's surface (Jones and Segnit 1966; 3.1). Thus, the relatively high amount of Si–OH contained within this type of opal reflects its rapid formation (Langer and Flörke 1974).

Opal-CT showed a very low Si–OH fraction and it was reported that this may have mainly been incorporated into the surface layers of the polished platelets studied (Langer and Flörke 1974). Very low Si–OH contents would be expected from $SiO_2.nH_2O$ minerals that formed slowly from highly diluted true solutions at low temperatures (Langer and Flörke 1974).

2.6.2.3. High Pressure

In a high-pressure IR study of opal and other silicates, Langer *et al.* (1979) reported that with increased pressure, the relative intensity of the IR absorbances between 4550 and 4250 cm^{-1} decreased. At higher water

pressures, however, the relative intensity of the band at 5260 cm^{-1} (due to non-hydrogen bonded Si–OH groups) decreases in favour of the broad component at 5100 cm^{-1} (due to hydrogen bonded Si–OH groups). This effect was more pronounced with opal-AG than opal-AN. Langer *et al.* (1979) concluded that the preferential increase of H-bonded silanol groups evident in opal-AG was possibly due to two factors:

1. The intrusion of water from interstices between secondary spheres into those between primary spheres.
2. The deformation of the sphere structure, which reduces distances between –OH groups.

2.6.2.4. Other IR studies

In an IR study of Brazilian agate geodes, Graetsch *et al.* (1985) detected both molecular and hydroxyl water within Opal-C and chalcedony. Graetsch also distinguished between two different types of hydroxyl bonds; hydroxyls that were internally bonded at structural defect sites (point defects, dislocations, low angle or twin boundaries) and also surface silanol groups which were more strongly H-bonded among neighbouring surface silanols. With increased H-bonding, the absorbances shift to lower energy and become increasingly broad. Of the opal-C samples that were analysed having a total water content of 1 to 2%, roughly 80% of the total was identified as molecular water and nearly all of the remaining 20% hydroxyl groups were identified as surface silanols rather than internal hydroxyl groups.

IR Spectra of opal-AN and opal-AG (from Andamooka and Coober Pedy) showed that traces of CO_2 were present in the samples (Langer and Flörke 1974). The refractive index decreased with increased water content (Langer and Flörke 1974).

2.6.2.5. Small Angle Neutron Scattering (SANS)

Opal-A investigated with SANS shows the strongest features in the spectrum at 75 meV, associated with excitations assigned to torsional motions of the H_2O molecule in water/ice (Sinclair *et al.* 1992; Sosnowska *et al.* 1997).

2.7. RAMAN SPECTROSCOPY

Opal has been investigated using Raman spectroscopy (Champagnon *et al.* 1997; Smallwood *et al.* 1997; Ostrooumov *et al.* 1999). Most of the vibrational modes were evident in the region below 1800cm^{-1}, apart from the broad –OH stretch at 3300cm^{-1}. The peaks observed at 335cm^{-1} for three volcanic samples were not characteristic of pure silica either in the crystalline or amorphous states, and were therefore attributed to presence of impurities, as silicates exhibit vibrational modes in the 300 – 400 cm^{-1} region (Smallwood *et al.* 1997). Spectra of volcanic opal-CT were sharper than those of opal-AG. The spectra of volcanic opal-CT samples were found to correlate fairly well with the spectrum of α-tridymite, but there were also similarities between α-tridymite and the sedimentary opals, indicating that they contained some crystallinity (Smallwood *et al.* 1997).

2.8. ATOMIC FORCE MICROSCOPY

Atomic Force Microscopy (AFM) is able to resolve extremely fine (atomic-scale) textures in three dimensions. Tsunekawa *et al.* (1997) first used AFM to characterise the incorporation of CdS nanoparticles in synthetic opal. Larson *et al.* (1996) used AFM to investigate the similarities between opals, synthetic glass and LDG (4.1.7.1). In a more recent study (Frischat *et al.* 2001), AFM was also carried out on LDG and precious opal samples to compare their microstructures. In both studies, opal displayed an average roughness [Root Mean Square (RMS)] of 5±1nm, z-ranges (height changes) of 30±10nm, with "outcrops" on the order of 100-200nm diameter; whereas LDG displayed an RMS roughness of only 0.6±0.1nm, with z-ranges of 4±1nm and there was no indication of bigger outcrops. This indicated that precious opal had a more porous, open structure than LDG. Although the precious opal examined was X-Ray amorphous, some of the outcrops observed in the AFM images displayed straight edges[1]. Crystal-like (hexagonal) polygons were also present on some images, indicating the presence of a crystalline phase with extremely small grains.

[1] Note that the straight edges discussed here are present on the atomic scale, it does not refer to the larger scale of colloids.

2.9. PHOTONIC CRYSTALS

Recently, there has been immense scientific interest in the synthesis of artificial opal structures for use as photonic band gap materials; literally thousands of papers have been published in the literature since the late 1990's (Astratov *et al.* 1996; Bogomolov *et al.* 1997; Romanov *et al.* 1997; Vlasov *et al.* 1997; Davydov *et al.* 2000; Zakhidov *et al.* 2001). Opals are used as templates in the manufacture of "photonic crystals" by impregnating them with semiconductors. Photonic crystals possess a band gap that forbids propagation of a certain frequency range of light. Applications exist for highly efficient opto-electronic devices [waveguides; cavities; mirrors; 90° light bending with 100% transmission; perfect channel-drop filters; low (zero) threshold micro lasers, all-optical transistors]. The need to control the ordering and placement of spheres in the opal template is of primary concern if the fabrication of such devices is to be a success.

3. MECHANISMS OF OPAL FORMATION

"What is a scientist after all?
It is a curious man looking through a keyhole,
the keyhole of nature,
trying to know what's going on."
–Jacques Cousteau, Oceanographer

3.1. INTRODUCTION

This chapter provides pertinent information on the various formation mechanisms of both opal-AG and opal-CT. Opal-AG is discussed foremost, as most samples investigated in this thesis were opal-AG. Several other essential processes regarding the post-depositional changes of the opal microstructure will also be discussed. The remainder of the chapter is devoted to the incorporation of elements during the period of opal formation.

3.2. OPAL-AG FORMATION

Opals are naturally occurring and are produced by the polymerisation and precipitation of silica colloids from supersaturated silica solutions over long intervals of time (Darragh *et al.* 1966; Jones *et al.* 1966; Darragh *et al.* 1976). There are several stages required in the formation of opal: cavity formation, dissolution of silica, nucleation, polymerisation (growth of colloids), sphere ordering, sedimentation, and solidification. These processes are discussed in further detail below.

Jones and Segnit (1966) clearly state that there is no evidence of recent deposition of opal, and that no soft gels appear to have been encountered by miners, although fluid inclusion studies have been carried out on Mexican opals (Koivula *et al.* 1983; Spencer *et al.* 1992). A personal communication with a Lightning Ridge opal polisher confirms that sometimes opal is found which contains a fluid phase.

One of the major aspects of opal formation that is yet to be determined, is whether the colloids were formed in the cavities in situ, or whether they were formed elsewhere and then transported into the cavities. It is commonly observed that opals fill the entire cavities they are contained within. Given that the quantity of silica in a supersaturated sol is not exceptionally high, it cannot readily form a dense opal precipitate that completely fills all the available space, simply because there is insufficient silica to begin with in the aqueous state. Hence, this evidence supports the latter idea of silica transport. It is also unlikely that several generations of

sols formed each opal consecutively, as opal nodules are generally homogeneous.

3.2.1. Geological environment associated with sedimentary opals

During the Jurassic and Cretaceous periods, the Great Artesian Basin was a vast shallow inland sea, into which immense thicknesses of sands and sandy clays were deposited. During the late Cretaceous and early Tertiary periods, the region experienced rapid climatic change. The temperate marine sea became a desert habitat (Keller 1990). The main opal fields of Australia are found inland in these currently arid regions, occurring in host rocks deposited more than 70 million years ago during the Cretaceous period (Darragh *et al.* 1966). Opal nodules, commonly referred to as "nobbies" by opal miners, are found at depths ranging from 5 to 40m; nobbies are also found at the surface where it has been exposed by post-Tertiary erosion.

All precious opal is thought to be deposited relatively recently on the geological timescale, as it cannot withstand the effects of heat and pressure that almost always accompany long-term geological processes (Darragh *et al.* 1976). Under such conditions opal undergoes diagenesis to other crystalline phases (3.4.1).

The following two points are regarded as general requirements for the formation of sedimentary opal (opal-AG):

1. An abundant supply of soluble silica. It is thought that the silica in opal is derived from the alteration of feldspar to kaolinite (with its erosional-breakdown from weathering) in the layers of claystone overlying the opal (Darragh *et al.* 1966), but it could also have originated from the dissolution of desert sandstones (Jones *et al.* 1966). Another possibility is that silica colloids could have formed from the breakdown of the natural mineral biotite; experiments have shown that 10% sulphuric acid decomposed biotite at ambient temperatures, removing all cations apart from silicon, and leaving an essentially amorphous silica residue, consisting of

small spheres with a diameter of 50nm (Jones and Segnit 1966; Jones *et al.* 1966).

2. The formation of underground voids to provide suitable 'traps' in which silica can accumulate. Subterranean crevices are created by earthquakes, shrinkage, or localised faulting. Voids may also form by the decomposition of organic matter such as wood, shells and bones, producing opalised wood, shell and bone, respectively. Even so, many of these cavities remain unfilled. There is also nearly always an impermeable bentonite layer just below or close to the opal levels (Darragh *et al.* 1966). The ground water, which contains dissolved silica, can then be confined to these cavities by an impervious bed of underlying bentonite (Jones and Segnit 1966).

Sulphate deposits are often found in association with the environment of opal deposition. Examples of this include the occurrence of gypsum at Andamooka; alunite at Cobber Pedy and Lightning Ridge; and glauberite at White Cliffs (Jones *et al.* 1966).

3.2.2. SiO_2 solubility

During rainfall, rainwater permeates down through sedimentary deposits to the underlying water table. Silica which is dissolved in this water is transported directly to these subterranean cavities (Darragh *et al.* 1966). Silica is soluble in water and its dissolution involves a chemical reaction (hydrolysis) in an excess of water, producing monosilicic acid:

$$SiO_2 + 2\ H_2O \rightarrow Si(OH)_4$$

Silica's solubility in water depends on the pressure, pH, temperature, as well as its crystallinity (Figure 3-1), the radius of curvature of silica surface (e.g. size of silica particles), and also the purity of the solution. The solubility of silica in water is roughly 100-130 ppm for amorphous silica at 25°C, below a pH of 8 (Krauskopf 1956; Okamoto *et al.* 1957). Analysis of water samples from bores near Andamooka show silica concentrations of up to 84 ppm at a pH of 8 to 9 (Jones and Segnit 1966). The solubility of silica increases as the temperature or pH of the solution is raised (Figure 3-2).

Impurities such as metal cations reduce the solubility of silica. Trace amounts of Al, for example, reduce the solubility of silica (Okamoto *et al.* 1957; Iler 1973; 3.4.3.4; 3.2.3.1). Enrichment of the silica solution occurs through gradual evaporation of the water through the porous overlying rock, or rather, the permeation of the water into the overlying sandstone (Darragh *et al.* 1976).

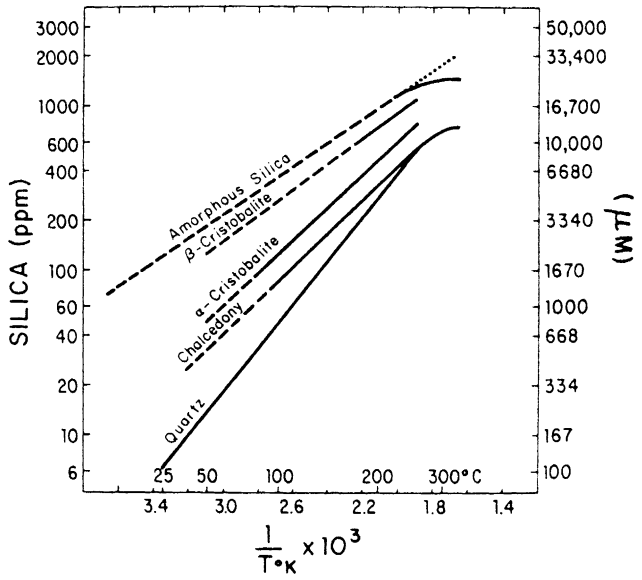

Figure 3-1: Silica solubilities of various silica polymorphs vs. temperature. From Kastner et al. (1977).

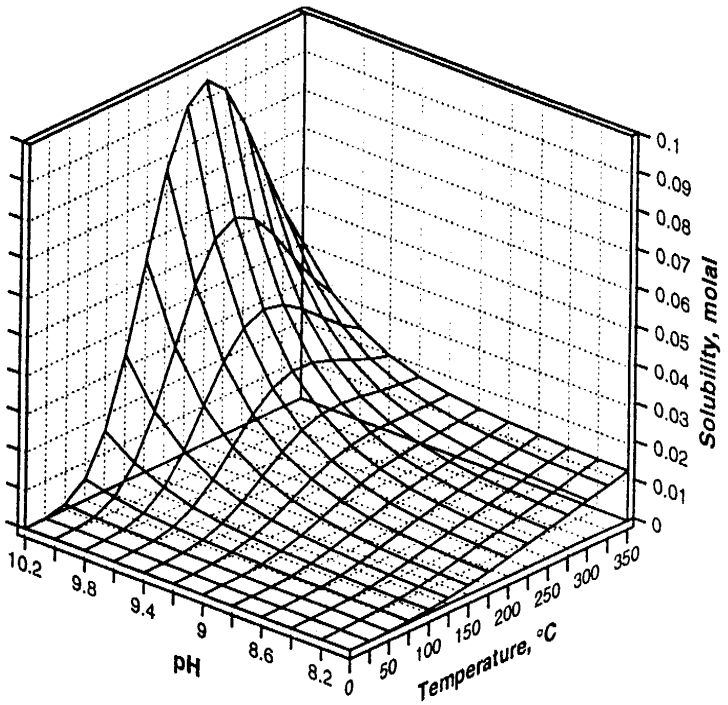

Figure 3-2: Silica solubility at various pH and temperature values. From Dove and Rimstidt (1994).

At a pH above 10.5, silica dissolves and forms silicic acid (Figure 3-3).

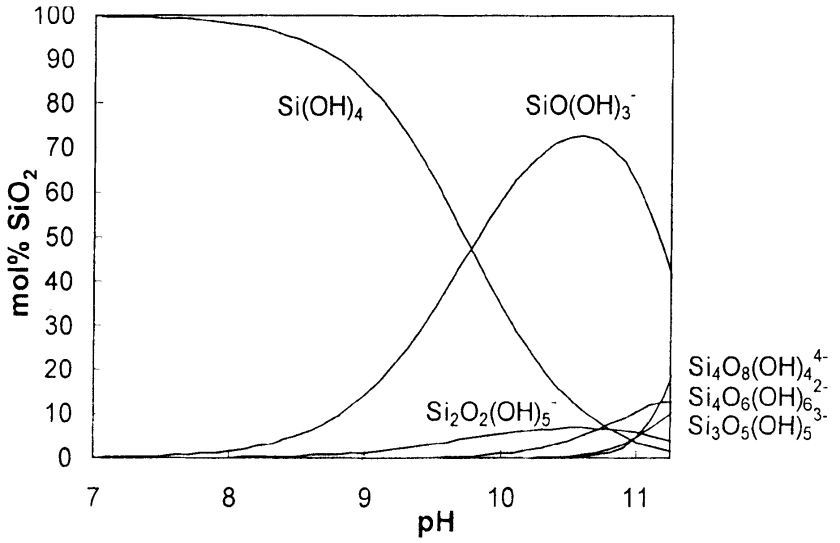

Figure 3-3: Silica species present at various pH values. From Dietzel (2000).

3.2.3. SiO_2 nucleation

Once a low concentration silica solution exists with monosilicic acid monomer present, it may form a sol or colloidal silica solution. Under certain environmental conditions[1], the silica concentration of the solution can increase until it is above solubility limit for amorphous silica. This supersaturated state is thermodynamically unstable and nucleated particles begin to form as silica proceeds to polymerise from the solution. Alternatively, a gradual temperature or pH reduction (or even a gradual increase in metal cation impurities) could theoretically decrease the solubility of silica. Amorphous silica will nucleate directly rather than quartz because amorphous silica has a lower critical dissolved silica concentration for nucleation (Kastner *et al.* 1977; Iler 1979; Williams and Crerar 1985; Steefel and Van Cappellen 1990; Hinman 1998).

3.2.3.1. Presence of electrolytes during nucleation

Alkali metal ions provide a large positively charged surface for the aggregation of silicate and hydroxide anions (Hinman 1998). As silica possesses a negatively charged surface, nucleation is more likely to be initiated at the surfaces of these cations. Iler (1979) suggested that metal hydroxide surfaces provide a mechanism of silica concentration that nucleates quartz.

[1] This condition may be met by invoking the following processes: enrichment of the solution may occur by additional silica leaching from the surrounding sandstone, until silica reaches its solubility limit. If there is subsequently a gradual evaporation of water through the semi-permeable overlying rock, a supersaturated solution is capable of being formed.

3.2.4. Particle formation and polymerisation

The polymerisation of silica involves the condensation of silanol groups according to the following reaction:

Equation 3-1:

$$-Si-OH + HO-Si- \rightarrow -Si-O-Si- + H_2O$$

or

$$Si_nO_{2n} + mSi(OH)_4 \rightarrow Si_{n+m}O_{2n+2m} + 2mH_2O$$

As this reaction proceeds, the molecular weight of the silica increases. The rate of polymer growth and silica precipitation is influenced strongly by temperature, pH, ionic strength and the degree of supersaturation (Crerar *et al.* 1981). Silicic acid has a strong tendency to polymerise in such a way that there is a maximum of siloxane (Si–O–Si) bonds and a minimum of uncondensed silanol (Si–OH) groups in the polymer network. Therefore, the silica nucleates as spherical particles to reduce the number of interfacial Si–OH groups, because a sphere has a higher volume to surface area ratio than other particle geometries (Figure 3-4).

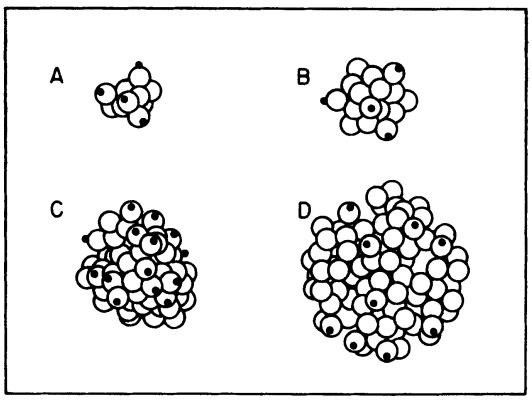

Figure 3-4: Models of (A) cyclic trisilicic acid, and (B) cubic octasilicic acid. (C) and (D) are theoretical colloidal particles formed by condensing monomer to form closed rings with one surrounding layer of silica bearing silanol groups. Spheres represent oxygen atoms; black dots, hydrogen atoms. From Iler (1979).

The rapid generation of amorphous silica surface area ensures that the concentration of $SiO_{2(aq)}$ cannot remain above saturation with respect to amorphous silica for very long periods (Steefel and Van Cappellen 1990).

It is only within the pH range of 6.5 to 10.5 that the silica particles possess a negative surface charge, allowing them to repel each other and grow without aggregation to a relatively large size of between 20 and 50 nm (Figure 3-5; Iler 1979). These primary particles reportedly have the ability to coacervate (Kruyt 1949); this is a process where the primary particles spontaneously accrete around a central primary particle (Iler 1979). During the formation of opal-AG, primary particles are said to form much larger secondary particles with up to five "shells" (Darragh *et al.* 1976). However, Iler (1979) noted that this process only transpired under certain conditions of pH, when the salt concentration was low and the silica concentration was below 1%. The idea that the secondary spheres in opals are composed of smaller primary particles is also accompanied by the following problems:

1. Apart from the observation of 'rings' in the SEM microstructures of opals, primary particles have never been directly observed without etching the fracture surfaces with HF acid. This is still the case even when thin opal fragments of opal are examined directly by TEM using very high magnifications (Sanders 1975; Darragh *et al.* 1977).
2. It is highly improbable that a multitude of these primary particles suspended in a sol motivate themselves to accrete around other primary particle 'cores', and that perfectly spherical secondary spheres with the exact same number of shells arise simultaneously. If this were the case, imperfect spheres would be more likely to occur, such as spheres of significantly different sizes (different number of shells), incomplete spheres and ovoid-shaped spheres would also be expected to form. Yet these are rarely observed in the SEM microstructures of opals.

3. The formation of large monodisperse sols (>100nm diameter) is possible without the coacervation of primary particles, through the Ostwald ripening process (3.2.6).

4. In many cases, opals show gradual transitions in secondary sphere size across the sample. This is easily demonstrated by the change in the play of colour observed throughout the sample, as the maximum wavelength of light observed is proportional to the sphere size (2.3.1). The spheres invariably increase in size towards the bottom of the sample, the colour changing from violet to red. (Darragh *et al.* 1966). The finding that sphere size gradually changes across a sample is generally not consistent with the primary particle coacervation model; it is more likely to occur if the spheres grow directly from a single nucleus.

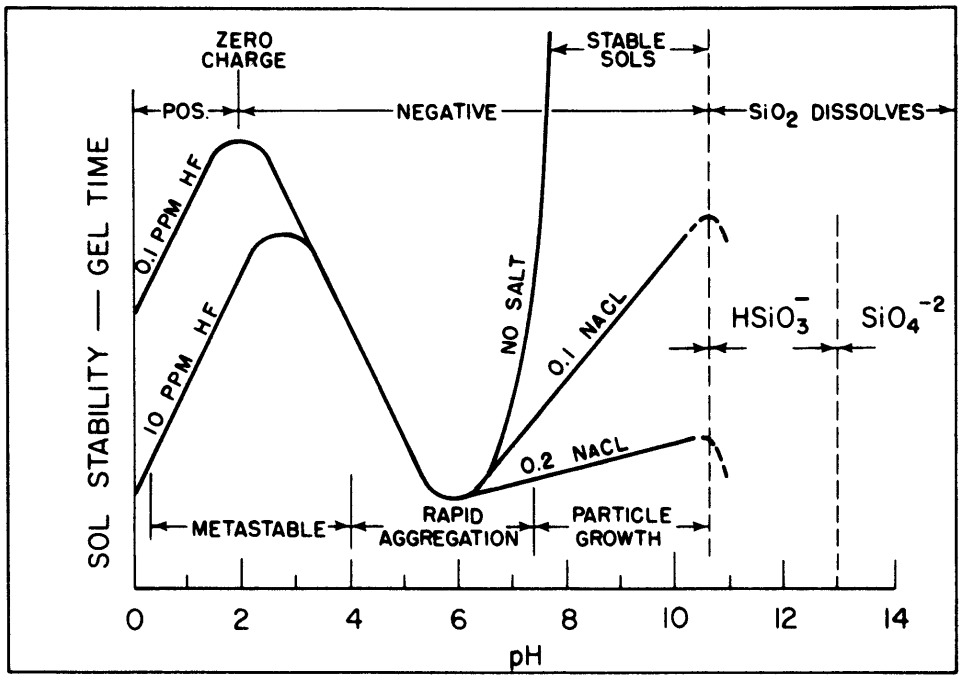

Figure 3-5: Effect of pH on sol stability. From Iler (1979).

3.2.5. Gels and precipitates

It should be noted that the term "gel-like opal" can be quite misleading, since, in colloidal chemistry, a gel implies an open (or porous) structure which is continuous, somewhat like a sponge. Figure 3-6 illustrates the structure of a gel and a precipitate. The original definition of opal-AG states that it has an amorphous "gel-like" structure, yet precious opal-AG specimens are known to have a close-packed sphere structure, which is definitely not an "open" morphology. However, a true gel does not necessarily contain colloids, and with respect to opal-AG, the spheres themselves could be gel-like. Nevertheless, to avoid ambiguity in this discussion, the term "gel" will refer to an open structure, not merely one which contains colloids.

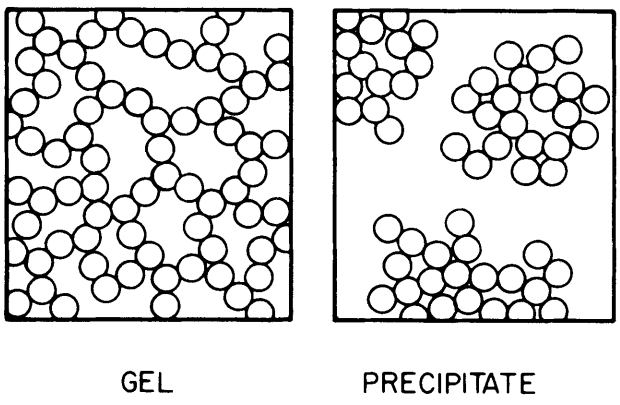

Figure 3-6: The fundamental distinction between a gel and a precipitate. From Iler (1979).

Iler (1979) noted that below the pH value of 7, a gel structure forms in the absence of salts; above a pH value of 7 the presence of mono- and di-valent salts still leads to the formation of a gel structure. This flocculation process influences the microstructure, leading to a more open, gel-like structure than a regularly coagulated colloid (Figure 3-7). Only at a pH of greater than 7, and in the absence of salts, will a large stable sol form from a supersaturated silica solution (Figure 3-8). The concentration of salts required for gel-formation or coagulation is ~0.1-0.3 mol/L, dependent on the type of ion (Iler 1979).

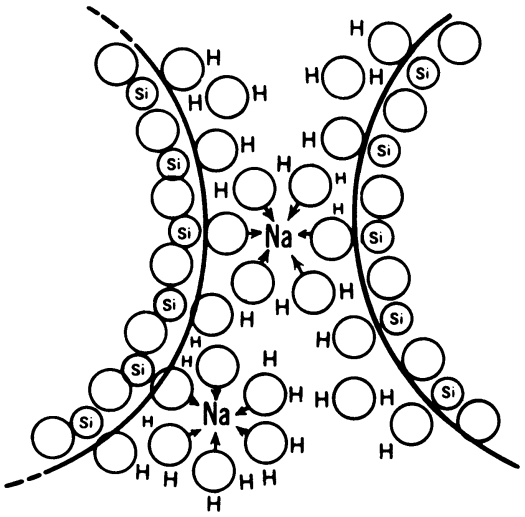

Figure 3-7: Flocculation aided by the presence of an alkali element (in this case, Na). From Iler (1979).

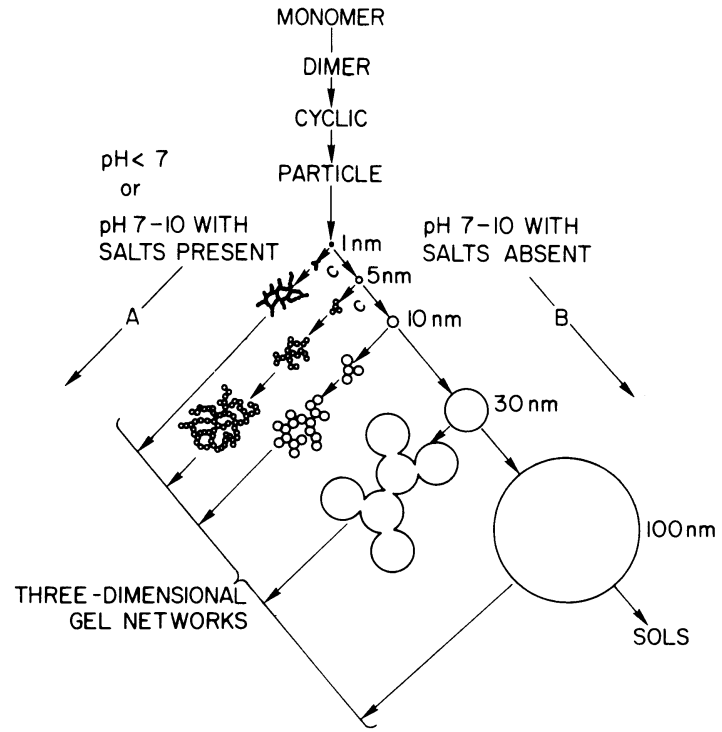

Figure 3-8: Initial stages in the formation of a sol or gel network. From Iler (1979).

3.2.6. Ostwald ripening mechanism

Darragh *et al.* (1966) stated that a possible mechanism for the formation of monodisperse colloids was that the colloids grew "by the operation of a substantially linear growth rate law", and were possibly being supplied with nutrient [silica] at a steady rate. However, such a postulation is not required to explain the development of monodisperse colloids, as there are many examples of systems in which finely dispersed suspensions or nucleated particles spontaneously achieve monodisperse particle sizes. This process is known as Ostwald ripening, and the mechanism is discussed below.

For a given degree of supersaturation with respect to the bulk mineral, a solution saturated with particles of size r^*, is given by the Gibbs-Kelvin equation:

Equation 3-2:

$$r^* = \frac{2\sigma V_o}{RT \ln(C / C_{eq})}$$

where C is the concentration of the mineral in solution, C_{eq} is the bulk solubility (i.e. the solubility of very large particles), σ is the interfacial free energy, and V_o is the molar volume of the mineral (Steefel and Van Cappellen 1990).

Solid surfaces have an associated excess Gibbs free energy. Ordinarily, the contribution to the total free energy is small, but if the surface area-to-volume ratio is large, as in the case of very small particles, the surface free energy can affect the solubility of that surface (Williams *et al.* 1985) as the Gibbs-Thomson equation shows (Equation 3-3):

Equation 3-3:

$$L_r = L_\infty e^{K/r}$$

where r is the radius of a particle, K is a constant, L_r is the solubility of a particle with radius r, and L_∞ is the solubility of an extremely large particle (Landmesser 1995).

The free energy of a surface is dependent on the curvature of that surface. The smaller particles, with a higher radius of curvature, also have a higher free energy and are metastable. Smaller particles, therefore, have a higher solubility than larger particles (Figure 3-9). This is a direct consequence of the Kelvin effect (Adamson 1990). Not all of the small particles in the sol are exactly the same size in the initial stages, and for smaller than average sized particles ($r < r^*$), the solution is undersaturated, and there is a tendency for these smaller particles to dissolve and the molecules to diffuse and re-precipitate elsewhere. The only stable place for the molecules to re-precipitate is onto the surfaces of the larger, less soluble particles. Since Ostwald ripening involves a mass transfer from smaller particles to a lesser number of large particles, it has the effect of decreasing the total number of particles in the system. Thus, the particles grow in average size, while the total number of particles in the sol decreases, as seen in Figure 3-10 (Steefel and Van Cappellen 1990). Growth of the particles continues in this manner until the size is so large that the difference in solubility between the smaller and larger particles becomes negligible.

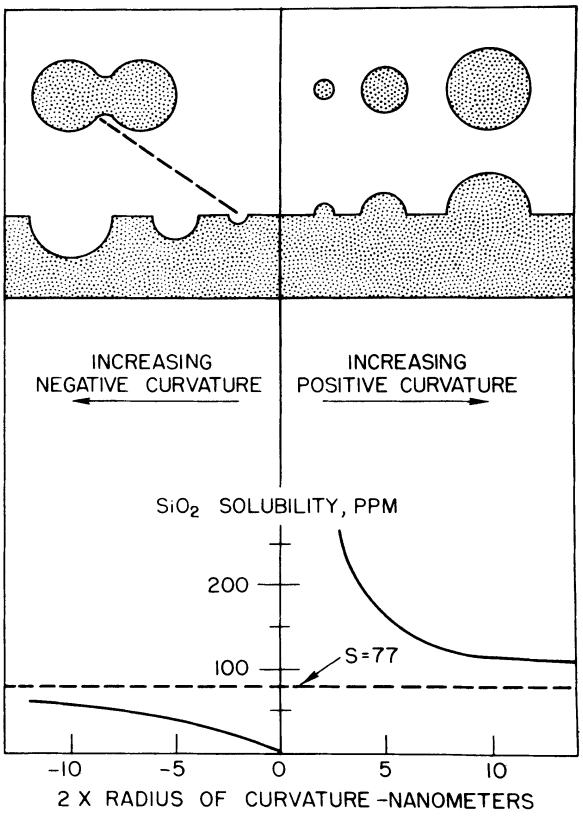

Figure 3-9: SiO_2 solubility vs. radius of curvature. From Iler (1979).

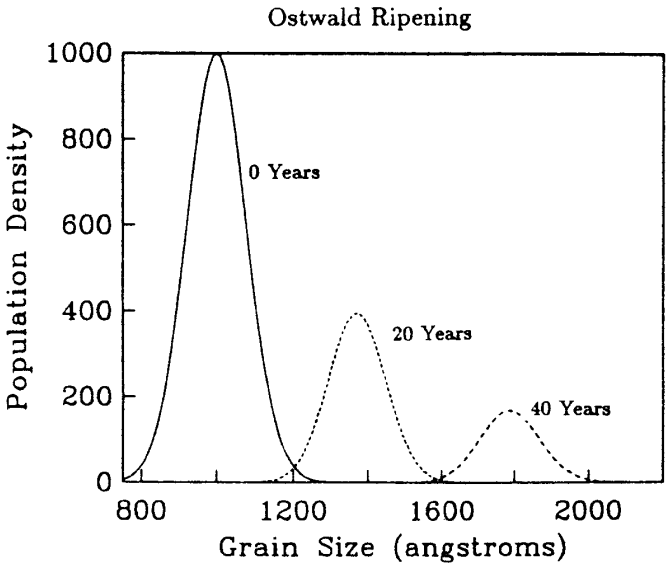

Figure 3-10: Effect of Ostwald ripening on the quantity and size of an initially Gaussian population of gibbsite crystals with an average size of 1000Å, using an interfacial energy of 350 mJ/m^2. From Steefel and Van Cappellen (1990).

Assuming the electrolyte concentration is low enough to prevent aggregation, eventually, monodisperse colloids will develop[1] to a final size that is dependent mainly on the temperature (Iler 1979). The spheres exist as free units held in suspension by Brownian motion (Darragh *et al.* 1976). The silica colloids that maintain a negative surface charge will repel each other without coagulation, provided the concentration of impurity cations remains very low. The silica colloids will remain suspended and dispersed throughout the sol, as long as these conditions are satisfied.

3.2.7. Sedimentation and solidification

Once the colloids have grown to considerable sizes (>100nm), they may settle as the effect of gravity dominates over the repulsive charges on the colloids. Alternatively, the water may simply evaporate or permeate through the cavity walls increasing the sol concentration and causing the colloids to coagulate (Jones and Segnit 1966).

After the colloids coagulate, the opal subsequently hardens with the general lowering of an otherwise fluctuating water table, due to the extremely arid conditions. Measurements on the permeability of the claystone from Andamooka suggest that there would have been a maximum rate of deposition (at a depth of 10m), of 1cm in 200,000 years (Darragh *et al.* 1966). Other models suggest more rapid precipitation (Iler 1965; Epova *et al.* 1983).

3.2.8. Purity of the sol (cationic sol purification)

The formation of a stable silica sol requires high purity solutions (less than ~1% total impurities) in order for the spheres to reach a large size (300nm). It is unlikely that initial silica solutions (from rainwater or groundwater) have a sufficiently low level of impurities for the production of large spheres. It has been proposed that the purity of a silica solution may

[1] In a closed system, initially the size distribution of the particles is skewed with a tail towards the smaller particles, and the maximum sized particles are 1.5 times the average size (Finsy 2004). As $t \rightarrow \infty$, the number of particles in the system theoretically approaches one, at which point there is technically no distribution of sizes (Kahlweit 1975). In real systems however, neither of these conditions are usually met. The diagram in Figure 3-10 is therefore not technically correct as the size distribution of the crystals should also reduce (narrowing the bell-curve) as Ostwald ripening proceeds.

be increased by the cation exchange properties of surrounding clays, through three mechanisms (Deniskina *et al*. 1981).

1. Destruction of bonds at the edges of aluminosilicate groups cause an increase in the number of uncompensated charges, which are balanced by adsorbed cations (from the solution).
2. Replacement of Si^{4+} within the structure by Al^{3+}, and Al^{3+} by Mg^{2+} or Ca^{2+} may remove additional impurities from the silica sol.
3. Hydrogen atoms bonded to hydroxyl groups within the clay can also be replaced by a cation (usually Mg^{2+}, Ca^{2+}, Na^{+}, K^{+} or NH_4^{+}), further purifying the sol.

Decomposition of organic material during weathering releases humic acid into the groundwaters containing silica. These acids form negatively charged colloids and form efficient adsorbents of cations, tens of times more capacious than clays (Deniskina *et al*. 1981).

3.2.9. Ordered arrangements of spheres with two sizes

Microstructures have also been observed that contain ordered arrangements of spheres with two different sizes (Sanders and Murray 1978; Murray and Sanders 1980; Sanders 1980; Sanders 1985). Depending on the ratio of diameters of the two sphere sizes, the packing-structure obtained is analogous to metal "alloy" systems, which exhibit long-range order of the atomic structure (Figure 3-11). Using the phase diagram provided by Murray and Sanders (1980), numerous types of structures (with alternate unit-cells) may be predicted based on the ratio of the sphere diameters. The packing factors may also be determined in this manner. Although opals of this type are extremely rare, the investigation of this unique microstructure has resulted in a more complete understanding of the factors governing the colloidal formation of opals.

3.2.9.1. Mechanisms responsible for bimodal size distributions

Two mechanisms have been postulated for the formation of long-range ordering; one where gravity is the controlling factor, the other where long-range double layer repulsions are dominant (Sanders 1978, 1985).

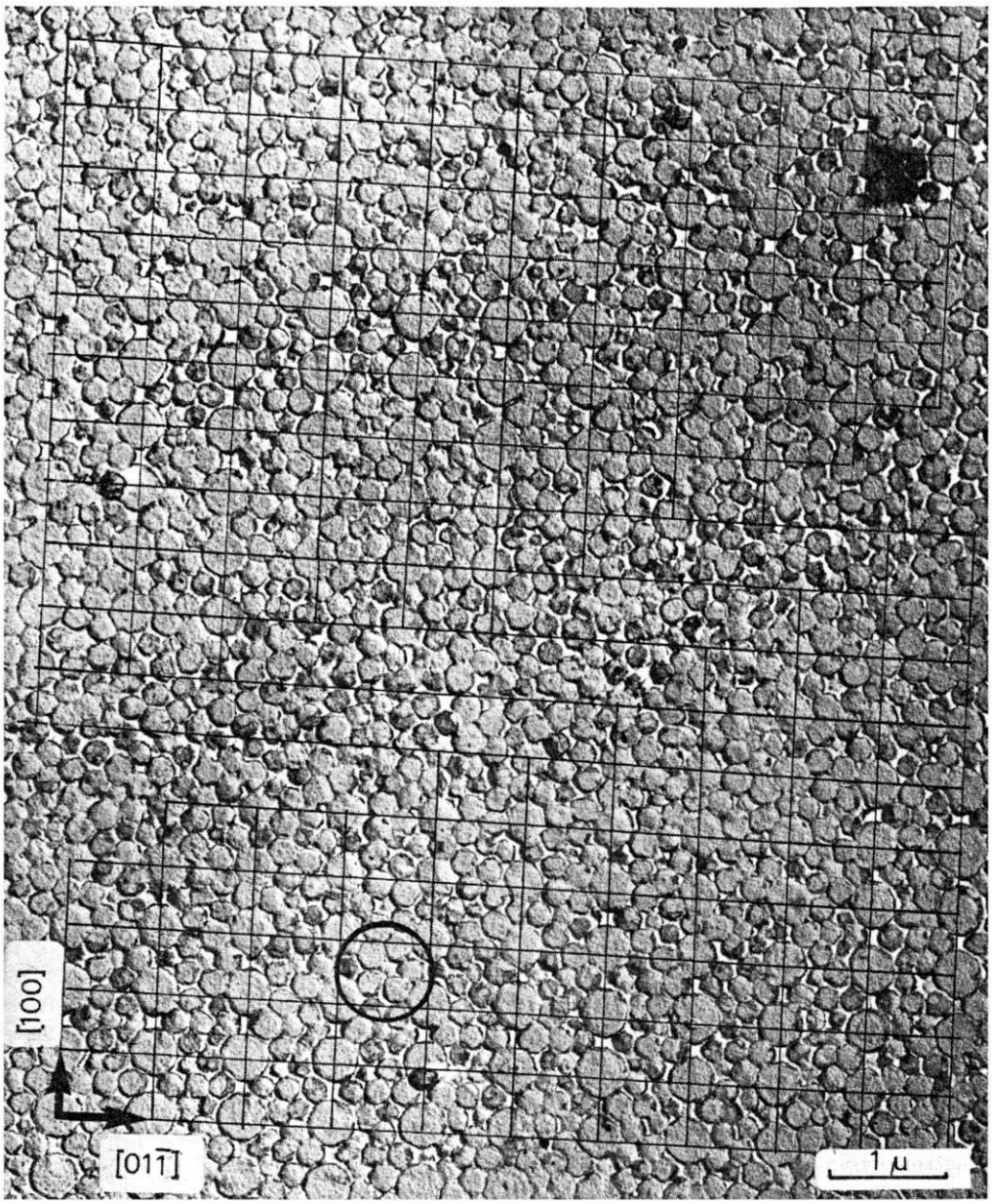

Figure 3-11: Ordered arrangements of bimodal sphere distribution. From Sanders (1980).

Although no reference to these bimodal sphere structures were made, it is interesting to note that this type of structure may also have arisen from the potential energy well that develops in the interactions between silica colloids in the presence of bi- and tri-valent cations (Serdobintseva and Kalinin 1998). The researchers proposed that when a certain concentration

of salts exists in the system, the spheres may become fixed with a certain distance of separation. This point can be demonstrated in the potential-energy curve of interactions of two monodisperse silica colloids.

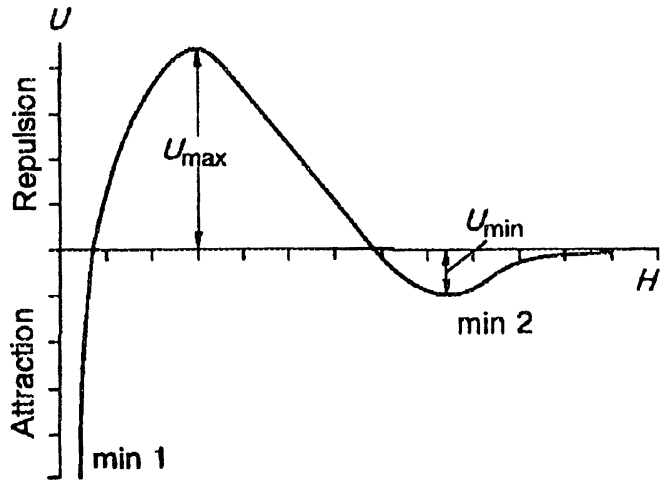

Figure 3-12: Potential energy curve for interaction between two monodisperse silica spheres in the presence of salts of bi- and trivalent cations. From Kalinin et al. (1998).

Normally there is only one point of minimum repulsion (min 1), which corresponds to spheres which are in very close proximity (Figure 3-12). In that case, the spheres will move closer to one another as they are simultaneously attracted. However, in a bimodal sol such as this, the larger spheres that are able to maintain their separation at a fixed distance from each other (min 2) may allow smaller spheres to enter between the gaps, forming the ordered structural arrangement of spheres with two different sizes. Due to the shallowness of the secondary minimum, this aspect only affects the stability of larger particles, those with diameters of approximately 200nm or more (Popiel 1978).

3.2.10. Bacterial model of opal formation

It has been proposed that the black opals of lightning ridge may have contained aerobic bacteria during the stage of their formation (Behr *et al.* 2000). It was hypothesised that these microbes lined the walls of cavities consisting of host rock, and that they not only assisted weathering of these

rocks to form silicic acid, but they also produced other pollutants such as AlO(OH) and Fe-oxides. Bustillo (1995) also observed that bacteria had possibly influenced the structure of opal-CT specimens.

3.2.11. Banded opal-AG

Potch opals are frequently composed of different coloured layers, thought to be a consequence of the depositional sequence from an original supersaturated silica solution (Darragh *et al.* 1966). These layered opals have been found in the major opal mining regions of Australia, and they are referred to as banded opals (Jones and Segnit 1966; Males 1974; Sanders 1976, 1980; Ball 1985). The South Australian fields of Andamooka and Coober Pedy produce opals which consist of grey, white or translucent layers, while opals from Lightning Ridge have layers that are usually black, grey or colourless.

Precious opals are also commonly banded. Very rarely, an opal specimen develops in which a poc layer forms adjacent to an opaque black potch layer (Males 1974; Ball 1985). This black "background" enhances the play of colours when observed from the opposite side, and greatly increases the value of the opal as a gem. Moreover, black opals in any great quantity remain virtually unique to the Lightning Ridge Opal fields, not just within Australia but globally. Unfortunately, the current literature cannot adequately explain how these banded opal samples developed.

3.3. OPAL-CT FORMATION

The general mechanisms of formation of opal associated with volcanic environments are essentially the same as those of opal-AG from sedimentary environments (precipitation of colloidal silica solutions), however, the mechanism for the liberation of silica is still debated. Regardless, opal-CT is thought to be originally deposited as amorphous opal-A, undergoing a diagenetic transformation to opal-CT at a later stage. The reason for this is that certain types of opal-CT share sphere structures similar to that of opal-AG (2.4), albeit in a more crystalline form. It is therefore conceivable that opal-AG, once deposited, could undergo further structural changes resulting in opal-CT, through a process known as silica digenesis (3.4.1).

As opal-CT is often found in association with volcanic environments, it has been suggested that the action lava flows over opal deposits thermally transformed the opal-A into opal-CT, through the mechanism of silica diagenesis (3.4.1). However, opal-CT may also be found in predominantly sedimentary environments (Segnit *et al.* 1970).

Lepispheres are usually observed in opal-CT of diagenetic origin (3.4.1) and have not been observed for precious opal-CT associated with volcanic environments (eg from the Australian precious opal fields such as Tintenbar). Evidently, our present understanding of the formation of precious opal-CT of inorganic origin is inadequate. Nevertheless, Flörke *et al.* (1976) attributed the ultrastructure of opal-CT_M lepispheres to growth patterns attributed to the interpenetrating blades of certain crystallographic orientations.

3.3.1. Fluid Inclusion studies

Evidence from various inclusions in Mexican opal-CT (Koivula *et al.* 1983; Spencer *et al.* 1992) suggests that it was deposited in a fluid state at temperatures of approximately 160°C. The melting temperatures of several fluid inclusions ranged from -22°C to -2.1°C, which indicated that these were a mixture of hydrous silica gel and various quantities of NaCl. CO_2 was also detected in several gas-phase inclusions, but never oxygen or nitrogen. This provided further evidence that the inclusions were trapped during the formation of the opal, as they do not contain atmospheric gases. These findings suggested that the silica gel may have flocculated, leading to the formation of more open gel-like structures. Opal-CT of volcanic origin is commonly iron-rich, leading Segnit *et al.* (1970) to suggest that precipitation occurred at low-pH values. In another fluid-inclusion study of opal-silicite (from the East Rhodope paleogenic volcano-sedimentary complex), Yuliya and Khristova (1992) reported that gas-liquid inclusions had low salinities (≤1.7%) and yielded homogenisation temperatures of 280 to 320°C.

Experimental studies (thermal ageing) of opal performed by Sanders (1975), show that the onset of sintering preceded crystallisation, yet there was no sign of sintering in the microstructures of all the natural opal-CT

examined. This shows that the opal-A to opal-CT transformation must have taken place at relatively low temperatures.

3.4. Other Important Mechanisms

3.4.1. Silica diagenesis

At low temperatures, silica precipitates from natural aqueous solutions as amorphous silica. This occurs either inorganically, as in silcretes, geyserites, and precious opal deposits, or organically by diatoms, radiolarians, sponges and some terrestrial plants. Biogenic silica predominates in deep marine sea sediments, and it undergoes the transformation sequence outlined below (Williams and Crerar 1985; Williams *et al.* 1985). The rate of transformation is found to be remarkably dependent on the reaction temperature; higher temperatures increase the rate of transformation (Kano and Taguchi 1982; Kano, 1983; Kastner and Gieskes 1983).

Opal-A (siliceous biogenic ooze)

↓

Opal-A' (nonbiogenic amorphous silica)

↓

Opal-CT (poorly-ordered)

↓

Opal-CT (more-ordered)

↓

Cryptocrystalline quartz or chalcedony

↓

Microcrystalline quartz

The various phases of sedimentary sequences do not spontaneously appear in succession throughout the sequence; instead a more gradual transition exists, consisting of mixed phases. These transformations are accomplished by dissolution-reprecipitation mechanisms, which are controlled by thermodynamic and kinetic factors, rather than through solid-state transformations (Kastner *et al.* 1977; Williams *et al.* 1985; Chang and Yortsos 1994).

The concentrations of dissolved silica reflect the relative rates of dissolution, polymerisation, nucleation and growth of silica phases. The concentration of dissolved silica lies in-between the values for the phases involved in the reactions (Hinman 1998). Hence, silica concentrations closer to those of the dissolving phase indicate that precipitation of the subsequent phase limits the reaction rate; whereas values closer to those of the precipitating phase indicate that dissolution of the prior phase is the limiting factor.

3.4.1.1. Effect of temperature and other constituents

Elevated temperatures are not a required parameter with this model, but they increase reaction rates, allowing transformations to occur sooner than they otherwise would (Williams *et al.* 1985). The presence of detrital minerals[1] retards the opal-A to opal-CT transformation and the resulting opal-CT is more ordered. However, the opal-CT to quartz transformation should be faster in the detrital-rich system, than in the detrital-poor system (Williams *et al.* 1985). In the presence of organic matter, the reaction rates of silica phase transitions are reduced, and the opal-CT phase produced is more ordered [lower d(101) spacing] than that in the absence of organic materials (Hinman 1990). The presence of trivalent ions, especially Al, significantly decreases the dissolution rate of opal-A at a pH between 8 and 9 (Lewin 1961).

3.4.2. Silica transport and accumulation

In the paper "Mobility by Metastability", Landmesser (1995, 1998) proposed the following mechanism for the transport and accumulation of

[1] A detrital mineral is one which is produced by mechanical means (for example by disintegration or abrasion of a parent rock) and subsequently removed from its place of origin.

silica at low temperatures (incidentally, this not only applies to silica systems, but others as well). The rate of silica diagenesis at low temperatures is very slow, hence reactants and products of that series (opal-A, opal-CT, quartz) may be simultaneously present over long time periods at different sites within the same network of pore solutions. Due to the different solubilities of these silica polymorphs, monomeric silica of different concentrations can develop at different points in the pore solution, creating concentration gradients (as high as 1:10) within the pore network. Comparatively high concentrations of silica develop near less-mature forms of silica, whereas lower concentrations develop near riper forms of silica, resulting in diffusion from points of higher to those of lower silica concentration. This in turn results in supersaturation near the riper silica, and undersaturation near the less-mature silica. Therefore silica dissolves from regions of less-mature silica and precipitates at regions of riper silica. This causes silica transport over relatively long distances by diffusion of dissolved $Si(OH)_4$ molecules, even if the pore solution is static. One consequence of the mobility by metastability mechanism proposed by Landmesser (1995), is that a total silica deficit of more than 15 wt.% will eventually develop, because of the different specific gravities of the various silica polymorphs (Table 3-1). This deficit may result in the formation of tiny voids in the transformed silica body (Landmesser 1995). The sluggish character of silica phase transitions causes an increased silica mobility at low temperatures.

Silica Phase	Density (g/cm^3)
amorphous silica	2.2
opal-CT (lussatite)	2.0 – 2.1
opal-C	~2.27
cristobalite	2.33
tridymite	2.27
quartz	2.65

Table 3-1: Densities of common silica polymorphs. From Landmesser (1995).

A similar process of solution transport can be seen in Figure 3-13, although it is based on thermodynamic factors (Ostwald ripening), governed by the variable solubility of silica at differently curved surfaces. Unlike the

metastability by mobility mechanism, Ostwald ripening is applicable to particles of the same phase. This type of solution transport occurs over much shorter distances than the mobility by metastability mechanism, which is a process controlled by kinetics.

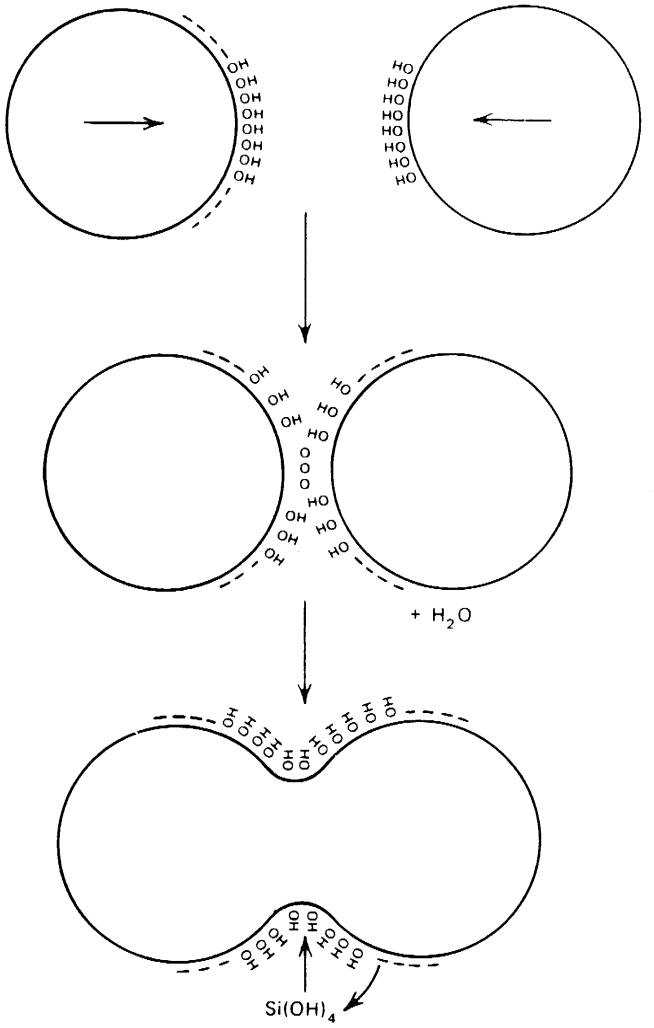

Figure 3-13: Transport of silica from regions of low solubility (positive radius of curvature) to regions of lower solubility (high negative radius of curvature). From Iler (1979).

Landmesser (1998) also suggested that the vigorous solution flows (or 'silica cement') proposed by other researchers in the formation of precious opal (Darragh *et al.* 1976) would easily destroy the fragile sphere packing.

Segnit *et al.* (1970) discuss the peculiar microstructure of Mexican opal, in which the silica spheres have been preferentially etched with HF, while the silica contained in the voids has been left behind. The researchers

proposed that the difference in etching was due to different levels of porosities of the silica. Attempts at analysing this 'honeycomb structure' with XRD gave no evidence that the crystallinity of the spheres and interstitial silica were different. However, it is likely that the solution transport mechanism proposed by Landmesser (1995, 1998) still applies to samples such as this, as the various phases only need to posses a slightly different crystallinity or solubility (surface area) to undergo this process.

3.4.3. Incorporation of Elements

3.4.3.1. Aluminium in opal

When a mineral is formed from an aqueous solution, if any other residual ions (which are not an essential part of the mineral) are present in sufficient dissolved concentrations, they may be incorporated into the mineral structure as it precipitates, but only to the extent that the molecular structure allows for. This effect is due to the mass-action law (Merino *et al.* 1989). Smallwood *et al.* (1997) reported that the Raman spectra of opal-CT, although similar to α-tridymite, may bear a resemblance to that of metal ion silicates. In silicates containing aluminium, some of the silicon atoms forming the network structure may be substituted by Al atoms; the resulting structure is usually termed an aluminosilicate (Field and Sternhall 1989). Replacement of Si^{4+} by Al^{3+} results in a charge imbalance that must be compensated for by entry of monovalent or divalent interstitial cations (Li, Na, K, Mg, Ca), or by the substitution of an -OH group for an oxygen atom to form silanol groups (Smith and Steele 1984). Furthermore, the mole fraction of Al^{t} is also proportional to the concentrations of aqueous monovalent cations. The cathodoluminescence study of opal by Stevens-Kalceff *et al.* (1997), indicated the presence of uncompensated Al^{3+} centres.

3.4.3.2. Coordination of aluminium at various pH values

Aluminium hydroxide is insoluble at intermediate pH values, but is amphoteric and therefore reacts at higher and lower pH values. At low pH values, the dominant species of Al in aqueous solutions is $[Al(H_2O)_6]^{3+}$, in which the Al ion is coordinated octahedrally (Al^{0}) by six water dipoles (i.e. aluminium in a 6-fold coordination). At higher pH values, some of the

hydrogen ions disassociate, and the remaining hydroxyl ions are attracted more strongly by the inner Al ion. This lowers the effective radius, leaving less room for other coordinated hydroxyl groups around the Al and hence reducing its coordination from 6 to 4. Accordingly, at high pH values the dominant aqueous complex becomes $Al(OH)_4^-$, tetrahedrally coordinated aluminium, or Al^t. This transition from predominantly Al^0 to predominantly Al^t takes place over a narrow pH range of 5.5 to 6.5 at 25°C, seen in Figure 3-14.

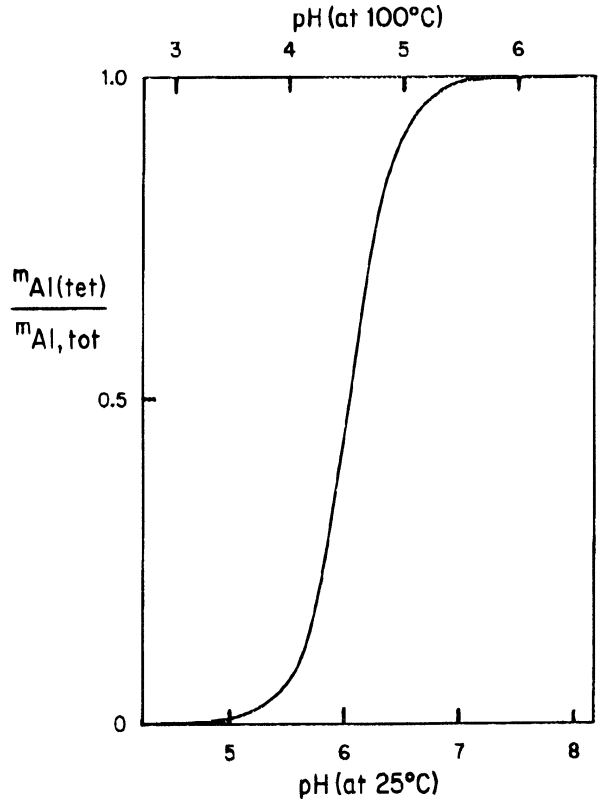

Figure 3-14: Predicted ratio of Al^t in Al, at 25°C and 100°C. From Merino et al. (1989).

3.4.3.3. Literature concerning aluminium substitution in opal

The largest trace element constituent of opals (apart from silica and water) is usually Al; the concentration of Al in opals can be as high as 13,000 ppm (5.3.2).

A small vibration mode has been observed in the infrared spectrum at 550-560 cm^{-1} in opal speleothems, representing the vibration of

octahedrally coordinated aluminium in the gibbsite sheet of clays (Webb and Finlayson 1987). The presence of this peak in the spectra indicated that an occluded clay phase such as kaolinite or allophane was present in many samples.

A very strong vibration mode was observed in the infrared spectrum at 1090-1100 cm^{-1} for the opal samples investigated by Webb and Finlayson (1987), due to antisymmetric Si–O–Si stretching vibrations. In tectosilicates, the wavenumber of this mode decreases regularly with increasing substitution of tetrahedral Al into the framework of the mineral (Si–O–Al). Thus, a fraction of the Al present could also be tetrahedrally coordinated in the opal samples, meaning the Al atoms substitute for silicon atoms in the silica network.

3.4.3.4. Relationship between silica solubility and Al content

Huang and Vogler (1972) undertook an experimental study involving the dissolution of various opals (from Nevada, Australia and Mexico) in 0.01M solutions of strongly complexing salicylic and citric acids. The researchers noticed a linear relation between the water content of the opals and the concentration of dissolved Al in the solution. This was attributed to the formation of Al-salicylate or Al-citrate complexes during dissolution.

Bartoli and Wilding (1980) also noted an inverse relationship between the Al content of opals and their respective surface area dissolution characteristics. This reduction of silica dissolution by Al was ascribed to two factors: its chemisorption to the silica surface rendering the silica less reactive; and its impact on reducing the surface area, presumably by a coagulative effect during silica synthesis.

3.4.3.5. Magnesium in opal

The magnesium ion (Mg) is more likely to be interstitial than substituting for silica, as Mg has a larger ionic radius and a lower charge than Si or Al. Spaces in the poorly ordered opal structure can easily accommodate ions of this size, as even the well-ordered structures of α-quartz, α-cristobalite and α-tridymite all contain voids large enough to allow Mg to enter (Webb and Finlayson 1987). The incorporation of interstitial Mg within the opal-A structure is not unexpected, as $Mg(OH)_2$ displays a strong

affinity for silica and can flocculate undersaturated silica solutions. Because $Mg(OH)_2$ carries a positive surface charge under most natural conditions, it can neutralise the negative surface charge of silica particles in solution and allow them to precipitate (Figure 3-15). The neutralising cations are readily incorporated into the growing surface of the silica precipitate. Although $Mg(OH)_2$ in this manner produces open framework structures, displaying high porosity and not densely packed colloidal aggregates like opal.

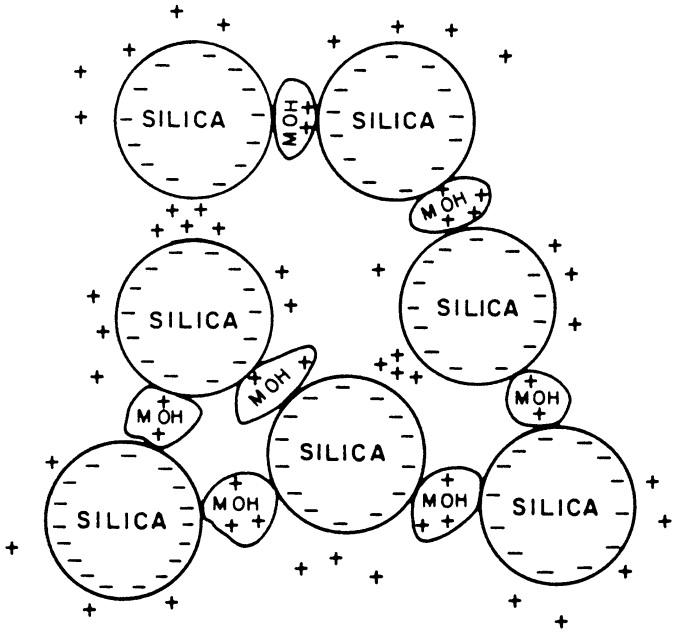

Figure 3-15: Flocculation of negatively charged silica particles in a sol by positively charged hydroxyl complexes. From Iler (1979).

3.4.3.6. Carbon in opal

In the study "Black opal from Honduras", by Banerjee and Wenzel (1999), significant amounts of carbon were detected using Fourier Transform Infrared Spectroscopy (FTIR). This was deduced to be a "porphyrin-like" organic compound.

Ball (1985) also detected carbon in Australian opals, and noted that the concentration was up to three times higher in black opal centre (0.09%) than in the surrounding grey rim (0.03%) of opal nobbies from Grawin, New South Wales. Wilding (1967) also examined the properties of occluded

carbon in biogenetic opal, although the opals in that study were of a biogenic origin.

Kulchitskaya *et al.* (1997) undertook a detailed study of numerous opals, involving XRD, SEM and gas-chromatography. The opals investigated differed in their structure, physical properties, the type of water present and chemical composition (of volatile products). Based on these results, the researchers suggested that some types of opals are the result of hydrolytic polycondensation of organic silicon compounds ('organoopals') while others were formed as a result of polycondensation of silicic acid molecules ('hydroxylopals').

4. THERMAL AND NITROGEN ADSORPTION ANALYSIS

"To me exploration isn't about conquering natural obstacles, planting flags...
It's not about going where no one's gone before in order to leave your mark,
but about the opposite of that - about making yourself vulnerable,
opening yourself up to whatever's there
and letting the place leave its mark on you."
– Benedict Allen, Explorer – 2000

4.1. INTRODUCTION

4.1.1. Thermogravimetric Analysis

Thermogravimetric analysis (TGA) is an analytical method based on characterising the thermal behaviour of substances (Haines 1995). By observing the temperature(s) at which the mass change of a substance occurs, and the magnitude of this change in mass, a better understanding of the thermal behaviour of that substance is gained. For example, based on a reasonable understanding of the chemical nature of the sample, thermal analysis can be used for the identification of possible reactions taking place at elevated temperatures. As such, it is a useful means for studying the evolution and consumption of gases of a sample as well as the thermal degradation of substances. In addition, thermogravimetric analysis allows semi-quantitative chemical data of samples to be obtained, and the chemical composition at ambient temperatures can then be inferred. Furthermore, if the rate of change in mass is calculated, it can provide clues to the nature of a sample's microstructure. Thermal analysis can also characterise unidentified or unknown substances, based on the previously documented thermal behaviour of numerous substances.

4.1.2. Thermomechanical Analysis (TMA)

Thermomechanical Analysis (TMA) essentially measures the change in length of a sample as it is heated (Haines 1995). The primary function of TMA is to calculate linear thermal expansion coefficients (CTE); this is not the same as the volume CTE. It also permits the identification of phase changes that may occur in materials at particular temperatures. The only provision is that suitable samples are required to be cut with parallel end faces.

4.1.3. Differential Thermal Analysis and Differential Scanning Calorimetry

A differential thermal analyser essentially consists of two identical sample pans. Superficially, they both undergo the same heating cycle throughout the experiment, yet one of the pans remains empty (the reference pan), while the other pan contains the sample to be tested. Each

of the pans has separate thermocouples, and the temperature of each is measured simultaneously. Thus, the difference in temperature between the reference pan and the sample pan is recorded as a function of temperature. The primary information obtained with DTA is whether there are endothermic or exothermic reactions taking place, over what temperature range, and of what magnitude (Haines 1995). DTA may be also be combined with TGA to give multiple acquired data (eg: mass loss and presence of temperature differences) for comparison on the same specimen and at the same temperature.

4.1.4. Thermal behaviour of opal

When opal is heated for prolonged periods at high temperatures (>900°C), the structure transforms from an amorphous state to α-cristobalite (Jones and Segnit 1971). The amorphous phase of opal is however retained if thermal treatments are carried out below 500°C. Characterisation of the thermal properties in the ambient temperature to 500°C range can aid in understanding the dehydration behaviour of opal and hence the character of the water contained within the opal structure. During heating, water is driven out of the structure; the temperature and the rate at which this occurs clarifies the behaviour of the water at elevated temperatures, and thus inferences about the microstructure of opal can also be made. Due to the relatively large internal surface area of opals (Bustillo *et al.* 1993), the water is tenaciously held at the surfaces of voids in the silicate structure, long beyond the expected boiling point of 100°C.

Published DTA results of different types of opals show considerable variation, especially between 100 and 200°C. The first dehydration study was undertaken by Taliaferro (1935), who noted that some opals dehydrated rapidly at temperatures as low as 120°C, while others required as much as 10 hours at 350°C. Generally speaking, the current literature concerning the data on thermal behaviour of opal-A and opal-CT is seen to be quite variable, especially at lower temperatures where the water loss is presumed to occur. There have been a small number of papers written on the subject of thermal analysis (predominantly DTA) of opal (Jones *et al.* 1963; Segnit *et al.* 1965; Jones and Segnit 1969; Jones and Segnit 1971). The different phases of opal (opal-A, opal-CT and opal-C) generally show

markedly different thermal behaviour. As thermal analysis is dependent on the physical characteristics of the sample, differences in the microstructures of these opals may be responsible for some of the observed inconsistencies in the results.

4.1.5. DTA-TGA

The first systematic thermal analysis study of opal-A, opal-CT and opal-C was completed by Jones *et al.* (1963). The researchers broadly classified DTA curves of thirty naturally occurring opals into three groups:

1. Opals of this type had either no endotherm[1], or else a very small endotherm was detected between 100 and 200°C.
2. The second group of opals had prominent rounded endotherms, which started at about 90°C, with a peak between 125 and 140°C.
3. The last type showed a strong sharp endotherm, which started at 90°C and peaked at 140°C.

Most 'glassy' opals fell into group 1; opals of group 2 were commonly opaque. Only two samples fell into group 3, and were somewhat 'glassy' red and brown opals from different localities. All amorphous opals fell into group 1, but no such correlation could be made for crystalline opals.

Opals of group 1 were still losing water at 500°C, but those of group 3 were almost dehydrated at only 200°C. No correlation was found between composition of silica and/or water and DTA results. Nor was any correlation found between the degree of crystallinity and the chemical data. The results strongly indicated that most of the water was not chemically bound in opals.

[1] An endotherm is a peak where the temperature of the sample falls below that of the reference material, indicating an endothermic reaction at that temperature.

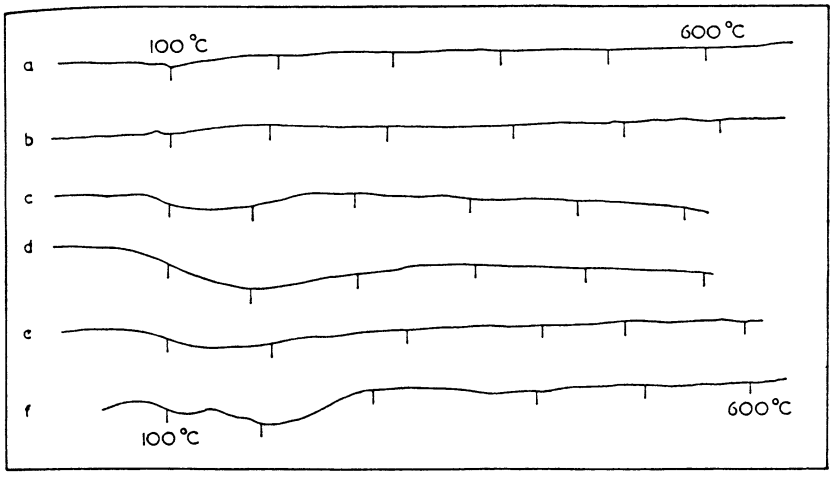

Figure 4-1: DTA curves of amorphous opals. Legend; a: milky precious opal (Coober Pedy, South Australia), b: colourless hyalite (Melbourne, Victoria), c: opaque white opal (locality unknown), d: milky precious opal replacing wood (White Cliffs, New South Wales), e: siliceous sinter (Whakarewarewa, New Zealand), f: Diatomite (Victoria, Australia) From Segnit et al. (1965).

In a further study by Segnit *et al.* (1965) all opals of the amorphous type gave no more than a broad, shallow endotherm, as shown in Figure 4-1. There was no correlation between DTA results and water content. Nor was any relationship found between the nature of the endotherm and the degree of crystallinity. Several opals gave broad endotherms at temperatures as high as 210°C. Opals that gave a prominent sharp endotherm in their DTA curves gave a corresponding sharp weight loss at low temperatures and little loss thereafter (Figure 4-2). Opals with little or no DTA endotherm showed a gradual weight loss extending to 500°C or higher. In summary, DTA of opal showed marked differences in the rate of water loss which could not be correlated with differences in the crystal structures or physical characteristics of the samples.

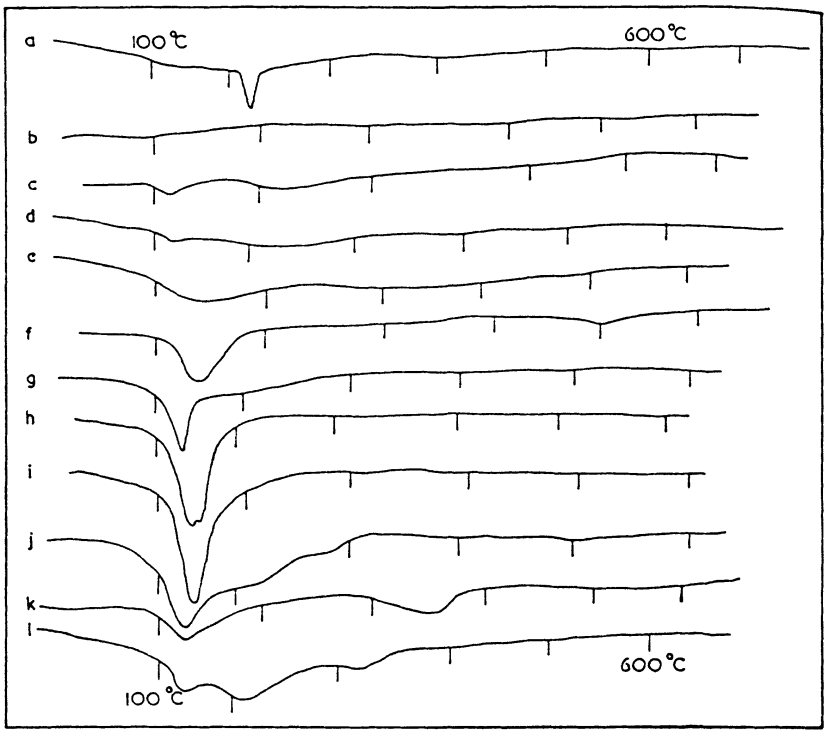

Figure 4-2: DTA curves of 'crystalline' opals (opal-CT). Legend; a: cristobalite, b: Mexican fire opal (Guanjuato), c: green common opal (Washington, USA), d: creamy coloured opal (Angaston, South Australia), e: transparent wood opal (Lake Eyre, South Australia), f: Dark brown opal (Sunbury, Victoria), g: white opal replacing wood (Berwick, Victoria), h: milky wood opal (Lake Eyre, South Australia), i: grey opal (Yinnar, Victoria), j: brown opal (Glengower, Victoria), k: yellow brown opal (locality unknown), l: brown opal (Riddell, Victoria). From Segnit et al. (1965).

Segnit *et al.* (1965) also noted that in the case of opal-A with a close-packed sphere structure, the maximum pore size is limited to 0.225 times the diameter of the spheres. Most of the water in an open network of this type should be driven off readily with small amounts being retained to higher temperatures in the smaller capillaries. TGA measurements for these types of opals showed a slower loss of water than would be expected through such a pore system. This may have been due to the inter-sphere pores being partly filled with additional 'silica cement', which reduces the pore size and also forms a discontinuous pore space. Dehydration

experiments determined that at least 20% of the total water is chemically bonded which further inhibits the water from escaping (Segnit *et al.* 1965).

Jones and Segnit re-examined opals in a further investigation in 1971. They found that opal-C gave an almost flat DTA line, showing little or no thermal effect; opal-A showed either no thermal effect or in some cases a very shallow broad endotherm; while opal-CT displayed variable results. Some samples showed no thermal effects at all, some gave rounded but distinct endotherms at 120°C, while others gave sharp strong endotherms at the same temperature. All these endothermic effects were attributed to the loss of water from the structure. Opal-CT showed no changes up to 1400°C, but opal-A showed a very strong exothermic effect at about 1350°C due to the rapid crystallisation of the material to a well-ordered cristobalite.

Langer and Flörke (1974) found that opal-AN dehydrated at relatively high temperatures and showed relatively featureless DTA curves when compared to opal-AG or opal-CT. The maximum dehydration occurred at temperatures between 200 and 280°C for opal-AN, between 50 and 200°C for opal-AG, and between 75 and 220°C for opal-CT. This indicated the presence of strong bonding of water in the network structure of opal-AN. Furbish and Schrader (1979) also noted that opal-AN samples that were sourced within close proximity to each other (within one metre of each other in the same depositional environment) exhibited variable DTA curves.

Bayliss and Males (1965) briefly examined opal using thermal analysis and found that both the thermogravimetric and differential thermal curves for precious and common opals from various localities in Australia (Lightning Ridge, Coober Pedy and Andamooka) were very similar.

4.1.5.1. Structural Inversions

An endothermic peak in the DTA curve at 160°C was also reported by Veniale (1972). This peak was previously ascribed by Flörke (1967) to the $\alpha \leftrightharpoons \beta$ cristobalite inversion (Figure 4-3), but is more likely to correspond to a water loss (Giuseppetti and Veniale 1969b; Jones and Segnit 1971; Veniale 1972).

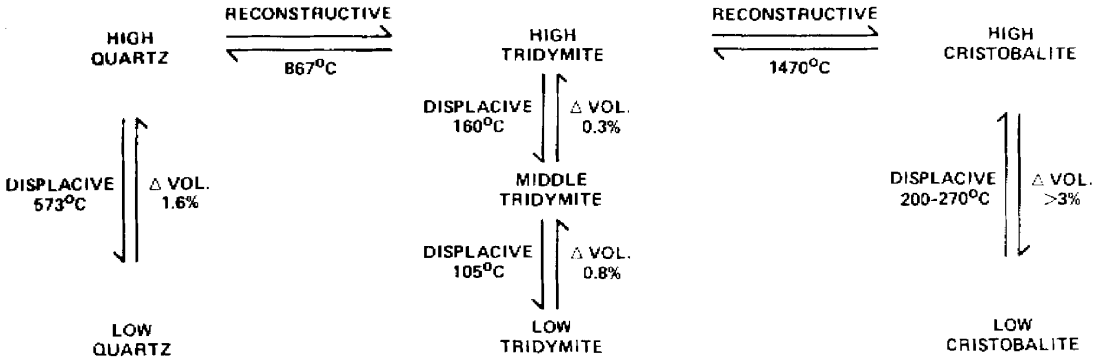

Figure 4-3: High temperature silica phase transformations. From Richerson (1992).

Six opal specimens (from Coober Pedy and Copetoun) were examined by DTA by S. St. J. Warne (1970). All but one opal were considered X-Ray amorphous, as no effects of silica inversions could be detected for the remaining samples. The exception was the sample from Copetoun, which showed that it contained some degree of crystallinity. These samples showed virtually identical and featureless thermal analysis curves except for an initial moderately defined endothermic peak caused by low-temperature water losses.

4.1.5.2. High Temperature Crystallisation

Simonton *et al.* (1986) investigated natural white opal from Australia using thermal analysis and found that the corresponding DTA curves exhibited two maxima at 1250 and 1350°C. The two peaks observed were attributed to the rapid crystallisation of the disordered silica to cristobalite. The observed variability in the position and sharpness of the exotherms for such disordered samples was not considered unusual. Powder XRD confirmed that well-crystallised cristobalite had formed after the exotherms in the DTA experiments.

4.1.6. Water content determined by thermal analysis

The total water content of Australian opal-AG is generally in the range of 6-10% as measured by thermogravimetric analysis (Jones and Segnit 1971; Pearson 1985). The results of previous TGA studies have shown that the total water content in opal-AN was between 3.0 and 6.5%, while opal-

AG contained 5.0 to 6.3% water, and opal-CT contained 3.5 to 7.3% (Langer and Flörke 1974; Table 2-3). More recent studies (Adams *et al.* 1991; Esenli *et al.* 2001), however, indicate that the water contents of opal-AG and opal-CT may be significantly higher. The water content of opal-CT from Simav, Turkey, determined by thermo-gravimetric methods ranged from 10% to as high as 15% (Esenli *et al.* 2001).

The pore spaces in precious opals are not entirely filled with water. The largest effective pores are large enough for spontaneous evaporation of water, so that physically adsorbed water remains only in the smaller parts of the inter-sphere pores (Flörke *et al.* 1991; Graetsch 1994). Kulchitskaya *et al.* (1995) reported that up to 90% of the water contained in 'noble opal' minerals was incorporated in closed pores, while in 'ordinary opal' the majority of water was contained in open pores as adsorbed and capillary water.

4.1.6.1. Silanol Water

Silica surfaces are covered by a chemically bonded monolayer of hydroxyl groups (Iler 1979; 2.6.2). These can occur as either single (Q^3) or geminal groups (Q^2) (2.6.2.1). The minimum temperature under vacuum for the condensation of twin groups on pure silica is about 200°C (Hockey and Pethica 1961). Once the temperature reaches 400°C, the position of the bonds at the silica surface are permanently transformed and the twin groups cannot be regenerated. Some of the single silanol groups are retained even upon heating to 1000°C (McDonald 1958). IR spectra show that hydroxyls are present both as single silanol groups and as twin groups attached to a single Si atom (Hockey and Pethica 1961). The location of these groups relative to the sphere surfaces and inter-sphere silica was not known. Twin groups probably make an important contribution towards the larger amount of combined water in opal-A, as the calculated surface areas of the spheres is less than the measured surface area.

Water can be physically held in capillaries up to about 150°C; water lost above this temperature (at the inflection point) may be assumed to be chemically bonded (Lakhanpal *et al.* 1955). This amounts to about 2.0%, which is readily accounted for by the internal surface area available. The

TGA curve shows that at 200°C, 1.6% water remains, and at 400°C, 1.0%. The residual water must represent single silanol groups (2.6.2.1) and would be consistent with a figure of 1.2% for a complete surface cover of these groups on spheres 200Å in diameter, or an incomplete cover on smaller spheres.

Jones and Segnit (1969) found that once opals were heated, twin hydroxyls were lost preferentially to single hydroxyls. Twin hydroxyls were removed between 200 and 600°C, while above 600°C most of the remaining hydroxyls were stripped off. They suggested that the reason for the inconsistency noted in their previous paper (Segnit *et al.* 1965, op. cit., neither the measured or theoretical internal surface area was adequate to account for the proportion of water found to be chemically bound by IR and NMR) was that the opal might have a smaller particulate structure than previously thought, with a diameter of 100 to 200Å (Jones and Segnit 1969). This leads to a theoretical value of 1.2 to 2.4% assuming a monolayer of single hydroxyl groups covering the silica surface. This value would increase if there were twin hydroxyls, multi-layers, or hydroxyl groups residing in the interior of the silica spheres.

Surface area and dehydration measurements (Segnit *et al.* 1965) of opal-CT (wood opal) revealed that only a small proportion of the total water content could be chemisorbed water. Approximately 0.5 wt.% of the opal was water present as surface hydroxyls (Segnit *et al.* 1965). This corresponded to less than 10% of the total water present. Opal-A on the other hand, had a greater proportion of its water as surface hydroxyls. Dehydration experiments by Segnit *et al.* (1965) indicated that at least 20% of the water was chemically bound; this figure differs from NMR results that show up to 70% of the water may be chemically bound (Segnit *et al.* 1965). This difference remains unresolved. After removal of physically adsorbed water by heating, an opal from Coober Pedy showed the reappearance of specific IR absorbances (Segnit *et al.* 1965).

4.1.7. TMA

The thermal expansion curves for various types of opals do not always fit into specific categories. For example, opals within the same group (such as opal-A) often exhibit diverse TMA results.

Opal-C specimens have shown the typical thermal expansion curve of well-ordered cristobalite, with a very sharp reversible expansion taking place at 200°C due to the inversion from $\alpha \rightleftharpoons \beta$ cristobalite (Jones and Segnit 1971). Opal-CT showed a moderate expansion up to 400 to 500°C, with a variable behaviour at high temperatures. Mostly opal-CT had almost zero thermal expansion above this temperature, or shrank to its original length (or less than its original length) by 900°C. This was evidently due to the loss of physically and chemically bound –OH groups. In the well ordered samples, weak inflections appeared in the early part of the curve at about 120 and 200 to 250°C corresponding to the $\alpha \rightleftharpoons \beta$ inversions of tridymite and cristobalite, respectively. Opal-A showed great variability in the thermal expansion curves, but effects due to structural inversion could not be detected (Jones and Segnit 1971).

The 200°C thermal expansion (TMA) curve inflection tentatively correlated with the onset of loss of twin hydroxyl groups and the 600°C inflection with final loss of most of the single hydroxyls (Jones and Segnit 1969). The variation observed in thermal expansion curves between 200 and 600°C could be related to the nature of the opal's porosity. A discontinuous pore phase would affect the water loss and may have caused the high rates of expansion observed with some samples.

4.1.7.1. Libyan Desert Glass (LDG)

McPherson *et al.* (1989) noted similarities in the TMA curves of precious opal and LDG, a naturally occurring high purity amorphous silica material (Figure 4-4). The expansion behaviour of precious opal and LDG was observed to change from dilation to contraction at a certain temperature. The temperature at which this onset occurred for LDG and precious opal was 950 and 300°C, respectively (McPherson *et al.* 1989). However, the potch opal sample investigated behaved differently to precious opal and LDG, it contracted up to below 300°C, with a decreasing

rate at higher temperatures. SEM also showed that the LDG samples contained an ordered array of microscopic voids similar to those observed in precious opal, although these voids were spherical. These results inferred that LDG formed through a sol-gel process similar to precious opal, although the spherical voids indicated LDG samples experienced a low temperature heat-treatment in their environment (McPherson *et al.* 1989).

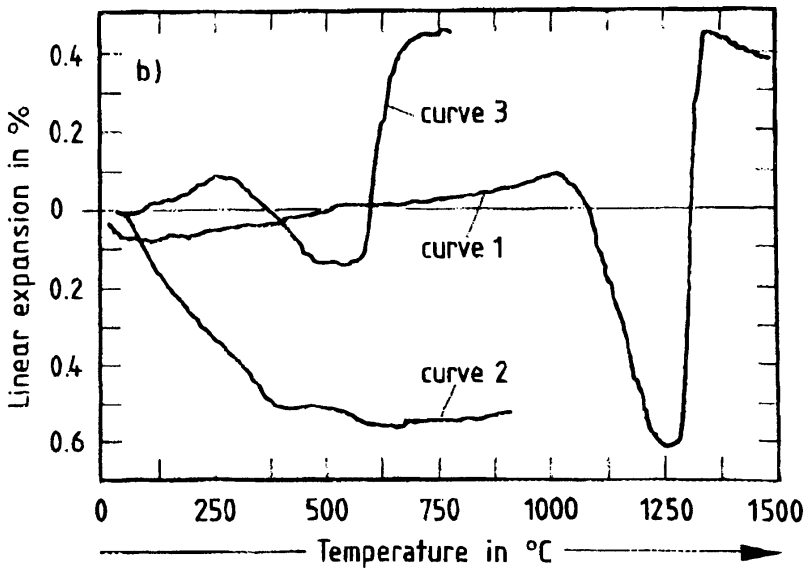

Figure 4-4: TMA curves of Libyan Desert Glass (1); potch opal (2); and precious opal (3). From McPherson et al. (1989).

Frischat *et al.* (1989) also used TMA to investigate LDG and ascribed the thermal expansion behaviour to be similar to the effect of viscosity-dependent flow. That study concluded LDG was more analogous to a synthetic silica glass, and that LDG may have formed through a high-temperature impact such as a comet or meteorite striking the Libyan Desert. An opal sample from Hungary was also investigated by Frischat *et al.* (1989) for comparative purposes, and the TMA curve shows markedly different behaviour to either precious or potch opal investigated by McPherson *et al.* (1989). Instead, the Hungarian opal shows two temperature ranges during which expansion was observed; from 0 to 200°C and the other between 500 and 700°C. At the temperature range between

200 to 500°C and also between 700 to 1500°C, the coefficient of thermal expansion (CTE) was almost zero (Frischat *et al.* 1989). The original model of formation of LDG through extraterrestrial origin (Frischat *et al.* 1989) has since been revised to the fusion of a terrestrial material (Frischat *et al.* 2001).

4.1.8. Sintering

Heating causes crystallisation and internal morphological changes due to sintering in both volcanic and sedimentary opals. In all cases sintering precedes the onset of crystallisation by approximately 700°C. Sintering changes the shape of the cavities into spherical voids (Sanders 1975; Kazantseva *et al.* 1987).

Sanders (1975) heated opal-AG samples from Lightning Ridge, Andamooka, and White Cliffs at temperatures up to 1100°C. For each set, sintering became appreciable at temperatures between 350 and 480°C. The majority of sintered specimens contained spherical voids, although some specimens showed no signs of sintering. This indicated either heterogeneity of the specimen, or that the time was insufficient for temperature equilibrium to have been attained. Sanders (1975) also found that once precious opals had been heated to 700°C, although the shapes of the voids changed, their spatial arrangement was not altered so that they still formed a regular array. This was consistent with the observation that heating to 1000°C generally does not destroy the play of colour in opal (Sanders 1975). The onset of sintering was less easily detected with opals from volcanic sources [opal-CT], but was found to be in the range 400 to 600°C (Sanders 1975).

4.1.9. Low-temperature DTA

Buerger and Shoemaker (1972) investigated the freezing behaviour of water in opal-C (wood opal); originally this study intended to detect the high to low cristobalite transition, as all cristobalite in opal-C and opal-CT exists in the high-temperature form (2.5.2). Buerger and Shoemaker (1972) reported that the freezing point of the water contained in opal occurred at a temperature much lower than expected. For wood opal (type opal-C) an endotherm was detected at -50°C on heating and an exotherm

was detected at -40°C on cooling (Buerger and Shoemaker 1972). A similar transition was observed for a variety of opals, whether in powdered or bulk form. At temperatures below this thermal transition, cristobalite was still in the high-temperature form in the low temperature XRD results reported for Buerger and Shoemaker (1972). The observed transformation, therefore, could not be attributed to cristobalite. The thermal transition was not observed in opals that had been dried at high temperatures. At a drying temperature above 422°C, no thermal effect was noticed. The heat effects are therefore ascribed to the water present in the opal. Pure, distilled water and water that was exposed to opal for 10 days had very similar DTA curves, indicating that the distilled water did not absorb any of the opal's impurities. Therefore, these heat effects were not due to the presence of dissolved impurities during the period of the experiment. It appeared that the curious thermal behaviour of water in opal was associated with the capillary aspect of the spaces in which the water was contained. The curious thermal effect noted by Buerger and Shoemaker (1972) appears to be a recurrence of the notorious "anomalous water" reported in the literature several decades before (Bascom *et al.* 1970; Prigogine and Fripiat 1971; Brummer *et al.* 1972; Deryagin and Churaev 1973; Van Steveninck 1991).

4.1.10. Other studies concerning microstructure

Chojcan and Sachanbinski (1993) investigated the positron annihilation behaviour within opal-AN, a hyalite specimen originating from Poland. Using a lifetime spectrometer, the researchers concluded that the sample contained micropores that were approximately 8 to 10Å in diameter. Mikhailov *et al.* (1963) also noted that opal probably contained many small pores less than 12Å.

4.1.11. Nitrogen adsorption studies

Despite an extensive literature search, very few references could be found concerning gas-adsorption analyses of opal. Bustillo *et al.* (1993) reported that the specific surface area (SSA) of opal-A (diatomite) was 23.87 m^2/g, and the SSA of opal-CT (from siliceous rocks and silcretes of the Miocene age) was between 7.76 and 14.05 m^2/g.

Graetsch *et al.* (1985) determined the SSA of one opal-C sample, obtained from a Brazilian agate geode (using the BET method); this was calculated to be 1.2m^2/g.

Segnit *et al.* (1965) investigated a crystalline wood opal from Lake Eyre and a banded opal from Coober Pedy. The wood opal yielded a SSA of 0.41 m^2/g, while the SSA figures for the banded opal from Coober Pedy were different for each band; the 'milky' band yielded 40 m^2/g SSA, while the transparent band yielded only 0.61 m^2/g.

The sorption properties of opal have also been investigated[1] by other researchers using mercury porosimetry and nitrogen adsorption methods (Zabelin 1968; Khimicheva *et al.* 1991). Zabelin (1968) reported that the thermal ageing of opal (at temperatures greater than 350°C) reduced the sorption activity of water vapour, benzene and carbon tetrachloride; this change was ascribed to the dehydration of the internal surfaces of opal. The thermal ageing of opal at temperatures above 500°C sharply decreased the opal's sorption activity; this was accompanied by strong changes in the porous structure, with the decrease in volume of pores smaller than 10 nm in diameter. Significant changes in the porous structure of opals were observed at temperatures greater than 750-800°C. After thermal treatments at 1050°C, the opal samples lost their adsorptive properties, becoming practically nonporous.

4.1.12. Objectives

The difficulty with observing the microstructure of opals directly by SEM is that etching of the opal with hydrofluoric acid is required to provide relief; otherwise it is practically impossible to focus at the high magnifications necessary to observe the colloidal microstructure. It is expected that this thermal analysis investigation of opal will reveal information about the dehydration behaviour of opals, and in conjunction with nitrogen adsorption analysis, the results should provide information concerning the fine textures associated with opal-AG.

[1] Two Russian papers (Zabelin 1968; Kazantseva *et al.* 1987) were translated into English by first using an optical-character-recognition (OCR) software program (Cuneiform Pro 6.0 or Omnipage Pro 12.0), to achieve editable cyrillic text from the photocopied journal papers. The cyrillic text was then converted into English through the multilingual translator service available online at www.altavista.com.

4.2. EXPERIMENTAL

4.2.1. Australian opal fields

Each opal "region" (for example Andamooka, Lightning Ridge and Coober Pedy, etc) is divided up into smaller areas called "fields" (Big Flat, Southern Cross, Dead Mans Gully). Each of these "fields" is then subdivided into "mines", and each "mine" may be further divided into "levels" (Figure 4-5).

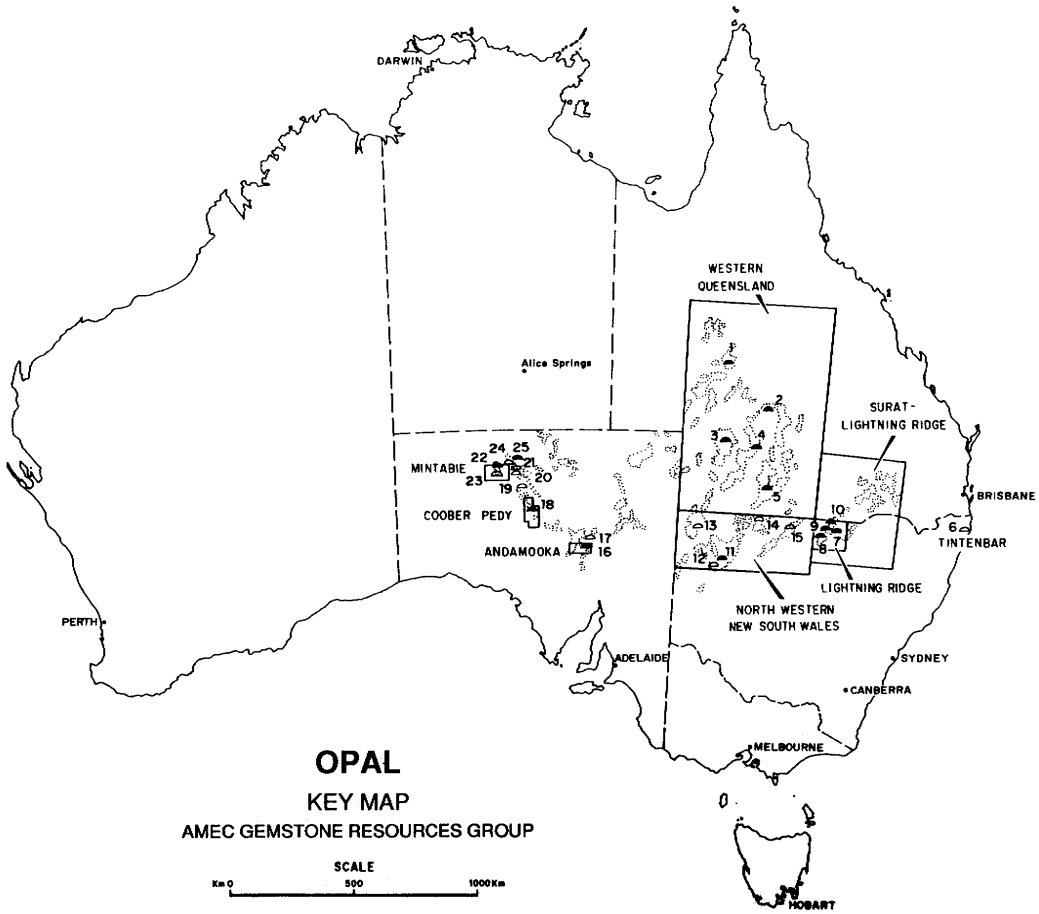

Figure 4-5: Mining Regions of Australia. The White Cliffs opal field is located at point 11, in the North Western corner of New South Wales.

4.2.2. Sample Acquisition

There are no major opal mining corporations in Australia; all opal mining is done either by solitary miners, or by small cooperatives of miners.

Miners, although friendly enough, are generally wary of outsiders; they are understandably a little suspicious and sceptical of anyone they do not personally know. One consequence of this is that often, miners are very secretive about their valuable finds within their privately leased mines. They are reluctant to reveal any information about their opal finds that could be potentially beneficial to their competition. The quantity, quality and location of opals found is not usually divulged, let alone detailed attributes such as the orientation in which they were found.

4.2.2.1. Opal mining

Opals are mined by first scooping the "opal dirt" from the opal level; most often this is performed with the aid of pneumatic or hydraulically driven machinery. The opal dirt then undergoes a process known as 'trummeling'. During this stage, the opal dirt is usually introduced into a converted cement-mixer, which allows water to drain out. When the opal dirt is mixed with water and the drum is rotated, it forms a slurry and any solid objects (such as the opal nobbies) are easily sorted and separated by hand. Under these circumstances, it is practically impossible to determine the exact orientation and position of a particular opal sample in connection with a particular mine or level in a mine.

The samples considered here were generously donated by miners that were obtained through a fellow UTS colleague (Smallwood, A.G.). They were samples that had been collected over the years, and the miners could not always recall the exact field in which a particular sample was mined. Furthermore, most of the Australian opal fields are fairly remote (Lightning Ridge is approximately 800km North-West of Sydney). Given the above set of circumstances, it is difficult to ascertain a sample's exact origin (i.e. its position and orientation within a mine), other than the general region from which it was obtained. Although the opal fields within a region are geologically similar, there might be implications with respect to the localised formation of opals. Detailed knowledge of the sample's provenance (within an opal mining region) would facilitate our understanding of some of the more unusual specimens (especially for multi-banded samples), since different local environments would most likely influence some of the mechanisms discussed previously, most notably the composition of the

original sol and the ability of water to be transported throughout an opal-generating system.

The opals studied in this project were from four different Australian regions: Andamooka and Coober Pedy in South Australia, as well as Lightning Ridge and White Cliffs in New South Wales. Samples characterised by TMA, TGA and N_2 adsorption analyses are listed in Table 4-1. Photographs of samples LR1 and LR2 are provided in Figure 5-1.

Sample	Colour	Opacity	Nature of sample
Coober Pedy (CP9)	White	Opaque	Non-banded
White cliffs (A and B)	White	Translucent	Non-banded
Lightning Ridge (LR2black)	Black	Opaque	Banded
Lightning Ridge (LR1clear)	Clear	Transparent	Banded
Lightning Ridge (LR17poc)	Play of colour	Translucent	Banded
Andamooka (ANDA 8)	Pale violet	Translucent	Non-banded
Tintenbar	Brown	Translucent	Non-banded

Table 4-1: General appearance of the samples used in TMA, TGA and N_2 adsorption analyses.

4.2.3. TMA

The experiments were carried out using a TA Instruments TMA 2940 Thermomechanical Analyser using the instrument as a dilatometer. This study was undertaken at the Department of Chemistry, Materials and Forensic Science (CMF), at the UTS city campus. The instrument was previously calibrated by analysing the baseline; this was done by performing a separate TMA run with an Al_2O_3 standard. A total of twenty six specimens were analysed, nine of which were from Coober Pedy, six from Lightning Ridge, eight from Andamooka, and three from White Cliffs.

4.2.3.1. Sample Dimensions

Ideally the specimens were cut to a length of between 6 and 7mm long, with a width and depth of approximately 3mm. These dimensions were chosen for several reasons. Elongated specimens attain results of a

higher precision than those of shorter dimensions; this is because the instrument is measuring a proportionally larger dimensional change with a longer specimen, yet the minimum ΔL sensitivity of the instrument stays the same. On the other hand, limiting the size of a specimen reduces the time it takes the temperature to equilibrate throughout the specimen. Since the thermocouple is some distance away from the centre of the opal, erroneous measurements of temperature may be caused, potentially leading to inaccurate results. Therefore, in order to strike a balance between these two opposing characteristics, where possible, long and narrow specimens were cut as the expansion was only measured in the longitudinal direction, not across the thickness of the specimen.

4.2.3.2. Sample preparation

The opal specimens were cut using a diamond tipped circular saw (wafering blade). The opal was cut so that the ends of the specimen were parallel. Any burrs remaining from the cutting stage were removed by grinding them off at a steep angle to the parallel faces, resulting in a facet usually on the corner of the opal specimens. A diamond impregnated abrasive wheel lubricated with water was used for this procedure. The opal specimens were thoroughly cleaned of all traces of cutting oil using detergent, then ethanol, and finally washed in water and dried with paper towelling.

4.2.3.3. Heating rate

The heating rate was set at 1.5°C per minute, except where otherwise stated. This is a slow heating rate, but necessary to prevent the opals from cracking or decrepitating during the experiment. The opals were heated up to 690°C and cooled back to 30°C. The cooling curve was used to verify if dehydroxylation was complete. The maximum temperature was limited to 690°C because initial trials showed that most of the opals behaved similarly above approximately 600°C. Furthermore, the part of the TMA that was in contact with the opal specimen is also made of silica, and it was feared that the opal might fuse to the TMA apparatus if a higher temperature was used.

For the opals from Coober Pedy, eight specimens were tested to check the precision of the experimental method. This was done by testing two

specimens cut from the same opal sample (or piece), and then comparing those results to those acquired from other opal pieces.

4.2.4. TGA

Thermogravimetric experiments were performed with a TA Instruments 2960 Simultaneous DTA-TGA, located at the Department of CMF, UTS city campus. The instrument was previously calibrated by analysing the baseline (with an empty sample pan); this was automatically subtracted from the TGA curves in each case. A total of fourteen specimens were analysed, four of which were from Coober Pedy, four from Lightning Ridge, four from Andamooka, and two from White Cliffs as the supply of that material was very limited.

4.2.4.1. Sample Preparation and Dimensions

A diamond impregnated abrasive wheel lubricated with water was used to obtain the sample dimensions required to fit in the sample pan of this instrument. The opal samples were washed in water and dried with paper towelling.

The specimens used for the TGA were somewhat smaller than those used for TMA, as the balance is limited to a maximum of 200 milligrams of sample. Where possible, however, the proportions of the TGA specimens were kept similar to those of the TMA specimens. In most cases, the opal cut-offs from the TMA sample preparation were used for TGA specimens. This ensured that the opal used for TGA was from the same piece as that used for the TMA. As the amount of substance can affect the experimental results obtained with thermal analysis, care was taken to select similarly sized samples. The samples were mostly rectangular prisms, but occasionally small "chips" were used. The samples were weighed before being heated to 1200°C at 1.5°C/min. The initial mass of the specimens ranged from 15 to 70 mg.

4.2.4.2. Calculation of the rate of weight loss

The weight loss from the sample was recorded, and the derivative of this weight loss was also calculated, with respect to time. This calculation provides the rate of weight loss at each temperature. This was determined at each weight-loss data point by taking the slope of the nine points

surrounding the data point in question, and determining the slope (line of best fit) by linear regression of those points. Taking the slope over several points rather than just two or three significantly improves the smoothness of the curve. There are often small but abrupt steps in the weight loss curve, and between those particular points the slope tends towards infinity. The number of steps and their size become greater with increased heating rates, hence they are thought to be caused by microcracking in the samples. Where practical, however, the larger of these jumps were removed from the data to aid in the interpretation of the graphs. This was accomplished by subtracting the appropriate amount of "erroneous" weight loss from all the data points (to compensate for the step) beyond the temperature where the step first occurred.

4.2.5. Nitrogen Adsorption

The nitrogen adsorption analyses were performed on a Micromeritics TriStar 3000 instrument located at Particle and Surface Science Laboratories (Gosford, NSW, Australia). An N_2 adsorbate at 77.35 Kelvin was used for all analyses, with a molecular cross-sectional area of 0162 nm^2 used in subsequent calculations. Pressure was increased over the range of 4 to 766 mmHg. Equilibration interval was set to 15 seconds and the minimum equilibrium delay (at $P/P_o \geq 0.995$) was 600 seconds. N_2 gas was used to backfill (purge) the sample chamber at the start and end of each analysis. Warm freespace was equal to (8.5±0.3)cm^3; cold freespace was equal to (25.5±1.0)cm^3. All samples were thermally treated to remove water from the void spaces prior to the analyses; the samples were heated at a rate of 5°C/min to 300°C, soaked at this temperature for two hours and then equilibrium-cooled to room temperature. The samples were weighed before being analysed, to enable the specific surface area (SSA) to be calculated; The initial mass of the specimens ranged from 350 to 600 mg. Pore size distribution and SSA values were calculated using the Barret-Joyner-Halenda (BJH) adsorption isotherm.

4.2.5.1. Sample Details.

Six opal samples were analysed in total. These included the same samples (CP9, LR1clear, LR2brown, ANDA8, and Tintenbar) analysed with

TMA, TGA, LA-ICPMS, SIMS and NMR (see sections 4.3.1; 4.3.2; 5.3; 6.3; and 7.3) and an additional sample (LR17POC) not previously studied.

4.3. RESULTS

4.3.1. Thermomechanical Analysis

4.3.1.1. Transition Temperature

For all specimens, the TMA curves showed a characteristic appearance. The opals initially expanded up to a certain temperature (210 to 420°C), beyond which they contracted. The temperature at which the opals changed from a positive to negative thermal expansion coefficient (i.e. point at which the thermal expansion coefficient equals zero) will be referred to as the transition temperature.

These transitions occurred at various temperatures depending on the type of opal (Table 4-2). For instance, the Andamooka opals showed the highest transition temperature followed by the Lightning Ridge specimens with the Coober Pedy specimens displaying the lowest transition temperature. In general, the Coober Pedy opals showed a relatively sharp transition from expansion to contraction making the estimation of their transition temperature relatively simple in contrast with the Andamooka opals, which exhibited gradual transitions from expansion to contraction. One of the Andamooka specimens (A81) showed a second transition from contraction to expansion (Figure 4-6). The two types of opals from White Cliffs displayed considerably different transition temperatures (Table 4-2). In addition, White Cliffs A opal showed a more distinct transition from expansion to contraction than White Cliffs B. Typical TMA curves can be seen in Figures 4-6 and 4-7.

Type of Opal	TMA Transition Temperature (˚C)	TMA coefficient of thermal expansion (µm/m˚C)
Coober Pedy	212	6.22
	213	6.42
	218	6.87
	205	7.05
	222	5.75
	217	6.55
	195	7.95
	211	5.78
White Cliffs A	292	6.22
	292	6.41
Lightning Ridge (black)	303	6.76
	315	7.38
Lightning Ridge (transparent)	347	6.44
	284	6.66
White Cliffs B	345	7.13
	373	–
Andamooka	406	9.59
	377	4.83
	404	6.24
	407	6.22
	385	6.24
	414	5.83
	402	3.92

Table 4-2: Transition temperatures of opals from various localities.

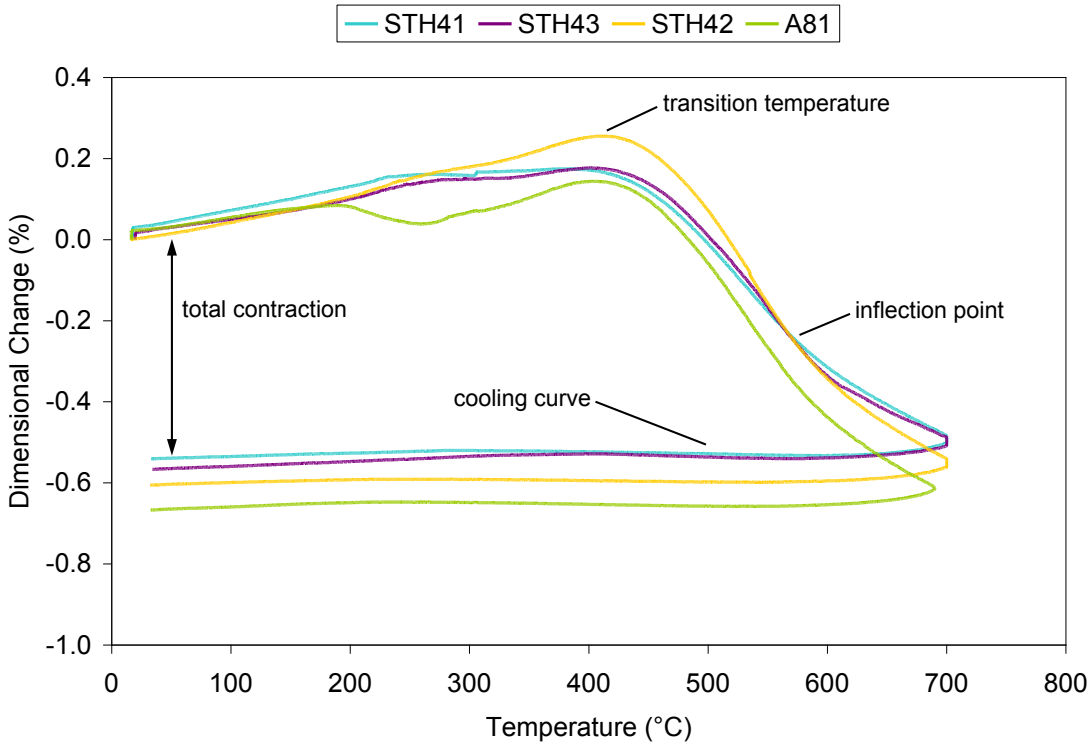

Figure 4-6: Thermal expansion curves of various Andamooka samples.

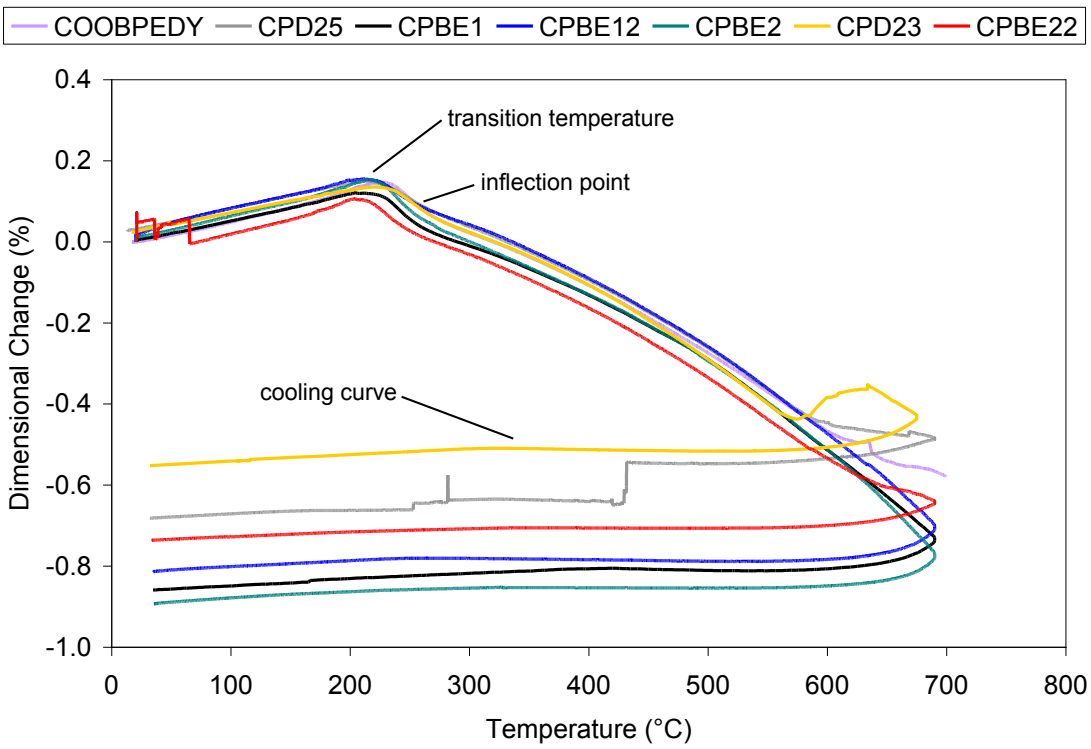

Figure 4-7: Thermal expansion curves of various Coober Pedy samples.

The results described in this section are generally consistent with those reported elsewhere (Jones and Segnit 1969; Jones and Segnit 1971; Frischat *et al.* 1989; McPherson *et al.* 1989). For the Coober Pedy samples, the transition temperature was estimated to be between ±5°C of the value stated. For all others, the transition temperature was estimated to be within ±10°C of the reported value.

4.3.1.2. Thermal Expansion

The thermal expansion coefficients were measured over the greatest temperature range possible, from the lowest temperature possible (usually ambient laboratory temperature, ~25°C) up to the point that the slope became noticeably non-linear (the transition temperature varies depending on the sample) or until a step was encountered. The values recorded are listed in Table 4-2. The temperature at which the thermal expansion coefficient was measured could not be standardised, because of the way some samples spontaneously cracked.

The expansion rates up to the transition temperature for each opal were surprising fairly similar. However, the total amount of expansion up until the transition temperature varied depending on the opal sample. Opals exhibiting high transition temperatures expanded more than those showing low transition temperatures. The total amount of contraction at the completion of the experiment also displayed variation; generally it was less in the Andamooka samples and more in the Coober Pedy samples.

The cooling curves were typically featureless with no detectable expansion-contraction transitions. Once heated, all samples changed in appearance to an opaque white colour, while all except one sample also lost most of their play of colour. Curiously, one sample from Lightning Ridge retained most of its play of colour even after the completion of the TMA experiment. This result is consistent with the literature, as Segnit *et al.* (1965) reported similar findings.

Another interesting result is that the different types of opals showed variable contraction rates. For example, most Coober Pedy samples showed an inflection point just after the transition temperature, at about 250°C (Figure 4-7). At higher temperatures than this, the rate at which the Coober

Pedy samples contracted increased as the temperature increased. Conversely, all of the opals from Andamooka showed an inflection point well beyond the transition temperature, at about 560°C. Notice that beyond the transition temperature, the contraction rate initially increased, but then decreased as the temperature continued to increase (Figure 4-6).

4.3.2. Thermogravimetric Analysis

The temperature at which a maximum rate of water loss was observed varied over a broad range between 215 and 350°C, depending on the location of the opals (Table 4-3). Other workers (Jones and Segnit 1963; Segnit *et al.* 1965) have reported that opals generally lose water between 200 and 500°C. The Coober Pedy specimens examined were found to lose water over a narrower temperature range than the other opals. The water content was calculated from the amount of silica residue remaining after heating the opal to 1200°C. This value was subtracted from the initial mass of the specimen to determine the total water content.

Type of Opal	TGA Temperature of Maximum Dehydration (°C)	Water content (%)
Coober Pedy (CP9)	215	7.82
	233	>5.5
	222	7.95
White Cliffs A	275	7.06
	234	6.84
Lightning Ridge (black)	325	7.19
	322	7.24
Lightning Ridge (transparent)	317	9.05
	334	>4.5
White Cliffs B	316	6.75
Andamooka (ANDA8)	344	6.64
	343	7.12
	352	6.64
	356	6.40

Table 4-3: Maximum Dehydration Temperatures and total water contents of various opals

The Andamooka opals showed the highest temperature at which there was a maximum rate of dehydration (Figure 4-8); they were followed by those from Lightning Ridge with Coober Pedy specimens displaying the lowest dehydroxylation temperature. The dehydration of Coober Pedy opals was initiated at lower temperatures than the other types of opals, and they

also exhibited a considerably faster rate of dehydration. For one Coober Pedy sample, the rate of weight loss curve has a shoulder, probably the superposition of two peaks, each having a different rate of dehydroxylation (Figure 4-9).

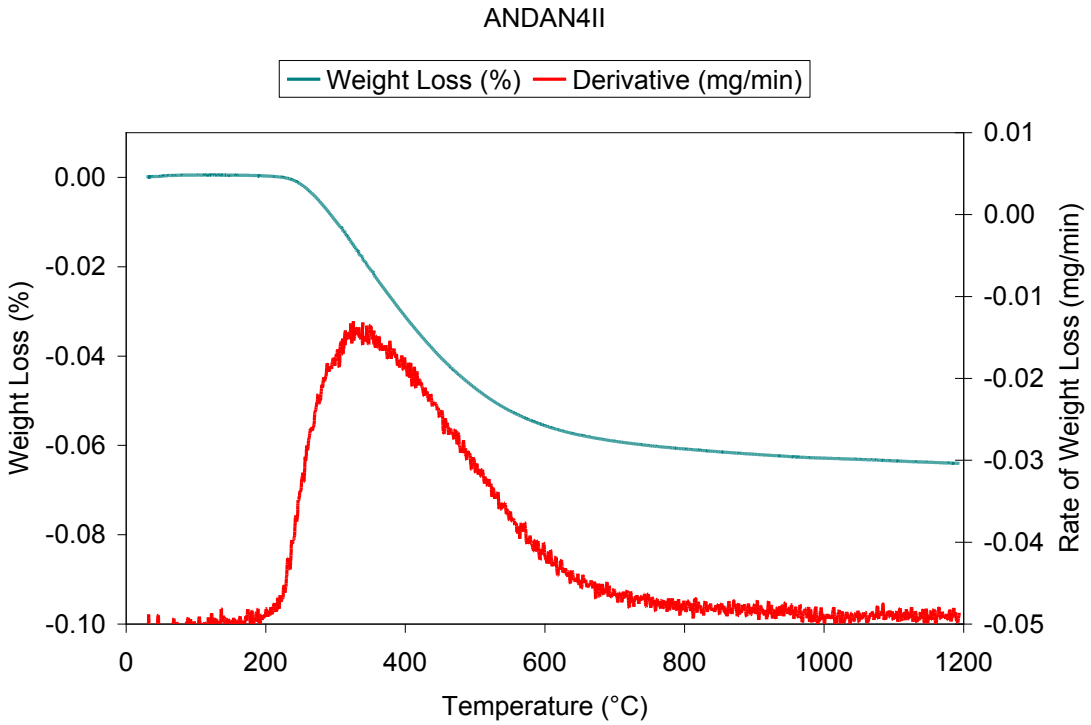

Figure 4-8: Weight loss curve and rate of weight loss curves for an Andamooka sample. The maximum rate of weight loss occurs at ~350˚C.

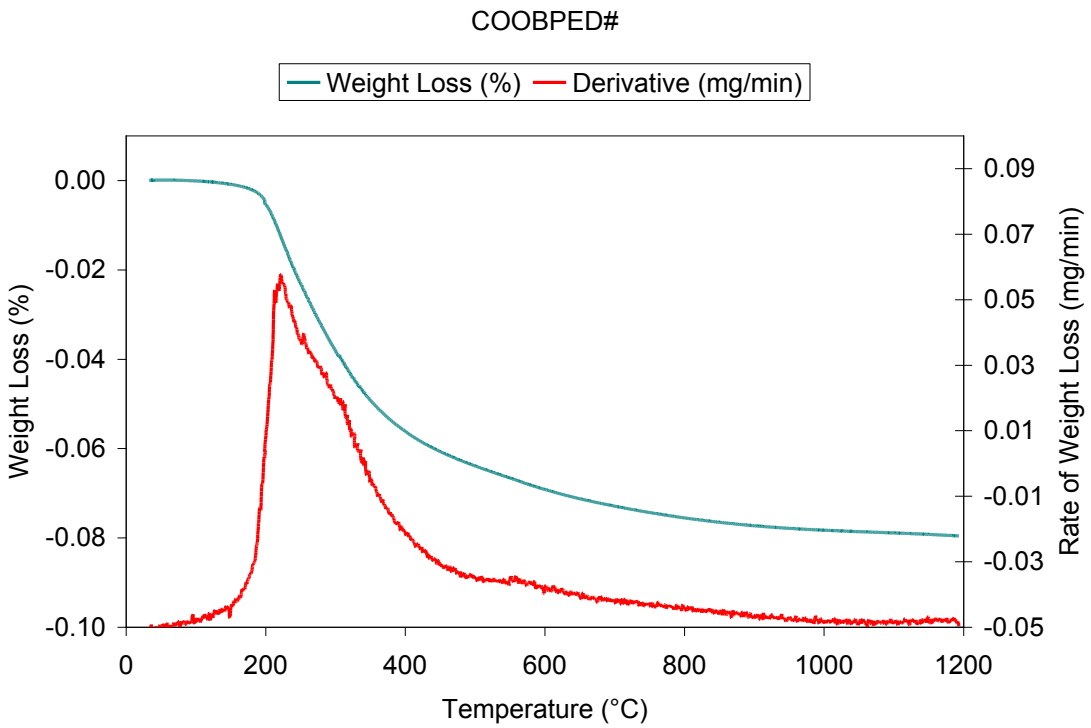

Figure 4-9: Weight loss curve and rate of weight loss curves for a Coober Pedy sample. The maximum rate of weight loss occurs suddenly at 220˚C.

Due to the broad nature of the peaks and the microcracking of the opal specimens, it was often difficult to precisely pinpoint the maximum dehydration rate. The error in determining the exact position of the peaks where the maximum rate of water loss occurred was estimated to be ± 4˚C for the Coober Pedy samples and ± 15˚C for all other opal samples.

The maximum dehydroxylation temperature measured in this study for the Coober Pedy specimens correlates well the temperatures for dehydration of amorphous Coober Pedy opal by Segnit *et al.* (1965); the rate of water loss being greatest at around 230˚C and most of the water having been lost by 500˚C.

4.3.3. Nitrogen Adsorption

4.3.3.1. Total porosity and SSA

Nitrogen adsorption experiments revealed that various opal-AG samples from Lightning Ridge, Coober Pedy and Tintenbar contained different levels of porosity. Transparent and translucent samples contained the least total porosity, while opaque samples contained the greatest level

of porosity (Table 4-4). The precious gem-quality opal displaying a play of colour exhibited significantly higher total porosity and SSA than all other potch opals. The SSA values were for the most part lower than those reported elsewhere for various types of opal (Segnit *et al.* 1965; Zabelin 1968; Graetsch *et al.* 1985; Khimicheva *et al.* 1991; Bustillo *et al.* 1993).

Sample	**Description**	**Total porosity (mm^3/g)**	**SSA (m^2/g)**	**Average Pore Size (nm)**	**Modal Pore size (nm)**
LR1clear	Transparent; pale yellow	0.33	0.25	5.3	flat distribution.
ANDA8	Transparent; pale violet	0.34	0.26	5.2	~2 to 4
LR2black	Opaque black	0.78	0.50	6.2	2.1
CP9	Opaque white	1.4	0.89	6.4	2.1
Tintenbar Opal-CT	Translucent brown	0.30	0.28	4.2	< 1.8
LR17	Opaque; play of colour	3.3	2.6	5.0	3.1
17015	Coober Pedy "Milky" precious opal-AG	–	0.41	–	–
1445C[1]	Transparent wood opal-CT from Lake Eyre	–	0.61	–	–
1445M[1]	Milky wood opal-CT from Lake Eyre	–	40	–	–
CNS-4[1]	Freshwater laminated diatomite (opal-A)	47.5	23.87	–	2.4
TJ-36(IR)[2]	Diagenetic opal-CT nodule in sepiolite	128	91.2	–	~1.5
ANG-94[2], ANG-74[2], ANG-87[2], ANG-82[2]	Opal-C	4.60 – 6.74	1.93 – 2.56	–	–
226-B1[3]	Opal-C	–	1.2	–	–
№ 21[4]	Unknown opal	–	30 – 40	–	–
205/1[5]	Opal-CT from USSR	–	77	–	–

Table 4-4: Total porosity, SSA and pore sizes for various opal samples. [1] Data from Segnit et al. (1965). [2] Data from Bustillo et al. (1993). [3] Data from Graetsch et al. (1985). [4] Data from Zabelin (1968). [5] Data from Khimicheva* et al. *(1991).

4.3.3.2. Pore size distribution

While the average pore size was fairly constant, between 4.2 to 6.4 nm for all the samples, the distribution of pore sizes was sample dependent. The transparent opal samples maintained a relatively flat pore size distribution between pore diameters of 1.7 and 100 nm. On the other hand, the opaque samples yielded a characteristic mode of pore sizes; the greatest number of pores were found with diameters between 2 and 4 nm, the least number of pores ranged between sizes 20 to 50 nm and an increased number of pores were seen with diameters above 50 nm. The majority of pores in the Tintenbar opal sample were only 1.7 to 1.8 nm in diameter[1]; the number of pores greater than 3 nm in size was significantly less; whereas pores with sizes greater than 10 nm were practically non-existent.

4.4. DISCUSSION

4.4.1. Thermomechanical Analysis

4.4.1.1. Thermal expansion

The thermal expansion coefficient values showed considerable variation, even among specimens from the same region (Table 4-2), and therefore cannot be used to distinguish between opals from different regions. The opals from Andamooka were still expanding well beyond 350°C, while those from Coober Pedy were contracting at this temperature. At first, this effect was thought to be due to the variable proportion of water in the different types of opal, but since the water content did not vary by more than 20% for the opals (in relative terms; the actual water content changed by only ~1.2% by weight of opal), this result is most likely caused by the nature of inter-sphere pore spaces instead (this is discussed further in section 4.4.1.5).

4.4.1.2. Transition temperature

For all opal samples analysed in this study, a change from positive to negative thermal expansion coefficient was observed. The reason for that characteristic is unclear, but a possible explanation is presented below. It is

[1] The calculation of the void size using the BJH adsorption isotherm only remains valid for pore diameters ranging from 1.7 to 300nm.

envisaged that there are two competing processes operating. Initially, the opals show expansion because the water that is trapped within the mesopores expands during heating (in addition to the hydroxylated water that is bound to the silica network). Once all the water has been expelled, the expansion ceases and the opals behave like pure silica. These 'anhydrous' opals will have a tendency to collapse or shrink because of their semiporous void structure. Upon further heating, the structure becomes more pliable, and it will progressively contract. The degree of contraction will depend on experimental factors including temperature and time, and on intrinsic factors such as size, shape and packing of spheres in individual opals. Since the CTE of synthetic silica glass is only ~0.5µm/m°C at this temperature (Bansal and Doremus 1986), this theory adequately explains why the cooling curve in all cases is almost a straight line, because once all the water has been lost, what remains is a product consisting of approximately 98-99% silica, with an inherently low thermal expansion coefficient.

The spheres in opal-A are believed to be partially coalesced (Sanders 1964; Darragh *et al.* 1966; Darragh *et al.* 1976; Landmesser 1998; 3.4.2), and the results of the opals investigated here support the idea that these spaces are filled to varying degrees by virtue of the different transition temperatures. This is inferred because the structure is collapsing at different temperatures (4.4.1.3). Furthermore, opals which consist of interconnected pores (i.e., an "open" void type of structure) would result in a lower transition temperature than opals with an isolated ("closed" void structure) pore structure.

4.4.1.3. Sintering

Essentially, above the transition temperature, solid state sintering is a likely event. While the initial stage of neck formation between individual spheres in the opal structure might have reached completion when it originally formed, a second stage of sintering in the solid state is conceivable during the heating cycle of the thermal analysis. This may be observed in difference between the microstructures of thermally aged opal, and un-aged opals, as seen in Figure 4-10.

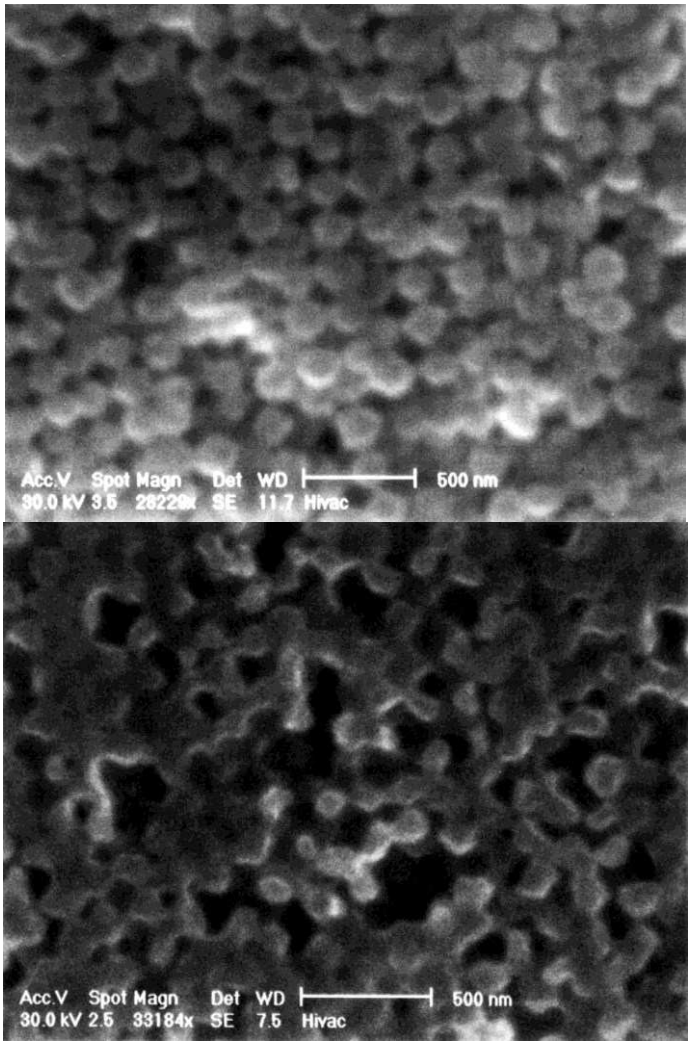

Figure 4-10: Normal Andamooka opal-AG (top) and Andamooka opal-AG after completion of TGA run at 1200˚C (bottom). Note the change in the shape of the voids in the heat-treated sample; the spherical nature of the voids is indicative of sintering.

Equation 4-1 is a mathematical model for solid state isothermal sintering (Richerson 1992):

Equation 4-1:

$$\frac{\Delta L}{L_0} = \left(\frac{K\gamma a^3 D * t}{kTd^n} \right)^m$$

Where: $\frac{\Delta L}{L_0}$ = linear shrinkage

K = constant dependent on geometry

γ = surface energy

a^3 = atomic volume of the diffusing vacancy

D^* = self diffusion coefficient

t = time

k = Boltzmann constant

T = temperature

d = particle diameter

$n \approx 3$

$m \approx 0.3$ to 0.5

4.4.1.4. Shrinkage/Contraction

From Equation 4-1, the shrinkage is seen to be dependent on: temperature; time; particle size; volume of diffusing vacancies; uniformity of particle packing; particle shape; and particle size distribution. A microstructure consisting of smaller spheres results in a greater sintering rate than one with larger spheres. The opals from Coober Pedy had a greater propensity towards contraction than the other types of opals analysed, indicating that they are more readily sintered than other types of opals investigated. This suggests that the Coober Pedy samples could contain pores with a smaller diameter than other samples. Pore size distribution results showed that the mode of pore sizes calculated for the Coober Pedy opal was ~2.1nm and ~4.2 nm for the Andamooka opal; whereas LR1clear contained a relatively flat pore size distribution, apart from spikes.

4.4.1.5. Contraction after the Transition Temperature

The total amount of contraction after the run was completed varied with the type of opal, being generally less in the Andamooka samples (as low as 0.54% for the STH41 sample) and more in the Coober Pedy samples (as high as 0.90% for the CPBE2 sample). This result might be due to the proportion of water in the opal, but is more likely related to the pore structure. This suggests that the Coober Pedy samples contained pores that were relatively less filled with additional silica than the Andamooka samples. This is confirmed by the N_2 adsorption results, which showed that the Coober Pedy opal sample had four times the total porosity of Andamooka

opal sample, and twice the porosity of the LR2black sample. The contraction rate would also be influenced by this factor, and the inter-connectivity of the pores would also contribute to the contraction rate. Thus, a slow contraction rate indicates that a discontinuous pore phase is present; while a faster contraction rate is a sign of a continuous pore phase

The opals that expanded more in the initial stages also contracted less at higher temperatures. This would at first seem to be contradictory; if a large or open void structure allows for more expansion of water inside these voids, then it should also contract by a greater amount upon dehydration. What this perplexing result signifies is that the nature of the voids is complex. They may be partially 'filled' with water and silica, and not necessarily to an equal degree. Therefore the opals that contract the most (Coober Pedy) have overall the highest proportion of unfilled pores (by silica- as the water has already been removed); those that have little capacity for contraction (Andamooka) are probably already filled with some silica, so are unable to sinter to the same extent. The reason the opal samples from Andamooka expanded more than those from Coober Pedy in the first place could be due to the aforementioned inter-connectivity of the pore phase, in that it is discontinuous, so dehydration takes longer. Also, if the Andamooka opal samples have voids that are filled with more silica than the Coober Pedy samples, the remaining air space is likely to build up greater water vapour pressure as the water is forced to escape.

Another possibility is that as the –OH groups are released through the reaction shown in Equation 3-1, new Si–O–Si bonds are formed. This process most likely occurs initially at sites where the surface energy is at its highest, such as where the sphere surfaces are close together; in this way, the coalescence of the opposite walls of the smallest micropores permits contraction of the network structure.

4.4.1.6. Speculations on low-temperature sintering

Sintering of opal is initiated at lower temperatures than other silica glass polymorphs. The glass-transition temperature (viscosity ≈ 10^{13} Poise) is approximately 740°C for synthetic aluminosilicate glass and ~540°C for soda-lime-silica glass, although both are essentially non-hydrated, unlike

opal (Doremus 1973; Bansal and Doremus 1986). The viscosity of silicate glass is highly dependent on chemical composition, decreasing markedly with increased composition of network modifying cations and increased water content (Bansal and Doremus 1986; Richerson 1992). However, the opals investigated here are composed of less than 2% total cation impurities (2.2). Moreover, addition of Al_2O_3 to synthetic silica glass typically *increases* the viscosity (Richerson 1992), and as much as half of the impurity atoms in opal are Al (See section 5.3). One explanation for the observation of sintering at such low temperatures is that the silica network contains micropores that are extremely small, on the order of 0.8 to 5 nm (Mikhailov *et al.* 1963; Langer and Flörke 1974; Bustillo *et al.* 1993; Chojcan and Sachanbinski 1993; Table 4-4). Obviously, pores of these dimensions have a very high negative radius of curvature, and hence have a very high surface free energy also. As the temperature is increased in the TMA experiments, the molecular structure is able to rearrange itself more easily, and the silica network would tend to collapse around these miniscule pores first, possibly explaining the onset of sintering at such low temperatures.

4.4.1.7. Double Inflection of Thermal Expansion Coefficient

The reason for the thermal behaviour of the anomalous Andamooka specimen (showing two transition temperatures), is uncertain. The most likely explanation is that there are two different sizes of pores in the opal (i.e. a bimodal distribution of voids). The smaller sized voids would sinter at a lower temperature than the larger sized voids. These two differently-sized voids could be attributed to octahedral (larger) and tetrahedral (smaller) voids in the close-packing arrangement of secondary spheres. Alternatively, the larger voids could be located between secondary silica spheres (both octahedral and tetrahedral), while the smaller voids could be located between primary silica particles (if they exist). Of course, this in itself does not explain the peculiar results of the two Andamooka specimens, but the smaller of those two types of voids discussed above may be relatively less filled by additional silica in these samples compared to the case of the other samples from Andamooka (that showed only one transition temperature). Indeed, Segnit *et al.* (1965) previously suggested that the multiple

endothermic peaks observed in DTA curves of various opals could be explained if the opal had a pore size distribution with two peaks.

In addition to the collapse of voids through sintering, the application of heat could also collapse the ultra-microporosity throughout the macromolecular network of the SiO_2, since the matrix is thought to contain pores small enough for a single water molecule to become trapped (Langer and Flörke 1974). This may explain why sintering of these opals can occur at such low temperatures, as these voids are extremely small.

4.4.1.8. Theoretical Considerations

A close-packed sphere structure (HCP or FCC) is theoretically comprised of 26% unoccupied space. Calculations of the resulting void sizes (both octahedral and tetrahedral) of opals based on a close-packed sphere model were undertaken, with the assumption that there is no silica transport. It is known that these voids are partially filled with silica, as the measured bulk density of opal indicates that it contains significantly less than 26% voids. Such an estimation, however, would tend to overestimate the sizes of the pores if they were partially filled with silica. The following theoretical void diameters were calculated assuming a close-packed sphere configuration and using the well-known limiting radius ratios: for tetrahedral voids r/R = 0.225, and for octahedral voids r/R = 0.414. For an initial sphere size of 100nm, the theoretical void diameters would be 41.4nm for an octahedral void and 22.5nm for a tetrahedral void; while an initial sphere size of 350nm would theoretically produce void diameters of 145nm (octahedral) and 78.75nm (tetrahedral). These theoretical void diameters are larger than the values that were obtained by nitrogen adsorption analysis, however, additional silica is expected to be transported and accumulated at these sites, reducing the sizes of the pores considerably. Using positron-annihilation methods, Chojcan and Sachanbinski (1993) concluded that opal-AN contained pores approximately 8 to 10Å in diameter. Mikhailov *et al.* (1963) also noted that opal contained many small pores less than 12Å.

4.4.2. Thermogravimetric Analysis

The temperature at which there was a maximum rate of water loss from the opal is somewhat higher than the boiling temperature of water since there is both molecular water and adsorbed water present. Hence, the water vapour pressure at high temperatures must be quite substantial. The fact that the onset of water loss is quite sudden implies that a minimum activation energy is required to decompose the system; this effect is probably manifested in the formation of new Si–O–Si linkages after Si–OH bonds have been broken (Equation 3-1).

All samples show asymmetric rate of weight loss curves, revealing that the samples lose water more rapidly at lower temperatures, and as the temperature is raised, this rate decreases proportionately. The fact that there is a slow decrease in dehydration rate, while the opals are still losing water at temperatures as high as 600°C can be explained by the following premise: the microstructure contains a limited number of mesopores through which water vapour can escape, these becoming even less interconnected as sintering proceeds. The escape of water is thus restricted to diffusion of water through the silica network, a process that involves breaking Si–O–Si bonds (Roberts and Roberts 1966).

Coober Pedy opals dehydrated at a lower temperature than the other opals, and also at a higher overall rate (Table 4-3; Figure 4-8; Figure 4-9). It is possible that this result is partly due to the Coober Pedy opals samples possessing a slightly higher water content than almost all other opal specimens, but it is more likely due to the interconnectivity of the pore spaces, and the total porosity (Giuseppetti and Veniale 1969a; Giuseppetti and Veniale 1969b). N_2 adsorption results showed that the Coober Pedy opal contained a significantly greater distribution of pore sizes than either the LR1clear or ANDA8 transparent opals, consistent with the TGA findings.

The rate of weight loss curve of one Coober Pedy sample exhibited what appeared to be a shoulder, inferring that this particular sample may have several dehydroxylation stages. The rate of weight loss curve of Figure 4-9 has been curve-fitted, revealing that it is comprised of multiple component peaks and therefore indicating a five-step process (Figure 4-11).

Although these theoretical curves are by no means an accurate representation of real events, it nevertheless allows an estimation of the thermal behaviour of this sample at elevated temperatures; the deconvolution of this curve into several Gaussian peaks indicates that additional water may be driven off at multiple temperatures, from 220°C up to approximately 260°C, 335°C, 420°C and 565°C. The largest primary peaks could be due to specific –OH groups being driven off at low and high temperatures, such as geminal and vicinal groups, or more likely, molecular and silanol water, respectively. However, that would not explain why all the other opal-AG samples studied do not show similar results, unless the degree of interconnectivity and size of the pore phase was again responsible. Hence, the various dehydroxylation stages are probably a consequence of the microstructure of this particular sample, for example it may contain pores of several different sizes. Since –OH groups residing in pores of diverse sizes exhibit different degrees of H-bonding, the result would be reflected in the TGA weight-loss curves. Unfortunately, this supposition could not be corroborated with the TMA results of other Coober Pedy opal specimens. However, variable contraction rates were evident in the TMA curves of some Andamooka specimens, indicating those particular samples contained mesopores of more than one size.

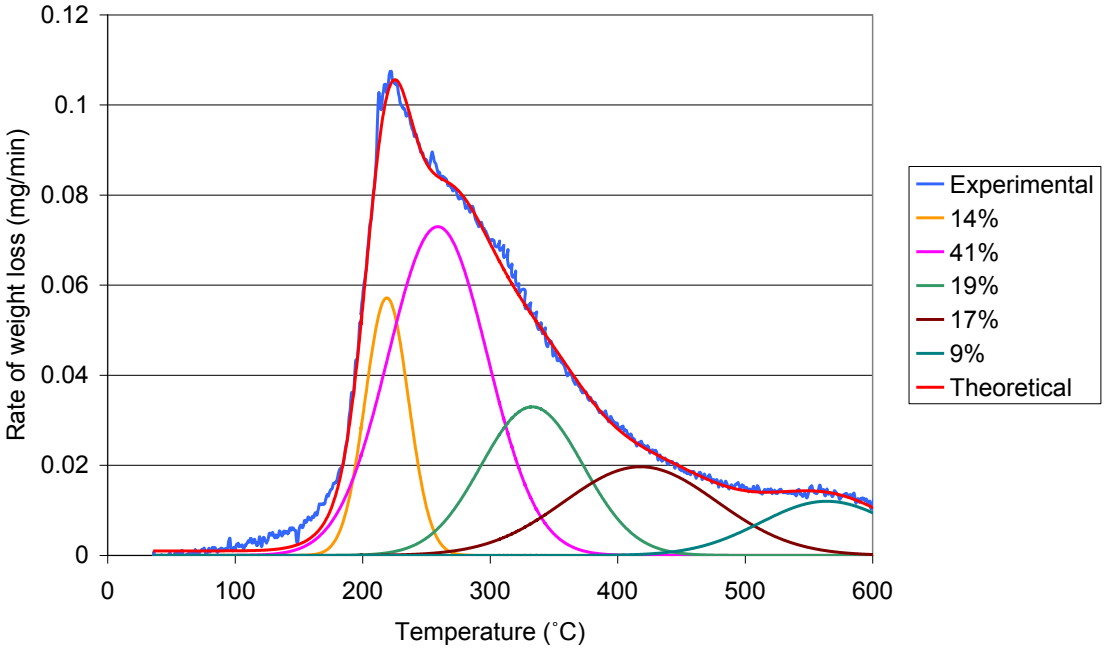

Figure 4-11: Deconvolution of the rate of weight loss curve for Coober Pedy opal sample.

One sample from Andamooka (A82) and one from Coober Pedy (Coobped#) exhibited a slight fluctuation in the weight loss curve at about 570˚C, this is attributed to the α ⇋ β inversion of silica [quartz] at 573˚C (Figure 4-3). Previous researchers could not detect any effects due to structural inversion associated with opal-A (Jones and Segnit 1971). The α ⇋ β quartz inversion, being a displacive transformation, is a rapid reversible process and so cannot be verified without the aid of high temperature XRD.

4.4.2.1. TMA and TGA correlations

There seemed to be a general correlation between the transition temperature and the temperature of maximum dehydroxylation. This is consistent with the assumption that at the transition temperature there is a contention between dehydration and sintering. If the opal structure loses water at lower temperatures, that same structure is more easily sintered as the water vapour pressure is reduced. The accuracy of this relationship is affected by the variation in sample size and shape between TGA and TMA. This is because a smaller specimen (as used in the TGA) has a higher surface area to volume ratio, which makes the exodus of water somewhat easier. In addition, the samples used for TGA were not always of uniform

shape, whereas the specimens used for TMA were all rectangular prisms (4.2.4.1; 4.2.3.1).

4.4.2.2. Geminal and Vicinal Silanol Groups

Silanol groups in silica may be either vicinal or geminal (2.6.2.1). Even though one of the twin (or geminal) hydroxyls would probably be driven off at a lower temperature, the concentration of these hydroxyl groups is so low (7.3.2.2) that the effect is probably not detectable with the limitations of the instrumentation used.

4.4.3. Effect of chemical composition on thermal behaviour

The difference in trace element (chemical) composition for the various types of opals is not expected to significantly affect the thermal analysis curves. The reason for this assumption is that the opals are approximately 98% pure silica (not counting the water content), regardless of the type of Australian opal examined. Thus, the difference in *major* impurities between opal samples is not very significant, on the order of 0.5%. It is only the minor trace elements and rare-earths that are variable and most of those are below ppm levels (5.3.3; 5.3.4).

4.4.3.1. Sintering

Pure amorphous silica does not sinter below 1100°C, but the onset of sintering is lowered to about 600°C by the addition of 1 to 3% NaOH. Australian opals have been found to contain generally up to 0.5% Na. This suggests that impurities can control the sintering kinetics in natural opals, albeit to a limited extent (Sanders 1975). However, this assumes a homogeneous distribution of minor elements, which may not necessarily be the case (6.5.1.2).

4.4.4. Sphere size and distribution

A greater sphere size distribution leads to a higher sintering rate (Richerson 1992). If the sintering rate increases, the transition temperature would decrease; the shrinkage at lower temperatures due to sintering dominates over the expansion caused by water in the structure. Thus, potch opals with a greater sphere size distribution than precious opals (assuming

similar sphere size) would be expected to exhibit a lower transition temperature.

4.4.5. Porosity and permeability

Differences in the sphere size do not affect the relative porosity. For a perfectly close-packed structure, the void space always occupies the same proportion of space whether the spheres are large or small. Therefore, sphere size alone cannot really account for any of the differences due to the porosity, but it does influence the permeability. The sphere size becomes significant when the ability of the structure to undergo dehydration and sintering is considered.

The porosity affects the exodus of water from the structure, however, and porous bodies allow water to escape more easily than with non-porous bodies. Therefore, the level of porosity may account for some of the differences in the observed transition temperatures of opals from different regions; this is reflected in the different porosities of the opal samples, as measured by N_2 adsorption (Table 4-4).

The degree of porosity of a material influences the heat capacity, permeability of gases and thermal conductivity. Since the thermocouples are located near the surfaces of the samples, these factors can in turn affect the accuracy of the temperature measurement during the experiments, as the indicated temperature is not equivalent to the temperature at the centre of the sample. However, the differences in heat capacity and thermal conductivity are only considered significant for DSC and DTA, and negligible for TMA and TGA, as the latter instruments are less susceptible to changes in the heating rate. The fact that porosity influences the permeability of H_2O vapour is the most important aspect of all three.

4.4.5.1. Interstitial silica / Coalescing of spheres

The literature often refers to a 'silica cement' when the formation of opal-AG is discussed since the voids between the silica spheres are known to contain additional silica (Sanders 1964; Darragh *et al.* 1966; Darragh *et al.* 1976). One problem still remains; the existence of this additional 'silica cement' necessitates additional geological processes. However, it is unnecessary to resort to these unknown and superfluous geological

processes, as the mechanisms described in the publications by Landmesser (1995, 1998) for silica accumulation and transport may also be applied to opal formation (3.4.2). Occasionally microstructures are observed with SEM in which the 'spheres' are non-spherical and appear to have completely coalesced forming icosahedral shapes (Figure 4-12). In these cases the voids that are usually present between the spheres are absent, as they have been filled by silica that is transported by Landmesser's 'mobility by metastability' mechanism (3.4.2). Landmesser (1995, 1998) reported that silica transport and accumulation is essentially independent of the chemical composition of the solution (salinity, pH, etc). However, this process may be hindered by other conditions that prevailed during the formation of an opal; for example complete dehydration of the subterranean cavity during this phase would prevent the transport of silica. If the extent of silica transport following sphere deposition is considerable, the resulting voids would be smaller and also less inter-connected. Hence, the collapse of these voids during thermal analyses, and thus the shrinkage rate, may be seen to be a function of the extent of this process (coalescing of spheres).

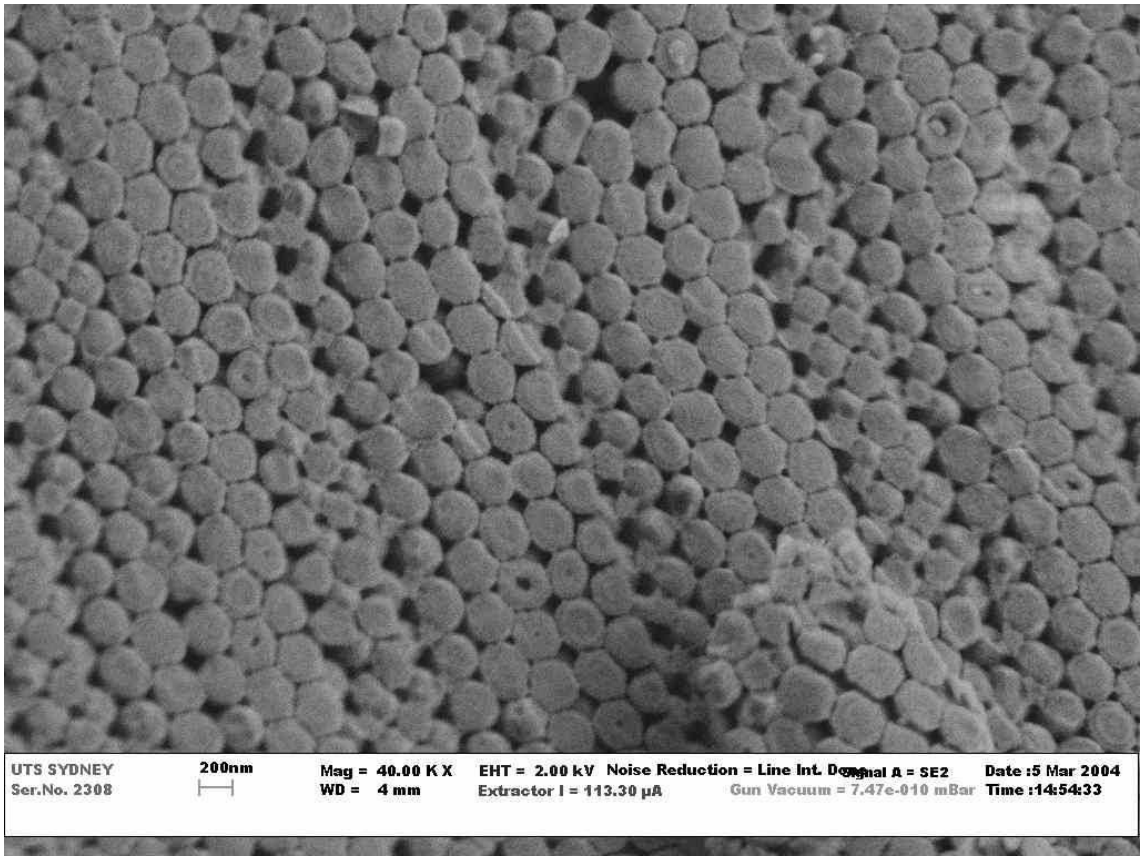

Figure 4-12: SEM micrograph showing non-spherical colloidal structures. This requires an optimal etching time. A secondary electron detector was used for imaging.

4.4.5.2. Pore size distribution

Water is more easily removed from the surface of a smaller particle (by heating) than from the surface of a larger particle. This is because hydrogen bonding of the adsorbed water molecules is stronger on larger particles, since the water molecules are more closely packed together (Figure 4-13). This effect becomes significant when the silica spheres approach sizes of 100nm. This point may seem irrelevant, but the sphere size of the opal is not exactly consistent throughout the various types of opals tested. The opal samples investigated with thermal analysis were also examined with SEM, the sizes of the spheres were roughly measured with SEM and their diameters ranged from (125±10)nm for Lightning Ridge (transparent) opal to (210±10)nm for the Coober Pedy opal samples.

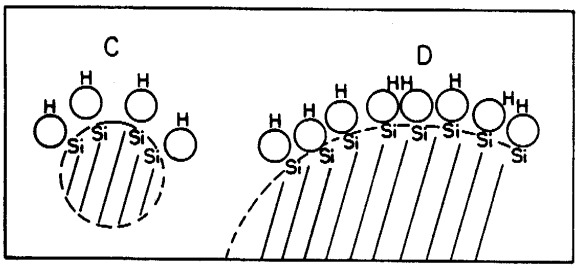

Figure 4-13: Effect of radius of curvature on the spacing of adsorbed water groups. From Iler (1979).

Water is expelled more easily from surfaces that have a positive radius of curvature (convex) than those with a negative radius of curvature (concave) as shown in Figure 4-14. This is also caused by stronger hydrogen bonding of water molecules that are on a concave surface. Thus, water molecules first escape from the convex surfaces before the concave surfaces. Therefore at high temperatures, there may be localised strain between the concave and convex regions due to the differing water content. Once the temperatures are high enough to enable the removal of silanol groups from concave surfaces, sintering can proceed relatively rapidly, as the surface energy is high in these regions.

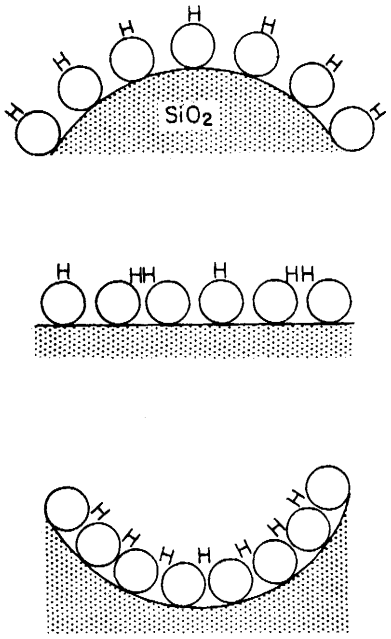

Figure 4-14: Effect of radius of curvature on the spacing of adsorbed water groups. From Iler (1979).

4.4.5.3. Precious opals

The ability for the thermal analysis results to correlate with precious opal of gem quality is not a certainty, because they are microstructurally different. The size of the silica spheres is much larger (up to 350nm) for gem quality opals, they are monodisperse (the sphere size distribution is very low) and these spheres are much more ordered in their packing than lower quality precious opals. Nitrogen adsorption analysis of one precious opal-AG sample has shown that it contained significantly greater SSA, as well as more porosity, than the potch opal-AG samples. Therefore, the nature of the inter-sphere void spaces in precious opals alters the ability of water to exit these structures. Unfortunately, it is not practical to investigate precious opals with thermal analysis, as it is a destructive analytical technique, and the extremely high cost of precious opal samples would be prohibitive.

4.4.6. Surface and internal silanol groups

A fully hydrated amorphous SiO_2 surface contains between 4.6 and 5.0 OH per 100Å^2; this figure is independent of the origin and structural characteristics of silica, such as the SSA, pore size distribution and network structure (Iler 1979; Zhuravlev 1989). If an opal has between 0.2 to 1.9 m^2/g SSA, a complete covering of the surfaces should correspond to a surface hydroxyl content of 0.01wt%. However, the concentration of surface silanols in opal-C determined by IR spectroscopy is much higher (Graetsch *et al.* 1985), so there must be inner surfaces covered with hydroxyls within the structure of opal-C. Although the nitrogen adsorption results indicate that the SSA of the opal samples is between 0.25 and 2.6 m^2/g, the microstructure may exhibit additional surface area that is inaccessible to nitrogen adsorption (Figure 4-15).

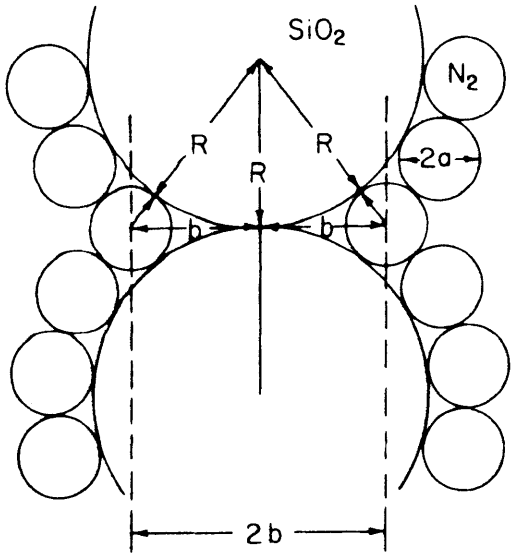

Figure 4-15: Surface area lost to nitrogen adsorption; areas inaccessible to nitrogen molecules are marked 'b'. From Iler (1979).

Assuming a higher specific surface area of 10 to 20 m^2/g (Bustillo 1993) for opal-A (diatomite), the theoretical surface silanol Si–OH content increases from 0.01 to 1wt%. This figure is lower than what is measured by TGA, however, water molecules also occur in multi-layers on surfaces (Figure 4-16) and additional –OH groups reside in the interior of the silica spheres (2.6.1; Langer and Flörke 1974).

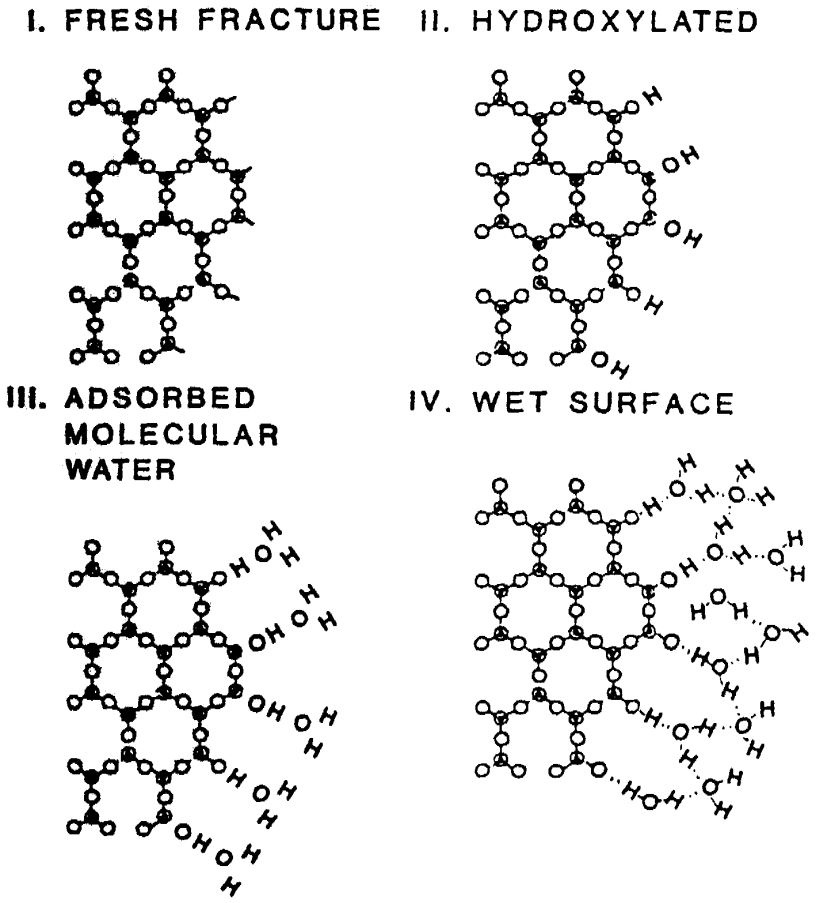

Figure 4-16: Adsorbed water on a silica surface. From Dove and Rimstidt (1994).

4.5. CONCLUSIONS

4.5.1. TMA

4.5.1.1. Thermal expansion

TMA revealed that for opal-AG, the thermal expansion coefficient before the transition temperature could not be related to the location or type of the opal. This was partly because a dependable method of measuring the thermal expansion coefficients could not be found, and also because sample variance was quite high in some samples of opal. The various types of opals also exhibited different contraction rates, as well as total percentage of contraction and expansion.

4.5.1.2. Transition temperature

The transition temperature of the opal was found to be dependent on the type of opal investigated, and its locality. The results are as follows: Coober Pedy 212±8.5°C; Lightning Ridge 312±26°C; and Andamooka 400±13°C. The transition temperature is most likely due to the combined effect of water loss and microstructural change (sintering), since these are the only attributes that alter once the opal has been heated. Therefore the differences observed in the transition temperatures are most likely influenced by the opal's total porosity and the inter-connectedness of the pores, but sintering could also be affected to a lesser extent by the sphere size and distribution, the ordering of the silica sphere array and the water content.

4.5.2. TGA

The water content of Opal-AG from various localities within Australia was found to range from 6.4 to as high as 9.1% (Table 4-3). TGA revealed that the temperature of maximum rate of dehydration was also related to the type of opal investigated. The magnitude of the dehydration rate was also found to be dependent on the type of opal; types with a lower dehydroxylation temperature had higher overall rates of dehydration. Several factors can influence the loss of water from opal and would therefore dictate when the transition temperature is reached and at what temperature maximum dehydroxylation occurs. These factors include: total

porosity; pore size distribution; sphere size distribution; total water content and whether the pore network has an open or closed microstructure. Sintering is also dependent on most of these factors, and is also influenced by the chemical composition, which can alter the viscosity.

There was also a general correlation between the transition temperature and temperature of maximum dehydroxylation. Shrinkage was observed to occur in opals at rates consistent with the onset of water loss. The TMA results infer that the rate of water loss, the temperature of maximum water loss and the transition temperature are correlated with the opal's microstructure. This elucidates the perplexing TMA results of opal that were done in previous studies (Jones and Segnit 1969; Jones and Segnit 1971).

4.5.3. Nitrogen adsorption

The nitrogen adsorption results correlate well with the thermal analysis results obtained. The amount of contraction observed in the TMA experiments corresponded well with the level of porosity measured by the nitrogen adsorption method. The rate of weight loss measured by TGA also correlated with the relative distribution of pore sizes determined by nitrogen adsorption. The precious opal sample analysed showed much higher SSA values than any of the potch opals; this result is consistent with the larger spheres that this sample is composed of (>300nm).

5. LASER-ABLATION INDUCTIVELY COUPLED MASS-SPECTROMETRY

"The world of neglected dimensions"
–Wolfgang Ostwald, Colloid Scientist, 1915

5.1. INTRODUCTION

5.1.1. Chemical composition of potch and precious opals

Since the original study by Jones and Segnit (1964), a number of reports on precious opals have been published to substantiate the origins of the "play of colour" phenomenon (Sanders 1964; Iler 1965; Baier 1966; Sanders 1968; Monroe *et al.* 1969; Sanders 1980). Accordingly, the most frequent studies concerning opal are those that observe the microstructure with SEM; the differences between the ordered sphere packing of precious opals and the random sphere packing of potch opals is often mentioned. It is not surprising that the research of opals has concentrated on imaging, as it was only relatively recently that opal's microstructure was discovered. However, it is not sufficient to merely identify the microstructural differences between precious and potch opals; an understanding of why these phases occur will greatly aid the understanding of the genesis of opal.

Although there have been several microstructural studies concerning potch and precious opals (Cole and Monroe 1967; Rau and Amaral 1969; Segnit *et al.* 1970; Sanders 1985), a correspondingly detailed chemical analysis study of potch and precious opals has not been forthcoming. Chemical analyses are important as they may yield further knowledge of the environment in which opals formed. A detailed investigation of chemical composition might therefore allow a better understanding of the formation processes which result in the unique microstructure of opal, and in turn help to explain the reason for nature's preference towards formation of potch over precious opal. If banded opals, in particular, are characterised, differences in chemical composition may further aid the understanding of opal formation as the bands are often formed at the same time. The crucial questions are:

- Can the formation of precious opal be attributed to environmental factors, or is it instead an aspect of the sol's elemental composition?
- Why does "banding" of opals occur? Why do some opals take on regular characteristics (such as black/clear or grey/honey bands), and not others? If it is a simple case of silica sphere sedimentation, how do samples with multiple layers then arise? Why are some boundaries very well defined and others much more diffuse?

Thus far, the general chemical distinction between precious and potch opals, has not been widely studied, especially in terms of their trace elements. Furthermore, much less research has been completed on potch opals in their own right, considering their far greater abundance.

5.1.2. Opal-genesis models

The origins of the subtle differences in the formation of precious and potch opals still remain a mystery, although a number of models have been postulated for their development (Darragh *et al.* 1966; Sanders 1980; Epova *et al.* 1983; Williams and Crerar 1985; Harder 1995; Kalinin *et al.* 1998; Serdobintseva and Kalinin 1998; Serdobintseva *et al.* 1998).

There are presently many unanswered questions with regards to the genesis of many peculiar banded opal samples (eg: the last point mentioned above) and with the current existing level of understanding of sphere sedimentation (Darragh *et al.* 1966; Jones *et al.* 1966), they cannot be answered. Recently, several alternate opal-genesis theories have emerged. Some of these (Epova *et al.* 1983; Kalinin *et al.* 1998; Serdobintseva *et al.* 1998) include underlying assumptions about opal which state that the order-disorder transformations are caused by environmental factors (such as temperature or time) other than the chemical composition of the sol. Even so, the effects of the sol's chemical composition in producing precious or potch opals cannot be completely excluded unless a chemical analysis of both types of opals is undertaken.

Harder (1995) speculated that Al may play a role in the sedimentation of silica colloids in the formation of opal, as it is present in substantial amounts. Harder inferred that the Al present acted as a flocculating agent. In that paper, the term "flocculation" was used several times, although no

chemical analyses involving aluminium (or any other element for that matter) of natural opal were undertaken.

5.1.2.1. Bacterial model

Behr *et al.* (2000) have recently proposed a model of opal formation involving microbacterial action. Briefly, microbes present at the time of opal formation are said to have assisted in the weathering of surrounding host rocks (clay minerals and feldspar), producing silicic acid, and oxides of Al and Fe. This model is discussed elsewhere in more detail (5.4.11). Other work (Deveson 2004) suggests that mound springs might also play a role, as they are often found in association with regions of opal deposits. These waters are quite alkaline and are thus able to dissolve high concentrations of SiO_2 (Figure 3-5). Unfortunately, none of these recent theories include chemical composition data to support their hypotheses. Jones *et al.* (1999) has reported that the growth of opal-A oncoids in geothermal pools is mediated by an assortment of microbes, at a pH of 6.6 to 6.9 and temperatures of 35-42°C.

5.1.3. Previous trace element studies

Perhaps the least studied area of opal research has been the elemental composition of opals, although there have been a small number of research papers written on the subject (Bayliss and Males 1965; Bartoli *et al.* 1990; McOrist *et al.* 1994; McOrist and Smallwood 1995; McOrist and Smallwood 1997; Erel *et al.* 2003; Brown *et al.* 2004). The majority of studies, however, have not included transition elements or rare-earth elements in their analyses (Darragh and Perdrix 1975; Webb and Finlayson 1984; Graetsch *et al.* 1987; Yoshida 1987; Hänni 1989; McPherson *et al.* 1989; Graetsch *et al.* 1990; Flörke *et al.* 1991; Milisenda *et al.* 1994; Esenli *et al.* 2001). The chemical composition of opals was deemed to be a secondary consideration in most of the references cited here. Furthermore, the chemical analyses performed in some of these studies were conducted using Energy Dispersive Spectroscopy (EDX) analysis, the quantitative ability of which is debatable in terms of its poor detection limit for many elements (Goldstein *et al.* 1992).

McOrist *et al.* (1994) undertook several studies to determine if the various base colours observed in opals were in any way related to the trace elements they contained. Neutron Activation Analysis (NAA), a non-destructive technique, was used to analyse the opals. In those studies, fifty samples of different colours were analysed, as well as eighteen colourless opals. The colours investigated were orange, yellow, green, blue and pink. These opals were obtained from Australia, Peru, Mexico and USA. The results are as follows:

- The mean concentration of most of the elements found in orange, yellow and colourless opals were similar but there were exceptions (such as Sc, Ti, V, Fe, Co, Th). Orange, yellow and colourless opals exhibited different proportions of trace elements than the green, pink and blue ones.
- Green opals were significantly higher in alkali metals (Na, K, Rb and Cs), Co and W than either blue or pink opals. Green opals also possessed the highest concentration of As and were the most deficient in rare-earth elements.
- Blue opals had a higher concentration of Mg, Zn, and U than either green or pink opals and also had the lowest Al concentration.
- Pink opals were higher in Al, V and Mn concentration than other opals, but also contained high amounts of As like the green opals.
- Black opals from NSW differed markedly from those originating from SA. With NSW opals, there was a higher concentration of trace elements in common opals than in precious opals. Yet common and precious opals from SA had similar trace element profiles.

5.1.3.1. Transition metals

Esenli *et al.* (2001) investigated red, orange and white opal-CT from Simav (Turkey) using EDX. The researchers stated that the red opals contained the highest content of Al, Fe, Ti, Cr and Ni. Cu was detected in red opal; Cr, Co, Cu and Zn in orange opal and V, Cu and Zn in white opal; unfortunately the concentration of these elements was not reported.

In the preliminary study by Bayliss and Males (1965), the authors merely stated that precious opal (from Lightning Ridge, Coober Pedy and Andamooka) was similar to the common opal associated with it in terms of its trace chemical composition (Ti, Zr, Co, Ni, Cu, and Mn).

The most recent trace element study utilised Laser Ablation Cyclotron Resonance Fourier Transform Mass Spectrometry to differentiate between synthetic and natural opal (Erel *et al.* 2003); the main objective of this paper was the evaluation of the above analytical technique in distinguishing ('fingerprinting') natural and synthetic opals. The presence of Hf and Zr were reported to be characteristic of synthetic opals. The researchers also concluded that Australian opals (location unknown) contained a high abundance of Sr^+, Cs^+ and Ba^+ when compared to Mexican opals. The detection of Lanthanides, Ti, Cr, Fe and Ni within all the gem-quality opal samples was attributed to surface pollutants incorporated during the cutting and polishing stages; after repolishing with 3µm diamond paste and ultrasonic cleaning in ethanol followed by water, these particular elements were not detected when the samples were re-analysed (Erel *et al.* 2003).

5.1.4. Banded opal literature

Even less consideration has been given to banded opals (Deniskina *et al.* 1981; Serdobintseva and Kalinin 1998), which can be the most valuable of all.

Serdobintseva and Kalinin (1998) investigated a potch opal that contained thin veinlets bands of precious opal (using a microprobe analysis). Although they did not elaborate on the experimental details, they found that the average (total) content of CaO, Na_2O, MgO, and K_2O impurities was 0.38wt.% for potch and 0.35wt.% for the precious opal veinlets. This difference was mainly attributed to Ca which was 0.185wt.% for potch and 0.15wt.% precious opal. They hypothesised that although the difference in Ca concentration was small, the crystallisation of monodisperse silica spheres is extremely sensitive to electrolyte concentration, and therefore the potch formation was likely caused by the greater abundance of electrolytes such as Ca.

Bustillo and Martínez-Fríaz (2003) investigated a green opal from Tenerife (Spain) that also contained areas of beige opal matrix, although the green regions showed a chemical composition intermediate between celadonite and opals. Consequently, these bands are technically two separate phases, unlike the opal-AG bands of Lightning Ridge samples, which have identical morphology.

The only detailed studies concerning a banded crystalline wood opal (from Lake Eyre) were done by Segnit *et al.* (1965) and Jones and Segnit (1969) using thermal analysis, nitrogen adsorption, IR and NMR techniques. The researchers noted that the near-transparent bands (sample 1445C) of an opal from Lake Eyre in South Australia exhibited significantly different behaviour to the "milky" bands (sample 1445M), yet the chemical composition and crystal structures of these bands were reported to be identical. They concluded that the milky and near-transparent bands contained open and closed-pore microstructures, respectively.

5.1.5. Objectives

The presently accepted model of opal-AG formation, sphere sedimentation from a silica sol, is a process that is only valid for homogeneous opal samples. The model has its limitations and cannot adequately explain how banded samples develop. The aim of this chapter is to undertake a chemical analysis of the bands within opals, as the trace element impurities may have contributed to the deposition of the bands themselves.

5.2. EXPERIMENTAL

5.2.1. Sample details

The opals that were investigated originated from three regions within Australia; Andamooka and Coober Pedy in South Australia, and Lightning Ridge in New South Wales. A total of nineteen samples were analysed; thirteen from Lightning Ridge, three from Coober Pedy and three from Andamooka. All but two of the samples exhibited a "banding" phenomenon. A brief description of each sample is given in Table 5-1, and photographs of selected samples can be seen in Figures 5-1, 5-2 and 5-3.

Sample Name	Band 1	Band 2	Band 3
LR1	translucent brown	transparent pale yellow	–
LR2	opaque very dark black	opaque light grey	–
LR3	opaque very dark black	opaque light grey	–
LR4	translucent dark grey	opaque dark grey	translucent light grey
LR5	opaque grey	transparent "honey"	–
LR6	opaque grey	opaque brown	transparent "honey"
LR7	opaque grey	red poc	–
LR8	opaque dark grey	opaque light grey	–
LR9	opaque white	transparent	–
LR13	opaque grey	transparent violet	–
LR14	opaque black	blue poc	–
LR15	opaque grey	poc	–
LR16	opaque dark grey	opaque grey	opaque light grey
CP1	opaque grey	opaque green	–
CP2	opaque grey	opaque green	–
CP9	opaque white	–	–
A1	opaque white	red poc	–
A2	opaque grey	transparent	–
ANDA8	transparent pale violet	–	–

Table 5-1: Sample details; LR=Lightning Ridge, CP=Coober Pedy, A=Andamooka.

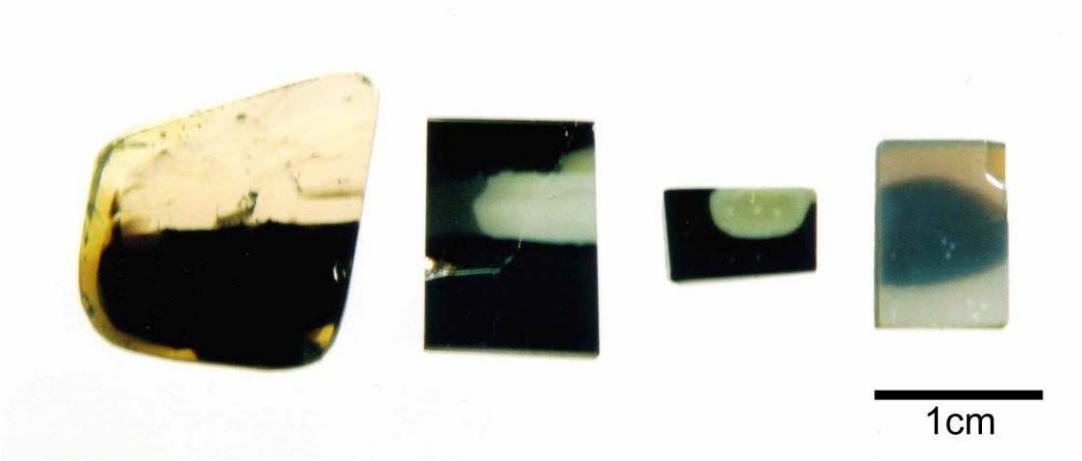

Figure 5-1: Left to right; LR1, LR2, LR3 AND LR4.

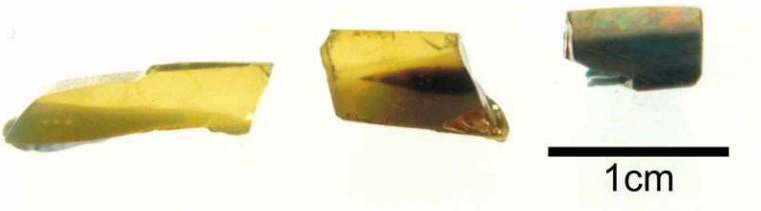

Figure 5-2: Left to right; LR5, LR6 and LR7.

Figure 5-3: Clockwise, from left; LR9, LR15, A1, A2, and CP9.

5.2.2. Sample preparation

To expose the various bands, the samples were cut in cross-section using a circular saw equipped with a diamond tipped wafering blade, using water as the lubricant. To improve the precision of the laser-ablation process in gathering mass-spectrometry data, the samples were polished until they attained optically smooth and flat surfaces. This reduces the tendency of the laser to unevenly ablate samples with rough surfaces. Polishing was accomplished by the following method. The surface of the samples to be analysed were ground with successively finer grades of silicon carbide paper down to 1200 grit, using water tap as the lubricant. They were then polished using diamond paste and a Leco lapping oil (a kerosene lubricant); the diamond paste used was first a 6μm grade with a nylon polishing pad and then a 1μm grade with a synthetic velvet polishing pad.

5.2.2.1. Errors

One source of experimental errors is contamination from the fluids used during the cutting and polishing stages, which could be adsorbed by the opal's high internal surface area. The most probable source of contamination originates from the tap water used for the initial cutting and grinding of the samples. The only other possible surface contaminant was ethanol, which was used to clean the samples prior to the analyses, as well as the leco lapping oil (polishing fluid), both of which have low impurity levels – yet the opals were cleaned with ethanol prior to the analyses. However, the opals studied contain significant quantities of water in the void spaces, which is maintained by their tendency to adsorb water vapour from the atmosphere. The adsorption of impurities would therefore be minimal as the void spaces would already be reasonably full. This uncertainty is further reduced as all samples experienced the same surface preparation treatments. Furthermore, banded samples nevertheless exhibited marked differences in trace element composition, even though the various bands could have adsorbed impurities uniformly. In any case, the results of the three spots analysed within each opal band were very consistent with each other (Table 5-3).

5.2.3. Mass spectrometry experimental methods

The chemical analyses were conducted using the technique of Laser Ablation ICPMS. This research was conducted at the Geochemical Evolution and Metallogeny of Continents (GEMMOC) laboratory, Macquarie University. A Continuum 266 Neodymium Yttrium Aluminium Garnet (Nd-YAG) Laser was used at frequency of 10Hz with approximately 1mJ of energy per pulse. Ablation was performed in an inert environment consisting of a mixture of Helium and Argon with an approximate 1:1 ratio. The diameter of laser spots on the surfaces of the samples were ~70μm. The ablated fragments of the sample were then transported with this gas mixture to an AGILENT 75005 model spectrometer for analysis. Prior to each analysis, the background was recorded for approximately 30 seconds with the laser switched off, to enable the software to automatically calculate errors and minimum detection limits of each element for each analysis. Following this time period, laser ablation times were approximately 120 seconds for each spot, during which time the acquisition of mass-spectrometry data continued.

5.2.4. Standardisation

The laser ablation elemental analysis requires the use of an internal standard against which the trace elements are referenced. As SiO_2 is the predominant component of opal, SiO_2 was used as the internal standard. The proportion of SiO_2 was determined using the energy-dispersive x-ray detector of a JEOL 6300 FEG SEM, and was determined to be 92±1% for the samples studied. This is in accordance with the published range of 4 to 10% water content for opals (Segnit *et al.* 1965; Brown *et al.* 2002). The internal standard for all specimens was therefore set at 92%.

Three calibration standards for the ICPMS analysis were used: synthetic glass (NIST standard 610), synthetic basalt (BCR-2G), and Mongolian garnet (Norman *et al.* 1996, 1998). The standards were analysed both before and after a run had been completed. There were between fourteen and twenty one spots in any one run of a total of nine runs. Repeated running of the standards compensated for the minimal drift

observed during acquisition of a data set[1]. The raw data of each spot was also graphically evaluated for each element analysed. Using this method, spikes in the data were manually removed (these relatively large and erroneous signals mostly occurred with elements that also yielded poor signals, such as Li, Cr, Sn and Lu). In addition, a few seconds of the initial and final data, which is unreliable as it is associated with switching the laser on and off, were discarded. The concentration of each element was then determined as the difference in intensity (counts per second) of the signal relative to the background.

5.2.5. Elemental Analyses

The isotopes analysed were ^{7}Li, ^{23}Na, ^{24}Mg, ^{27}Al, ^{39}K, ^{43}Ca, ^{45}Sc, ^{49}Ti, ^{51}V, ^{53}Cr, ^{55}Mn, ^{57}Fe, ^{59}Co, ^{60}Ni, ^{62}Ni, ^{65}Cu, ^{66}Zn, ^{69}Ga, ^{71}Ga, ^{85}Rb, ^{86}Sr, ^{88}Sr, ^{89}Y, ^{90}Zr, ^{118}Sn, ^{133}Cs, ^{137}Ba, ^{139}La, ^{140}Ce, ^{146}Nd, ^{147}Sm, ^{153}Eu, ^{157}Gd, ^{165}Ho and ^{167}Er. In all cases, a minimum of three separate spots were analysed within each band, and the values averaged.

[1] This is a normal procedure for this analytical technique.

5.3. RESULTS

A total of more than 120 spots were analysed for all of the aforementioned elements; with the calculated minimum detection limits and errors for each element of each spot, this extensive assemblage of data is challenging to display quantitatively in a manner that is easily assimilated, without resorting to sizeable tables. The data presented here concerning the average elemental composition of various opal samples is listed in Table 5-2. The standard deviation (1σ) of the elemental concentration (for three spots) is listed in Table 5-3. The minimum detection limits for each element were determined based on the counting statistics method set out in Norman *et al.* (1996) and are listed in Table 5-4. For banded samples, the ratio of the average elemental composition between the various bands is listed in Table 5-5.

A relative comparison of the concentration of elements between each band gives a better portrayal of the quantitative differences between various bands than a table; a number of these graphs can be seen in Figure 5-4 to Figure 5-8. These graphs are plotted as a function of multiples of ten; the ppm values for each element are divided by the factors given in Table 5-6. This allows the data to be presented without resorting to logarithmic scales.

The results for this chapter will be conveyed according to each group of elements; the overall trends in the data with respect to the samples will initially be reported, and the behaviour of specific samples which are deemed to be out of the ordinary will be then be elaborated on for each element in question.

It should also be noted that the data concerning the elements Li, Cr and Sn, consistently showed extremely low signal to noise ratios, therefore no definitive conclusions can be drawn on the basis of Li, Cr or Sn content. Hence, the results relating to these elements are not referred to.

Table 5-2: Average elemental concentration for each opal band (ppm).

CP9 white	CP1 grey	CP1 green	A8 clear	A2 grey	A2 clear	A1 white	A1 poc	LR15 grey	LR15 poc	LR14 black	LR14 poc	LR13 grey	LR13 violet	LR9 white	LR9 clear	LR7 grey	LR7 poc	LR5 grey	LR5 honey	LR2 black	LR2 grey	LR1 brown	LR1clear	
1510	-	-	155	67.7	151	-	-	843	805	502	444	477	428	826	818	-	-	956	739	2030	3290	1040	1010	*Na23*
204	187	173	157	204	112	120	119	338	329	192	176	95.8	101	181	179	243	244	289	273	349	371	388	365	*Mg24*
7950	5280	5070	4800	5150	4010	3730	3670	9320	8780	6360	5590	4290	4150	7600	6950	8970	5590	8650	6980	13400	11500	9650	8720	*Al27*
876	1800	1390	1170	1250	704	1570	1400	1630	1260	1600	1170	1100	824	2300	1630	2880	887	2320	1150	-	-	-	-	*K39*
3130	1740	1630	410	590	280	1050	1040	3090	2980	1660	1520	758	772	2460	2410	1890	1640	2280	2260	2830	2760	3070	2790	*Ca43*
1.24	2.67	2.8	1.22	1.29	1.24	2.62	2.71	1.25	1.11	2.16	1.62	1.64	1.36	1.55	1.45	5.08	2.5	1.44	1.08	-	-	-	-	*Sc45*
6.11	145	37	8.11	59.4	18.7	22.4	17.4	97.6	46.4	538	51.4	91.6	15	24.6	16.5	1710	50.1	261	46.6	1770	1260	454	18.9	*Ti49*
0.092	1.09	0.546	0.129	0.383	0.202	0.271	0.525	0.775	0.339	4.87	0.431	1.24	0.348	0.315	0.232	6.53	0.531	1.67	0.37	12	12.2	1.84	0.17	*V51*
6.8	9.83	8.47	10	10.1	5.18	5.82	5.77	29.3	28.8	21.8	18.4	10.7	9.94	5.19	5.05	26.9	27.5	21.6	20.3	31.5	28.5	22.6	22.1	*Mn55*
528	688	592	786	993	569	546	558	1080	1020	815	569	382	360	436	423	1170	988	741	669	1280	1240	647	608	*Fe57*
0.033	2.43	0.518	0.0174	0.089	0.046	0.639	0.898	1.99	0.799	6.51	0.386	1.91	0.186	0.12	0.056	41.6	1.64	1.59	0.389	48.1	14.6	4.9	0.232	*Co59*
0.268	4.86	4.46	0.4	0.368	0.407	3.92	4.7	1.58	0.885	3.62	0.625	1.39	0.363	0.39	0.288	32.3	4.13	0.947	1.24	26.3	8.45	4.2	1.21	*Ni60*
0.103	3.02	0.226	<det.lim.	0.296	13.5	4.26	4.47	2.07	0.944	100	3.37	1.94	0.84	0.166	0.129	65.8	2.87	26.9	2.83	177	93.8	16.1	0.428	*Cu65*
0.216	7.25	6.26	0.492	0.623	0.77	3.66	5.81	1.54	0.975	9.63	0.817	1.63	12.1	0.755	0.325	11.8	4.45	1.69	0.677	64.3	19.4	1.56	0.467	*Zn66*
8.28	3.71	3.38	7.25	21.2	9.41	5.04	5.7	5.02	4.2	4.87	3.23	1.81	1.55	13.1	11.5	8.88	5.22	6.53	4.62	-	-	-	-	*Ga69*
0.046	0.316	0.351	0.0511	0.101	0.062	0.1	0.448	0.226	0.107	0.439	0.077	0.34	0.078	0.144	0.078	1.85	0.297	0.461	0.073	-	-	-	-	*Ga71*
13.7	19.2	15.7	16.9	18.5	13.2	19.6	19.4	14.1	12.9	11.8	10.8	10.8	9.12	15.7	13.9	9.42	17.3	15.1	12.1	15.5	7.83	11.8	11.4	*Rb85*
142	57.5	50	11	24	10.1	49.8	48.2	87.5	80.2	46.7	38.9	23.6	18.9	125	121	73.7	46.1	66.5	57.8	76.5	72.1	71.6	63.1	*Sr86*
143	56.1	47.8	11.5	23.8	10.2	47.1	45.4	88.7	81.1	47.2	39.1	23.4	19.3	127	122	72.6	45.2	66.7	58.7	77.9	73.8	73.7	64.4	*Sr88*
0.563	2.42	0.565	1.9	1.76	0.908	0.263	0.5	2.01	1.13	3.35	0.64	3.47	0.368	0.691	0.553	27.4	0.78	5.92	0.891	15.1	10.6	5.19	0.549	*Y89*
169	110	94.7	295	222	188	76	73.7	86.2	81.9	177	148	138	107	151	147	301	52.5	111	94.3	230	189	69.8	48.3	*Zr90*
3.37	3.66	3.39	3.44	3.43	2.79	3.4	3.6	2.75	2.63	1.76	1.73	3.15	1.87	3.64	3.47	2.85	2.97	2.04	1.92	3.08	2.34	2.02	1.97	*Cs133*
207	67	53.2	218	492	214	108	102	130	110	103	73.3	45.5	40.1	279	256	153	81.3	151	118	267	249	147	125	*Ba137*
0.505	2.71	0.568	0.951	1.53	0.804	0.282	0.235	2.61	1.06	4.72	0.744	6.21	0.448	0.786	0.586	24.2	1.17	8.44	1.06	25.3	19.2	6.9	0.469	*La139*
0.884	12	2.13	2.41	3.16	1.67	1.29	1.18	5.31	2.2	10.2	1.65	18.3	1.08	1.6	1.22	69.2	4.13	19	2.19	62.4	48.4	16.6	1.03	*Ce140*
0.46	3.72	0.7	1.38	1.57	0.767	0.306	0.245	2.34	0.981	4.33	0.726	8.35	0.484	0.726	0.549	26.7	1.07	9.41	1.02	25.6	19.2	7.74	0.442	*Nd146*
0.092	0.716	0.146	0.304	0.308	0.159	0.142	0.27	0.445	0.19	0.814	0.142	1.72	0.096	0.143	0.103	5.35	0.175	1.91	0.192	5.19	3.85	1.63	0.091	*Sm147*
0.035	0.209	0.045	0.0779	0.098	0.045	0.0648	0.032	0.163	0.071	0.237	0.047	0.48	0.034	0.05	0.038	1.45	0.161	0.576	0.07	1.46	1.06	0.46	0.036	*Eu153*
0.102	0.66	0.192	0.296	0.313	0.148	0.047	0.305	0.398	0.17	0.692	0.123	1.12	0.078	0.106	0.105	4.87	0.154	1.56	0.205	4.17	3.02	1.4	0.094	*Gd157*
0.02	0.13	0.02	0.0613	0.052	0.029	0.0073	0.01	0.073	0.038	0.127	0.022	0.16	0.012	0.021	0.017	1.04	0.026	0.231	0.034	0.614	0.422	0.203	0.017	*Ho165*
0.047	0.365	0.054	0.169	0.158	0.085	0.0222	0.063	0.2	0.112	0.353	0.06	0.36	0.034	0.066	0.048	3.06	0.074	0.588	0.088	1.64	1.13	0.534	0.047	*Er167*
0.037	0.214	0.042	0.143	0.132	0.063	0.0269	0.074	0.219	0.122	0.357	0.06	0.35	0.045	0.055	0.042	3.34	0.119	0.541	0.101	1.53	1.05	0.504	0.042	*Yb172*
0.044	3.05	1.48	0.0188	0.102	0.149	0.152	0.131	4.13	1.12	17.8	1.08	3.12	0.346	0.179	0.09	28.3	2.15	7.3	1.32	26	19.7	4.34	0.262	*Pb208*
0.077	1.61	0.309	0.215	0.423	0.213	0.148	0.122	1.15	0.692	2.61	0.425	4.32	0.571	0.498	0.386	12.3	0.632	4.89	0.806	14.7	13.1	3.27	0.207	*Th232*
0.032	0.695	0.114	0.125	0.216	0.134	0.0998	0.191	0.292	0.168	1.18	0.134	0.99	0.148	0.153	0.115	4.44	0.264	0.677	0.183	3.32	2.36	0.511	0.057	*U238*
14900	10200	9190	8070	9150	6320	7380	7130	16900	15600	12300	9870	7500	6880	14500	13100	17900	9700	16000	12500	22900	21300	15700	13900	*TOTAL*

Table 5-3: Standard deviation (1σ) of the average elemental concentration for each opal band (ppm).

CP9 white	CP1 grey	CP1 green	A8 clear	A2 grey	A2 clear	A1 white	A1 poc	LR15 grey	LR15 poc	LR14 black	LR14 poc	LR13 grey	LR13 violet	LR9 white	LR9 clear	LR7 grey	LR7 poc	LR5 grey	LR5 honey	LR2 black	LR2 grey	LR1 brown	LR1 clear	
31	-	-	92	3.8	3.1	-	-	22	96	17	12	22	3.5	35	43	-	-	39	6.8	110	50	9.9	92	*Na23*
0.93	11	8.5	1.7	8.1	1.8	4.5	9.5	7	6.2	0.73	3.6	1.5	2.4	3.2	3.4	2.2	13	6.5	1.9	6.1	11	4.7	5.7	*Mg24*
44	240	330	81	250	34	340	370	320	160	130	150	120	52	230	190	53	380	180	46	350	71	370	270	*Al27*
34	140	27	7.4	17	15	21	50	77	40	46	94	42	17	100	8.6	260	58	5.2	7.3	-	-	-	-	*K39*
23	110	110	19	23	17	110	120	110	69	40	18	45	27	47	30	96	120	65	28	65	26	94	61	*Ca43*
0.034	0.18	0.3	0.028	0.047	0.052	0.075	0.14	0.04	0.029	0.02	0.054	0.025	0.068	0.025	0.015	0.28	0.27	0.11	0.046	-	-	-	-	*Sc45*
0.3	4.2	3.7	0.32	1.1	0.8	1	3.9	30	5.9	15	31	2.3	1.2	0.38	0.3	170	3.3	6.6	2.2	33	20	240	0.97	*Ti49*
0.009	0.05	0.38	0.0076	0.008	0.006	0.025	0.27	0.23	0.041	0.21	0.2	0.037	0.034	0.015	0.01	0.93	0.14	0.05	0.018	0.15	3.8	0.9	0.012	*V51*
0.25	0.23	0.52	0.046	0.16	0.17	0.12	0.22	0.35	0.37	0.13	0.17	0.38	0.18	0.075	0.025	0.35	0.85	0.057	0.29	0.43	0.24	0.14	0.15	*Mn55*
3.7	53	15	5.7	11	13	32	47	8.8	9.5	4.6	6.5	9	5.2	1.8	2.9	33	34	3.2	2	22	330	27	5.3	*Fe57*
0.004	1	0.11	0.004	0.017	0.013	0.15	0.53	0.8	0.13	0.18	0.14	0.03	0.051	0.004	0.002	2.3	0.51	0.034	0.018	0.95	1.1	2.7	0.022	*Co59*
0.07	0.29	2.8	0.018	0.051	0.2	0.29	1.8	0.36	0.11	0.086	0.077	0.28	0.1	0.092	0.046	1.8	0.66	0.066	0.55	0.54	0.74	1.9	0.19	*Ni60*
0.027	3.1	0.14	0.038	0.13	2.4	4.8	6.2	1.2	0.22	6.2	1.7	0.19	0.2	0.02	0.024	68	2.8	2.4	0.53	2.8	23	8.5	0.061	*Cu65*
0.043	4.8	5.4	0.036	0.12	0.046	1.2	3.7	0.49	0.048	0.63	0.25	0.53	7.9	0.39	0.13	4.5	2.3	0.1	0.27	0.2	1	0.57	0.11	*Zn66*
0.13	0.2	0.082	0.09	2	0.24	0.68	0.5	0.41	0.17	0.25	0.14	0.043	0.1	0.73	0.37	0.34	0.7	0.078	0.075	-	-	-	-	*Ga69*
0.005	0.07	0.28	0.0081	0.011	0.002	0.028	0.33	0.05	0.013	0.005	0.024	0.032	0.022	0.019	0.004	0.33	0.076	0.027	0.013	-	-	-	-	*Ga71*
0.24	2.1	0.14	0.16	0.51	0.26	0.71	0.7	0.39	0.18	0.21	0.24	0.41	0.26	0.16	0.16	0.64	0.51	0.28	0.11	0.57	0.07	0.08	0.42	*Rb85*
1.5	5.5	4.1	0.21	1.5	0.5	4.5	2.3	5.3	2.4	1.2	0.93	0.42	0.37	3.9	2.7	17	3.8	1.8	1	1.2	1.8	2.6	1.6	*Sr86*
1.7	6.2	4.3	0.41	1.7	0.54	5.6	1.9	4.5	2	1.3	0.97	0.8	0.35	4	3.1	17	3.1	0.96	0.87	1.8	1.8	2.8	1.7	*Sr88*
0.002	0.16	0.019	0.03	0.092	0.011	0.036	0.25	0.48	0.14	0.076	0.24	0.13	0.045	0.038	0.009	1.7	0.2	0.1	0.029	0.39	0.26	2.8	0.02	*Y89*
2.1	12	10	4.7	13	3.2	12	6	5.2	2.4	5.9	6.1	4.7	0.34	5.2	3.5	4.6	5.1	1.8	1.3	2.9	4.5	9.9	1.5	*Zr90*
0.047	0.39	0.23	0.031	0.061	0.044	0.085	0.24	0.03	0.033	0.01	0.054	0.13	0.038	0.078	0.021	0.06	0.13	0.036	0.046	0.09	0.03	0.04	0.11	*Cs133*
1.7	9.1	5.5	2.9	36	9.6	9.5	2.9	9.1	3	2	2.1	0.71	0.23	9.4	6.9	9.1	7.1	2	1.8	3.3	20	6.9	2.5	*Ba137*
0.007	0.28	0.094	0.02	0.1	0.036	0.032	0.036	0.84	0.13	0.16	0.31	0.13	0.096	0.029	0.019	2.1	0.3	0.042	0.041	0.45	0.47	4	0.023	*La139*
0.015	0.85	0.13	0.05	0.074	0.077	0.075	0.16	1.6	0.23	0.09	0.67	0.49	0.23	0.023	0.011	6.6	1.2	0.14	0.055	0.69	0.6	9.6	0.047	*Ce140*
0.009	0.59	0.078	0.0099	0.13	0.054	0.051	0.042	0.71	0.16	0.17	0.28	0.13	0.099	0.033	0.011	2.7	0.28	0.2	0.022	0.37	0.34	4.6	0.022	*Nd146*
0.003	0.09	0.037	0.01	0.01	0.014	0.16	0.4	0.14	0.038	0.035	0.046	0.025	0.038	0.015	0.005	0.55	0.041	0.12	0.015	0.11	0.12	1	0.007	*Sm147*
0.004	0.02	0.0096	0.0006	0.013	0.003	0.037	0.02	0.04	0.01	0.009	0.017	0.021	0.0015	0.001	0.004	0.15	0.16	0.003	0.004	0.03	0.02	0.26	0.002	*Eu153*
0.018	0.07	0.12	0.0089	0.022	0.026	0.005	0.4	0.13	0.012	0.048	0.046	0.049	0.02	0.015	0.007	0.51	0.048	0.036	0.024	0.12	0.09	0.85	0.004	*Gd157*
0.004	0.04	0.0004	0.0068	0.005	0.001	0.002	0.003	0.02	0.004	0.006	0.008	0.008	0.0008	0.001	0.001	0.06	0.005	0.012	0.006	0.02	0.01	0.12	0.001	*Ho165*
0.002	0.09	0.0039	0.0079	0.03	0.021	0.004	0.067	0.05	0.02	0.02	0.021	0.012	0.0097	0.007	0.004	0.13	0.015	0.046	0.01	0.04	0.08	0.31	0.002	*Er167*
0.002	0.02	0.0079	0.0046	0.009	0.003	0.007	0.082	0.05	0.023	0.01	0.032	0.041	0.018	0.009	0.008	0.04	0.057	0.025	0.012	0.04	0.02	0.28	0.009	*Yb172*
0.003	0.34	0.29	0.0061	0.015	0.027	0.031	0.11	2.8	0.29	0.51	0.6	0.23	0.052	0.04	0.003	2.1	0.47	0.35	0.05	0.16	2.8	2.1	0.02	*Pb208*
0.004	0.38	0.019	0.0025	0.022	0.013	0.047	0.015	0.23	0.058	0.13	0.23	0.11	0.094	0.013	0.009	0.22	0.16	0.14	0.023	0.39	0.81	1.9	0.009	*Th232*
0.006	0.15	0.0014	0.0037	0.011	0.007	0.008	0.14	0.06	0.014	0.035	0.054	0.047	0.014	0.007	0.005	0.12	0.014	0.016	0.009	0.04	0.14	0.24	0.003	*U238*

	LR1 clear	LR1 brown	LR2 grey	LR2 black	LR5 honey	LR5 grey	LR7 poc	LR7 grey	LR9 clear	LR9 white	LR13 violet	LR13 grey	LR14 poc	LR14 black	LR15 poc	LR15 grey	A1 poc	A1 white	A2 clear	A2 grey	A8 clear	CP1 green	CP1 grey	CP9 white
Na23	830	780	520	520	2000	1700	-	-	690	600	2700	2600	620	580	670	600	-	-	2300	2000	760	-	-	690
Mg24	21	22	16	27	330	270	3.2	2.4	23	20	460	440	20	19	22	19	5.1	3.4	360	310	24	8.8	2.9	22
Al27	80	79	52	54	340	280	11	9.7	50	43	520	440	46	44	53	47	20	14	370	320	64	23	10	53
K39	-	-	-	-	1100	900	72	60	810	690	1400	1400	740	690	810	730	120	77	1200	1000	860	140	64	840
Ca43	25000	25000	16000	16000	26000	21000	2200	1900	10000	8900	35000	32000	9400	8700	11000	9800	4000	2700	30000	26000	13000	4700	2000	11000
Sc45	-	-	-	-	140	110	2.9	2.5	13	11	180	170	12	11	13	12	5.2	3.6	150	130	15	5.9	2.8	13
Ti49	200	210	140	140	310	220	28	22	170	140	390	360	150	140	160	140	46	36	320	300	180	52	22	180
V51	24	23	16	16	30	25	3.2	1.9	14	12	43	39	12	12	14	12	4	2.7	33	29	15	4.4	2	14
Mn55	61	60	42	43	77	65	6.9	5.8	46	39	98	92	42	39	47	42	12	8.3	94	83	53	17	6.4	51
Fe57	1900	1900	1400	1500	3200	2600	170	150	1100	960	4000	3900	1000	930	1100	980	290	180	3800	3400	1200	430	190	1100
Co59	26	26	18	18	20	15	1.1	2.1	6.5	5.4	29	26	6	5.3	6.4	6	1.6	1.2	24	19	6.8	2.1	2.9	6.4
Ni60	41	41	26	27	150	120	5.1	3.5	28	24	220	210	26	24	30	26	7.3	5.1	160	140	31	8.9	4.8	30
Cu65	91	91	62	62	290	240	7.1	5.9	65	55	430	400	62	56	72	63	12	6.9	330	300	79	21	6	72
Zn66	180	180	120	130	290	240	7.3	6	42	34	410	400	37	37	41	40	12	8.1	320	290	46	21	9.7	38
Ga69	-	-	-	-	76	60	1.3	1.5	11	9.5	97	90	10	9.7	11	11	2.3	1.7	85	77	13	2.7	3	12
Ga71	-	-	-	-	33	26	0.78	0.7	8.3	7.4	47	37	7.3	6.9	7.9	7.2	1.3	0.89	32	30	9.3	1.7	0.82	8
Rb85	14	14	9.5	9.4	36	30	2.1	2.8	9.4	8.3	44	42	8.7	7.8	9	8.3	3.7	2.9	44	40	10	4.7	2	9.4
Sr86	220	220	150	150	290	240	31	26	200	170	340	320	190	170	210	190	56	36	350	300	230	64	29	210
Sr88	2.5	2.6	1.6	1.4	7	6.5	0.31	0.42	2.3	2	9.2	8.5	2.1	1.9	2	2.1	0.57	0.47	8	7.5	2.3	0.86	0.52	2.2
Y89	2.8	3.2	1.8	2	4.5	2.2	0.46	0.42	2.1	2	4.6	4.6	2.3	1.9	2.2	2.1	0.85	0.6	4.3	4.1	2.5	0.98	0.41	2.3
Zr90	5.5	5.3	3.6	3.2	6.8	5.3	0.86	0.76	5.2	4.1	7.5	8	4.3	3.7	4.4	4	1.7	1.1	9	5.3	5.3	2.6	0.9	6.7
Cs133	8.5	8.3	5.8	5.9	17	14	1.3	1	6.9	6.1	19	18	6.1	5.8	6.4	5.8	2	1.5	20	18	7.4	3.3	1.4	6.9
Ba137	14	14	7.4	7.1	16	19	2.9	1.7	15	14	29	19	15	12	16	14	2.4	2.1	22	29	18	7.7	1.4	18
La139	2.1	1.6	1.2	1.2	2	2.2	0.26	0.21	1.9	1.5	2.5	2.8	1.9	1.6	2	1.6	0.43	0.31	1.9	2.3	1.9	0.49	0.23	2
Ce140	1.7	1.4	0.86	1.2	8.5	2.4	0.2	0.15	1.9	1.6	2.7	3	1.7	1.6	1.8	1.5	0.4	0.26	2.1	2.3	2	0.52	0.16	1.9
Nd146	8	7.6	5.5	5.1	13	7.6	1.2	0.96	9.8	8.4	9.8	13	8.9	8.8	11	8.9	2.4	1.6	11	14	11	2.7	0.96	11
Sm147	8.4	11	7.1	7.4	14	13	1.3	1.6	12	10	11	13	11	9.9	12	10	2.5	2	15	12	12	2.7	1.3	12
Eu153	1.8	3	1.7	1.7	3.6	2.6	0.44	0.35	3.1	2.6	4	4.2	2.8	2.5	3	2.9	0.66	0.45	4.3	3.5	3.5	0.78	0.29	3.5
Gd157	7.6	10	8.4	7.9	11	1.5	1.5	1.3	10	10	14	12	10	9.2	12	10	2.9	2.1	16	11	13	3.8	1.3	12
Ho165	1.6	1.4	1.2	1.2	1.6	2.1	0.2	0.34	1.8	1.6	3.3	2.4	1.7	1.6	1.8	1.6	0.48	0.34	3.1	2	2	0.55	0.55	1.9
Er167	8.9	6.9	6.1	6	7.7	8.1	1	0.81	6.7	6.3	8.7	8.2	7	6.3	7.3	7.4	2.5	1.3	9.6	9	8	2.2	0.92	7.4
Yb172	8.3	8.3	6.1	6.5	9.4	8.8	1.1	0.94	8.1	6.3	14	11	7.2	7.3	7.6	7.2	2.1	1.5	11	9.7	8.9	3.1	1.2	9
Pb208	25	26	19	20	12	9.2	1.4	1.3	8.5	8.9	16	14	6.6	7.2	7.7	6.8	2.4	1.5	17	15	7.6	3.9	1.3	7.5
Th232	3.8	2.9	2.6	2.6	3.3	3.7	0.39	0.31	3	2.7	4.5	3.3	2.8	2.6	3.1	2.7	0.75	0.45	4.3	3.1	3.8	0.88	0.29	3.3
U238	1.8	2.5	1.7	1.7	4.1	2.1	0.25	1	2.7	2.2	6.6	3.7	2.3	2.2	2.8	2.5	0.45	0.21	3.7	4.2	2.8	0.49	0.22	2.8

Table 5-4: Minimum detection limit (ppb) for each element within an opal band.

	LR1 brown/clear	LR2 black/grey	LR5 grey/honey	LR7 grey/poc	LR9 white/clear	LR13 grey/violet	LR14 black/poc	LR15 grey/poc	A1 white/poc	A2 grey/clear	CP1 grey/grey
Na23	1.0	0.6	1.3	-	1.0	1.1	1.1	1.0	-	0.5	-
Mg24	1.1	0.9	1.1	1.0	1.0	1.0	1.1	1.0	1.0	1.8	1.1
Al27	1.1	1.2	1.2	1.6	1.1	1.0	1.1	1.1	1.0	1.3	1.0
K39	-	-	2.0	3.2	1.4	1.3	1.4	1.3	1.1	1.8	1.3
Ca43	1.1	1.0	1.0	1.2	1.0	1.0	1.1	1.0	1.0	2.1	1.1
Sc45	-	-	1.3	2.0	1.1	1.2	1.3	1.1	1.0	1.0	1.0
Ti49	24	1.4	5.6	34	1.5	6.1	10	2.1	1.3	3.2	3.9
V51	11	1.0	4.5	12	1.4	3.6	11	2.3	0.5	1.9	2.0
Mn55	1.0	1.1	1.1	1.0	1.0	1.1	1.2	1.0	1.0	1.9	1.2
Fe57	1.1	1.0	1.1	1.2	1.0	1.1	1.4	1.1	1.0	1.7	1.2
Co59	21	3.3	4.1	25	2.2	10	17	2.5	0.7	1.9	4.7
Ni60	3.5	3.1	0.8	7.8	1.4	3.8	5.8	1.8	0.8	0.9	1.1
Cu65	38	1.9	9.5	23	1.3	2.3	30	2.2	1.0	0.0	13
Zn66	3.3	3.3	2.5	2.7	2.3	0.1	12	1.6	0.6	0.8	1.2
Ga69	-	-	1.4	1.7	1.1	1.2	1.5	1.2	0.9	2.3	1.1
Ga71	-	-	6.3	6.2	1.9	4.3	5.7	2.1	0.2	1.6	0.9
Rb85	1.0	2.0	1.2	0.5	1.1	1.2	1.1	1.1	1.0	1.4	1.2
Sr86	1.1	1.1	1.2	1.6	1.0	1.2	1.2	1.1	1.0	2.4	1.2
Sr88	1.1	1.1	1.1	1.6	1.0	1.2	1.2	1.1	1.0	2.3	1.2
Y89	9.5	1.4	6.6	35	1.2	9.4	5.2	1.8	0.5	1.9	4.3
Zr90	1.4	1.2	1.2	5.7	1.0	1.3	1.2	1.1	1.0	1.2	1.2
Cs133	1.0	1.3	1.1	1.0	1.0	1.7	1.0	1.0	0.9	1.2	1.1
Ba137	1.2	1.1	1.3	1.9	1.1	1.1	1.4	1.2	1.1	2.3	1.3
La139	15	1.3	8.0	21	1.3	14	6.3	2.5	1.2	1.9	4.8
Ce140	16	1.3	8.7	17	1.3	17	6.2	2.4	1.1	1.9	5.6
Nd146	18	1.3	9.2	25	1.3	17	6.0	2.4	1.2	2.0	5.3
Sm147	18	1.3	9.9	31	1.4	18	5.7	2.3	0.5	1.9	4.9
Eu153	13	1.4	8.2	9.0	1.3	14	5.1	2.3	2.0	2.2	4.6
Gd157	15	1.4	7.6	32	1.0	14	5.6	2.3	0.2	2.1	3.4
Ho165	12	1.5	6.7	40	1.2	13	5.7	1.9	0.8	1.8	6.4
Er167	11	1.5	6.7	41	1.4	11	5.9	1.8	0.4	1.9	6.7
Yb172	12	1.5	5.4	28	1.3	7.8	5.9	1.8	0.4	2.1	5.2
Pb208	17	1.3	5.5	13	2.0	9.0	16	3.7	1.2	0.7	2.1
Th232	16	1.1	6.1	19	1.3	7.6	6.1	1.7	1.2	2.0	5.2
U238	9.0	1.4	3.7	17	1.3	6.7	8.8	1.7	0.5	1.6	6.1

Table 5-5: Ratio of elemental abundance between dark and light bands for banded samples.

Element	Division Factor	Element	Division Factor
Li7	0.1	Sr86	10
Na23	100	Sr88	10
Mg24	10	Y89	1
Al27	1000	Zr90	10
K39	100	Sn118	1
Ca43	100	Cs133	1
Sc45	1	Ba137	10
Ti49	100	La139	1
V51	0.1	Ce140	1
Cr53	0.1	Nd146	1
Mn55	10	Sm147	0.1
Fe57	100	Eu153	0.1
Co59	1	Gd157	0.1
Ni60	1	Ho165	0.01
Ni62	1	Er167	0.1
Cu65	1	Yb172	0.1
Zn66	10	Lu175	0.01
Ga69	1	Pb208	1
Ga71	0.1	Th232	1
Rb85	10	U238	0.1

Table 5-6: Division factors for Figure 5-4 to Figure 5-8.

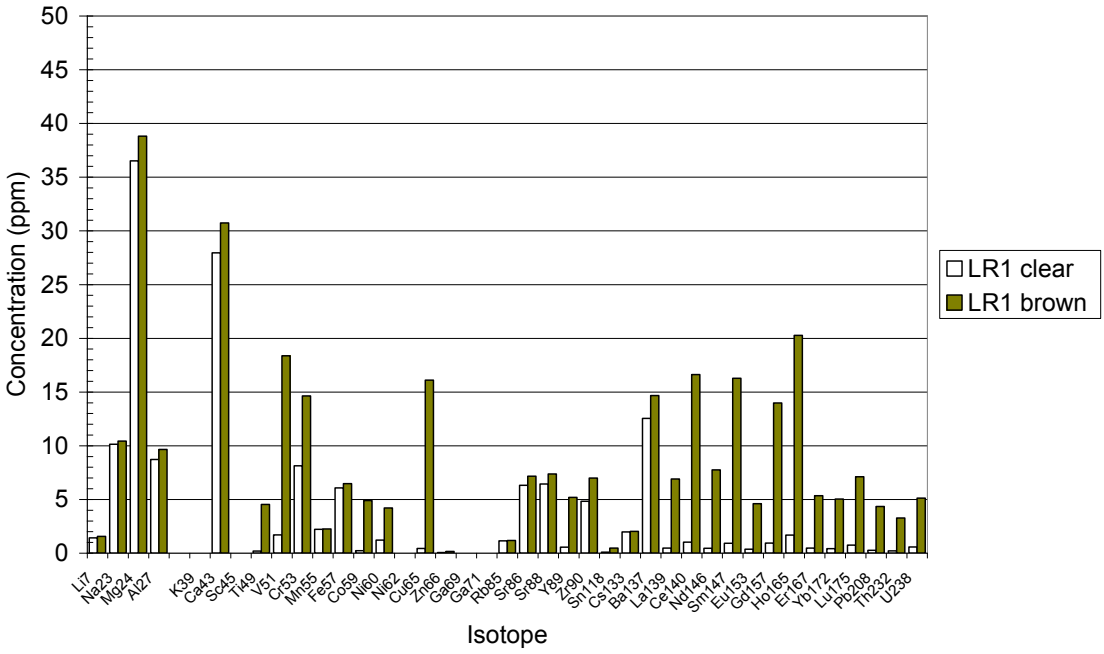

Figure 5-4: Elemental profile of Lightning Ridge sample LR1; relative elemental abundance between brown and transparent bands.

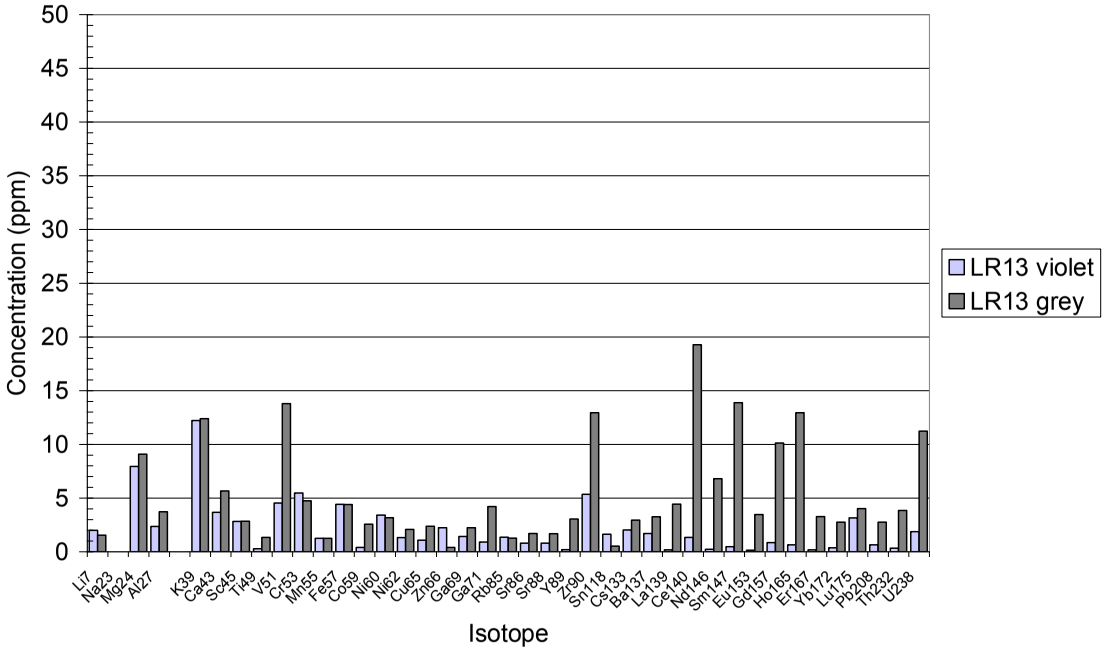

Figure 5-5: Elemental profile of Lightning Ridge sample LR13; relative elemental abundance between grey and violet bands.

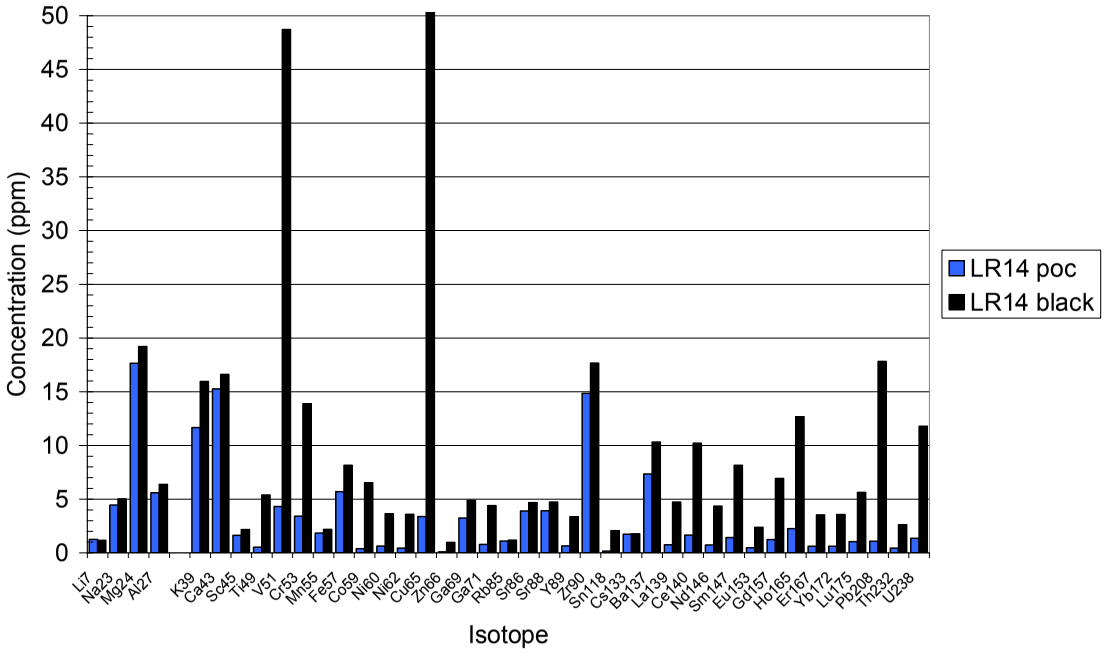

Figure 5-6: Elemental profile of Lightning Ridge sample LR14; relative elemental abundance between black and blue poc bands.

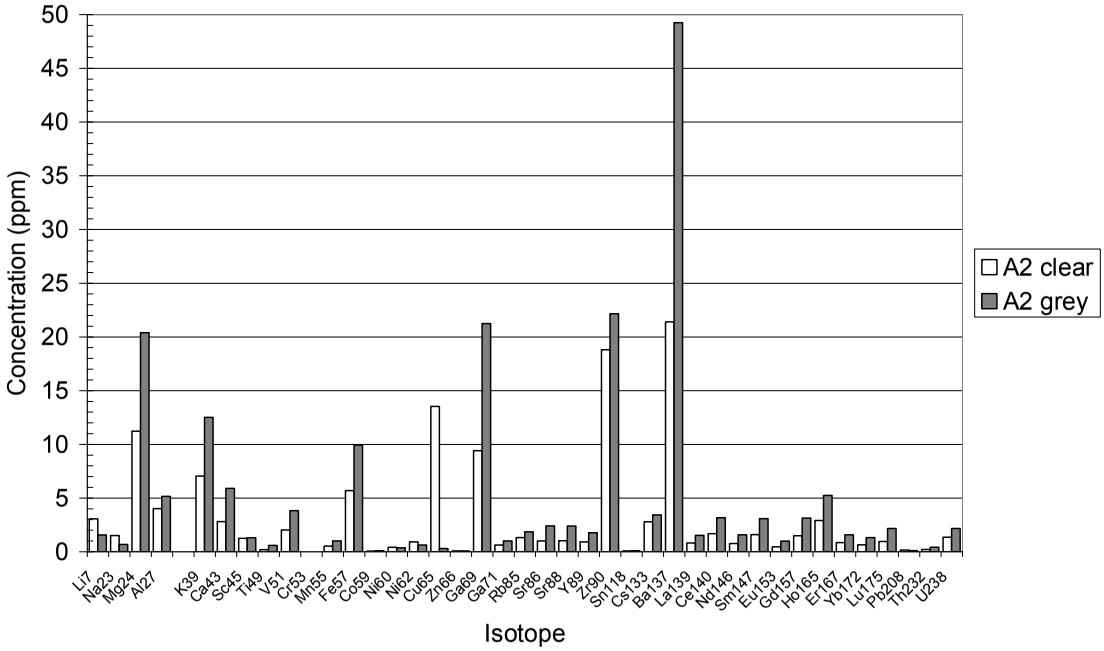

Figure 5-7: Elemental profile of Andamooka sample A2; relative elemental abundance between grey and clear bands.

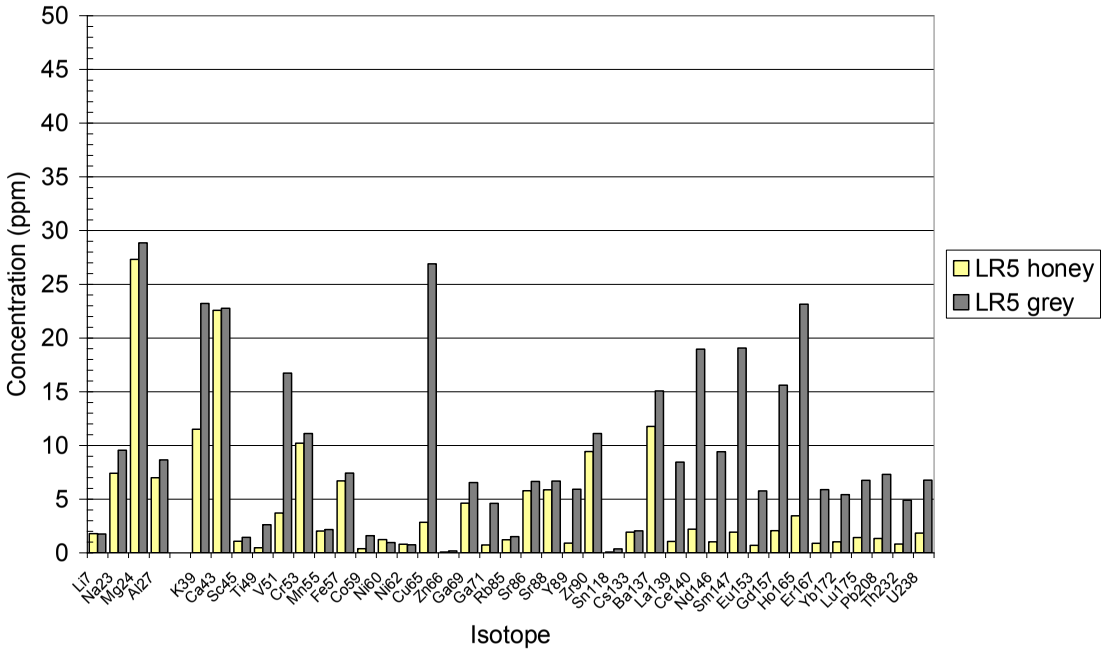

Figure 5-8: Elemental profile of Lightning Ridge sample LR5; relative elemental abundance between grey and honey-coloured bands.

5.3.1. Alkali and alkaline-earth elements

The following figures were found to be representative of the concentration of alkali and alkaline-earth elements of opals from all the Australian regions researched: Na from 100 to 3000 ppm; K from 700 to 3000 ppm; Ca from 300 to 3000 ppm; and Mg from 100 to 400 ppm (Figure 5-9). The results for each element are discussed separately below.

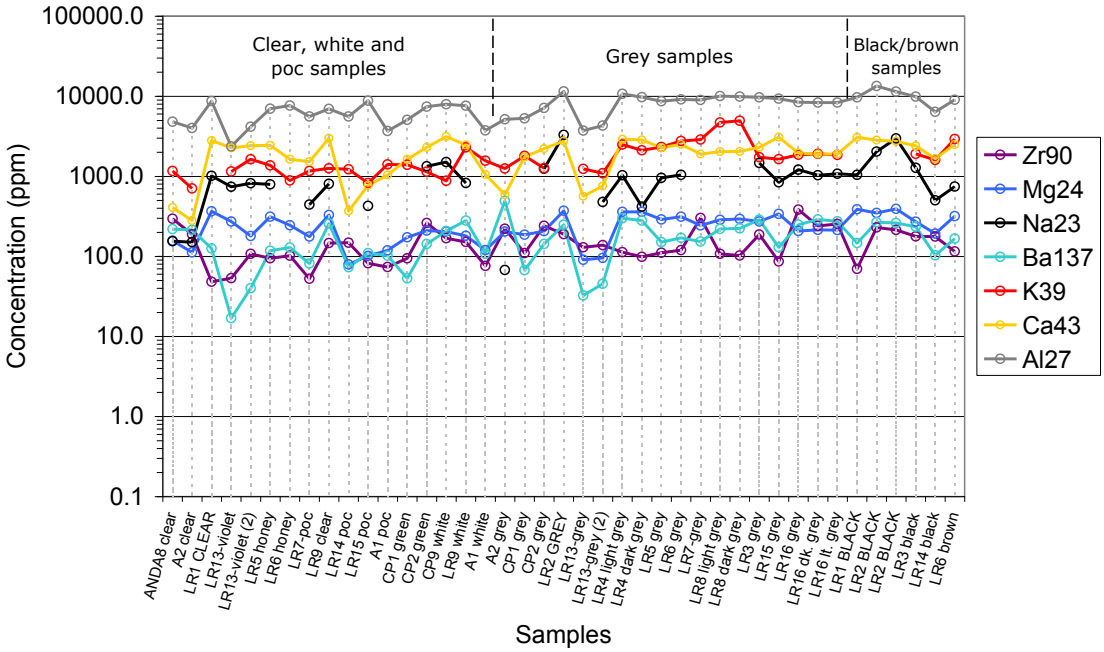

Figure 5-9: Concentration of Na, K, Mg, Ca, Ba, Al and Zr for all samples.

5.3.1.1. Calcium

The Ca concentrations varied by an order of magnitude amongst the various samples, from 280 ppm to 3100 ppm. This trend could not be correlated to samples having a particular colour/opacity or those coming from a particular mining region. For instance, the white CP9 sample had a higher concentration of Ca (3100 ppm) than even the jet-black potch sample LR2 (~2500 ppm), which normally has more impurities than any other sample.

For all but two of the banded samples, the difference in Ca concentration of each of the bands was less than 10%, and this difference was often only 2 to 4%. There was one notable exception: for sample A2,

the Ca level of the grey band was over twice as high as the transparent band. Sample LR7 showed a 16% higher calcium level in the grey potch band than the band displaying a red poc, however, this result was not reproduced in the other banded precious opal samples.

5.3.1.2. Magnesium

No correlations on Mg concentration and sample locality or sample opacity could be drawn, but it ranged from 80 to 390 ppm, depending on the sample. For banded samples, the Mg concentration never varied by more than 10% between the bands belonging to any one sample, and this difference was frequently less than 5%. Once again, sample A2 was the only exception (the grey band was 80% higher in Mg than the transparent band).

5.3.1.3. Potassium

The concentration of K was more varied than Mg or Ca, and in some cases was up to 330% higher in the darker bands than the lighter bands (sample LR7). For most samples, transparent bands contained approximately half the K concentration of the opaque bands (A2, LR1, LR5, LR6 and LR9). This result was also true for samples with poc bands (LR7, LR14 and LR15); although in most cases the K level in the poc band was not quite half of the adjacent opaque bands, but still noticeably lower. The bands of sample LR13, which were analysed twice, showed in one case a similar distribution of K, and a dissimilar K level in the other. For the first analysis, the K concentration was within a value of 1% between the grey and violet bands; for the second analysis, the K concentration was 33% higher in the grey band than in the violet band.

5.3.1.4. Sodium

The concentration of Na was generally between 400 and 1500 ppm for all of the samples investigated. Sample A2, however, showed a concentration of only 70 ppm in the grey band and 150 ppm in the transparent band.

Na was the only element of all those investigated that was shown to behave in a manner opposite to the trends shown by the remaining elements; the concentration of Na was frequently higher in the lighter

bands than the darker bands of some samples (A2, LR2, LR3, LR4, LR6 and LR16). The Na concentration was extraordinarily high in the very opaque sample LR2 (3900 ppm in the grey band; ~2500 ppm in the black band).

5.3.2. Aluminium

Al was the most abundant element present (besides Si and O) in all the opals considered, and ranged between 3700 to 13,500 ppm (i.e. up to 1.35%). The concentration of Al, however, was relatively unchanged in banded samples, and typically never varied by more than 10 to 20% between bands (Figure 5-9). The Al content was always lower in the more transparent or translucent bands than in the more opaque bands. The sample showing the greatest Al variation was LR7; the grey band had an Al content of 9000 ppm, while the Al content of the poc band was only 5600 ppm (Figure 5-10).

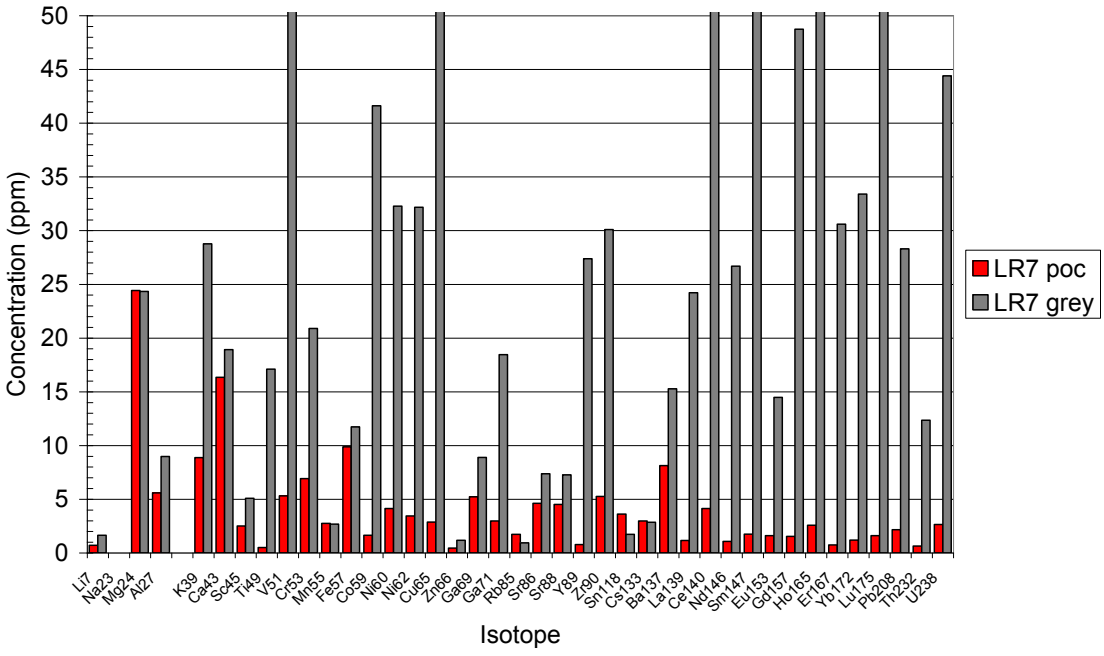

Figure 5-10: Elemental profile of sample LR7; relative elemental abundance between grey band and adjacent band with red play-of-colour.

5.3.3. Transition metals

It is evident that the black and grey opals contain significantly higher quantities of certain transition metals than white or colourless opals (Table 5-2; Figure 5-11; Figure 5-12). The following elements in particular are notable for having consistently higher concentrations in the darker coloured opals: Ti, Co, V, Ni, Cu, Zn, and Y. These elements are generally at least double the concentration in the darker section of opal than in the lighter section, and this difference is often more than an order of magnitude. Zr also displayed similar trends, though not in all samples, and not to the same magnitude as the elements listed above. The results of banded samples are more clearly seen in Figures 5-4 to 5-8.

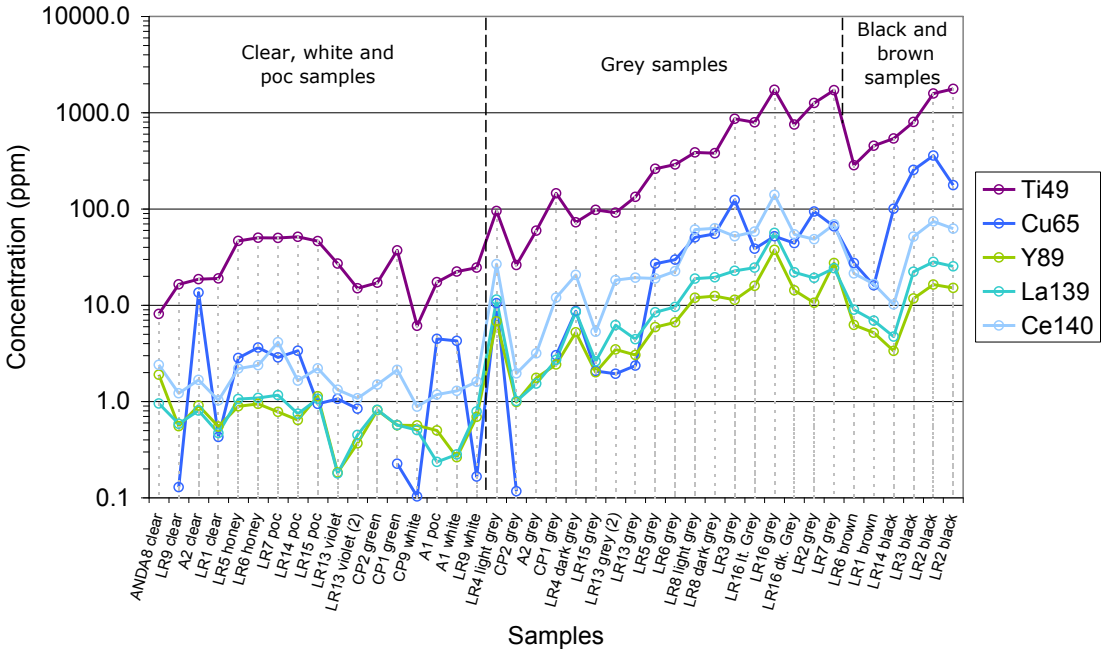

Figure 5-11: Elemental abundance of Ti, Cu, Y, La and Ce for all bands within the samples investigated.

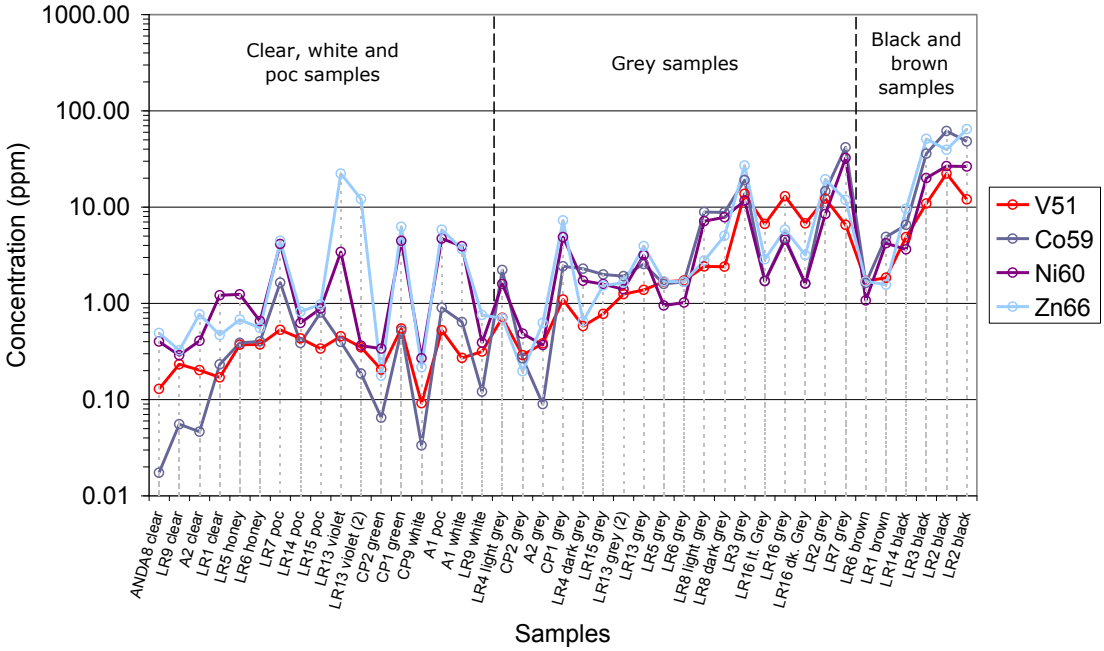

Figure 5-12: Elemental abundance of V, Co, Ni and Zn for all bands within the samples investigated.

5.3.3.1. Fe and Mn

While most of the transition elements had variable concentrations between bands, Fe and Mn, for example, were consistently the same from one band to the next, with the exception of two samples; the grey band of sample A2 showed almost twice the concentration of both Fe and Mn of the transparent band; while the black band of LR14 was 40% higher in Fe and 20% higher in Mn.

5.3.4. Rare-earth elements

The rare-earth elements (La, Ce, Nd, Sm, Eu, Gd, Ho, Er, Yb and Lu) were also significantly more abundant in the darker sections than in the lighter sections of opal samples (Table 5-2; Figure 5-11). The difference in these values is also commonly greater than an order of magnitude from a clear to a black section of opal. These results are clearly seen in Figures 5-4 to 5-8.

5.4. DISCUSSION

5.4.1. Colourant ions

The results indicate that, regardless of their origin, grey and black opals contain higher concentrations of most of the transition and rare-earth elements than the white and colourless opals. The effect of transition metal impurities on the colour of silicate glasses has been well studied elsewhere (Bamford 1977; Nassau 1981; Volf 1984); most of the transition elements present in the opals studied are known to impart some degree of colouring to silicate glasses (Bamford 1977; Nassau 1981; Volf 1984). Furthermore, colouring is often more effective if more than one colourant ion is present. For example, while not a strong colourant on its own, Ti^{4+} strongly affects the colour of glasses in the presence of even trace amounts of some polyvalent transition metal ions (Volf 1984). V, Cr, Mn, Fe, Co, Ni and Cu are all colourant ions (Bamford 1977); the most effective colourant ion, Co, produces blue colouring at concentrations between 0.01 and 3 ppm in silica glass (Volf 1984).

Since the transition metals present are known to impart colour to silicate glasses in the concentrations observed (from 0.02 ppm Co in sample ANDA8 to 48 ppm Co in the black band of sample LR2), it is likely that these elements are responsible for the colouration of the darker bands in the opals examined.

5.4.1.1. Laporte's selection criteria

The generation of different colours in glass is caused by the excitation of transition metal ions to higher energy states through the absorption of electromagnetic radiation (Rawson 1980; Nassau 1981). Certain energy-level transitions are forbidden, for example, Laporte's selection rule dictates that in centro-symmetric environments, transitions can only occur between opposite polarity[1] (Rawson 1980). Consequently, if the electron transitions for a particular ion are not allowed, the absorption bands corresponding to those forbidden transitions are relatively weak. However, Laporte's rule is relaxed to some extent when the ion is accommodated in an electric field

[1] For example, the excitation of an electron from one d orbital to another.

which is not entirely symmetrical (Rawson 1980). Using Electron Spin Resonance (ESR) / Electron Paramagnetic Spectroscopy (EPS), Hutton *et al.* (1997) reported that low symmetry Fe^{3+} and Mn^{2+} ions were indeed present in all the spectra of natural opals (from Coober Pedy and Lightning Ridge). The Electron Paramagnetic Resonance study by Temniskova-Topalova *et al.* (1990) presented similar results concerning the presence of Mn^{2+} in opal-A diatomite.

The separation between the number of energy levels of an ion is also greatly affected by the resultant field which the transition metal ion experiences and by interactions between the ion and its immediate neighbours. The energy difference between the ground state and the excited state, and hence the wavelength at which the absorption occurs, depends on the immediate environment of the ion (Rawson 1980). Therefore, the colour produced by a transition metal ion is dependent on whether it exists in a four-fold or six-fold coordination. The colours generated are also affected to a degree by the nature of the ligands, especially for ions in tetrahedral coordinations. It is well known that the colour of silicate glasses is influenced by the glass composition; the concentration of Alkali metals in particular, can control the oxidation states of colourant ions (Rawson 1980). This has been attributed to an octahedral-tetrahedral transition of an ion above a certain threshold of alkali concentration (Rawson 1980). Given the same transition metal concentration, a higher concentration of Alkali metals leads to a higher intensity of colour.

Interestingly, other transition metals such as Fe and Mn, also known to produce colouring, mostly showed an identical elemental distribution between differently coloured bands. In addition, ions such as Zn, Mn, Ce and Mg are known to decolourise synthetic silica glasses in which other colourant ions are present (Volf 1984). However, the colourless samples (such as CP9) only show Zn, Mn and at quantities of a few ppm, and while the concentration of Mg is roughly 100 to 300 ppm for these samples, its absence could not be linked to the degree of colour of these samples. This is not all that surprising, since the imparted colour is dependent on the ions

present[1], their concentration and their oxidation states, attempting to attribute the base colour of an opal band to any of the trace elements present is extremely difficult.

5.4.2. Banded opals

The chemical investigation of white and colourless opals has established two aspects relating to their microstructure:

5.4.2.1. Play of colour

Bands of opal exhibiting a play of colour do not necessarily have a lower level of impurities than a similarly transparent band of opal lacking a play of colour, as might be expected. The results for A1, a sample with poc and white bands, can be seen in Table 5-2. This is confirmed by the results of Deniskina *et al.* (1981) who reported that precious opals did not always have a lower amount of impurities than conventional [common] opals. Deniskina *et al.* (1981) explained this curious result by the fact that common opals, consisting of disordered spheres, theoretically have a higher packing density (and thus contain less porosity) than precious opals which are comprised of monodisperse spheres. It was within these capillaries that the impurities were assumed to remain (5.4.3.2).

5.4.2.2. Opacity

The opacity of opals is not implicitly related to the degree of impurities contained within the opal, with the possible exception of the elements K and also Ca. This is clearly demonstrated with the results of sample LR9, a banded sample containing transparent and opaque white bands (Table 5-2). The concentration of elements in the transparent band is generally the same as those in the opaque white band (i.e. the ratio is mostly one-to-one). In fact, the white band of sample A1 and the white opal CP9, which were both completely opaque, contained some of the lowest levels of transition and rare-earth elements of all of the samples, indeed lower than almost all of the transparent opals. On the other hand, the white samples (A1, CP9, LR9) contained higher amounts of K and Ca than the transparent

[1] Transition metal ions impart a synergistic effect on the presence of colour in silicate glass; i.e. the combination of several colouring ions result in a greater degree of colourisation than the sum of what can be attributed to each of the individual ions alone.

samples. Nitrogen adsorption results (Table 4-4) showed that the opaque white samples (CP9 and LR17) contained the greatest overall porosity; the black opaque sample (LR2black) contained an 'intermediate' level of porosity; while the translucent and transparent potch opals (LR1clear, ANDA8, Tintenbar) contained the least porosity. Therefore, the differences in the opacity are evidently caused by the variable amount of porosity that these samples contain.

Specifically, the chemical composition of the various bands of sample A2 was interesting. This sample often opposed the trends shown by all the other samples. This remains the only sample in which the concentration of most of the alkali and alkaline-earth elements was significantly different in adjacent bands. Furthermore, the abundance of Fe was different across the bands. This is discussed further in the SIMS chapter (6.4.5; 6.5.2.4), as linescans revealed more information about the distribution of the elements Fe, K, Ca, Na, Mg and Ba in this sample.

5.4.3. Porosity

5.4.3.1. Effect of salt concentration and pH

The presence of salts during the colloidal aggregation process generates three-dimensional gel-like networks (Iler 1979; 3.2.5; Figure 3-8). These gel-like networks have a higher porosity than a coagulum that is formed in the absence of these salts (Figure 3-6). The samples analysed that contain white and clear layers show a variation in the concentration of the element K, in particular, for samples A1 and LR9 (Table 5-5). This suggests that the opaque white layer, since it contains a slightly higher concentration of K, has more of a gel structure than the clear layer (which contains a lower concentration of K) leading to a slightly higher porosity. Alternatively, the opaque white bands of samples LR9 and A1 may have formed at a slightly lower pH than the adjoining bands, leading to the formation of network structures that are more gel-like (Figure 3-8). This conclusion is consistent with the results of a study concerning banded crystalline wood opal from Lake Eyre (Segnit *et al.* 1965; Jones and Segnit 1969; 5.1.4). This higher level of porosity could be the reason for the layer's opacity; a higher level of internal voids has the effect of scattering the incident light. One of the findings of the previous chapter was that the

microstructures of various samples contain varying amounts of voids (4.4.1.5).

5.4.3.2. Infilling of voids by additional silica

Epova *et al.* (1983) has shown that opal of different transparency can be synthesised by limiting the exposure of an artificially grown opal to a silica sol. The resulting opal's pores are infilled with further silica by varying amounts. In this case, the porosity is dependent on the degree of this infilling. If this process occurs with the types of opals discussed here (specifically sample A1), the slightly higher elemental concentrations observed in the poc band (A1) could merely reflect the additional impurities included within those pores, impurities which are included along with the greater quantities of infilled silica. In other words, the greater level of alkali- and alkaline-earth elements in a particular band could be attributed to the additional interstitial silica, which in-fills the pores contained within the microstructure, rather than the higher proportion of these elements directly contributing to the microstructure's porosity via gel formation (5.4.3.1).

On the basis of the presumed microstructures, a transparent layer is expected to have a slightly higher level of impurities than an opaque layer, as the void spaces are assumed be filled with interstitial silica (which, of course, also contains additional impurities).

In the case of CP9, it may be the interstitial silica which is higher in K and Ca, making it appear as though these elements are directly responsible for influencing colloidal precipitation. However, if that were the case, the greater amount of interstitial silica (which accommodated the extra K) would, if anything, have led to a more transparent opal, as more of the voids would have been filled, leading to less light-scattering. For sample CP9, this assumption does not correlate well, as thermal analysis shows that it contains more voids, yet LA-ICPMS reveals it also has a higher impurity level. Perhaps the high concentrations of alkalis are indicative of gel-like formations.

5.4.4. Charge neutralisation

The sedimentation model suggests that opals are sedimented from supersaturated silica solutions, through a process of colloidal aggregation.

The silica spheres (or colloids) coagulate as the water content is reduced, finally solidifying into a single mass (Jones *et al.* 1966; Iler 1979). However, banded opals are not discussed in the context of that model, because it is not comprehensive enough to account for all the types of opals commonly found.

5.4.4.1. Sedimentation model for potch opal

Between a pH of 6.5 and 10.5, a silica sol is inherently stable; the individual colloids are suspended by thermal Brownian motion, and separated from each other by the repulsive negative surface charges generated by interacting electrical double layers (Einstein 1956). Figure 5-13 illustrates the electrical double layer surrounding a negatively charged surface, while Figure 5-14 shows the interaction of two double layers in close proximity to each other.

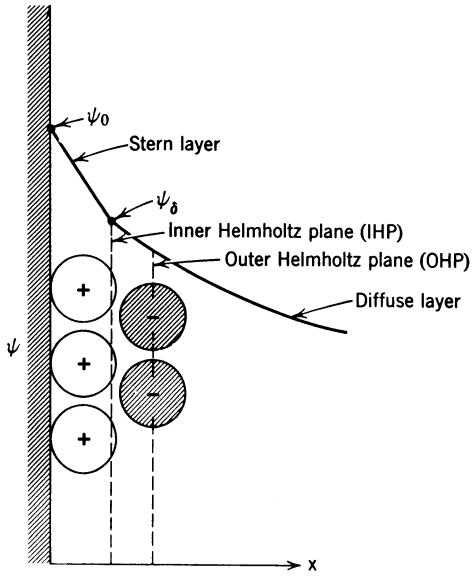

Figure 5-13: The stern layer (assuming the charge on the surface is positive).

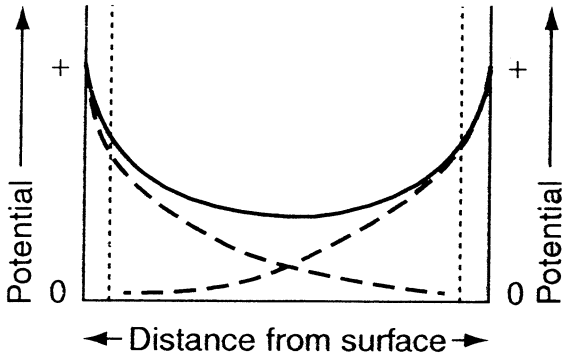

Figure 5-14: Interaction between two double layers; the two overlapping curves result in a higher electrical charge. From Holmberg (2001a).

The presence of transition metal cations in the solution can contribute to the precipitation of the silica spheres through a process of charge neutralisation (Adamson 1990; Shaw 1992; Myers 1999). These highly charged cations (Ti, Y, etc) in the silica sol are adsorbed onto the surfaces of the negatively charged silica colloids, effectively neutralising them, and the colloids then attain the point of zero charge (ZPC). The process of charge neutralisation allows the particles to coagulate, as the spheres are not able to repel each other. Hence, the colloids sediment relatively rapidly as the force of gravity dominates over the mutual forces of sphere repulsion.

The charge-neutralised spheres would likely result in the production of a polydisperse silica sediment, as there may be insufficient time for Ostwald ripening to occur prior to sedimentation. It has previously been established that polydisperse sols inherently lead to faster coagulation rates than monodisperse sols (Holmberg 2001b). As polydisperse colloids sediment at different velocities due to Stoke's law (6.1.3.4), a greater number of inter-colloidal collisions occur and hence the coagulation rate of polydisperse sols is increased, compared to monodisperse sols (Holmberg 2001b). Irrespective of whether the spheres are poly- or mono-disperse, they are sedimented too fast to take up ordered positions and can therefore only agglomerate into a disorderly manner. These randomly deposited silica spheres co-precipitate with the highly-charged cations (also colourant ions)

and may therefore form a dark potch layer. According to the research of Vosel and Kalinin (1999), rapid coagulation of low-charge[1] colloidal particles results in the chaotic aggregation of new particles and therefore a regular structure cannot be formed.

In a series of precipitation experiments, Moxon (1996) reported that presence of up to 1:96 Fe^{3+}:SiO_2(colloidal) was no more effective in precipitating silica at 25°C than the control runs. Coincidentally, the concentration of Fe was virtually identical between the constituent bands of almost all the opal samples investigated (Table 5-2). It therefore seems that the presence of up to 1300 ppm of Fe in these samples does not contribute to the deposition of the corresponding opal bands.

5.4.4.2. Charge neutralisation sequence

The stage at which charge neutralisation takes place is important; less cations are needed for the charge neutralisation of secondary spheres than primary spheres, as the Brownian motion is not as strong with the former and hence the secondary spheres are more prone to sedimenting. In the case of banded opals, the charge neutralisation stage must occur after the primary particles accrete to form the secondary particles. If charge neutralisation occurs before this, the primary particles would attain the ZPC, which would result in a random agglomeration of primary particles. Numerous SEM studies have demonstrated that microstructures of this type are absent (Cole and Monroe 1967; Monroe *et al.* 1969; Rau and Amaral 1969; Segnit *et al.* 1970; Sanders 1985). Accretion of primary silica spheres to form secondary spheres reportedly occurs spontaneously; i.e. charge neutralisation is not required for this process (Iler 1979). If charge neutralisation takes place after the primary spheres coacervate, this leads to a randomly deposited structure of secondary spheres, which is commonly observed with SEM (Sanders 1964; Cole and Monroe 1967; Darragh *et al.* 1976).

The fact that these spheres are of a fairly similar size suggests that charge neutralisation has taken place towards the end of the colloidal growth phase. As the silica is still being deposited onto the surfaces of the

[1] In this case they refer to the charge on the surfaces of silica colloids not the charge of the cations.

colloids, progressively more cations are attracted to these negative charges, until there are sufficient cations inside the stern layer and the zeta potential is overcome. At that time, the force of gravity dominates, leading to sedimentation. Charge neutralisation could have been a continuous process as the colloids were forming, although in that case, the question is how the spheres managed to keep growing to the large size consistently observed, whilst having no mutual forces of repulsion to aid dispersion of the colloids.

5.4.4.3. Presence of cation impurities at the core of colloids

Alternatively, in the model proposed by Deveson (2004), it is stated that positively charged nuclei attract negatively charged silica which then "seed" around these nuclei. Although this process no doubt occurs, the concentration of impurities contained within most of the potch opals analysed is significantly more than that required to initiate nucleation. Furthermore, opals that have a low level of impurities (the white or transparent opals) also manage to nucleate similarly sized spheres. NMR experiments (7.4.5) have also shown that all of the Al atoms are bonded within the silica network, forming Al–O–Si linkages, and that they do not exist as separate AlO_2 inclusions (Al–O–Al bonds) that might be present in core impurities.

5.4.5. Solution depletion mechanism - sol purification

Regardless of the stage at which charge neutralisation takes place (within the potch band), it leads to a purification of the remaining sol by depleting the solution of highly-charged cations. Once most of the highly charged cations have accumulated along with the precipitated silica spheres (5.4.4; Figures 5-15 and 5-16), the remaining colloids within the sol would have time to grow uniformly by the Ostwald ripening mechanism. Hence, the sol that remains is able to form monodisperse spheres and these may or may not deposit in an ordered array in the subsequent opal band (Figure 5-17). The reason that spheres deposit into either ordered arrays or disordered arrays is a complex one and is discussed elsewhere (6.1.1; 6.1.2).

5.4.6. Sedimentation model for banded opal

Considering the results presented here concerning the trace element chemistry of banded opal samples, the charge neutralisation and sol purification mechanisms are proposed to account for the formation of an opal containing a black or grey opal layer adjacent to a white or colourless layer. The generation of a dark potch layer has already been discussed (5.4.4.1). An overlying opal band would simply form a white or clear layer, depending on the presence of salts (5.4.3.1) and the extent of the transport of silica towards coalescing the spheres (3.4.2; 4.4.5.1).

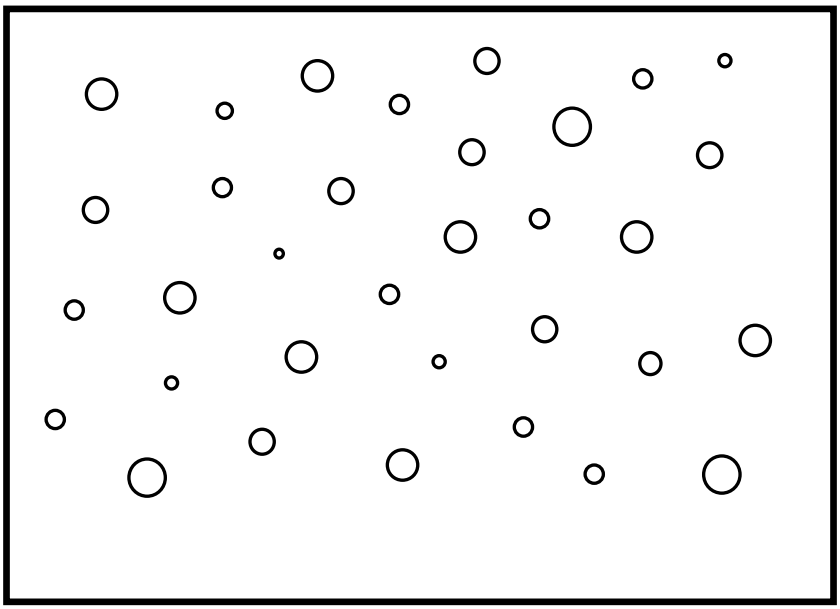

Figure 5-15: First stage in the formation of a banded opal: The negative surface charge of the silica colloids results in mutual repulsion. The dispersion of colloids forms a metastable silica sol. Note: polydisperse colloids are shown with an exaggerated size distribution.

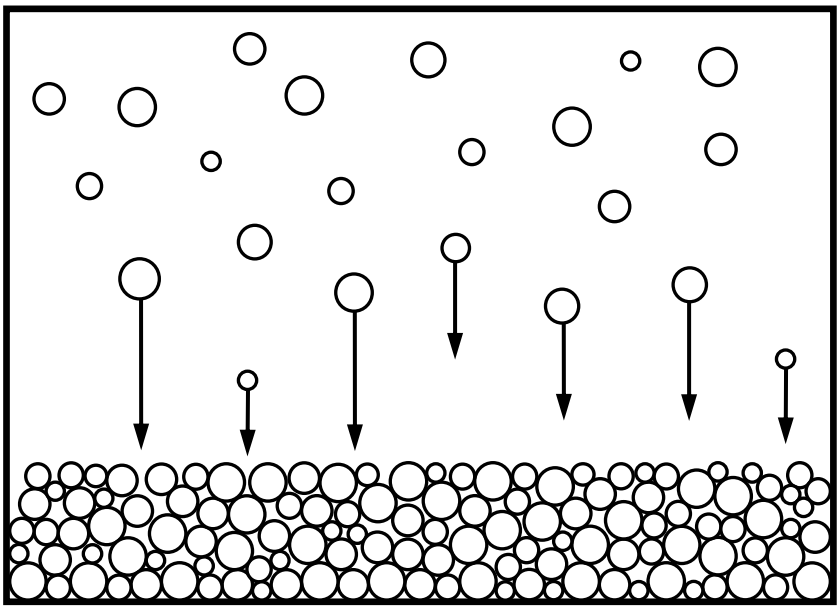

Figure 5-16: Second stage in the formation of a banded opal: In the presence of impurities, a large fraction of the silica colloids are charge-neutralised by the adsorption of highly charged cations (Ti^{4+}, Y^{6+}). This leads to rapid sedimentation and the formation of a layer consisting of disordered, polydisperse spheres. These cations accumulate in the coagulated layer, purifying the remaining sol.

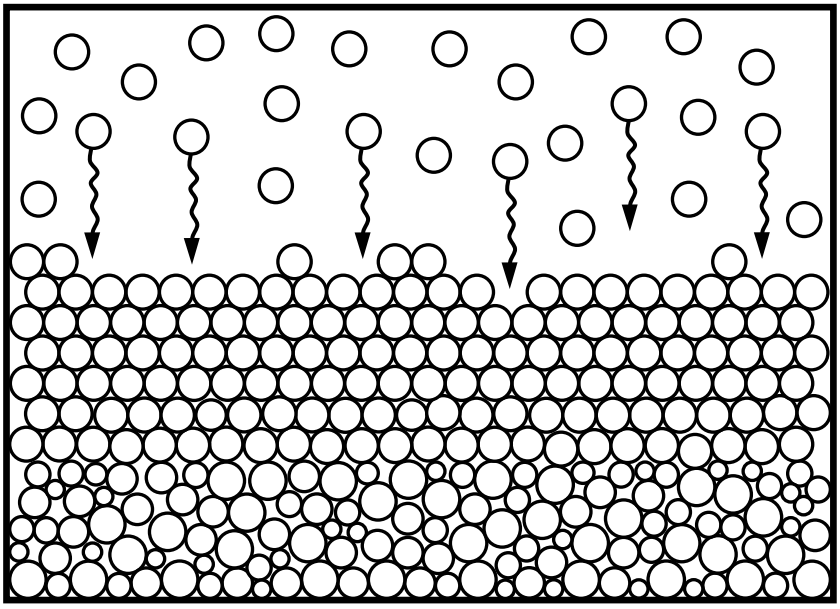

Figure 5-17: Third stage in the formation of a banded opal: Ostwald ripening progresses in the remaining colloids. Slow removal of water then allows the spheres to settle very slowly. This results in the deposition of monodisperse spheres into an ordered layer on top of the previous sediment.

With this model, a banded opal containing two layers only results when the initial sol contains an appropriate quantity of highly-charged ions, which is depleted during the coagulation of the colloids. The interface between the potch and poc layers which results thus corresponds to the moment in time when the highly-charged ions in the sol were depleted. If the sol contains too many of these ions, an opal consisting entirely of dark-coloured potch is formed; whereas if the sol contains insufficient ions for the charge neutralisation, a light-coloured opal is formed, which may display a poc. This consequence accounts for the variability in the observed samples; at the lightning ridge fields for example, both dark and light opals are regularly found, but banded opals are considerably rarer. This model adequately accounts for most of the banded opals samples we have encountered, although there remain a number of samples that suggest this is not the only mechanism at work (6.5.1.1).

5.4.6.1. Potch opal formation - further considerations

It is thought that the ordering of the silica spheres (which gives rise to opals with a play of colour) is due to a slow sedimentation or settling process. If the presence of greater quantities of transition elements increases the deposition rate of colloidal silica, thereby allowing insufficient time for Ostwald ripening (generation of monodisperse spheres), the process of charge neutralisation precludes ordered arrays of spheres from developing in the darker potch opals, as they generally contain abundant quantities of trace elements. It is interesting to note that ordering of the spheres (which gives rise to the desirable play of colour in an opal), has yet to be observed in the darker coloured opal samples, only in the white or transparent samples, an observation that supports the charge neutralisation hypothesis.

5.4.6.2. Deposition sequence

This model assumes the different bands formed from the same sol. It has been suggested that the layers could also have formed at different times, from different sols. This may hold true for the odd sample, but most of the banded samples investigated here possessed an interface that was formed in the semi-solid state. When the transparent and translucent samples are examined with an optical microscope, the interface appears to

have formed in the fluid state, as there are globules of one colour in the band on the opposite side of the interface, and vice versa. Often, an interphase is observed where light and dark regions appear to be mixed. Perhaps more convincing is the elemental data itself. There are several elements that have a relatively uniform concentration across the interface, including Si, Mg, Ca, Fe and Mn. (5.3.1; 5.3.3; 6.3.2 to 6.3.5), which indicates that the various bands could not have formed at different times, or else the different layers would have significantly different elemental profiles.

5.4.7. Origin of polyvalent cations

There is some uncertainty in the origin of these impurities in the sol, for example, whether they were present in the sol from the beginning or arrived at a later stage of sol formation. The original source of these impurities is yet another mystery, and is beyond the scope of this thesis.

5.4.7.1. Impurities arrived at a later stage

At first it would be logical to assume that the highly-charged ions might not have been in the solution prior to the growth of the colloids, since it is only the pure silica solutions that are able to form a stable sol (Deniskina *et al.* 1981). In this case, it is assumed that these trace metals appeared in the solution at a later time, after the formation of the secondary spheres, perhaps through the subsequent percolation of contaminated rain or ground water. However, one of the reasons for the second hypothesis discussed in the following paragraph is the following dilemma: if the impurities arrived after the stable sol had formed, as postulated above, this then raises the question "wouldn't the spheres in both potch and precious opal layers all be of the same size due to the effect of Ostwald ripening process?". This is clearly not always the case, as SEM microscopy has shown that randomly sized spheres are seen in potch layers, which are adjacent to poc layers. One explanation is that the impurities could have arrived in the solution before the Ostwald ripening had time to take effect, but only after a stable sol had formed, yet these two processes still occur simultaneously.

5.4.7.2. Impurities were always present

The second alternative is if the transition metals were present in the solution initially. The colloids (in the potch band) may have grown in the presence of these impurities; since the negative surface charge of the silica colloids is reduced by these continually adsorbed cations, the repulsion is less intense and therefore the effect of gravity is relatively high. Hence, the spheres may be readily and continually sedimented with disordered sizes.

The points raised above regarding the constraints of the purity of the sol in forming a stable monodisperse sol, while still valid, can be accounted for by the solution depletion mechanism described above (5.4.5) and additionally by the purification via the cationic exchange properties of surrounding clays as proposed by Deniskina *et al.* (1981) mentioned earlier (3.2.8).

5.4.8. Cationic valence

The effectiveness of the adsorbed cations toward coagulation is highly dependent on valence of the ion, since the surface potential is lowered while the double layer thickness is also reduced (Adamson 1990). The concentration of cations required for the rapid coagulation of a weakly charged colloid is inversely proportional to the sixth exponent of the ion charge (Churaev 1999):

$$C \propto \frac{1}{z^6}$$

Equation 5-1: Relationship between the ionic charge and the critical concentration of electrolyte required for rapid coagulation.

This is known as the Schulze-Hardy rule (Adamson 1990; Shaw 1992; Hiemenz and Rajagopalan 1997; Myers 1999). From Equation 5-1, the following table may be calculated:

Ion charge	Order of effectiveness of specified ion in causing coagulation of colloid
Monovalent ions	1
Divalent ions	64
Trivalent ions	729
Tetravalent ions	4,096
Heptavalent ions	15,625
Hexavalent ions	46,656

Table 5-7: Order of effectiveness of ion charge in coagulating colloidal suspensions, calculated by using Equation 5-1.

Since the coagulation of the spheres is so highly dependent on the charge on the adsorbed cations, the highly-charged ions (Ti^{4+}) of relatively low concentration contained within the opals may not be so quickly disregarded.

5.4.8.1. Ion-specific ability to control coagulation

Equation 5-1 shows that highly-charged ions at concentrations of 100 ppm (Ti^{4+}) or even 10 ppm may be just as effective as the monovalent and divalent ions (Na^{+} ~1000 ppm, K^{+} ~1000 ppm and Ca^{2+} ~2000 ppm) in coagulating the silica colloids. For example, with sample LR1, the concentration of Al is 900 ppm greater in the translucent brown section than in the transparent section, while the concentration of Ti is 430 ppm greater in the translucent brown section than in the transparent section. At first glance, it may appear as though Al is probably the ion that governed the coagulation of the darker band. However, the following deductions may be calculated from Table 5-7: if the concentration of trivalent ions (Al^{3+}) required for coagulation is an extra 900 ppm in the dark layer, then the concentration of tetravalent ions (Ti^{4+}) having the same coagulating ability is only 160 ppm. As the concentration of Ti in the dark band is in fact 430 ppm higher than in the clear band, it may be seen that Ti is the overriding coagulant for this opal sample. The other samples may also be considered in this manner: with sample LR7, the low concentration of the elements Y and Ce appear to be much more effective in controlling the coagulation of the grey band than the elements K and Al. In this respect, the elements Ti,

Y and Ce appear to be the "potential determining ions" for these samples, while Al and K appear to be the "indifferent ions" (Hunter 2001).

5.4.8.2. Critical coagulant concentration

The critical coagulant concentration (c.c.c.) is defined as the specific concentration of coagulant required to initiate rapid coagulation of all the colloids in a sol. If the concentration of coagulant is below the c.c.c., slow coagulation takes place. A coagulant with a concentration greater than the c.c.c. will sediment all the colloids within the sol, leaving just a clear supernatant liquid. Below the c.c.c. a coagulant will still rapidly sediment a number of colloids, but an uncoagulated colloidal dispersion will remain above this layer (Hiemenz and Rajagopalan 1997; Hunter 2001).

5.4.8.3. Hofmeister series

Ions of a given type or valency possess an order of effectiveness for the coagulation of a sol, called the Hofmeister (or 'lyotropic') series (Popiel 1978; Hunter 2001). For example, the coagulating ability of each cation in the following list decreases towards right:

$$Cs^+ > Rb^+ > NH_4^+ > K^+ > Na^+ > Li^+ > Ba^{2+} > Sr^{2+} > Ca^{2+} > Mg^{2+}$$

Assuming the number of adsorbed cations required at the c.c.c. can be as low as 1 per 100Å^2 for silica colloids (Iler 1979), a simple calculation can be undertaken to determine the concentration of cations required to cause coagulation within an opal layer. Given the diameter of colloids is 200nm, and the density of opal-AG is 2.1 g/cm^3, the number of cations required for coagulation is ~125,000 per colloid. Presuming for the sake of simplicity opal is composed of 100% SiO_2, this figure represents a c.c.c. concentration of ~910 ppm. Not surprisingly, this is roughly the same concentration as the difference in the total concentration of cations between light and dark bands within the opal samples, as determined by LA-ICPMS (Table 5-2).

5.4.9. Counter-ions

Since Al atoms have a similar ionic radius to silicon atoms, they have the ability to substitute for silicon atoms within the silica framework.

However, Al has a positive charge of three, and silicon has a positive charge of four, hence additional cations must be present within close proximity to balance the net charges to zero (neutral) (Smith and Steele 1984).

In some instances, the concentration of Al is roughly 10% higher in the darker bands than in the lighter ones. The results also indicate that for the same samples, the darker bands generally contain higher levels of K than the lighter bands, whereas other monovalent and divalent cations, such as Na, Mg and Ca tend to have a similar distribution between bands.

5.4.9.1. Preferential accommodation of specific cations

Whilst the Al is being incorporated into the silica molecular structure from the sol, certain counter-ions that are still in solution adsorb onto the surfaces of the growing spheres. Obviously, the counter-ions with the highest charge and least solubility (Mg^{2+}) will be attracted first, followed by the other ions (Ca^{2+} and Na^{+}). The most soluble ion (in this case it is K^{+}, as the only other monovalent ions that were analysed were Li^{+} and Na^{+}) would thus tend not to be incorporated until last, additionally because it has a relatively large ionic radius and will not be as easily accommodated into the silica network. It is interesting to note that Webb and Finlayson (1987) have previously shown a direct link between minor element composition (Mg) in opal speleothems and silanol content in opal-A.

The difference in K concentration in the samples mentioned earlier may be attributed to this fact. The counter-ions Ca^{2+}, Mg^{2+} and Na^{+} are probably all delegated to the charge balancing of the substituting Al ions in the first opal band. If the concentration of Al happens to be greater in a dark band than a light band, it is the K^{+} which is likely neutralising the additional Al ion charge imbalances. This conclusion can be drawn from the following results. Sample LR7, for example, contains approximately 3370 ppm more Al in the grey band than in the poc band; K is also 2010 ppm higher in the grey band than in the poc band. For the banded samples LR13, A1, CP1, and CP2 which contain similar Al levels between bands, the K also remains relatively unchanged. However, each alkali ion must also first remove the hydration layer before incorporation into the structure. The various ions possess different enthalpies of hydration, the order of difficulty

in removing water molecules is Ca^{2+} > Li^{+} > Na^{+} > K^{+} > Rb^{+} > Cs^{+}, therefore K^{+} might be more suitable than Ca^{2+} for inclusion into sites where the size of the ion is not a constraint (gel networks, not dense coagulates).

5.4.10. Monodisperse colloid growth

According to the theory, Ostwald ripening gives rise to the growth of spherical particles with uniform diameters. The degree of monodispersity of the spheres is a time dependent process as it involves dissolution and re-precipitation; the final size of the spheres is dependent mainly on the temperature of the sol, provided the solution maintains a low level of cation impurities to prevent coagulation (Iler 1979). This suggests that spheres contained in precious opal bands, with large monodisperse spheres (poc) merely took longer to form than those whose spheres are not uniform in size (potch). This deduction matches the earlier results and hypothesis of banded opal formation, which in the case of sample A1 shows that the samples with ordered or disordered spheres may not necessarily be influenced by elemental composition (Table 5-2).

5.4.11. Microbial model of opal genesis

Although bacterial action during sol formation could possibly have take place, it is certainly not one of the requirements or constraints of sol formation; indeed, a silica sol containing colloidal spheres will arise from a saturated silica solution spontaneously (Iler 1979).

The data presented here shows that the concentration of both Al and Fe are practically identical between various layers of the opal nobbies investigated. However, SIMS does show an altered Fe content between bands (Figure 6-17). This casts a shadow of a doubt over part of the model proposed by Behr *et al.* (2000), as they predicted that the amount of Al and iron in the bottom bands of opal nobbies would be greater than the top bands. Nevertheless, the existence of biological action during the formation of opal cannot be ignored, and at the very least, it could be a source of origin for the high valency cation impurities. In this case, solution depletion, charge neutralisation, and all other mechanisms discussed here still remain applicable.

5.5. CONCLUSIONS

The most significant differences in the elemental composition of opal bands within an opal sample were observed in the transition metal and rare-earth elements. The following elements in particular were notable for having consistently higher concentrations in the black or grey coloured bands than the white or clear bands: Ti, Co, V, Ni, Cu, Zn, Y, La and Ce.

Although the alkali and alkaline-earth elements were in most cases much more abundant than the transition metals, they generally did not show the same magnitude of difference between various bands in the banded samples.

The chemical analysis data of banded opals allowed a hypothesis to be suggested for the process of colloidal formation of banded opals, involving charge neutralisation and solution depletion mechanisms. Due to the Schulze-Hardy rule, highly charged transition metal ions (Ti^{4+}) may in fact influence the deposition of a potch opal band more so than other elements with lower charge but a higher concentration (eg Al^{3+}). In order for the Ostwald ripening mechanism to reach maturation and produce a monodispersed colloid, a low concentration of highly charged metal ions in solution is required. Since there is insufficient time for Ostwald ripening during this stage, these rapidly deposited spheres are unable to form close-packed arrangements, therefore a dark potch opal band is initially formed.

Depending on the time available for the settling of the remaining silica colloids, they may be poly- or mono-disperse; this controls whether the adjacent layer is able to form ordered arrays of spheres that result in the formation of precious opal. The colour of this subsequent opal band is generally white or clear, as it is deficient in the transition metal ions that are able to cause colour in silicate glasses.

As the elemental composition of transparent and translucent bands within the same sample was often similar, this finding suggested that the degree of opacity of an opal might instead be due to a higher level of internal voids, which have the effect of scattering the incident light.

6. SECONDARY ION MASS SPECTROMETRY

"Chaos is a name for any order that produces confusion in our minds."
–George Santayana, Philosopher

6.1. INTRODUCTION

According to published SEM studies on opal (Jones *et al.* 1964; Cole and Monroe 1967; Rau and Amaral 1969; Segnit *et al.* 1970; Sanders 1985), the fundamental difference between precious opal and potch lies in their arrangement of silica spheres. One intriguing fact regarding the distribution of opal-A is that the random packing of spheres commonly seen in potch is more prevalent than ordered packing of precious opal; this contradicts the research quoted below, which states that ordered arrangements of spheres generally arise spontaneously (6.1.1). Clearly, a reason exists for the greater frequency of potch opal deposition. It is well known that polydisperse spheres will not form close-packed structures, but the size distribution alone is unlikely to be the only factor in determining the ordering of sphere sequences within opal. This is because opal is often observed to contain relatively monodisperse spheres that are not close-packed. Curiously, ordered stacking arrangements (FCC, HCP and simple cubic) are commonly seen immediately adjacent to randomly packed spheres in opal, in some cases, these regions and domains are separated by only the scale of the sphere's dimensions (100 to 350nm) (Figure 6-1; Cole and Monroe 1967).

6.1.1. Theoretical simulations of ordered and disordered sphere packing

Several computer simulation studies involving theoretical sphere sedimentation and packing have been previously carried out (Visscher and Bolsterlie 1972; Rintoul and Torquato 1996; Woodcock 1997; Torquato *et al.* 2000; Bezrukov *et al.* 2001). Although it was shown that ordering of monodisperse spheres generally arises within domains spontaneously in these systems, the various researchers found contradicting results: depending on the model used, either simple cubic or HCP stacking resulted. It has also been shown (Torquato *et al.* 2000) that random packing of spheres ($\rho_{RCP} \approx 0.64$) yields a lower density than ordered sphere packing ($\rho_{FCC} = 0.74$), normally however, nature tends towards the highest obtainable density structures.

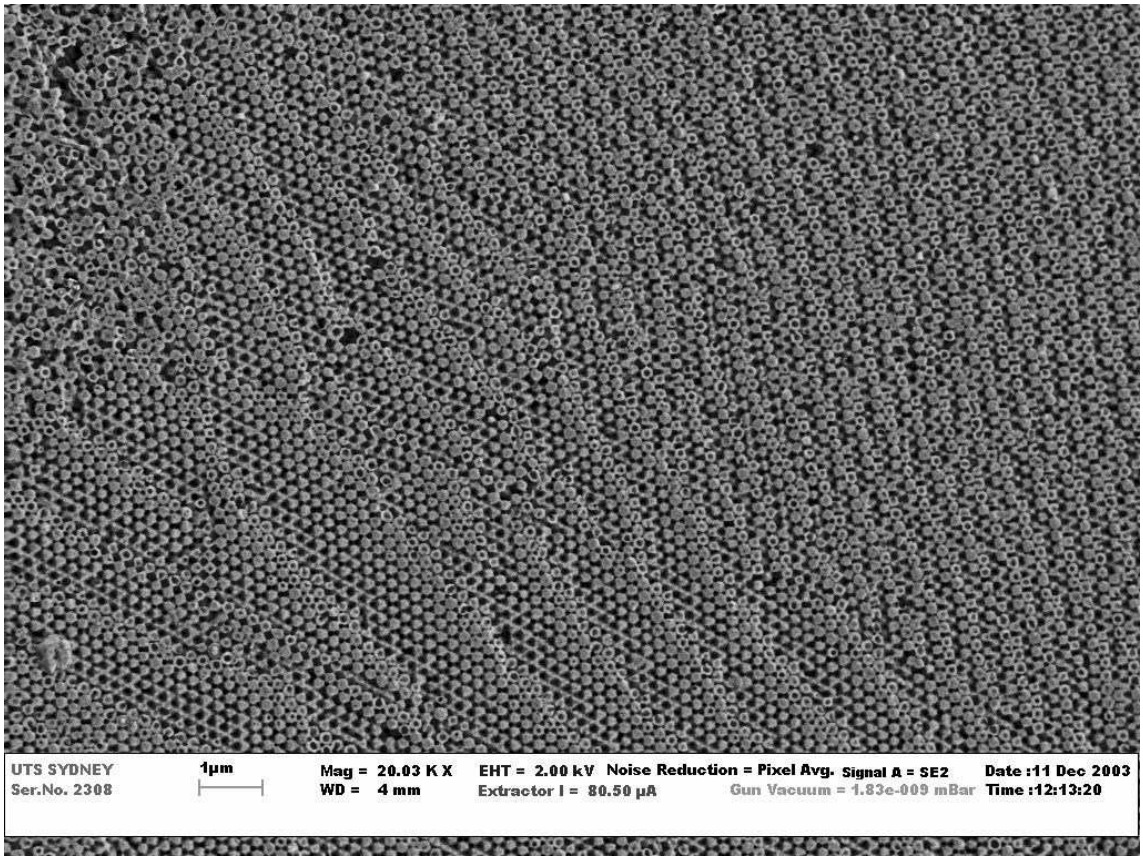

Figure 6-1: SEM micrograph showing a region of close-packed ordered stacking sequence in the centre and a disordered stacking sequence in the top left. Three ordered domains can clearly be seen in the figure; a large one at the centre; another one at the right; and a smaller domain at the bottom left. A secondary electron detector was used for imaging.

6.1.2. Order-disorder phase transitions

Vosel and Kalinin (1999) have demonstrated with their thermodynamic model of colloidal coagulation that packing of spheres into ordered arrays requires long range forces in the liquid state. The spheres may be 'fixed' at regular distances apart, which correspond to the potential energy minima of the interacting spheres. These minima only occur at specific ranges of pH and salt concentration (Figure 6-2). At these distances the spheres are sterically bound, as the repulsive forces between interacting spheres increase at all other distances of separation (apart from spheres in direct contact, when they experience the greatest forces of attraction). Thus, the spheres are attracted -not to each other- but to specific points or positions in the sol. As the effective volume per particle, v_f, is lowered, (for example,

by evaporation of the water) the sedimentation and solidification of the colloids may then lead to the formation of an ordered array.

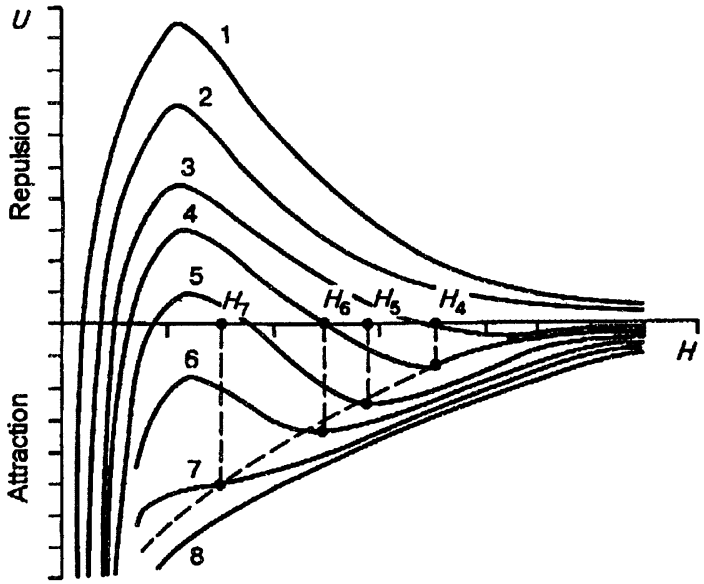

Figure 6-2: Changes of potential energy curves for interaction between two monodisperse silica spheres with increasing concentration of salts of bi- and trivalent cations in the system (from curve 1 to curve 8). From Kalinin et al. (1998).

The following two equations determine the forces acting on monodisperse particles with radius, *r*:

$$U_a = -\frac{Ar}{12H}$$

Equation 6-1: Attraction energy

where U_a is the energy of attraction of two particles, H is the distance between particles, and A is the Hamaker constant of molecular attractive forces.

$$U_0 = -\frac{\varepsilon \psi^2 r}{2} e^{-\kappa H}$$

Equation 6-2: Repulsion energy

where U_0 is the repulsion energy for weakly charged particles, where ε is the dielectric permeability of the medium, ψ is the potential of particle surfaces and κ is the Debye parameter (Vosel and Kalinin 1999). The Debye parameter κ in the exponent of Equation 6-2 is directly proportional to the charges (Z) and concentrations (n) of foreign ions that may also be present in the sol, as seen in the following equation:

$$\kappa^2 = \frac{8\pi(Ze)^2 n}{\varepsilon kT}$$

Equation 6-3: From Serdobintseva et al. (1999).

6.1.2.1. Implications for opal formation

Figure 6-2 shows that a gradual supply of bi- and tri-valent cations into a stable silica sol thus decreases the potential repulsion barrier. Simultaneously, a second potential energy minimum begins to form at a distance from the repulsion zone (Vosel and Kalinin 1999). As can be seen from the potential energy curves in Figure 6-2, there are several salt concentration ranges at which potential energy minima exist (curves 4 to 6, where the potential energy minima occur at separation distances of H_4 to H_6, respectively). In order to form an ordered array of spheres in contact with each other, the salt concentration must obviously be lowered to reduce the metastable separation distance (whilst maintaining the minimum attraction force).

The free energy, F, of an N-particle system can be defined by:

Equation 6-4:

$$F = -NkT \ln \frac{v_f \sigma}{L(T)} + N\frac{\mu}{2'}$$

where k is the Boltzmann constant, T is the temperature, $L(T)$ is a function of temperature, and μ is the average potential energy within the unit cell. The parameter σ is an indicator of the entropy of the system

(discussed below). The parameter v_f is the free, or effective, volume per particle[1].

Equation 6-4 is valid for both ordered and disordered phases. For crystals (ordered phases), σ = 1; for rarefied gases, σ = e (2.718…); and for liquids, σ has intermediate values. The value of σ is close to e for most concentrations of the solution, and changes drastically and approaches the value of 1 for high concentrations as a close-packed phase is formed (Vosel and Kalinin 1999). This equation assumes that the colloidal particles are monodisperse and have homogeneous internal structures. In reality, colloidal suspensions are not completely monodisperse, but this has little effect on the formation of thermodynamically stable regular structures (i.e. they still form).

Vosel and Kalinin *(*1999) showed that for ordered phases, particles with a low potential energy are only possible if they form from highly concentrated suspensions - they cannot form from diluted suspensions. Hence, for suspensions of fine silica, gel formation occurs instead of the expected ordering and coagulation processes (Vosel and Kalinin 1999).

6.1.3. Intrusion of larger or smaller spheres

6.1.3.1. Theoretical

Duran and Jullien (1998) reported that when larger spheres (greater than a certain size) were included in computer-simulated packings of monodisperse spheres, they invariably disrupted the ordered arrays of spheres.

6.1.3.2. Experimental

Cheng *et al.* (1999) noted that individual spheres of irregular size in artificially synthesised opal led to defects and dislocations of the ordered sphere arrays. For example, it was observed that larger spheres tended to force the array into a new alignment over a long distance. Furthermore, Cheng *et al.* (1999) also noted that if the concentration of the suspension

[1] The limiting volume is determined by the condition u(r) – u(0) ≈ kT, where u(r) is the energy of interaction of a specified particle with all other particles of the system (r is the distance from the centre of the unit cell).

was too large, the opal material did not exhibit any crystal-like characteristics.

6.1.3.3. Trickle Stratification

In a system of loosely deposited spheres, there is tendency for the finest spheres or particles to filter through the rest of the larger spheres, eventually stopping at the bottom of the system if there is sufficient time. As mentioned above, considerably larger or smaller spheres than the majority may affect the local ordering of spheres. Interstitial primary particles (spheres 20 to 50 nm in diameter) are very seldom seen in SEM micrographs in the literature. Thus, trickle stratification most likely occurs, although to a limited extent, as the effect of Ostwald ripening tends to produce monodisperse sols.

6.1.3.4. Terminal Velocity

The terminal velocity reached by a small spherical particle descending in a viscous fluid can be defined by Equation 6-5, which is based on Stoke's law (Hiemenz and Rajagopalan 1997). It can be shown the size of a descending sphere determines its terminal velocity; the larger spheres fall faster and therefore would occur at bottom of the system, while the successively smaller ones would deposit on top, leaving a gradual transition from large to small. This has been observed for some precious opal specimens: a red poc (diameter of spheres ≈ 300 nm) is seen on one side of the opal and a blue/violet poc (diameter of spheres ≈ 160 nm) on the other (Darragh *et al.* 1966).

$$v_s = \frac{2}{9}\frac{r^2 g(\rho_p - \rho_f)}{\eta}$$

Equation 6-5: For particles falling in a viscous fluid under their own weight, the frictional force can be equated to the gravitational force. v_s= particle's settling velocity; r = particle radius; g = force of gravity; η = viscosity; ρ_p and ρ_f are the density of the particles and fluid, respectively.

6.1.4. Other observations

Greer (1969) proposed that the ordering of the spheres in opals might have arisen through a spiral growth mechanism, as SEM showed evidence of a screw dislocation amongst the spheres. However, this was observed in a disordered sphere structure.

6.1.5. Synthetic opal

Several studies have examined the formation of synthetic opal (Darragh and Perdrix 1975, 1977; Schmetzer 1984; Davis *et al.* 1989; Philipse 1989). Although the opal-formation process may be approximated by using synthetic monodisperse silica spheres, the structure only approximates opal-AG. Columnar grains are often observed in synthetic opal (Jobbins *et al.* 1976), whereas these vertically elongated grains are not observed in natural opal-AG, probably a direct result of the higher rates of sedimentation in synthetic samples. Also, the water in synthetic opals is exclusively internal silanol groups, i.e. no molecular water is present (Graetsch and Ibel 1997).

6.1.5.1. Separation into visibly different bands

Iler (1965) was able to artificially produce synthetic opal in several test tubes, from the unassisted sedimentation of silica sols with a colloid diameter of 100nm. Intermediate opal layers showed the typical spectral colours denoting monodisperse spheres with well-ordered packing. These intermediate poc layers always occurred above a dense, white opaque opal layer, and below a more dilute opalescent sol. Poc layers were formed at all pH values tested (3 to 10), although the formation of poc layers occurred fastest in samples with a pH of between 5 and 7 (in three months as opposed to 2 years). The intensity of the poc layers were reduced substantially when these opals were dried out. It was reported that the 'pseudocrystals' were extremely fragile and easily disappeared with the slightest movements of the containers. Likewise, when attempts were made to speed up the process, by either increasing the evaporation rate or by centrifuging the sols, these processes disturbed the colloids too easily. Iler (1965) concluded that sufficient time was a necessary condition for spheres to attain perfectly ordered packing.

Davis *et al.* (1989), noted that synthetic silica colloidal suspensions separated into visibly different bands (clear, opaque and poc layers) under the influence of gravity; these layers were attributed to different packing densities (different concentrations of the sol) at different heights in the test tube. The sedimented layer at the bottom was within the packing density range of $0.60 < \rho < 0.68$, and order-disorder transitions were also observed between $0.53 < \rho < 0.60$.

Pusey *et al.* (1989) reported similar findings with polymeric colloids; a glass transition occurred at $\rho \approx 0.58$, at which point a long-lived amorphous phase was formed. At volume fractions between $0.494 < \rho < 0.545$, colloids crystallised spontaneously when left undisturbed.

Separate experiments with monodisperse colloidal silica in cyclohexane were undertaken by Davis *et al.* (1989). The average diameter of the colloids were 200, 310, 340 and 430 nm (std. dev. of less than 6% in each case). For the 200, 310 and 340 nm colloids, order-disorder transitions spontaneously arose when the colloids were left to settle; this was most obvious with the 310 and 340 nm colloids. Davis *et al.* (1989) reported that the 430 nm colloids only produced amorphous sediments; this was attributed to a sedimentation rate that was too high to form ordered regions.

6.1.6. Liesegang phenomenon

It has been known for some time that when anions diffuse through a gel medium containing cations, sparingly soluble reactants may precipitate in an intermittent sequence of parallel layers, yielding patterns known as Liesegang bands (Stern 1954; Büki *et al.* 1995; Sultan 2002). Extensive research has been carried out since the discovery of this rhythmic precipitation phenomenon, and one mechanism for the Liesegang effect includes the diffusion of the reactant ions into the dispersed reactant phase, and ion-complex formation behind this moving boundary. However this is still debated and thus far, no single theory of periodic precipitation is able to account for all the observed features, possibly because of the variety and complexity of the observed phenomena (George and Varghese 2002).

The concentration profile of the elements responsible for precipitation is seen to decrease exponentially within each clear layer (Figure 6-3). Mathematical expressions can be written for the concentration of electrolytes and precipitates at various distances and times (Vaidyan *et al.* 1981).

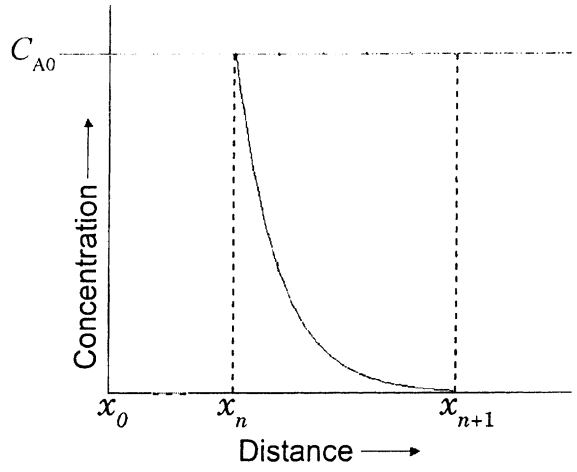

Figure 6-3: Concentration profile of the electrolyte vs. distance. C_{AO} is the initial concentration of the electrolyte.

The time that each band precipitates may be given by $x_n^2 \approx t_n$, where x_n is the position of the *n*th band measured from the interface of the reagents and t_n is the time of its formation. The width of each band has been observed to increase with n and obey a simple linear relation $w_n \approx x_n$ (George and Varghese 2002). Furthermore, the position of each band theoretically obeys the progression of a geometric series, which can be written as:

$$P = \frac{X_{i+1}}{X_i}$$

Equation 6-6: Jablczinsky's spacing law; P equals the spacing coefficient, i is the number of each band. From Büki et al. (1995).

6.1.7. Chemical composition of banded opal

Although a few studies have reported on the trace element composition of common and precious opals (Bayliss and Males 1965, McOrist *et al.* 1994, McOrist and Smallwood 1995, and McOrist and Smallwood 1997), none has presented data on banded opals, despite a fairly common occurrence throughout the major Australian mining regions. In fact there has been almost no mention of this banding phenomenon in the literature.

6.1.7.1. Chemical composition of banded LDG

Frischat *et al.* (2001) have analysed banded Libyan Desert Glass (LDG) with a microprobe analysis, but unfortunately the researchers did not give details of the experimental conditions, but merely stated instead that the sample contained 'compositional inhomogeneities' and referred to flow like patterns in the sample. The level of Al altered by more than a factor of two throughout the linescan. The concentration of Ti was also shown to be somewhat irregular throughout the sample, while the concentration of Fe and Si appeared to remain unaltered across the linescan shown.

6.1.8. Objectives

The study of banded opals presents a special opportunity to learn more about the manner of opal formation. Banded opal samples may contain both potch and poc bands of different colours (such as black grey, white or clear) and these bands are commonly found adjacent to one another (3.2.11). It is imperative to understand what causes this black colouration, which is so valuable to the gem industry, and what conditions might exist for its formation next to other layers, such as a layer displaying a poc.

Every opal specimen mined is unique, although there appear to be several categories to which the opals belong. Banded opals may either have extremely distinct and well-defined boundaries (Figure 6-4; Sample LR3) or they may have more vague, ill-defined boundaries. In some cases, the latter types of opals may show inter-mixing of the two bands during what appears to be the fluid state (Figure 6-5; Sample LR1). With samples of that type, wisps of coloured opal from one section appear to have flowed into

the other. In other cases, the boundary appears to be relatively wide; essentially a steady transition from one band to the other.

Banded opals are often composed of adjacent potch and precious opal layers. If the initial conditions required for the packing of silica spheres in both layers are better understood, this would help to distinguish what causes regions of ordered and disordered packing to arise simultaneously. Thus, it is important to identify the chemical conditions which could account for the formation of these layers.

Figure 6-4: Sample LR3; exhibiting the extremely well-defined interface between the grey and black regions.

Figure 6-5: Detail of interfacial region of Sample LR1. Note the fluid-like appearance of the interfacial region between the two bands.

The presently accepted model of opal-AG genesis (Darragh *et al.* 1966; Williams and Crerar 1985), the sedimentation of colloidal spheres from a silica sol, is a process that is only valid for homogeneous samples. It is currently rather limited and cannot adequately explain how banded samples develop. Furthermore, monodisperse spheres displaying random packing are occasionally seen in white potch and precious opal samples; the process of charge neutralisation (5.4.4) cannot easily explain this observation, as the polyvalent cation impurities are generally low in white potch.

The chemical composition of the aqueous phase is known to strongly influence the nature of inter-particle forces and therefore may determine whether spheres will form ordered or disordered packing sequences (6.1.2; Kalinin *et al.* 1998). By definition, precious opal contains ordered arrays of monodisperse spheres, while potch shows a random packing of spheres. In the special case of banded opals, layers of both precious opal and potch are occasionally found adjacent to one another. In this chapter it is hypothesised that the chemical composition of adjacent precious and potch

opal bands is a function of the distance (perpendicular to the interface) between these two bands. If this proves to be correct, analysing the various bands contained in banded opals may yield a mechanism for layered opal formation, one that applies not only to banded opal but specimens of opal-AG in general.

Hence, to better understand the occurrence and mode of formation of banded opals, the elemental profile through the boundary must be investigated. Thus the aim of this chapter is to carry out an elemental analysis of banded opals to compare the trace element composition of the various bands, and hence determine whether any differences might indicate the processes involved in the formation of different bands.

If an assorted collection of opals from different geological locations are analysed, a somewhat variable trace element composition is to be expected. The investigation of banded samples allows the difference in the chemical composition of various bands to be studied. In so doing, the variance in chemical composition normally associated with differently coloured potch opals of diverse origins can be negated. Hence, inferences about the formation of each band can be made with respect to the chemical composition of the precursor sol.

6.2. EXPERIMENTAL

6.2.1. Secondary Ion Mass Spectrometry (SIMS)

SIMS allows the well-defined interface of these types of opals to be examined critically, since it has a superior spatial resolution than comparable elemental analysis methods, such as Laser Ablation Inductively Coupled Plasma Mass Spectrometry (LA-ICPMS). SIMS can probe areas less than 20-25μm in diameter compared with approximately 70μm for LA-ICPMS. In addition, the elemental detection limit of SIMS is generally superior to most other microanalysis methods. SIMS is ideal for analysing samples that contain micro-scale variations in their trace element composition. Accordingly, SIMS was used to probe numerous spots within each area of the various opal bands, and several line-scans were also completed across the interfaces. SIMS analyses were undertaken at the Environment Division, a division within the Australian Nuclear Science and Technology Organisation (ANSTO). This research was funded by several successful grants obtained through the Australian Institute of Nuclear Science and Engineering (AINSE), which were awarded by the UTS in 2000, 2001 and 2003.

6.2.1.1. SIMS operational principles

SIMS functions by focussing a beam of primary ions onto a sample. This is achieved by accelerating ions from a source, which are then collimated through a series of electrostatic lenses, deflectors and apertures. When the ions in this beam impact the sample, 'secondary ions' are sputtered off the sample. These ions are collected, sent to an electrostatic analyser to be monoenergised, and detected using a mass-spectrometer (Benninghoven *et al.* 1987). This information is then processed by a computer. Equation 6-7 shows the linear relationship between the concentration of an element and the secondary ion current it generates when sputtered from the sample.

Equation 6-7:

$$I_S = I_P Y^n c T \eta$$

where I_S is the secondary beam current; I_P is the primary beam current; Y is the sputtering yield of an element in charged state n; T is the transmission coefficient; and η is the detector efficiency.

As shown by Equation 6-7, ions of different valency do not produce secondary ion currents of the same proportions, so the signal intensity of one element cannot be directly compared with other elements without standardisation.

6.2.2. Instrumental parameters

For this study, a Cameca IMS 5f SIMS was used with an oxygen ion (O^-) beam operating at (12.52±0.07)kV with a 60kV offset. Two detectors were used to provide a wide range of signal intensities to be detected. These were the electron multiplier and the Faraday cup. The background signal intensity of the electron multiplier was in the region of $1.00x10^{-1}$ counts per second (c/s), and between 10,000 and 300,000 c/s for the Faraday cup, depending on the analysis. The threshold for the transition from electron multiplier to the Faraday cup took place at signal intensities of between 600,000 or 800,000 c/s (depending on the analysis), while the threshold for the crossover from the Faraday cup back to the electron multiplier was 1,100,000 c/s. Electron multiplier dead time was 25ns, while the electron multiplier efficiency was between 70 and 100%.

6.2.2.1. Individual spot analyses

The beam was focused to a spot with a diameter between 20 and 25µm and the samples were pre-sputtered until the gold signal approached background level. For the individual spot analyses, the beam current was approximately 5nA for all analyses.

Within each band of the samples LR1, LR2, LR3 and LR4, at least two (but in most cases three) spots were analysed and the values then averaged (see below). For the individual spot analyses, the following isotopes were included in the analyses: ^{23}Na, ^{24}Mg, ^{27}Al, ^{30}Si, ^{39}K ^{40}Ca, ^{48}Ti, ^{51}V, ^{52}Cr, ^{55}Mn, ^{56}Fe, ^{58}Ni, ^{59}Co, ^{63}Cu, ^{64}Zn, ^{85}Rb, ^{88}Sr, ^{90}Zr and ^{138}Ba. The

isotopes were analysed in groups of ten and scanned on a rotational basis, with an acquisition time of 1 second for each element. The total acquisition time of all the isotopes in each set was at least 400 seconds. Sample LR2 was subsequently re-analysed with the additional isotopes ^{89}Y, ^{140}Ce and ^{208}Pb, in exchange for the isotopes ^{39}K and ^{85}Rb from the previous list, as ^{39}K and ^{85}Rb were not observed to vary in the sample.

6.2.2.2. Linescans

To further investigate the relative abundance of the elements between the bands and across the boundary, several line-scans were also performed. A total of eight line-scans were completed on the samples LR2, LR5, LR6, and LR7 with the following list of isotopes being analysed: ^{23}Na, ^{30}Si, ^{48}Ti, ^{51}V, ^{52}Cr, ^{58}Ni, ^{59}Co, ^{63}Cu, ^{64}Zn and ^{89}Y. These specific elements were chosen as their distribution was known to vary for banded Lightning Ridge opals (5.3.3). Four line-scans were completed on sample LR5; two were carried out on LR7; one linescan was also done on each of samples LR2 and LR6. Two samples in particular (LR5 and LR7) were selected for the majority of these experiments because they exhibited a very abrupt and discernible interface. Moreover, the bands of samples LR5 and LR7 were expected to be easily distinguishable from each other with SIMS since they were already known to contain considerable variation in the abundance of certain elements from the previous LA-ICPMS analyses (Table 5-2). The numbers of spots analysed for each of the line-scans were between eight and eighteen. The step distance between each of the spots was between 70 and 80μm, depending on the sample being analysed. The pre-sputter time for every spot was set at a constant 90 seconds. The acquisition time was 5 seconds for the elements Na, Si and Ti, and 20 seconds for the remainder of the elements (V, Cr, Ni, Co, Cu, Zn and Y). Beam current was in the region of 2.5 to 3nA.

A total of seventeen line-scans were also completed on the samples CP2, A2, LR15 and LRT3 with the following list of isotopes being analysed: ^{23}Na, ^{24}Mg, ^{28}Si, ^{39}K, ^{40}Ca, ^{47}Ti, ^{48}Ti, ^{54}Fe, ^{56}Fe, ^{90}Zr and ^{138}Ba. Seven line-scans were completed on sample A2; four were carried out on sample LRT3; three on sample LR15; and two on sample CP2.

The step distance between each of the spots for these samples was in most cases 50µm. The pre-sputter time for every spot was set at a constant 90 seconds. The acquisition time was 1 second for the elements Si; 5 seconds for the elements Mg, Na, K, Ca and Fe; and 10 seconds for the remainder of the elements (Ti, Zr and Ba). Beam current was in the region of 3.0 to 5.0nA for these samples.

6.2.3. Sample details

Nine samples were investigated from the Australian Lightning Ridge area, one from Coober Pedy, and one from Andamooka; all except three are classified as "potch" opal (i.e. lacking a play of colour). The samples selected for the analysis were only those that exhibited two or more base colours (colourless, grey or black) in the form of different layers or "bands" of colour within each sample. The regions of colour within each band were quite homogeneous in appearance, while a distinct interface existed between the layers. A summary of the coloured layers in each sample can be found in Table 5-1, while photographs of most samples are shown in Figures 5-1, 5-2 and 5-3.

6.2.3.1. Sample LR1

Sample LR1 was an opal "nobbie" about 20mm in diameter. The centre was divided into two colour layers, one was almost colourless (a very pale yellow colour) and transparent, the other layer was a translucent dark brown (almost black) layer.

6.2.3.2. Samples LR2 and LR3

Sample LR2 originated from a much larger piece of opal approximately 100mm long and had an exceptionally opaque, jet black centre. Surrounding the outer edge of the opal was an opaque light grey coloured rim with a very even depth that traced the contours of the host rock. Sample LR3 was similar to LR2, because it also originated from the same, large opal piece as LR2. However, sample LR2 possessed a grey colour that was not part of the peripheral grey edge, but instead had a larger bulk grey section; in this case it resembled a colour band and not a zone around the edge of the opal.

6.2.3.3. Sample LR4

Sample LR4 was also a spherical nobbie, which had an opaque dark grey centre surrounded by a lighter grey translucent band. This outer band was not entirely of the same opacity; it was more translucent on one side (top) and became more opaque on the other side (bottom). The sample was cut in a rectangular shape so that the middle was the opaque dark grey centre; one end was translucent grey (top), the other end being the translucent grey (bottom).

6.2.3.4. Sample LR5 and LR6

Sample LR5 displayed two very well defined bands; an opaque grey band and a transparent "honey" coloured band. Sample LR6 possessed three bands; an opaque brown centre layer with an opaque grey on one side and a transparent "honey" colour on the other adjacent side.

6.2.3.5. Sample LR7

Sample LR7 was a precious opal of gem quality. It was originally cut and polished into a cabochon shape and has subsequently and spontaneously crazed. It was predominantly an opaque grey colour with an adjoining layer of opaque white precious opal, which displayed a red play of colour.

6.2.3.6. Sample LR15

Sample LR15 was a precious gem-quality opal. It had an opaque grey band and a poc band that displayed a red colour. The interfacial region of this sample was very abrupt and flat.

6.2.3.7. Sample A2

This is an exceptional sample; it was predominantly opaque grey in colour, but it also contained numerous thin colourless transparent bands mostly in a parallel arrangement throughout the whole opal.

6.2.3.8. Sample LRT3

Sample LRT3 contained very narrow blue poc bands throughout a mostly grey/black-coloured sample; these 'veins' were less than a millimetre in width.

6.2.3.9. CP2

This sample consisted of opaque grey and green bands. The green band appeared to contain several undulating striations.

6.2.4. Experimental procedure

6.2.4.1. Sample Preparation

The rough opals were first broken into smaller and more manageable pieces. The few portions that revealed two or more colour regions within the one opal piece were chosen for analysis. To obtain a flat surface suitable for analysis, the opals were either initially cut with a diamond-impregnated copper wafering blade, or were abraded with coarser grades (320 grit) of SiC paper. The sample surfaces to be analysed were prepared by grinding on a wheel with SiC papers down to P#1200. The samples were then polished with 6µm, then 1µm, and finally ¼ µm diamond paste using Leco lapping oil. They were washed with detergent, ultrasonically cleaned in ethanol and rinsed with acetone between each of the final polishing stages in order to remove any traces of Leco lapping oil. Finally, they were gold coated just prior to the analysis in the SIMS to increase the electrical conductivity, hence reducing the amount of charge build-up while sputtering during the analyses.

6.2.4.2. Normalisation of signal intensity data

With SIMS, the signal intensity of the secondary ions is proportional not only on the concentration of that particular species in the sample, but it is also dependent on the sputtering ability of the sample. This, in turn, is dependent on the surface geometry of the sample, among other factors[1]. One of the reasons for polishing the samples is to reduce these errors. Nevertheless, even the signal strength of the secondary Si ions is seen to vary from one spot to another by as much as a factor of two or three in some instances, even though the sample mostly consists of ~90% silica[2]

[1] Secondary ion generation is a complex process involving interaction of the primary beam with the sample. Some contributing factors include: the type of primary ion beam used; the sample's material structure; sample heterogeneity or homogeneity; primary beam impact energy and angle of impact; electrostatic charging effects on insulators; and the selected ion to be analysed (Benninghoven *et al.* 1987).

[2] The remaining 10% consists of approximately 8% water as determined by thermal analysis, and ~2% trace elements.

and is known to be fairly consistent for all samples. To account for this, the results from each spot analysis were normalised to ^{29}Si. Si was chosen for this procedure, as the proportion of SiO_2 in all samples is approximately constant at 98% on an anhydrous basis, regardless of the trace element composition.

6.2.4.3. Standardisation

The results of the spot analyses of all the samples were normalised with each other, so that all of the samples yielded the same signal intensity of Si as the dark brown translucent band of sample LR1. Si was chosen for this procedure as it is assumed to be fairly constant at 90%. All of the other elements were adjusted by the corresponding amounts. As none of the SIMS signal intensities were quantified in terms of elemental concentration, this normalisation process is to account for the slight drift or variance of some of the SIMS instrument parameters with time so that results obtained at different times could be directly compared.

6.2.4.4. Positioning the linescans

Scratches were marked on the surface of the gold coating with a scalpel at the location where the beginning of the line-scan was required, since it was not possible to observe the interface of the sample once inside the SIMS, due to the gold coating. Afterwards, the samples were examined under a light-microscope to confirm that the line-scan had indeed included the analysis of the interface. The line-scans were normalised to ^{29}Si and to the first analysis spot of each set, so that all of the signals from the first spot had a value equal to 1.00, and the value of the other spots were adjusted by the same amount. This was done so that the relative change of the elements across the boundary could be easily determined.

6.2.5. Errors

The most probable source of errors with these experiments were random spikes in the signal intensity, which were occasionally observed with the SIMS detector. For the separate spot analyses, the elements were scanned on a rotational basis for 1 second each, the entire scan totalling over 400 seconds. Once the data points for each element are plotted against time, any spikes in the data become noticeable amongst the rest of

the data and can be removed. However, with the line-scans, each of the elements is only scanned once, for either 5 or 20 seconds, before physically moving to the next spot. Consequently, with the line-scans, it is difficult to determine if the spikes are caused by instrumental factors, or if they are due instead to heterogeneities in the sample. The only way to know with certainty is to repeat the linescans; if the sample is heterogeneous, this will be revealed in subsequent linescans.

Another source of errors involves the possibility of more than one secondary ion combining following the sputtering from the sample, and these multiple-ions (mass interferences) hitting the detector(s) with an increased mass thereby falsifying the results. For this reason, where possible isotopes have been chosen to minimise the chances of interferences from other such events. In addition, to minimise the effects of mass interferences, all SIMS analyses were collected with an energy offset of -60V. This energy offset slightly reduces the possibility of measuring molecular species, which are the major cause of mass interferences. Even so, the likelihood of some mass interferences in the data remains. Hence, for the linescans of samples A2 and LRT3, two elemental isotopes were chosen, such as ^{47}Ti, ^{48}Ti, ^{54}Fe, ^{56}Fe, ^{137}Ba and ^{138}Ba to authenticate the results.

6.3. RESULTS - INDIVIDUAL SPOT ANALYSES

As relatively few samples were analysed with SIMS, the results for this chapter will be described according to each sample, and the behaviour of each element (or groups of elements) for each sample will be then be discussed separately.

6.3.1.1. Calculation of average signal intensity values

Figure 6-6 shows an example of the spot analyses carried out on sample LR1, for the element Ca. This graph shows that the signal intensity of the curves rises in the initial stages, and then settles down to a fairly constant value; this is due to the gold coating being sputtered off and the ion beam subsequently settling down to a relatively constant sputtering rate. Hence, the first parts of these curves were disregarded, and the averages of the last 25 values of these curves were calculated. The standard deviations over this range were also calculated. If the data contained obvious spikes (i.e. c/s = 0), those values were not included in the calculation of average signal intensities. The results collected in this manner are shown in Table 6-1. The standard deviation (1σ) of each element for each spot analysis is shown in Table 6-2. The ratio of the signal intensity of each element between dark and light bands is listed in Table 6-3.

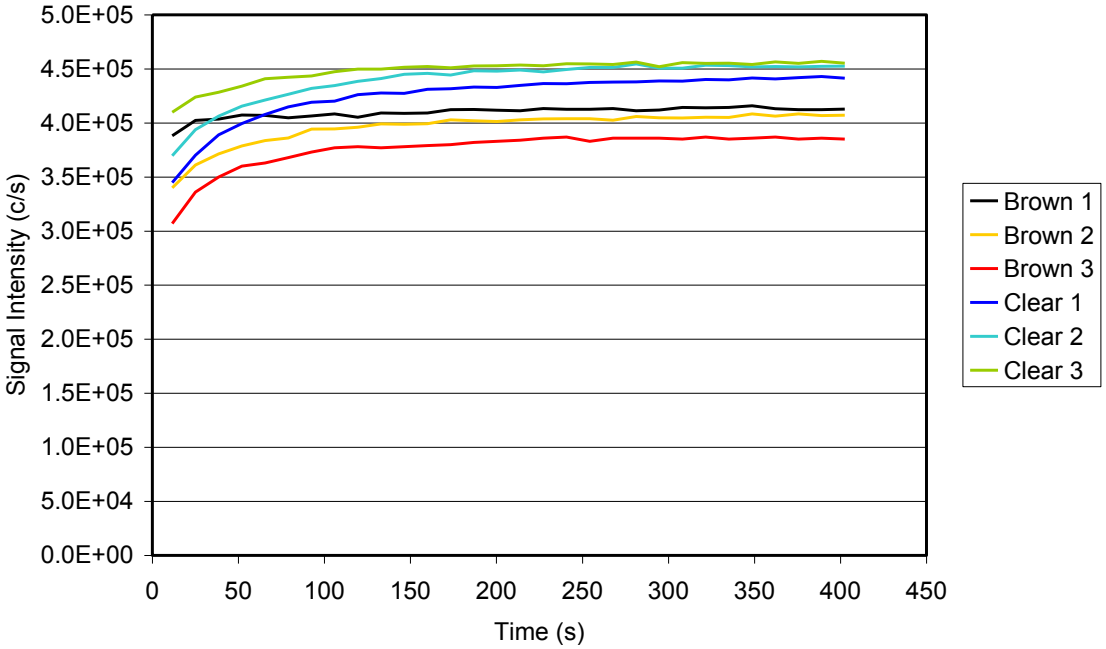

Figure 6-6: Depth profile for the element Ca contained within sample LR1.

Element	LR1 Brown	LR1 Clear	LR2 Black	LR2 Grey	LR3 Black	LR3 Grey	LR4 Dk. Grey	LR4 Lt. Grey
Na	1.18E+05	1.16E+05	9.27E+05	1.03E+06	1.33E+06	1.98E+06	1.62E+05	5.16E+05
Mg	5.58E+04	5.47E+04	2.12E+05	2.09E+05	8.37E+04	7.99E+04	9.16E+04	9.90E+04
Al	2.22E+06	2.10E+06	1.12E+07	1.12E+07	4.20E+06	3.65E+06	3.42E+06	4.18E+06
Si	1.42E+06	1.42E+06	1.42E+06	1.42E+06	1.42E+06	1.42E+06	1.42E+06	1.42E+06
K	1.32E+05	1.03E+05	1.84E+06	1.24E+06	1.73E+06	1.13E+06	8.26E+05	1.29E+06
Ca	4.67E+05	4.48E+05	1.76E+06	1.61E+06	8.03E+05	8.21E+05	7.91E+05	9.52E+05
Ti	5.57E+04	2.35E+03	3.86E+05	4.35E+05	1.27E+05	7.99E+04	7.61E+03	1.03E+04
Fe	7.49E+04	6.99E+04	4.11E+05	4.70E+05	1.77E+05	1.50E+05	1.63E+05	1.83E+05
Ba	3.38E+03	2.98E+03	9.79E+03	9.71E+03	1.10E+04	8.53E+03	8.86E+03	1.04E+04
V	4.66E+02	5.51E+01	5.46E+03	7.32E+03	2.04E+03	1.84E+03	1.49E+02	3.04E+02
Cr	1.44E+02	7.53E+01	6.36E+02	7.97E+02	5.32E+02	5.95E+02	1.53E+02	1.70E+02
Mn	2.27E+03	1.75E+03	5.84E+03	4.71E+03	5.72E+03	4.43E+03	5.03E+03	6.15E+03
Ni	3.75E+03	2.95E+03	4.69E+03	3.91E+03	4.37E+03	3.49E+03	3.08E+03	3.53E+03
Co	4.97E+02	1.64E+02	2.83E+03	1.14E+03	2.91E+03	9.31E+02	4.15E+02	5.06E+02
Cu	6.85E+02	2.73E+01	1.21E+04	6.30E+03	7.01E+03	3.59E+03	3.51E+02	4.42E+02
Zn	3.60E+03	1.40E+02	2.03E+04	2.24E+04	3.75E+04	2.30E+04	1.85E+03	2.69E+03
Rb	3.65E+02	2.84E+02	3.51E+03	2.63E+03	2.82E+03	1.66E+03	1.99E+03	2.67E+03
Sr	5.45E+03	4.08E+03	5.30E+04	4.60E+04	4.24E+04	4.65E+04	2.78E+04	3.62E+04
Zr	2.39E+03	1.41E+03	1.94E+04	2.01E+04	6.59E+03	5.98E+03	3.09E+03	3.94E+03
Sc	-	-	3.05E+05	2.75E+05	-	-	-	-

Table 6-1: Signal intensities for each of the elements for samples LR1, LR2, LR3 and LR4.

Element	LR1 Brown	LR1 Clear	LR2 Black	LR2 Grey	LR3 Black	LR3 Grey	LR4 Dk. Grey	LR4 Lt. Grey
Na	1.3	2.1	2.6	7.3	1.2	1.2	3.1	1.7
Mg	0.64	0.58	0.62	1.1	1.9	1.9	1.2	1.6
Al	0.97	0.85	1.1	0.8	1.5	0.84	0.89	0.95
Si	1.2	1	1.3	0.57	0.94	1	0.93	0.85
K	1.7	3.1	5.8	1.6	0.94	1.4	1.6	2.2
Ca	1.1	1.4	0.73	2.7	2.4	2	1.6	2.2
Ti	6.9	20	5.2	4.6	4.4	4.6	9.4	11
Fe	0.79	0.73	1.5	4.2	1.9	1.9	1.3	1.5
Ba	2.4	2.5	9.3	4.5	3	2.7	2.2	3.1
V	7.9	18	4.6	3.6	4.4	3.2	11	8.1
Cr	34	14	7.8	5	8.8	9.7	18	8.2
Mn	2.5	3	2	1.6	2.4	1.6	1.9	1.6
Ni	2.6	2.1	1.7	0.95	3.4	1.9	2.2	2.1
Co	15	11	6.9	2.7	7	5.2	8	6.2
Cu	17	39	11	5.5	5.6	4.4	19	15
Zn	7.6	22	8.1	6	5.3	5.2	18	22
Rb	5.4	7	4.1	1.9	2.9	2.7	2.6	2.3
Sr	2.6	1.6	2.5	1.7	2.2	1.3	1.5	1.5
Zr	5.2	3.5	3.8	3.5	3.5	2.1	2.8	2.9
Sc	-	-	6.1	3.2	-	-	-	-

Table 6-2: Standard deviation (%) of signal intensity for each of the elements.

Element	LR1 Brown/Clear	LR2 Black/Grey	LR3 Black/Grey	LR4 Dk. Grey/Lt. Grey
Na	1.02	0.90	0.67	0.31
Mg	1.02	1.01	1.05	0.93
Al	1.06	1.00	1.15	0.82
Si	1.00	1.00	1.00	1.00
K	1.28	1.48	1.52	0.64
Ca	1.04	1.09	0.98	0.83
Ti	23.7	0.89	1.59	0.74
Fe	1.07	0.87	1.18	0.89
Ba	1.13	1.01	1.29	0.85
V	8.45	0.75	1.11	0.49
Cr	1.92	0.80	0.89	0.90
Mn	1.30	1.24	1.29	0.82
Ni	1.27	1.20	1.25	0.87
Co	3.03	2.50	3.13	0.82
Cu	25.1	1.92	1.95	0.80
Zn	25.6	0.91	1.63	0.69
Rb	1.29	1.34	1.70	0.74
Sr	1.34	1.15	0.91	0.77
Zr	1.69	0.97	1.10	0.79
Sc	-	1.11	-	-

Table 6-3: Ratio of signal intensity between dark and light bands for each of the elements.

6.3.1.2. Uniformity of depth profile signal intensity

One trend that has emerged is that certain elements (Na, Ca, Mg, K, Al and Fe) appear to be have a constant signal intensity in all the depth profiles, while the signal intensity of other elements (Ti, Cr, Cu, Zn, Co and Zr) is much more erratic (Figure 6-7; Figure 6-8; Figure 6-9).

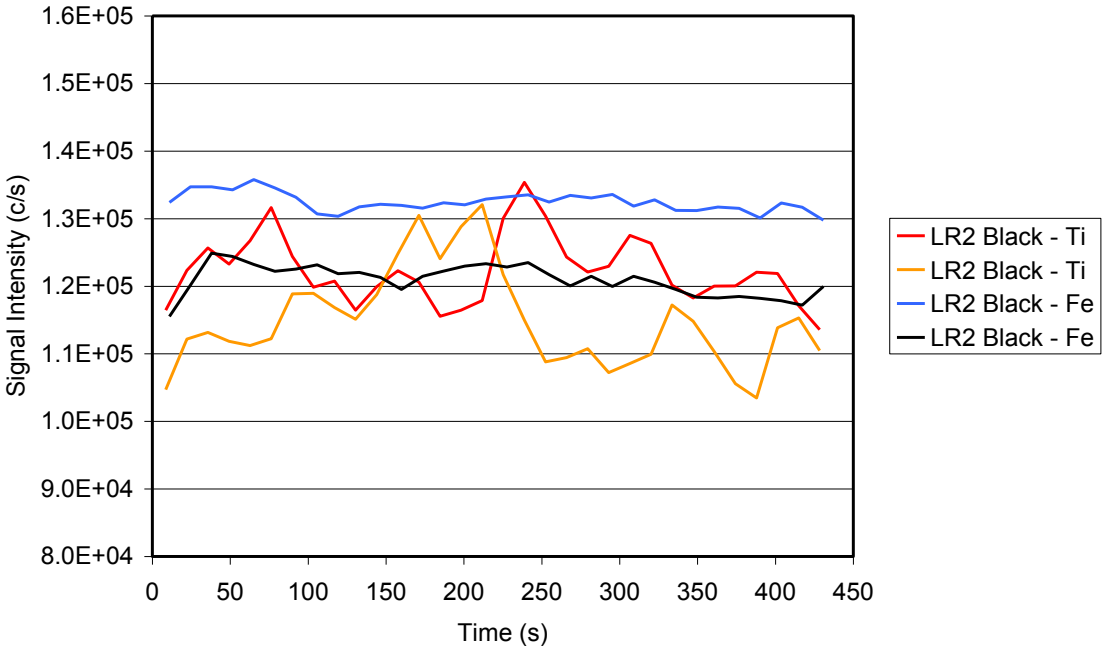

Figure 6-7: Depth profile for the elements Ti and Fe contained within the black band of sample LR2.

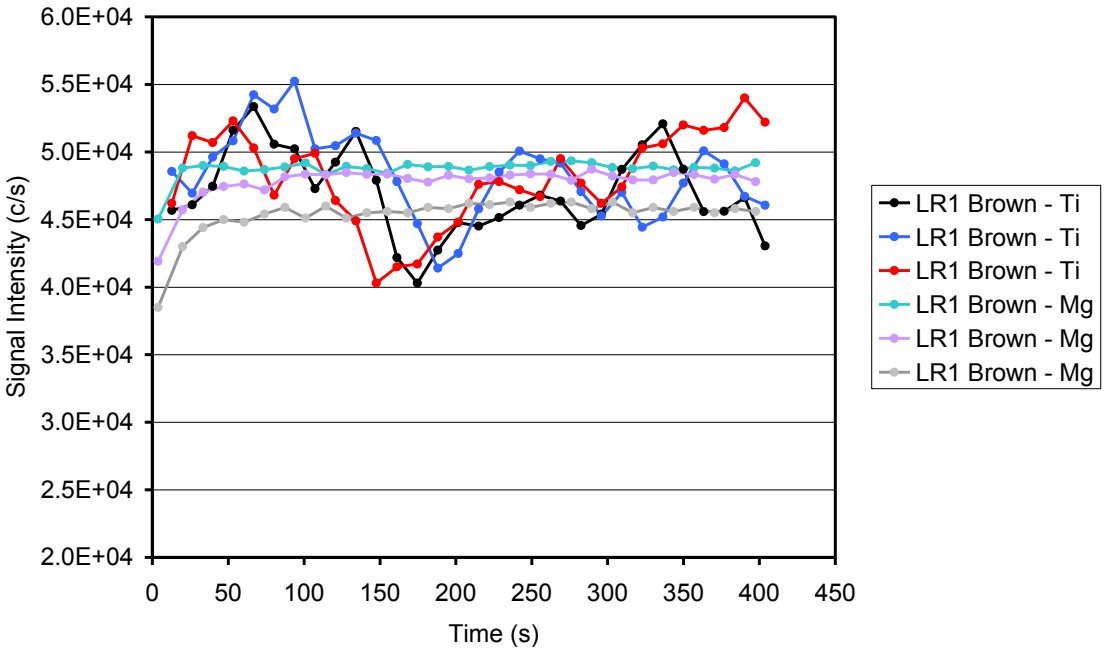

Figure 6-8: Depth profile for the elements Ti and Mg contained within brown band of sample LR1.

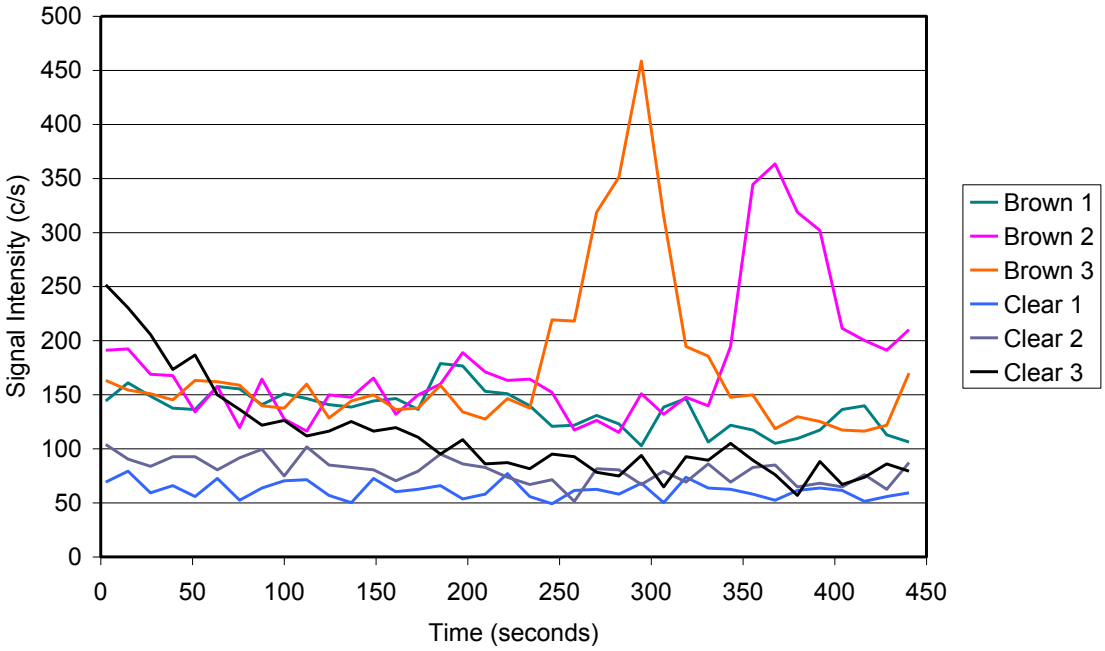

Figure 6-9: Depth profile for the element Cr contained within sample LR1.

6.3.2. LR1

For over half of the elements investigated (Na, K, Mg, Ca, Al, Mn, Fe, Ni, Rb, Sr and Ba) the differences in signal intensities (in c/s) between various layers were negligible. However, the intensities of Ti, Cu and Zn in the brown section were at least an order of magnitude greater than those in the transparent section (Table 6-1; Table 6-3; Figure 6-10). In addition, the elements V, Cr and Co were also significantly higher for the brown section than for the clear section, although to a lesser extent than Ti, Cu and Zn. SIMS also detected a slight variation in Zr concentration between the translucent brown and transparent sections, although this was less notable than some of the other elements. The remainder of elements investigated were all similar in proportion (I.e. close to a 1:1 ratio) between black and clear sections.

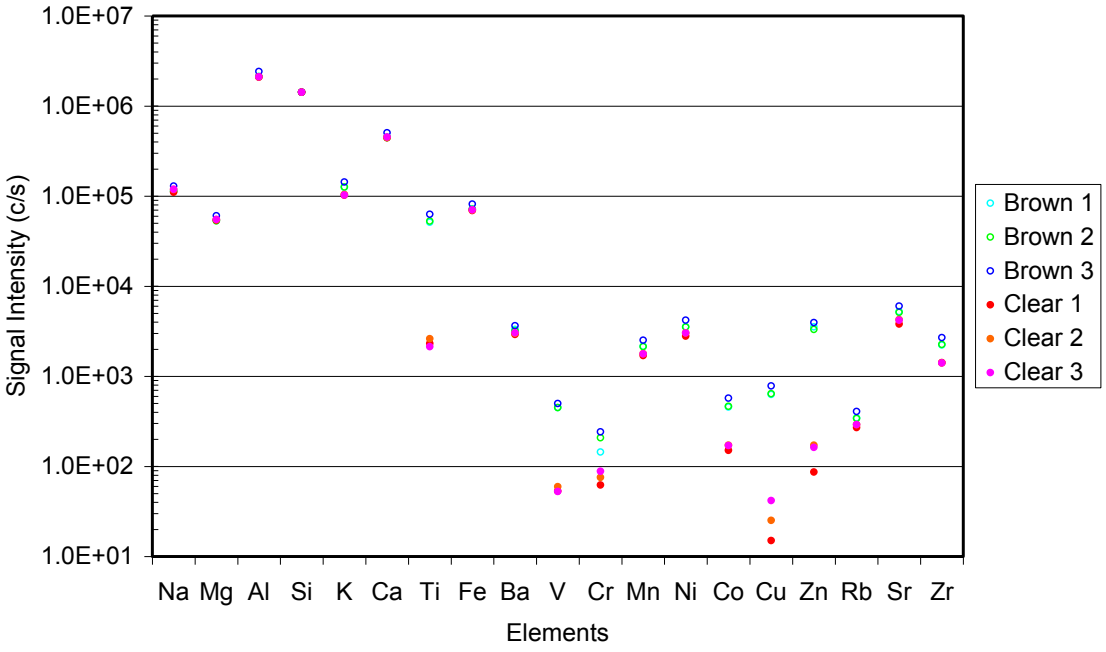

Figure 6-10: Graphical representation of the abundance of elements at each spot in sample LR1.

6.3.3. LR2

The only discernible differences in trace element concentration between black and grey regions of this sample are those of Cu and Co; the level of Co was 250% higher in the black region than the grey region, while Cu was almost 200% higher in the darker section (Table 6-3). There were no other major differences in the intensities of the elements between light grey and dark grey portions of the opal.

6.3.4. LR3

Like sample LR2, Cu and Co were the only elements that showed a major difference between the light grey and black areas of this opal for the elements analysed; the Co intensity was 300% higher, and the Cu was twice as high in the black section than in the grey coloured section (Table 6-3; Figure 6-11). In this respect, the results concerning the Co and Cu concentrations of this sample are consistent with the results of the LR2 sample, both samples having originated from the same large opal nobbie. Other elements such as Ti and perhaps Zn showed a slightly higher abundance in the black band of this opal (~60% higher) than in the grey band. K was also 50% higher in the black band. The signal intensities from the other elements were consistently higher in the black part than those of the light grey part, with few exceptions, suggesting that the abundance of all of these trace elements is slightly higher in the black portion. Interestingly, the Na level was actually 50% higher in the lighter grey region of the sample than in the black region.

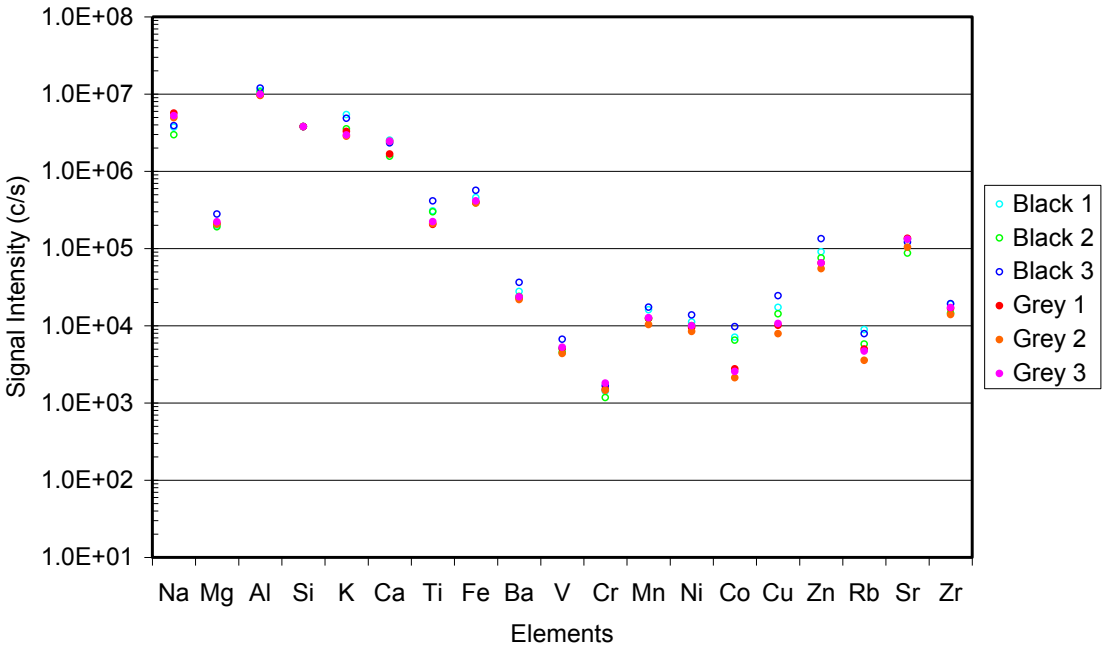

Figure 6-11: Graphical representation of the abundance of elements at each spot in sample LR3.

6.3.5. LR4

It seems much more difficult to determine the trends in the trace element concentration between colour bands of this sample, because the difference in the various bands is not as distinct as the other samples. In most cases, there appears to be too much variance in the results associated with the lighter grey outer band to be able to reliably compare the difference between the light grey ring and the dark grey centre. However, one worthwhile result is that the Na concentration of this sample is over 300% higher in the lighter grey band than the dark grey band (Table 6-3).

6.4. RESULTS - LINESCANS

The number of duplicate linescans completed on each sample depended on the results obtained at the time. In some cases, there was insufficient time for a second linescan. The minimisation of down-time[1] was also an important concern, hence the reason there are a disproportionate number of linescans completed on the various samples.

6.4.1. Sample LR5

Three separate line-scans of sample LR5 can be seen in Figures 6-12 and 6-13. In general, there was a definitive, sharp transition from the high concentration of certain transition elements (Ti, V, Cu, Zn and Y) in a dark region to the lower concentration of these same elements in the lighter region. The level of Co also varied across the interface, but the magnitude of this difference was not as great as with the elements Ti, V, Cu, Zn and Y. The level of Ni was constant across the two bands.

[1] Period of time where data was not accumulated. I.e. when the sample was being changed over.

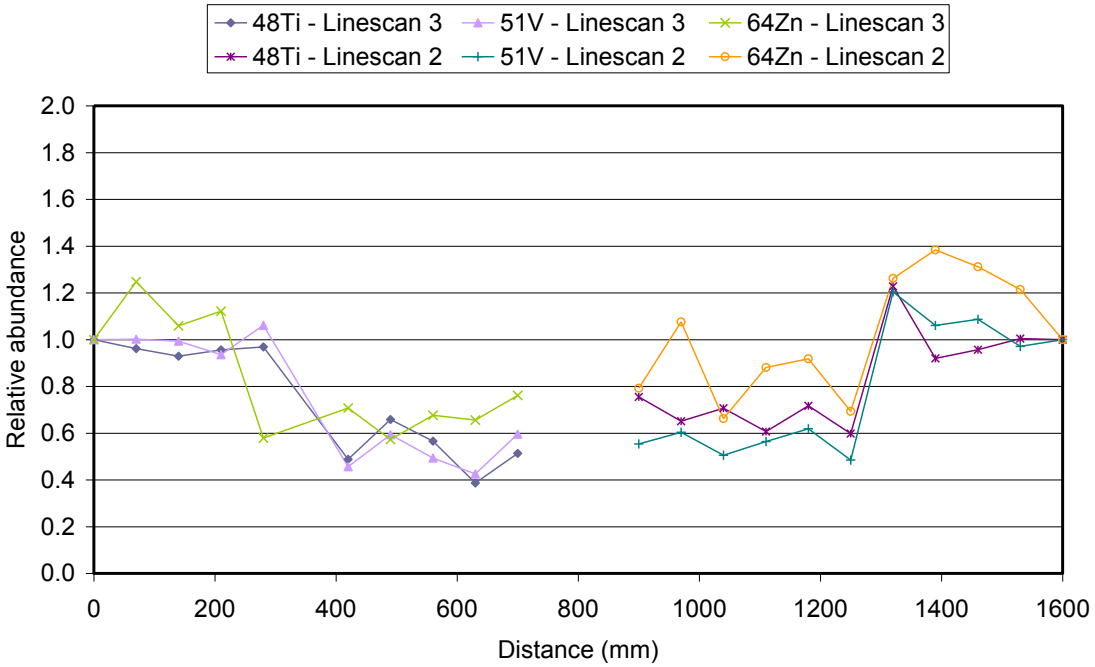

Figure 6-12: Sample LR5; Linescans 2 and 3. The linescans have been superimposed onto one graph. The honey-coloured band is in the middle of the graph, and the grey band is effectively on the left and right of the x-axis.

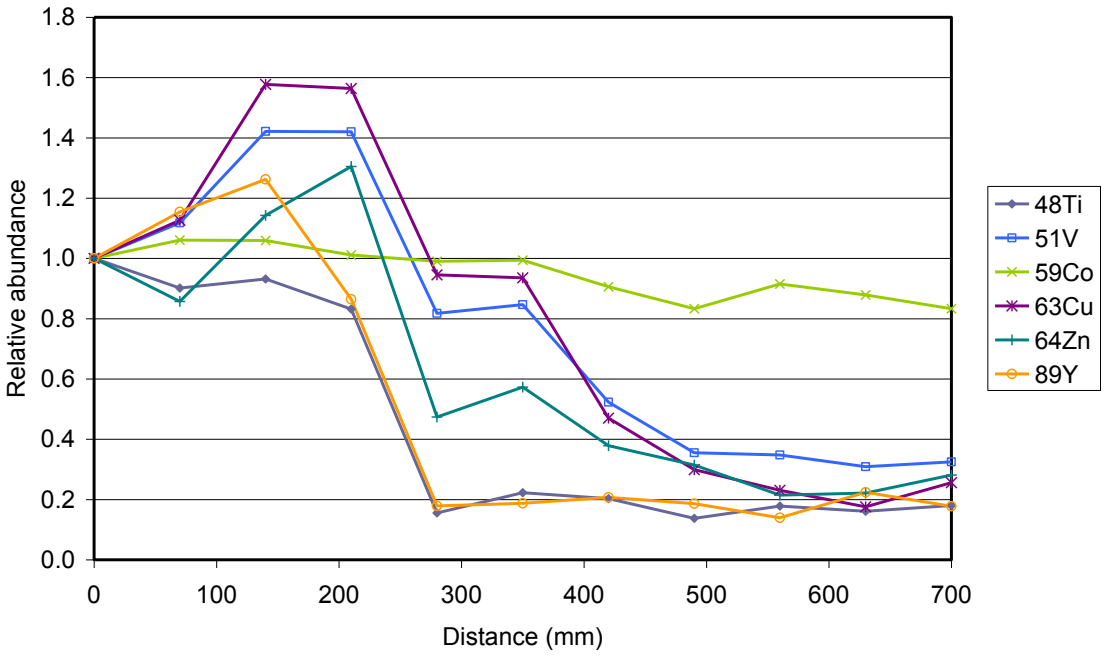

Figure 6-13: Sample LR5; Linescan 4. The grey band is on the left, and the honey band is on the right.

6.4.2. Sample LR6

The central part of this linescan, corresponding to the brown band, appears to contain a higher concentration of the elements Cr, Co, and V than the other regions, which were the grey and clear bands. However, the results concerning this sample were not conclusive. Presumably, this is because the linescan went through all three bands, and it was difficult to distinguish one band from another, as there were not enough spots analysed in each of the separate bands.

6.4.3. Sample LR7

One of the two line-scans completed on sample LR7 can be seen in Figure 6-14. Like sample LR5, a sharp and definitive transition of certain transition elements (Ti, V, Co, Cu and Zn) was unmistakably observed, going from a high concentration in the grey band to a significantly lower concentration (~400% less) in the poc band. This transition occurred within a distance of only 80μm. Ni showed a noticeable albeit much less pronounced variation between layers, being 10% less in the poc band than in the grey band. A definite trend for the element Cr could not be identified, but this might have been caused by spikes in the data. Na was ~50% higher in the grey band than in the poc band, and also appeared to have a more gradual transition across the interface, occurring over a distance of greater than 320μm.

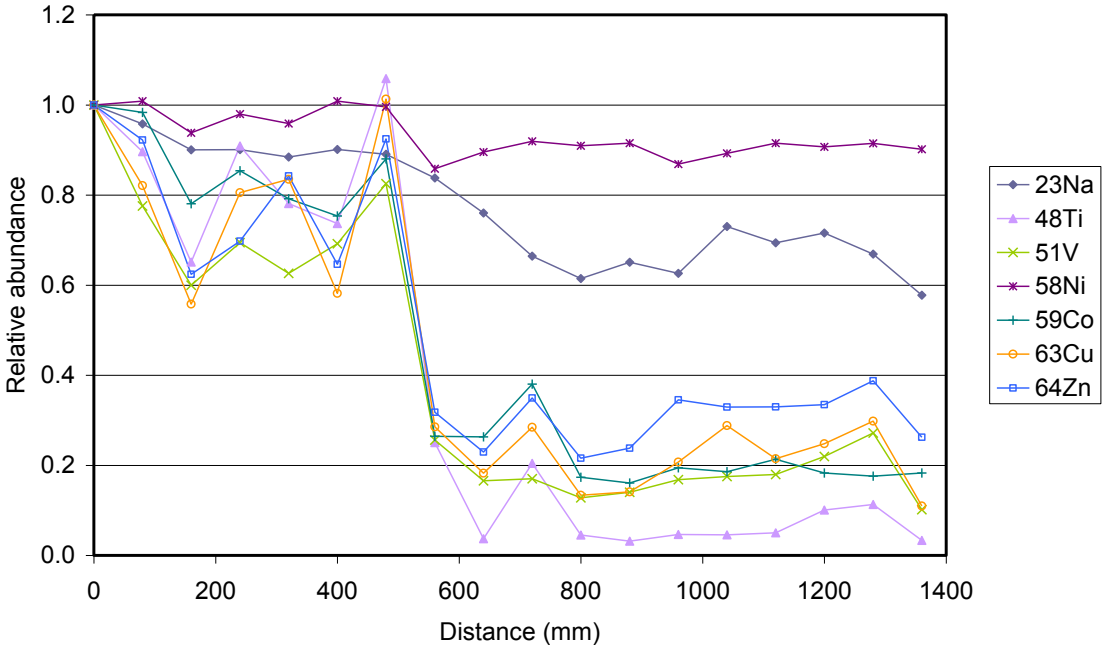

Figure 6-14: Sample LR7; Linescan 2. The grey band is on the left, and the poc band is on the right.

6.4.4. Sample LRT3

Two linescans of sample LRT3 are shown on the same graph in Figure 6-15. The concentration of elements such as Ti, Mg, and ^{54}Fe changed abruptly through the clear band over distances of as little as 50µm. In particular, the abundance of ^{48}Ti changed by a factor of more than seven between the two bands within a distance of only 50µm. The space over which this abrupt change occurs represents approximately 250 colloidal spheres of diameter 200nm. Since the step size of the linescan was 50µm, and the concentration of certain transition metals varied significantly either side of one of these intervals, the interfacial boundary may occur over even smaller distances than this.

The concentration of the elements Na and Mg also changed through the clear band, although the transition was not quite so abrupt, taking place over approximately 200µm. Elements such as K, Ba, Zr and ^{56}Fe, however, appeared to have a more gradual transition across the transparent band (middle), taking place over approximately 400µm.

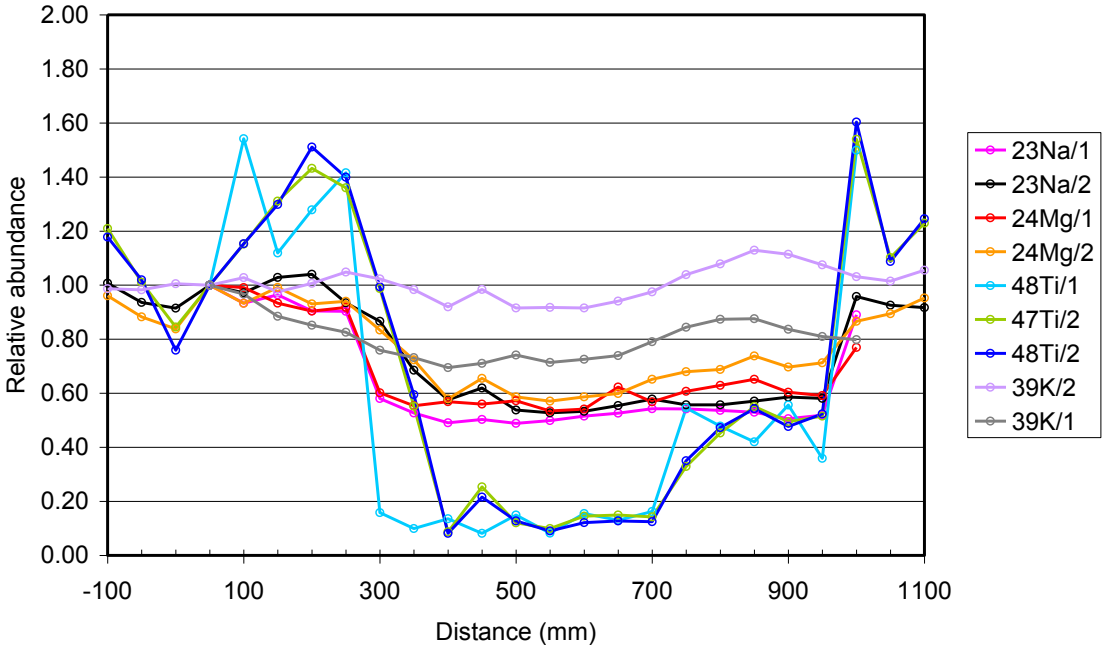

Figure 6-15: Sample LRT3; Linescans 1 and 2. The poc band is in the centre, and darker bands are on the left and right.

6.4.5. Sample A2

The results of two linescans on sample A2 are graphed in Figures 6-16 and 6-17. The concentration of Ti in the clear band is about half of that compared to the two outer grey bands. Fe is about two-thirds the concentration in the clear band than in the grey bands. The elements K and Na tended to steadily increase in concentration into the darker band, even well beyond the visible position of the boundary. This distance is approximately 600µm from the boundary. This is in contrast to the elements Ba and Fe, which plateaued after the boundary region was reached.

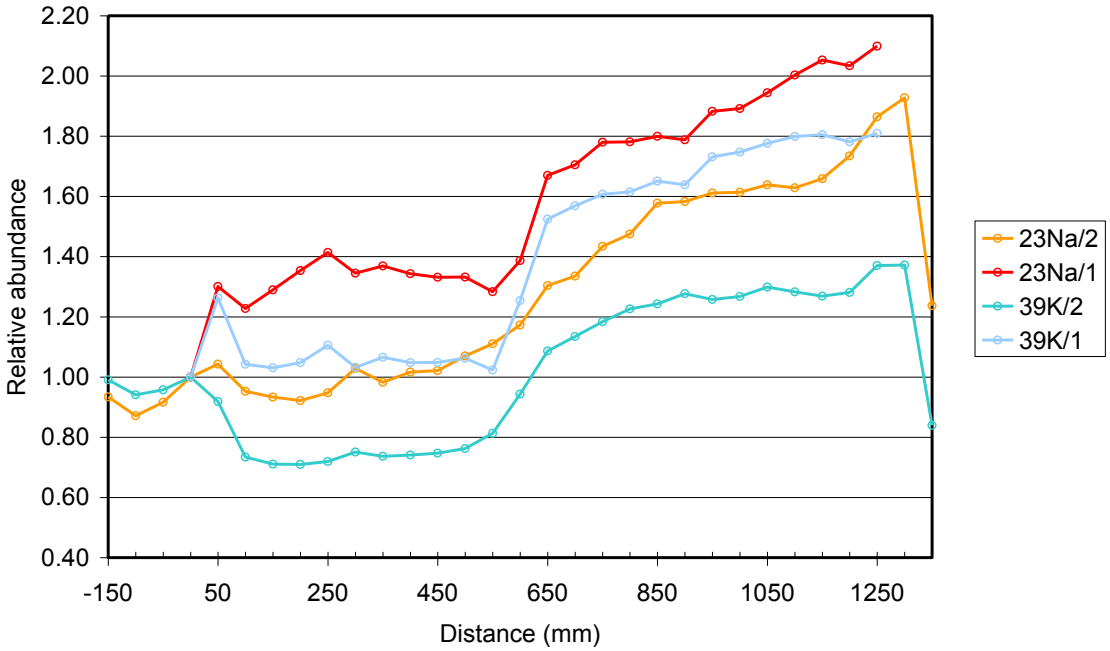

Figure 6-16: Sample A2; Linescans 1 and 2, for elements Na and K. The clear band is in the centre, and grey bands are on the left and right.

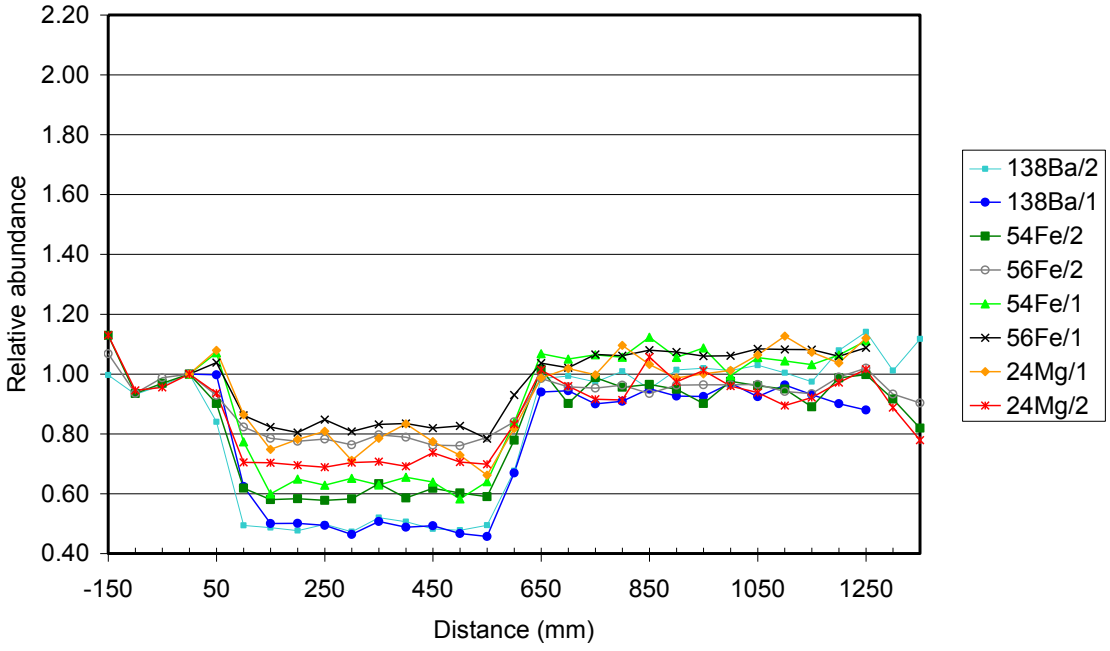

Figure 6-17: Sample A2; Linescans 1 and 2, for elements Mg, Fe and Ba. The clear band is in the centre, and grey bands are on the left and right.

Further linescans of sample A2 were completed across the interface in both directions, using more than one isotope of an element where possible to eliminate interferences.

6.4.5.1. Potassium

The element K once again shows a gradual slope going from a high abundance in the grey band to lower abundance in the clear band (Figure 6-18).

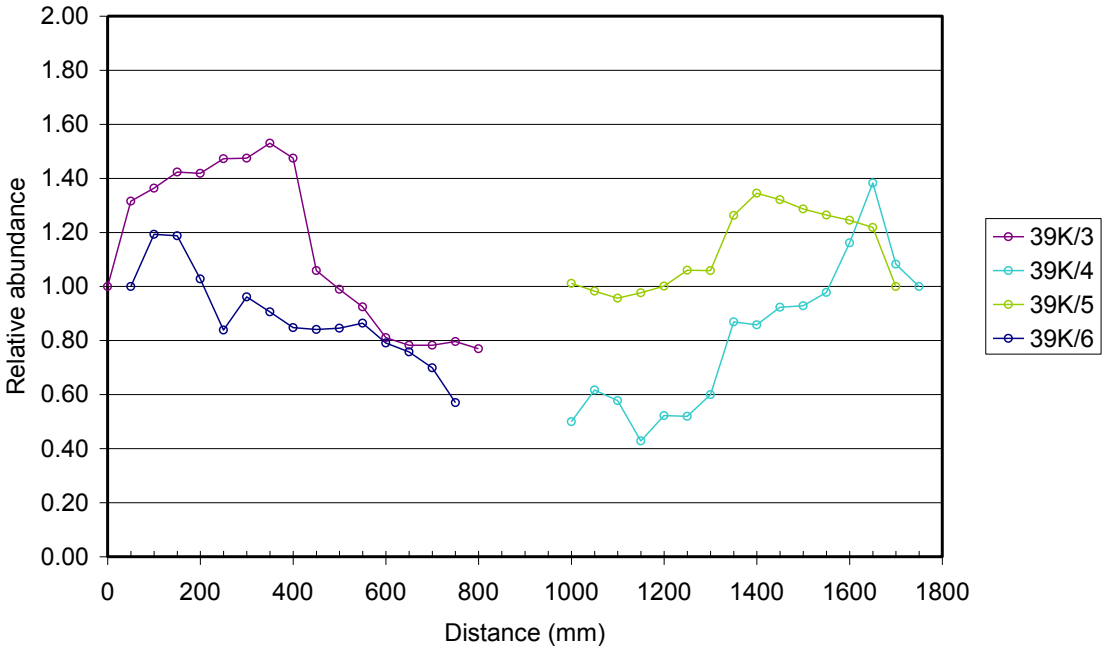

Figure 6-18: Distribution of K for several linescans across the interface of sample A2.

6.4.5.2. Barium

Ba exhibited a very sharp change across the interface of sample A2, although the magnitude of this change was less than other elements such as Ti. The signal was almost constant within each band (Figure 6-19).

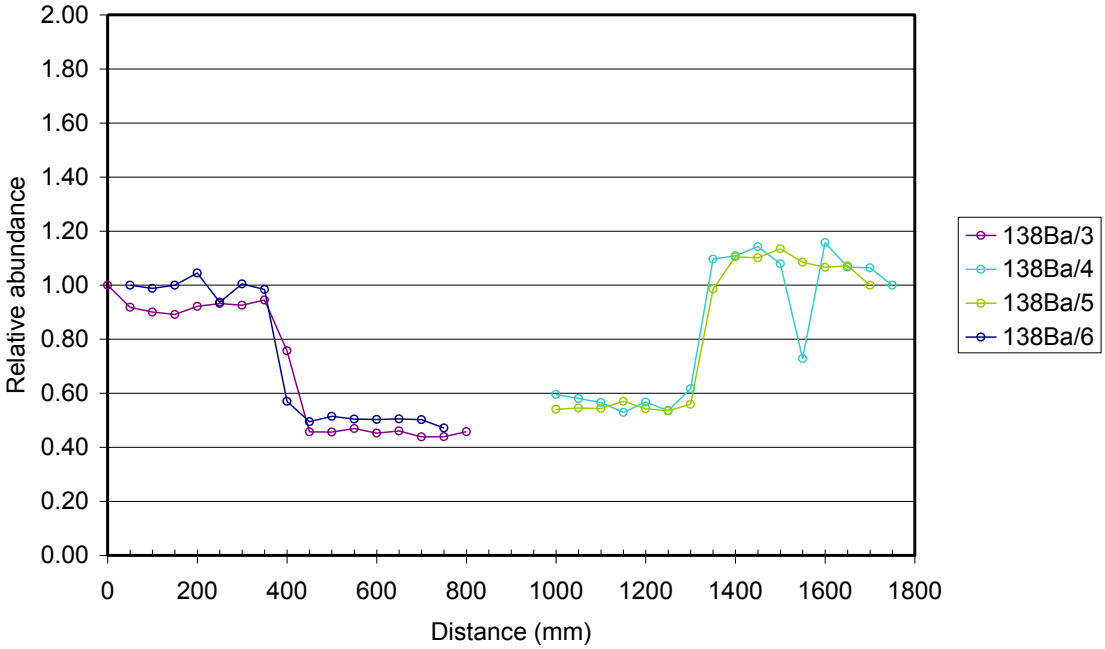

Figure 6-19: Trend of Ba across the interface of sample A2.

6.4.5.3. Titanium

Ti also exhibited a very sharp change across the interface of sample A2, although the data was more scattered within each band than for other elements such as Ba (Figure 6-20).

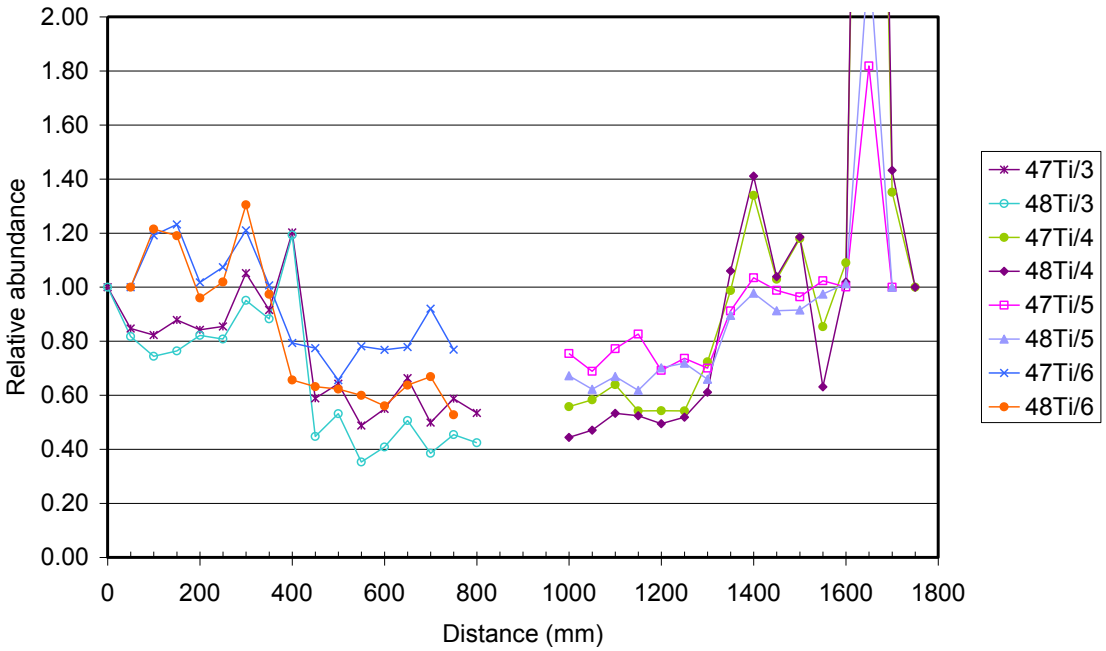

Figure 6-20: Profile of various isotopes of Ti across the interface of sample A2.

6.4.5.4. Iron

The concentration of iron was also markedly different between the transparent and grey bands; this result was unique to sample A2. Figure 6-21 shows several isotopes of iron were chosen for the analysis.

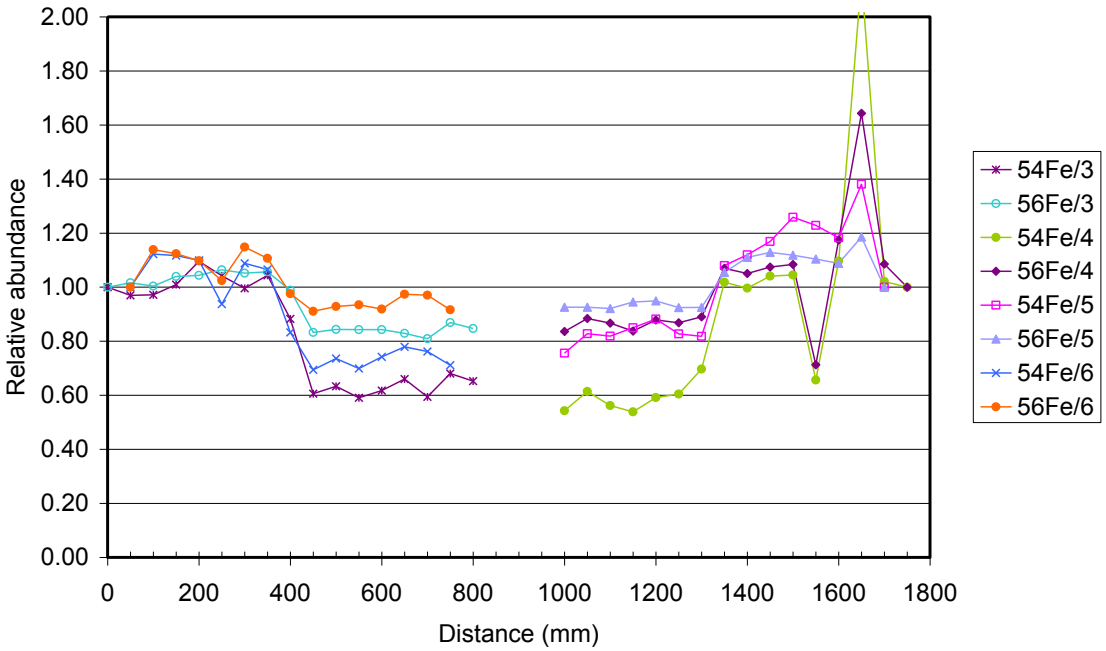

Figure 6-21: Profile of various isotopes of Fe across the interface of sample A2.

6.5. Discussion

6.5.1. Individual spot analyses:

Samples LR2, LR3 and LR4 demonstrated some variations in the levels of a few transition metals, particularly Cu and Co, consistent with the results of chapter 5 (Table 5-5; Table 6-3).

6.5.1.1. Grey 'reaction zone'

The lighter grey coloured bands (at the perimeter of a nobbie) contained a noticeably higher Na level than other coloured bands. This result is also confirmed by the ICPMS results of grey samples (5.3.1.4). It is assumed that the grey area of these samples is a reaction zone between the interior part of the opal and the surrounding claystone (Scrivener and Monteiro 1994), which is probably appreciably higher in alkali concentration (Carr *et al.* 1979; Robertson and Scott 1990). Deniskina *et al.* (1981) suggested that this outer edge of ordinary opal was not sufficiently purified to form precious opal. The researchers also noted that possible impurities were Na^{+}, Ca^{2+}, Mg^{2+}, Cl^{-}, CO_3^{2-} and NO_3^{2-}. However, though the quantity of Na was found to be greater in the surrounding opal than the centre, there was no evidence that the quantity of Ca or Mg were any different for opal samples possessing these bands around their perimeter. The remaining species discussed by Deniskina *et al.* (1981) were not investigated.

Since the outer grey contour accurately follows the edges of the specimen, it is obviously a post-depositional effect (i.e. formed after opal formation). Na appears to be playing a role in this process, and it is likely to be leaching from the surrounding claystones which are likely higher in alkali elements (Carr *et al.* 1979; Robertson and Scott 1990). The grey perimeter of the sample may alternatively contain a finely dispersed clay phase, which would obviously have originated from the adjacent claystone (Hiern 1967). This is observed in SEM micrographs of the opal bands adjacent to the host rock, as shown in Figure 6-22.

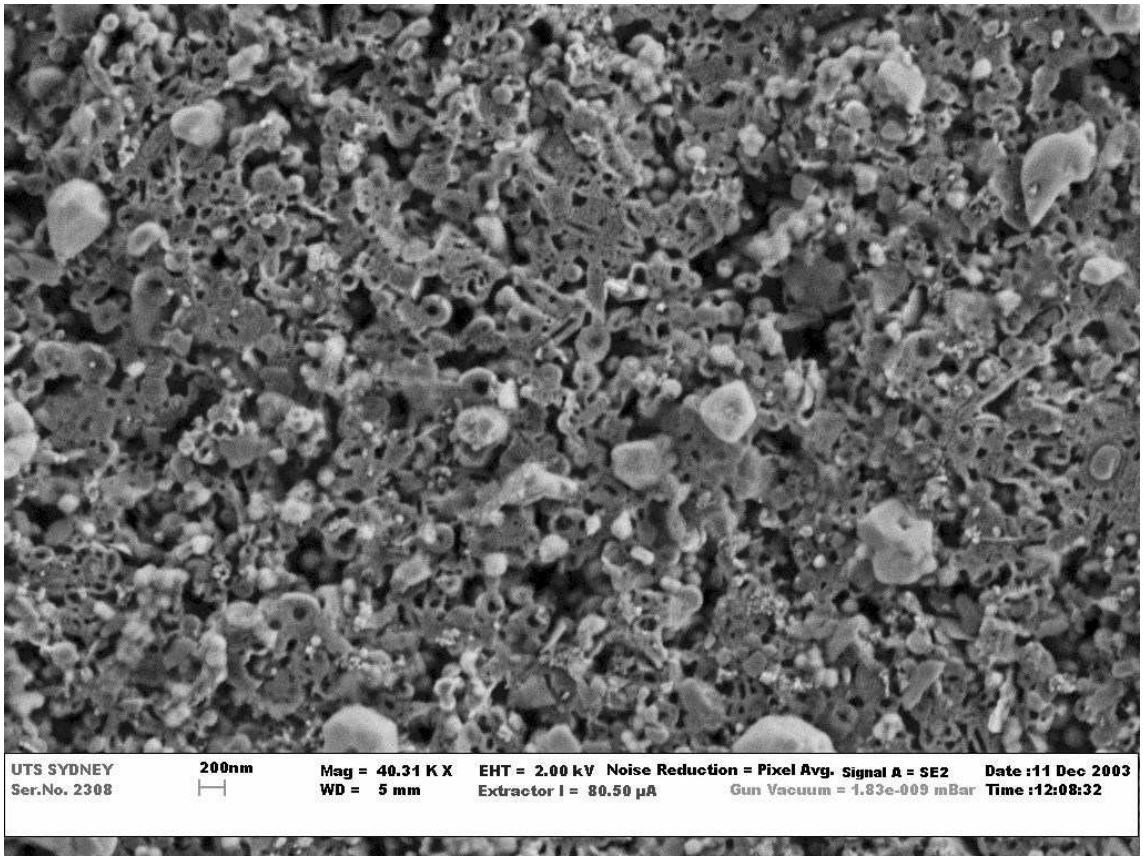

Figure 6-22: Possible existence of clay inclusions in the structure of sample LRT3.

Jones and Segnit (1966) proposed that the banding sometimes observed in horizontal opal veins was a case of the clay walls acting as a semi-permeable membrane, absorbing water and filtering the silica sol so that it remained in the crack. If this is the case, the outer edges of opals like LR2 and LR3 examined here might contain clay phases, and hence greater quantities of some elements (such as Na). Alternatively, these particular cations (K Na) are perhaps responsible for a slightly greater flocculation of the sol during the opals formation in that particular band.

6.5.1.2. Erratic behavior of certain elemental depth profiles

The erratic nature of the depth profiles for certain elements (Zn, Ti, Cr, Cu, Zn and Co) is not simply a case of these having a lower concentration, and thus more noise, than the depth profiles of other more abundant elements (Na, Ca, Mg, K, Al, Fe). There are two arguments for reaching this conclusion. When the depth profiles of various elements in a sample are compared, there is no obvious correlation between the signal intensity and

the signal/noise (S/N) ratio (which is indicative of uniformity) of the depth profiles. For example, Ti in sample LR1, having a signal intensity of ~4.8 x 10^4 c/s, is seen to be significantly more erratic than Fe in the same sample, which has a similar signal intensity value of ~6.5 x 10^4 c/s (Figure 6-7; Table 6-1).

The second argument is that the uncertainty in the signal intensity of an element (expressed as a percentage of the value) in the darker bands of opal is occasionally *greater* than that in the lighter band of the same sample. This is contrary to what is expected if the element was homogenously dispersed throughout the sample. In the previous chapter, darker bands were shown to contain significantly more impurities than lighter bands, and therefore the *uncertainty* in the signal of the darker band should be somewhat *less* than that of the lighter band. This is more appropriately quantified by comparing the standard deviation of the signal intensities for each of the bands (Table 6-2). For example, the signal intensity of Cr for the brown band of sample LR1 is 300% higher than that of the transparent band; however, the standard deviation of the Cr signal is also 240% greater in the brown band than the transparent band. Thus it follows that the darker bands of sample LR1 and LR2 contain a relatively heterogeneous distribution of the elements Ti, Cr, Cu, Zn and Co than the lighter bands, and a relatively homogeneous distribution of elements Mg, Ca and Fe. This argument should not carry as much merit as the first, because the error in the Si signals should be fairly equal, but this is not always the case.

6.5.1.3. Uneven distribution of trace elements

Assuming the diameter of the secondary silica spheres is 200μm and they exist in a simple cubic arrangement, there are estimated to be roughly 7850 spheres exposed at the surface of any 20μm spot. The calculation of this number also assumes the arrangement of spheres lies perpendicular to the SIMS ion beam. As the SIMS technique continually probes only the first few nanometres of surface, the results in effect represent the concentration of trace elements contained at different depths within the secondary silica spheres. Naturally, these undulations in composition would be averaged out to some extent by the number of spheres quoted above and their placement

with respect to the ion beam. Additionally, the orientation of the close-packed planes with respect to the ion beam would also influence the depth profiles. Consequently it is not possible to accurately demonstrate the pattern of heterogeneities that is manifested in the depth profiles without knowing the opal's sphere size, type of packing, and the direction that the array of spheres occupies with reference to the ion beam.

In spite of this, as the observed heterogeneities of the various depth profiles occur at approximately the same scale as the diameter of the secondary spheres (~100nm), these results support the charge neutralisation and solution depletion models presented in the previous chapter (5.4.4; 5.4.5) where it was established that the impurities contained in a darker band are present in the outer layers of the silica spheres.

6.5.2. Line-scans:

6.5.2.1. Interfacial width

The line-scans allow the estimation of the width of the interface between colour bands; it is quite narrow, less than the step size of 50μm in some cases. For samples that show such a distinct interface between bands, this evidence tends to refute the "bioturbidity" proposed in the Behr *et al.* (2000) model; that process would more likely lead to intermixing of the two layers resulting in a more diffuse interface, on the scale of millimetres, not of the order of 50 to 100 microns as observed here.

6.5.2.2. Behaviour of monovalent ions

In some cases, Na and K appeared to have a more gradual transition across the interfaces (Figure 6-15; Figure 6-16); this result is most likely due to the higher degree of mobility of these monovalent ions across the interface within the silica structure (Frischat 1975). These same elements also steadily increased in concentration at distances further from the interface. Unfortunately, it is not known how far the concentration of K and Na would progress if the linescan were to be continued. It is interesting to note that a gradual lowering of salts was proposed by Kalinin *et al.* (1998) to lower the repulsion barrier of monodisperse silica spheres and lead to a semi-coagulated state where spheres were suspended in an ordered array.

6.5.2.3. Ion specificity / Hydration spheres

The linescan data show that the monovalent ions gradually increase in concentration perpendicular to the interface of banded samples. It was proposed in the previous chapter (5.4.9.1) that different cations might be incorporated during the growth and sedimentation of the silica colloids at different times, as the charges and ionic radii of these ions differ. This hypothesis is supported by the linescan data (6.5.2.2) presented here, which suggest that specific ions may be preferentially accommodated into the structure as the aqueous conditions change. For example, as water is removed from the subterranean cavities during the formation of an opal and the concentration of the sol increases, then the solubility and concentrations of the ions present dictate when they can precipitate from the aqueous state.

6.5.2.4. Sample A2

This is an exceptional sample, as the larger nobbie contained numerous thin transparent bands, roughly parallel to each other. The remainder of this sample had a predominantly opaque grey colour. The multiple bands within sample A2 are more accurately described as numerous alternating thin layers of white and clear potch. This sample has been analysed previously with LA-ICPMS (5.4.2) and continues to defy explanation. These types of samples contravene the formation mechanisms discussed thus far. One possible mechanism that could be relevant in the formation of multiple bands within an opal is presented here, which is yet to be confirmed by experiment. The Liesegang phenomenon could potentially result in such patterns (6.1.6). One problem with suggesting such a mechanism is that it is uncertain what ions contribute to the grey precipitate. The concentration of the elements responsible should theoretically reduce exponentially in the transparent bands, and increase in a similar manner in the grey bands. Unfortunately, the steps in the linescans performed are too big to accurately verify whether this is the case or not. The signal for Ba is constant within each band, indicating that it is homogeneous within the sample.

6.5.3. Disorder by means other than charge neutralisation

Regions of disorder may arise by means other than charge neutralisation and sedimentation, for example by the intrusion of appreciably smaller or larger spheres into an ordered array of spheres (Duran and Jullien 1998; 6.1.3). This may happen by the process of trickle stratification; smaller spheres may settle down through the other spheres and disrupt ordered structures.

In some cases, regions of disordered spheres were observed with SEM to be surrounded by several domains containing ordered spheres. The obvious question is: how may a region of disordered spheres develop, when it is surrounded by ordered spheres? At first, this observation would tend to disprove the sedimentation model by charge neutralisation presented in the previous chapter. However, it is noteworthy that an SEM image is only a cross section intersecting the sample on an arbitrary plane. Hence, care must be taken when interpreting these microstructures. The extent of order above and below the plane of view is unknown. A region of disorder may develop when several ordered domains grow and intersect; it is impossible for the spheres at these locations to establish an ordered array.

6.5.4. Existence of primary spheres

Although the ring formations were observed in the spheres of SEM microstructures, these do not prove that these 'secondary spheres' consist of primary spheres. If the images are closely scrutinised, no evidence of primary spheres can be found (Figure 6-23). In some instances two secondary spheres appear to have grown in contact with each other, forming a kidney shape that would not have arisen if they were composed of primary spheres (Figure 6-24). These findings suggest that the so called 'secondary spheres' of opal-AG were formed by a simpler process than previously presumed, that of a suitable nucleation site (any positively charged ions) and simple growth around this core. Hence, they may not be composed of primary spheres, which would have coacervated to form the secondary spheres observed in these images.

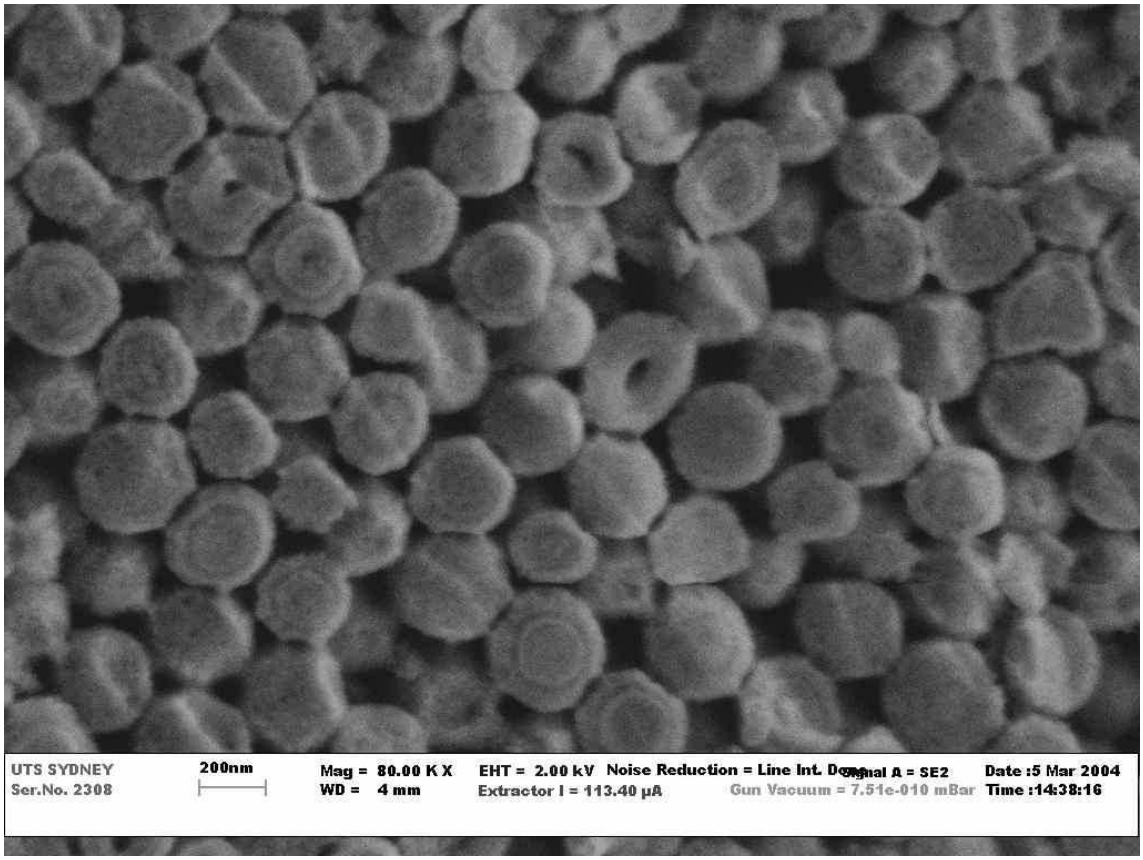

Figure 6-23: High magnification SEM micrograph. No primary spheres are evident. A secondary electron detector was used for imaging.

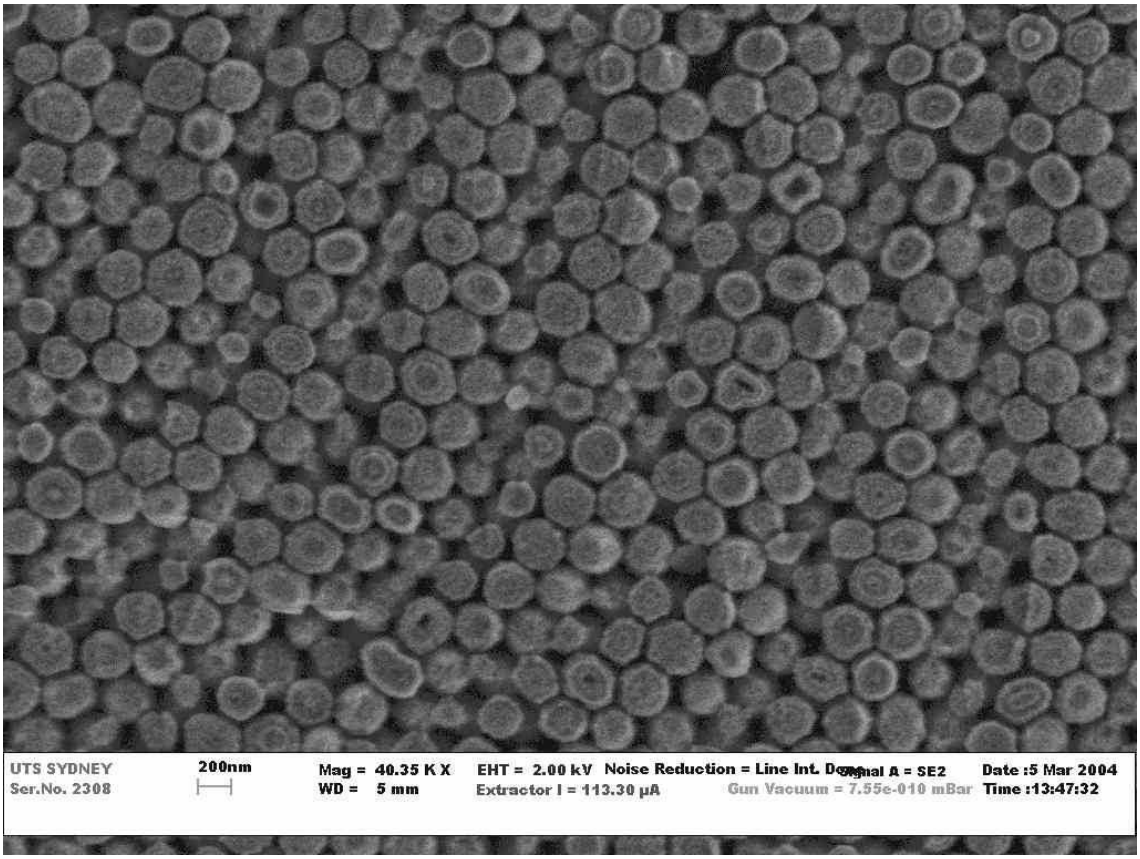

Figure 6-24: SEM micrograph of opal showing ring structure. A secondary electron detector was used for imaging.

6.5.5. Alternate hypothesis for observed ring structure

It is proposed that the observed ring structure develops as an opal is etched with HF acid, and is simply an artefact of this etching process. Since the core and surfaces of the secondary spheres are hypothesised to contain greater quantities of impurities (5.4.4.3; 5.4.4), and the reactivity of silica in HF acid is reduced if it contains more impurities, it follows that HF acid would preferentially react with the parts of the spheres which contain the least impurities.

When the microstructures are observed closely, it becomes apparent that the HF acid tends to selectively penetrate, firstly the spaces between the spheres, followed by certain individual spheres during which time it 'devours' the insides, often leaving the core and outer 'skin' intact as the HF acid molecules are consumed as the reaction proceeds (Figure 6-25). It is

believed the core and the outer-most surface of each particle contain higher impurities than the remainder of the interior (5.4.4; 5.4.4.3; 6.5.1.3). If the secondary spheres are in fact composed of smaller primary spheres, the primary spheres would be expected to be etched all to the same degree (it is known they must have formed at the same time in order to be monodisperse and cluster in the manner that they do), and in that case the outer shells of spheres would be dissolved first.

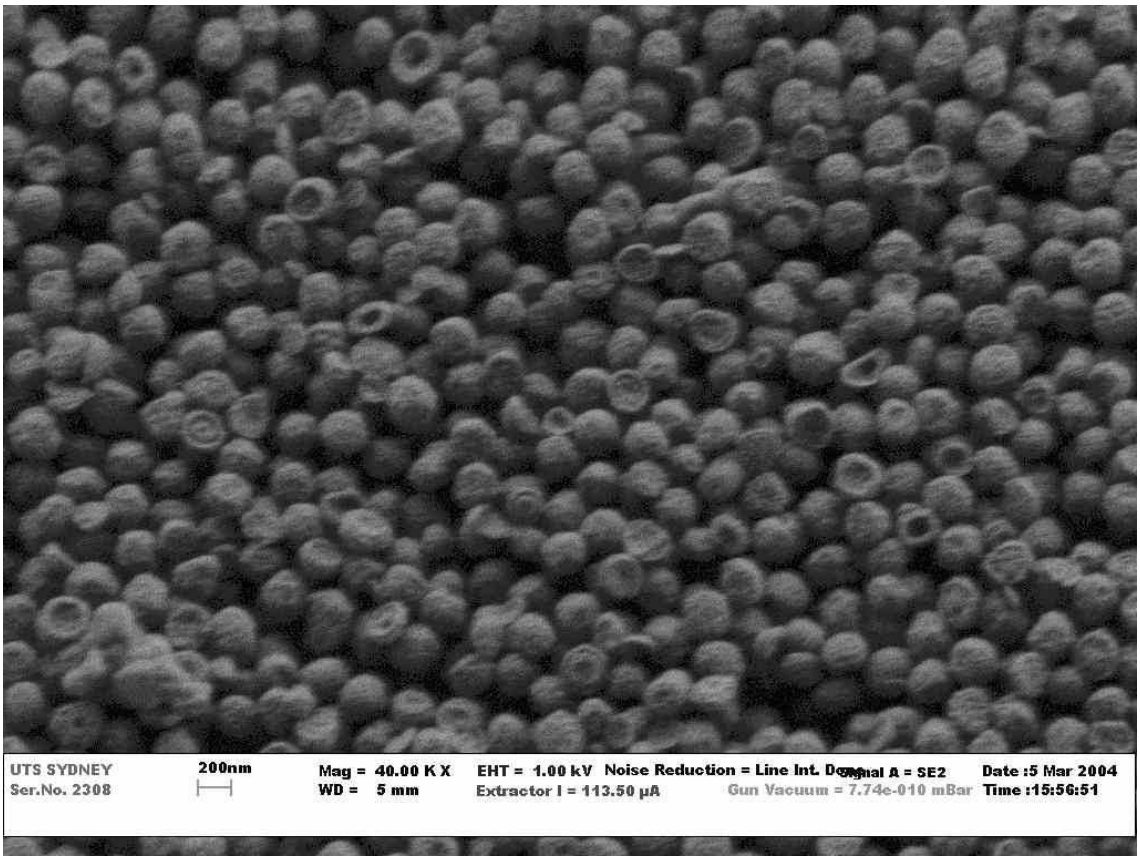

Figure 6-25: SEM micrograph of opal showing selective reaction between HF and silica. Some half-etched spheres are present with outer skin intact and others with etched cores. A secondary electron detector was used for imaging.

This hypothesis is even more significant when it is considered that the surfaces of spheres may contain significantly less than 90% silica, while the volume of silica between the surface and the core contains a higher proportion than this. If this is indeed the case, multiple rings might simply be the result of several generations of adsorbed impurities, of insufficient quantity to cause coagulation and sedimentation. Furthermore, ring

structures are not always observed when etching, often the 'spheres' appear as dodecahedral shapes when they are over-etched; perhaps these particular microstructures are from samples that contained fewer impurities adsorbed onto the surfaces of spheres (transparent and white opals). The problem with this theory is that a secondary sphere composed of primary spheres may still contain adsorbed impurities at its outer surface, therefore, HF would still preferentially react with the interior of the silica spheres. On the other hand, the arguments against primary spheres are as follows:

1. There is a very low probability that all the primary spheres will always form perfectly spherical secondary spheres with the same number of shells (as the secondary spheres are monodisperse).
2. The coacervation of primary particles during the formation of opal is an extra process that is not necessary for the formation of larger colloids (150-300nm).
3. At what stage do the primary particles coacervate? This is a real conundrum: if the impurities were present from the beginning, all the primary spheres would just sediment to begin with. Although large colloids will not form in the presence of large amounts of impurities.

Sanders (1985) reported that very large spheres (~6μm in diameter) contained shells or rings, whose thickness decreased as $1/r^2$, indicating that the volume of each shell was the same. This observation tends to suggest that the secondary spheres are not composed of primary spheres at all, as if they were, the thickness of each shell should be the same. Sanders (1975) reported that the concentric shells were not apparent in thin fragments of opal examined by TEM.

Since the volume of each ring is identical, it suggests that equal volumes of silica are deposited within each of those rings. Therefore other mechanisms of silica accumulation onto the surfaces of the colloids may be able to account for this. For example, one explanation that may possibly account for these rings involves a cycling of temperature, for example on a biannual timescale with the changing of seasons from summer to winter. This would alter the evaporation rate and rainfall patterns and hence raise

or lower the water table. Alternatively, the generation of amorphous $SiO_{2(aq)}$ from the decomposition of surrounding kaolinites (or leaching from sandstones) may also fluctuate on a seasonal basis. The net result of any of these seasonal processes is that the concentration of the dissolved silica in the subterranean cavity would naturally reduce or increase. As the concentration of dissolved silica increases, the sol becomes supersaturated and allows further growth of colloids. This process lowers the concentration of dissolved (aqueous) silica as $Si(OH)_4$ is deposited onto the surfaces of the growing colloids. Thus, once the silica concentration is just below the saturation level, there is no longer a sufficient driving force for precipitation. Hence, the concentration of dissolved silica may again increase above the saturation limit (if a continual source of monomeric silica exists), until it again can be precipitated. These fluctuations alter the polymerisation rate of silica at each stage; a high rate during times of supersaturation, and a low rate at times of undersaturation. The resulting colloids would consist of various layers, reflecting the different periods of polymerisation rates that were deposited while they were still suspended in the sol. As these layers could only be distinguished from each other by etching with HF acid, these inferences may account for the observed ring structures in the SEM images of opal-AG.

6.6. CONCLUSIONS

The distribution of the transition metals across the interface was examined for several banded opal samples. In most cases, opaque black coloured areas of the samples showed higher proportions of the transition metals Ti, Co and Cu than those of opaque grey areas. Lighter grey areas of the samples generally showed a higher abundance of Na than even the darker grey or blackest regions. When compared to transparent regions, black or grey areas of the samples showed significantly more Ti, V, Co, Cu, Zn and Y. For one sample, the concentration of Ni and Cr was also higher in the darker band than the lighter band.

The alkali elements generally exhibited a gradual change in concentration across the interface of a banded opal, whereas the transition metals displayed a sharp transition from high to low concentration between dark and light coloured opals bands. This result is thought to be caused by a gradual lowering of the concentration of certain alkali elements (Na, K) at the time of the opal formation, leading to order-disorder phase transitions as proposed by Kalinin *et al.* (1998). Additionally, by examining the depth profiles, certain elements (Fe, Mg, Ca, etc) appeared to be distributed more evenly than others within a particular band (Ti, Cr, etc), consistent with the charge neutralisation mechanism invoked in the previous chapter (5.4.4; 5.4.6). No single element can be ascribed to the formation banding in opals; depending on the sample investigated, groups of elements seem to be important (most transition metal ions and rare-earth elements). Only with further study will the nature of this relationship be elucidated.

It appears as though there are at least two different mechanisms responsible for the formation of different colours associated with these samples, the mechanism responsible for the formation of a darker layer in an otherwise transparent opal, and that of the transformation to light grey of the perimeter surrounding the dark grey interior. The Liesegang phenomenon may be responsible for the formation of multiple bands within one particular sample (A2), as it was the only sample to show significant differences in the concentration of Mg, K, Ba, and Fe between its multiple clear and grey bands.

An alternate proposal for the ring structure in opals was speculated upon, as rings are not always visible in SEM micrographs. It is suspected that rather than the rings attesting to the existence of primary colloidal particles, their presence might instead be an artefact of the etching process with HF acid.

7. NUCLEAR MAGNETIC RESONANCE

"Now that we know who you are, I know who I am."
–Elijah Price (a.k.a. "Mr. Glass"), from the movie 'Unbreakable'.

7.1. INTRODUCTION

7.1.1. Nuclear Magnetic Resonance (NMR) Spectroscopy

NMR spectroscopy is an analytical technique which allows the various local environments of certain nuclei to be investigated (Field and Sternhall 1989). Only nuclei with non-integral nuclear spin ($^5/_2$, $^3/_2$, $^1/_2$, etc) are distinguished by the NMR method[1]. The nuclei under investigation in an NMR experiment are shielded to varying degrees by the surrounding electrons from an externally applied magnetic field, B_0. The degree of shielding affects the nuclei's ability to absorb and emit radio frequency (RF) electromagnetic radiation (EMR). In a typical NMR experiment, a short RF pulse is applied to the sample, at a frequency appropriate to the nuclei (isotope) to be investigated. Essentially, the nuclei in the sample are excited and 'align' with the externally applied magnetic field, and in the absence of an RF field, they revert back to a lower energy state, radiating RF energy in the process[2]. An NMR experiment, in effect, measures this release of RF energy, which is detected in a second coil. The frequency of electromagnetic radiation absorbed by the nuclei, ν_0, is given by the Larmor equation (Equation 7-1):

Equation 7-1:

$$\nu_0 = \frac{\gamma}{2\pi} B_0$$

where γ is the magnetogyric ratio of the nuclei and B_0 is the applied field strength (Field and Sternhall 1989). Figure 7-1 illustrates the essential components of an NMR spectrometer.

[1] The natural abundance of the ^{29}Si isotope is 4.7% (spin $^1/_2$); the remaining 92.2% of ^{28}Si nuclei and 3.1% of ^{30}Si (with spin of 0 and 2, respectively) are not seen with ^{29}Si NMR.

[2] This radiated signal in turn is modulated by the frequencies of all nuclei excited by the pulse.

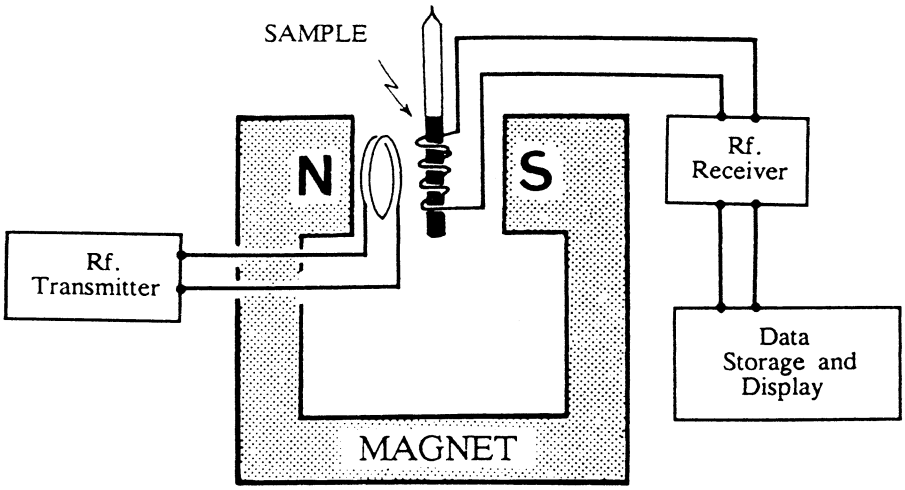

Figure 7-1: Basic components of an NMR spectrometer. From Field and Sternhall (1989).

7.1.1.1. Free-induction decay (FID)

The RF signal emitted exponentially decays from the moment the applied RF field is removed, and this is termed a free-induction decay (FID). Typically, the FIDs of many RF 'pulses' are constructively added together to improve the signal to noise[1] ratio (S/N increases as the square root of the number of FID emissions added). All the active nuclei re-emit RF radiation at specific resonance frequencies, creating an interference pattern in the resulting RF emissions with time. A single FID can be seen in Figure 7-2; note that the resonant frequency of this FID is generated by a particular nucleus within the sample.

[1] The largest source of noise is due to the Brownian motion of electrons in the conductors of the probe's receiving coils.

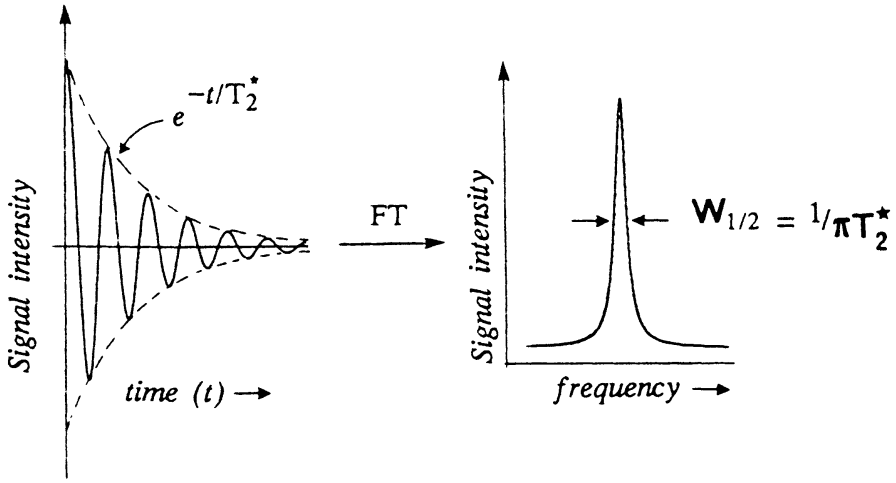

Figure 7-2: Fourier transformation of a single FID with exponential decay and a time constant of T_2^*. This gives rise to a Lorentzian lineshape whose FWHM is $1/\pi T_2^*$ hertz. From Field and Sternhall (1989).

Fourier Transformation of the combined (superimposed) FID emissions gives a more conventional representation of the signal by extracting the resonant frequencies of the respective nuclei (Figure 7-2). This result is expressed as a "chemical shift", usually relative to that of a standard reference compound. The chemical shift is expressed in dimensionless units parts per million (ppm), as these values are independent of the strength of the applied magnetic field. The NMR spectrum can then be presented as a plot of intensity as a function of frequency.

The fundamental principle of NMR spectroscopy is that nuclei in different micro-environments are shielded to different extents and hence have different frequencies. NMR spectroscopy is quantitative in that the integrated intensity of a signal is proportional to the concentration of nuclei giving rise to it.

7.1.1.2. Chemical Shift Anisotropy (CSA)

The shielding of a nucleus depends on the orientation of the molecule and its bonds with respect to the magnetic field. In the spectra of liquids, molecular reorientation is sufficiently rapid so that the shielding is averaged over all orientations. However, in the spectra of solids, where the

molecules[1] are not free to rotate, the chemical shift of a nucleus depends on the orientation of the molecule in the magnetic field. This directional dependence of nuclear shielding is termed the chemical shift anisotropy (CSA) (Field and Sternhall 1989). The chemical shifts in the NMR spectrum of a single crystal of a solid vary with the orientation of the crystal; whereas the spectra of powders and amorphous solids are usually broadened due to the overlap of spectra from molecules with all possible orientations with respect to the magnetic field. I.e. for amorphous structures, the nuclei are in subtlely different environments, therefore they possess slightly different degrees of shielding.

7.1.1.3. Magic Angle Spinning (MAS)

Previous research (Pines *et al.* 1973; Andrew 1981) has shown that if a solid sample is rapidly spun whilst its NMR spectrum is acquired, the observed shielding for any nucleus in the sample can be expressed by Equation 7-2 (Field and Sternhall 1989).

Equation 7-2:

$$\sigma_{obs} = \frac{1}{2}\sin^2\theta(\sigma_{xx} + \sigma_{yy} + \sigma_{zz}) + \frac{1}{2}A(3\cos^2\theta - 1)$$

where θ is the angle of the spinning axis with respect to B_0; σ_{obs} is the observed shielding constant; σ_{xx}, σ_{yy} and σ_{zz} are the respective shielding components of the principle elements represented in a shielding tensor; and A is a term dependent on the chemical shift tensor.

When θ is set to 54.7° (the magic angle), Equation 7-2 reduces to $\sigma_{obs} = \frac{1}{3}(\sigma_{xx} + \sigma_{yy} + \sigma_{zz})$, i.e. to the isotropic value. Therefore, CSA can be suppressed by rapidly spinning the sample at an angle of 54.7° relative to the magnetic field. Consequently, the spectra of solid samples acquired with MAS do not exhibit the broadness arising from the overlap of spectra resulting from nuclei in molecules with different orientations. To totally remove the effect of CSA from a spectrum, the rate of MAS must be large compared with the CSA. Typical rotation speeds range from 1 to 5kHz. If

[1] The molecular structure of silica consists of a macromolecular network, so in this context, it is essentially an extensively inter-connected molecule.

the spinning rate is not sufficiently rapid to average CSA completely, spinning sidebands result. These may be observed on an NMR spectrum as additional resonance peaks that occur separately at discreet frequencies either side of the principal resonance(s).

7.1.1.4. Proton Cross Polarisation

The technique of proton cross-polarisation (Pines *et al.* 1973) is used to more effectively study hydrous silicas (Maciel and Sindorf 1980; Sindorf and Maciel 1983; Farnan *et al.* 1987). Since the number of available proton (^{1}H) nuclear spins is much more abundant than the rare spins of ^{29}Si, the following technique may be applied to improve the signal intensity considerably. Essentially, a single RF pulse is applied to the protons, then two RF fields are simultaneously applied to the ^{1}H and ^{29}Si nuclei, enabling a transfer of polarisation to occur. The strength of these two fields, *H*, must be adjusted so that $\gamma_H H_H = \gamma_{Si} H_{Si}$ (the Hartmann-Hahn condition). When this condition is satisfied, the ^{1}H and ^{29}Si nuclei precess with the same frequency with respect to the spin-locking field. During this spin-locked period, the system proceeds rapidly to internal equilibrium by a population transfer from the ^{1}H spectrum to the ^{29}Si spectrum (the mutual ^{1}H and ^{29}Si spin flips via their dipolar interaction, becoming energy conserving). The result is a cooling of the ^{29}Si spin system by the establishment of ^{29}Si spin order, and a small heating of the ^{1}H spin reservoir (a small decrease in the ^{1}H magnetisation). The effect on the ^{1}H spins is very small since the ^{29}Si spins are rare. The process may be repeated by destroying the ^{29}Si spin order and again bringing them into contact with the ^{1}H spins. Spin decoupling is achieved by the same ^{1}H spin irradiation used for the spin locking. Following the contact of ^{29}Si and ^{1}H nuclei, the ^{29}Si spin decay is observed. The cycle is repeated and the ^{29}Si signals accumulated until the ^{1}H magnetisation is depleted. Extensive details of the technique are described elsewhere, but they are beyond the scope of this thesis. For further details of the method, the reader should refer to Pines *et al.* (1973). The method is commonly employed in solid-state NMR research (provided the nature of the samples is suitable) hence cross-polarisation programs are fairly easily utilised and operated.

The time during which the two RF fields are applied is called the contact time, and varying this parameter alters the relative intensities of peaks in the NMR spectrum. For short contact times, silicon atoms in close proximity to protons will give more enhanced signals than those further from protons (Farnan *et al.* 1987).

7.1.2. Relaxation time, T_1

During the FID period, the exponential rate of decline of the RF signal is determined by the relaxation time, T_1, which contributes to the linewidth of each NMR signal. If the nuclei return to equilibrium rapidly (T_1 is small), it is not possible to measure the resonance frequency accurately[1], and the NMR signals are broad and poorly defined (linewidth is large). Conversely, if a nucleus relaxes slowly (T_1 is large), then the NMR signals for that nucleus become sharp and well defined.

7.1.2.1. Dipole-Dipole Interactions

T_1 depends on many factors including the state of the sample (solid, liquid or gas), molecular size and mobility, temperature and the presence of paramagnetic impurities. Dipole-dipole relaxation (T_{1DD}) is a consequence of the interaction of nuclei with other magnetic dipoles in the sample. This relaxation arises because the tumbling motions of magnetic nuclei produce fluctuating magnetic and electric fields, which in turn assist the nuclear spins to relax. T_{1DD} is inversely proportional to the time of molecular reorientation. For large molecules where molecular tumbling is slow, the molecular reorientation time is long and the nuclei in these molecules relax rapidly. Thus, the nuclei of solids with very large molecules (i.e. silica, which possesses a continuous macromolecular network) generally give very broad NMR spectra due to efficient dipole-dipole relaxation.

7.1.2.2. Paramagnetic relaxation

The presence of paramagnetic species including oxygen and many transition metal ions (Co^{3+}, Cr^{3+}, Fe^{3+}, Ni^{2+}, Mn^{2+}) is particularly important because they have a large magnetic moment and therefore also cause rapid

[1] This can be viewed as a consequence of the Heisenberg uncertainty principle: to measure an energy difference accurately, one needs a long time. If the system relaxes rapidly, the time available is short, ΔE is poorly defined, and hence and the observed NMR resonances are broad.

relaxation of nuclei (Field and Sternhall 1989). However, de Jong *et al.* (1987) reported that there was no significant difference in NMR linewidths of samples with high or low concentrations of paramagnetic centres.

7.1.2.3. Saturation

If a sample is irradiated continuously with RF radiation at the Larmor frequency, the populations of the nuclei spin states rapidly equalise; the nuclei are said to be 'saturated', and no NMR signal is observed. For example, if the relaxation time is very long and the RF pulses are repeated too quickly, the nuclei may become saturated as they do not have enough time to fully relax; hence the resonance signal acquired will be very poor. Thus, the relaxation time is a factor which determines how often an RF pulse may be effectively (and efficiently) repeated.

7.1.3. Silica tetrahedra notations

In this discussion, the standard Q^n notation is used, where Q stands for a given silica tetrahedron, and n represents the number of associated bridging oxygen atoms (Si–O–Si) per tetrahedron. Silicon nuclei that are more shielded result in higher-field (more negative) chemical shifts. In this way, silicates in which the tetrahedra are fully polymerised (Q^4) yield chemical shifts progressively more negative than those that are not (Q^3). Similarly, increasing the number of substituted Al ions in each of the SiO_4 tetrahedra results in a correspondingly less negative chemical shift (Klinowski *et al.* 1982; Mägi *et al.* 1984).

7.1.4. ^{29}Si NMR of opals (single pulse)

De Jong *et al.* (1987) completed the first detailed ^{29}Si NMR study of opals. In that study, both opal-A and opal-CT yielded a single, broad resonance centred at about -112 ppm, between the resonances of cristobalite and tridymite (Figure 7-3). The full width at half maximum (FWHM) varied between 5.8 and 9.8 ppm for natural opals. The first conclusion to be made from this data was that the peak shape of NMR spectra of opals most closely resembled amorphous silica, and that the spectra of opals showed little resemblance to those of either silica gel or quartz. Of all the opals investigated (both opal-A and opal-CT), none of the spectra could be simulated by combining those of other silica polymorphs

such as cristobalite and tridymite (unlike XRD patterns; 2.5.2.1). Furthermore, opal-CT NMR spectra appeared to be more amorphous than their XRD patterns revealed, because the NMR detection of crystalline phases is less sensitive than amorphous phases (since the relaxation times of crystalline phases can be significantly longer than those of amorphous phases).

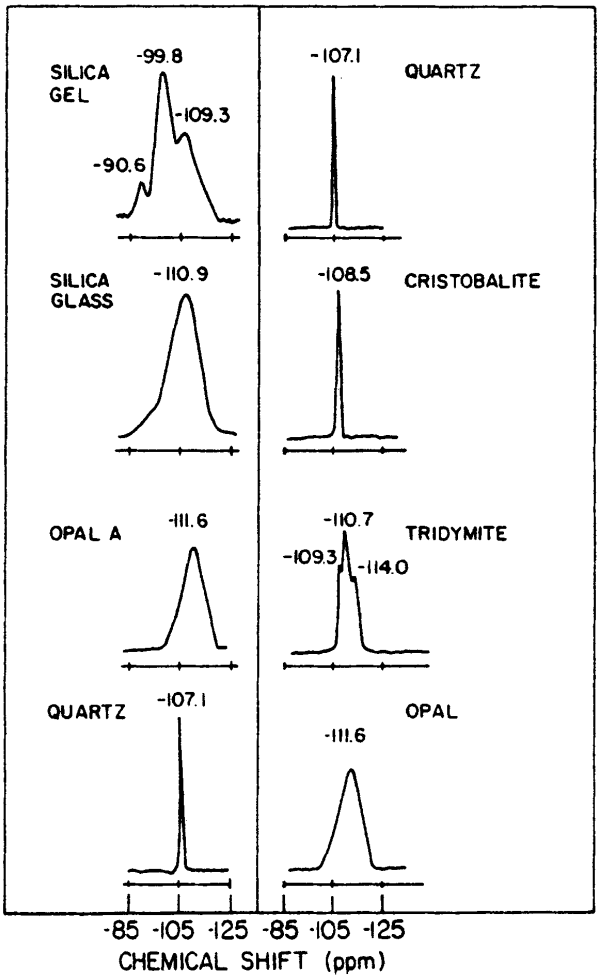

Figure 7-3: NMR spectra of various SiO2 polymorphs. From de Jong et al. (1987).

The difference between spectra of silica glass and opal was that the peak maxima of opal were more negative (silica glass = -110.9 to -111.5 ppm), while the FWHM for opal was also smaller than silica glass (silica glass = 11.6 ppm). The chemical shift of one synthetic opal sample was observed at -107 ppm, which was closer to the chemical shift of quartz (-

107.1 ppm) than those of the natural samples. The FWHM of that sample, 11 ppm, was also substantially broader than the natural samples.

7.1.4.1. Coordination of silica tetrahedra

The ^{29}Si MAS NMR spectra of opal-A and opal-CT involved a range of halfwidths; the major Q^4 resonance occurred over chemical shift values of -99 to -123 ppm (de Jong *et al.* 1987). This range indicated that within NMR detection limits, all Si atoms were coordinated to four oxygen atoms in a three-dimensional array of corner-sharing tetrahedra. Amorphous silicates consisting of edge-sharing tetrahedra or threefold-coordinated Si are known to give a chemical shift less negative than 60 ppm, while the NMR spectra of fivefold- or sixfold-coordinated Si give a chemical shift more negative than 130 ppm (de Jong *et al.* 1987). Thus, these uncommon configurations thought to exist in amorphous silica, if present, did not occur in sufficient concentrations in opal to be detected (de Jong *et al.* 1987).

A further set of experiments by de Jong *et al.* (1987) deduced that the width of the ^{29}Si NMR lines in opals was due to a distribution of silica species rather than to variations in relaxation effects (i.e. line broadening of the Si spectra was due to a distribution of chemical shifts and not caused through dipole coupling between protons and Si nuclei).

7.1.4.2. Silanol groups

The absence of silanol groups, i.e., Q^0, Q^1, Q^2, and Q^3, tetrahedra with protons attached to the non-bridging oxygens, was confirmed by the lack of line narrowing of the Si spectrum on proton decoupling, in accordance with the H_20 chemical analyses. The proton chemical shifts of opal were shifted by 1.1 ppm towards higher frequencies compared to the expected resonance in molecular water. A fairly strong interaction between water and silica was therefore suggested, however it was concluded that there was an absence of silanol groups in the opals studied (de Jong *et al.* 1987).

7.1.4.3. Bond angles

The chemical shift values obtained from silica polymorphs are known to correlate with the Si–O–Si bond angle (Thomas *et al.* 1983). The distribution of mean Si–O–Si angles per tetrahedron, $Q^4(0Al)$ ⟨Si–O–Si⟩, indicates a narrower range for natural opals than for silica glass (de Jong *et*

al. 1987). For opal-A, the ⟨Si–O–Si⟩ bond angle was determined to vary between 133 and 168° with an average of 151°. For Opal-CT, ⟨Si–O–Si⟩ bond angle varied between 138 and 170° and the average was 152°. For silica glass, ⟨Si–O–Si⟩ bond angle varied between 122 and 170° and the average was 148°. In terms of chemical shifts and variation in ⟨Si–O–Si⟩ distribution, local Si environments in opal most resembled those of tridymite than any of the other silica phases. The major difference was that for opals, tetrahedra with ⟨Si–O–Si⟩ angles as small as 133° existed, whereas tridymite contained no such tetrahedra (de Jong *et al.* 1987).

7.1.4.4. Other NMR studies of opal

Natural and synthetic silica glasses showed the broadest NMR signals (least local ordering), followed by opal-AG and opal-AN with approximately equal half widths, and opal-CT (Graetsch *et al.* 1990; Figure 7-4). The resonances for the opals were more negative than those of tridymite, while for silica glass they were about 0.5 ppm more positive than those of tridymite. The major contribution to the signal was the orientation of the Si–O bonds to the adjacent tetrahedral centres. Mean Si–O–Si angles of approximately 148, 150 and 151° were estimated for Libyan Desert Glass (LDG), opal-AG and opal-AN, respectively (Graetsch *et al.* 1990). Thus it seemed the broadening of the NMR signal was probably due to the occurrence of a range of different Si–O–Si angles. The asymmetric distribution of Si–O–Si angles in silica glass was extended to smaller values than in opals, i.e. the bond angle distribution was greater in silica glass than in opals, which indicated a lower degree of ordering in silica glass. This can be explained by the additional occurrence of non-planar five- or seven-membered rings with Si–O–Si angles smaller than 148°. This interpretation agrees with the finding of a bimodal distribution of Si–O–Si angles in silica glass by Raman spectroscopy (Champagnon *et al.* 1997). In opals, the number of rings other than interconnected six-membered rings was low or completely absent (Graetsch *et al.* 1990). Graetsch *et al.* (1990) therefore determined that non-crystalline opals were almost exclusively made of interconnected six-membered rings of silica tetrahedra (approximately hexagonal in shape), unlike silica glass, which can contain odd-numbered rings. It appeared as though the silica tetrahedra were irregularly twisted in

non-crystalline opals. It was also reported that there was also no simple correlation between half widths and chemical shifts.

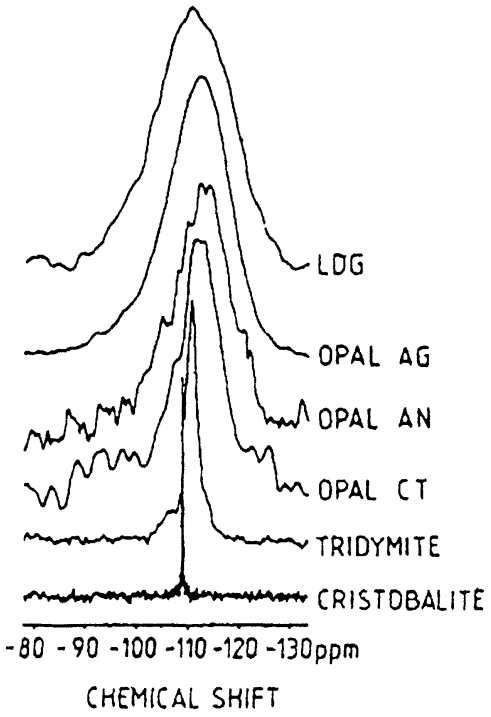

Figure 7-4: ^{29}Si NMR spectra of various silica polymorphs, including ordered low-cristobalite (L-C_0) and ordered MX tridymite (L3-T_0). LDG = Libyan Desert Glass. Spectra are displaced vertically for clarity. From Graetsch et al. (1990).

7.1.4.5. Relaxation times

The relaxation time, T_1 for quartz is approximately 5 hours, whereas T_1 for opals varies from between 0.25 and 10 seconds, presumably because of the presence of either paramagnetic centres or water in the latter (Gladden *et al.* 1986). Considering only T_1 variations, for a sample of opal-A containing quartz, a 30 second delay between pulses enhances the amorphous component by a factor of 600 relative to quartz (de Jong *et al.* 1987).

7.1.5. ^{29}Si NMR of opals (proton cross polarisation)

The ^{29}Si chemical shifts of opal-AG, opal-CT and opal-C were in the same range and thus the opal classes could not be differentiated on chemical shifts alone (Adams *et al.* 1991). However, the line-widths of both Q^3 and Q^4 resonances decreased with increasing structural order: Opal-AG = 9.8 to 9.9 ppm; opal-CT = 6.0 to 7.5 ppm; opal-C < 5 ppm. NMR experiments using ^{29}Si–{^{1}H} cross polarisation enhanced the signal produced by silicon atoms in close proximity to protons. Most opal samples showed silanol (Q^3) ^{29}Si resonances between -101.0 and -103.7 ppm, but there was no evidence of resonances due to $Si(OH)_2$ (Q^2) units (Figure 7-5). The spectrum of one opal-AG sample measured with different contact times showed the expected relative enhancement of the Q^3 resonance at shorter contact time (Figure 7-6). The spectra of opal-CT yielded broad featureless resonances with maxima in the region of δ = -111.6 to -114.3 ppm, and they did not appear to be composed of superimposed well-defined cristobalite and tridymite resonances. The major Q^4 signal of microcrystalline opal shifts to higher fields (lower ppm values) with increasing structural disorder (Graetsch *et al.* 1994). The FWHM of the signal also increases with increasing disorder.

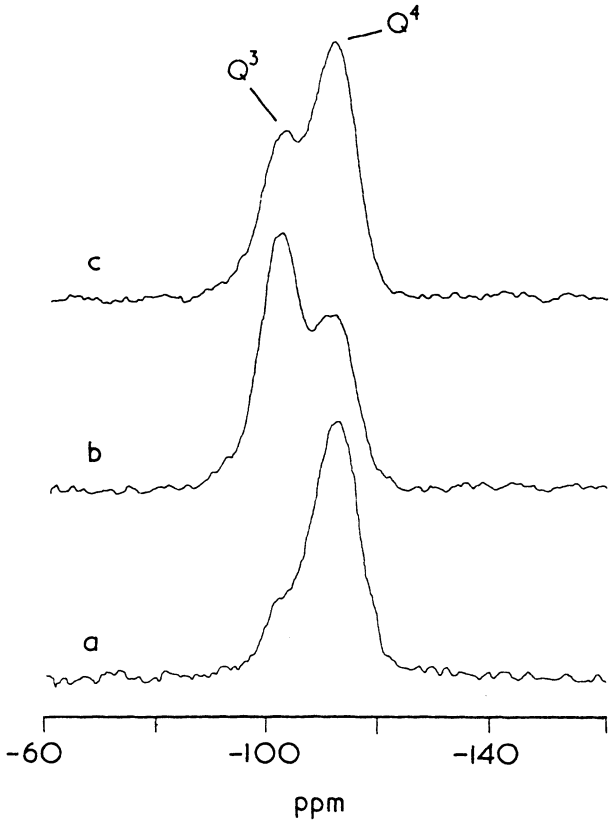

Figure 7-5: Relative enhancement of Q^3 resonance of an opal-AG sample with reduced contact times. Curve a = no cross polarisation. Curve b = contact time of 1ms. Curve c = contact time of 4ms. From Adams et al. (1991).

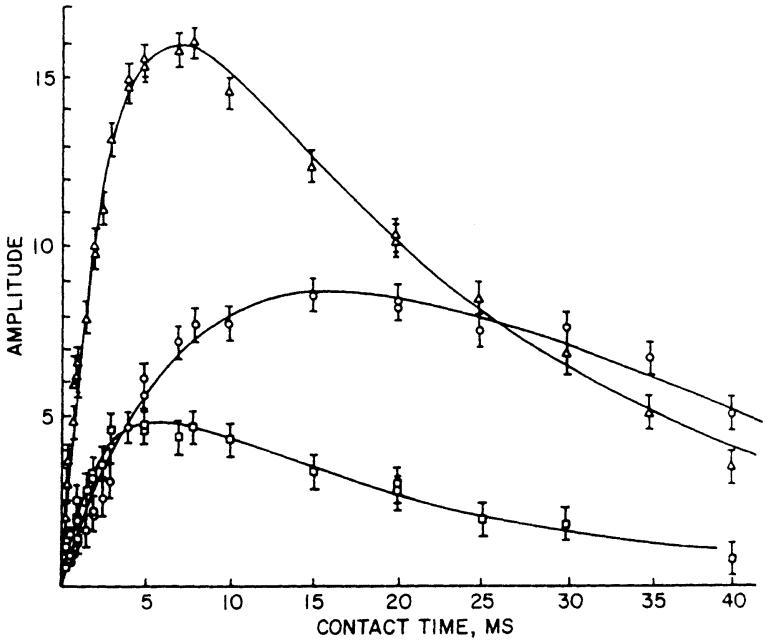

Figure 7-6: Plot of ^{29}Si CP/MAS NMR amplitudes as a function of contact time. Circles: data for -109.3 ppm resonance. Triangles: data for -99.8 ppm resonance. Squares: data for -90.6 ppm resonance. From Maciel and Sindorf (1980).

Graetsch *et al.* (1994) identified that the broadness of the NMR signals suggested variations in the local environments of the silicon atoms (rather than as a rapid nuclear relaxation effect associated with solids which also yields broad NMR signals). The small shoulder with a chemical shift of -100 ppm was ascribed to silicon in a Q^3 configuration (SiO_2 tetrahedra connected to three other tetrahedra instead of four). Geminal silanol groups still were not present in detectable amounts in microcrystalline opals and opal-AG, except for opal-AN, which shows very slight resonances at -90 ppm (Figure 7-7). Cong *et al.* (1993) detected a weak resonance at -94 ppm, indicative of geminal silanol groups (Figure 7-8).

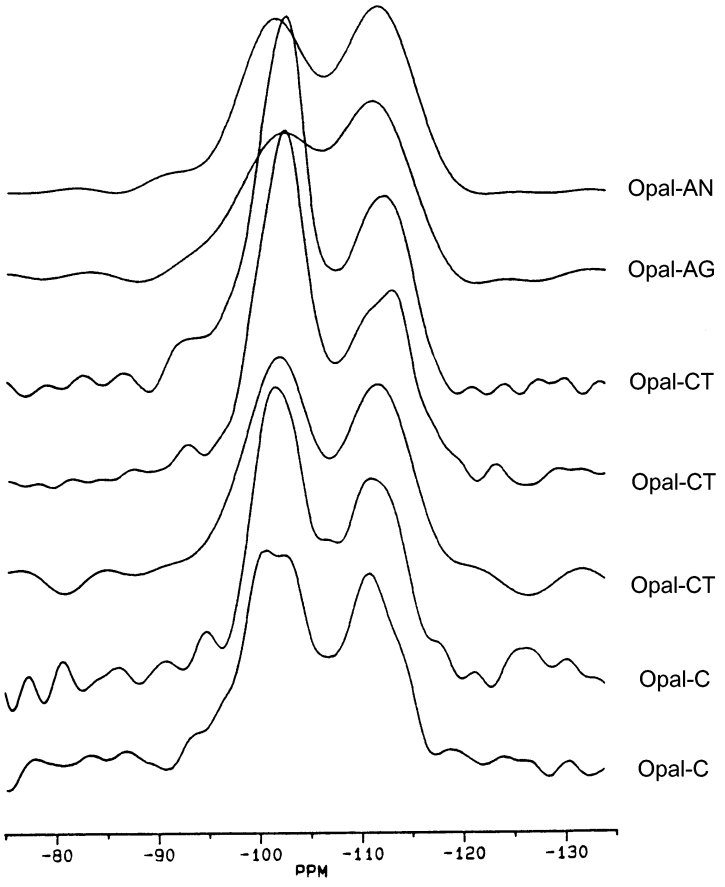

Figure 7-7: Proton Cross Polarisation ^{29}Si NMR spectra of various types of opal, each scaled to equal height at the -110 ppm resonance. From Graetsch et al. (1994).

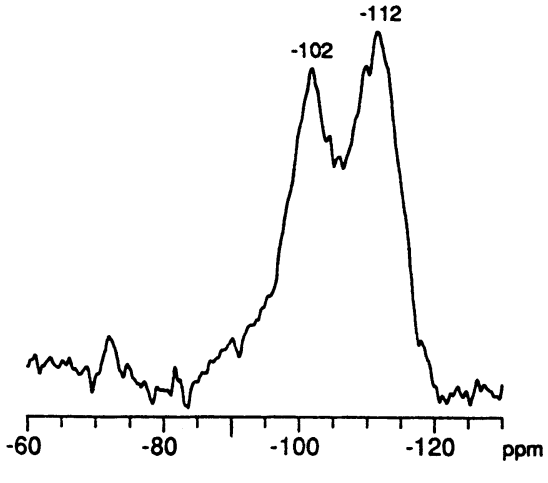

Figure 7-8 Cross Polarisation NMR spectrum of Nevada opal (opal-CT) showing Q^2 shoulder at -94 ppm. From Cong et al. (1993).

Graetsch and Topalović-Dierdorf (1996) also investigated opal-AN using NMR with samples of hyalite from Gran Canaria. The spectrum of opal-AN exhibited a major signal at a chemical shift of -111.6 ppm and a shoulder at -102.5 ppm. A proton cross-polarisation ^{29}Si NMR experiment enhanced the signal at -102.5 ppm, showing that this resonance was caused by single protons attached to the tetrahedra (Q^3 configuration). The Q^3 signal was reported to be broader [FWHM = (-13.7 ± 1.3)ppm] than the Q^4 signal [FWHM = (-8.7 ± 0.2)ppm], indicating a wider range of variations in the local arrangements of the –OH bearing tetrahedra. Again, the signal from geminal silanol groups (Q^2 configuration) that should show up near -90 ppm was also lacking in all opal samples investigated. Compared with non-hydrous silica glass (-110.9 ppm) and Libyan Desert glass (-110.8 ppm), the Q^4 signal of hyalite was shifted to a higher field, indicating configurational differences (i.e. a slightly larger mean inter-tetrahedronal Si-O-Si angle; Graetsch and Topalović-Dierdorf 1996).

The half widths of the Q^4 signals of hyalite (opal-AN), opal-AG and synthetic hydrous silica glass were smaller than those of synthetic and natural non-hydrous silica glass. The width of this signal reflected the distribution of average Si-O-Si angles due to variations in the local surroundings of the four connected silicon tetrahedra. The distribution was narrower in the water-containing samples than in the synthetic or natural silica glass, which illustrated the importance of the network modifying effect of protons in silica during the formations of the glasses (Graetsch and Topalović-Dierdorf 1996).

7.1.6. Objectives

In this chapter, ^{29}Si NMR is used to study the relative disorder of opal-AG and opal-CT, and also to clarify the silanol bonding arrangement, which constitutes the chemisorbed water. ^{27}Al NMR is also used to determine the chemical environment of Al in various opals. It is expected that the results obtained here will associate the collective results of the experimental work of preceding chapters, providing a more complete perspective of the opal structure. The results should also offer insight into the differences between sedimentary and volcanic opals and their respective modes of formation.

7.2. EXPERIMENTAL

7.2.1. Sample Preparation

Four opal-AG and two opal-CT samples were analysed with Magic Angle Spinning (MAS) NMR spectroscopy. The opal-AG samples were obtained from various locations within Australia: Lightning Ridge, Coober Pedy, Andamooka and White Cliffs; while the Opal-CT samples were from Tintenbar and Mexico. All samples were cut to ensure there was no contamination from the surrounding host rock, before being crushed with an agate mortar and pestle.

The larger pieces of crushed opal were selectively packed into the sample rotor. Zirconia rotors (5mm diameter) were used exclusively, and were marked at the bottom with a black-coloured permanent felt tip marker pen to permit the measurement of rotation speeds.

7.2.1.1. Errors

A simple calculation was performed, to determine what effect crushing the sample would have on the surface area of the sample. This is significant, since an increase in the surface area of a sample would also increase the number of surface silanol groups present (when a Si–O–Si bond is broken, two Si–OH groups will form at the silica surface) and hence influence the ^{29}Si NMR results. Simple mathematical calculations can show that if a solid sample with a volume 1 cm^3 is crushed into 1,000 smaller cubes (each 1mm in size), the total surface area is multiplied by a factor of 10. Likewise, the total surface area is multiplied by factors of 100 and 1000 if the initial sample is crushed to 100μm and 10μm cubes, respectively. Assuming that the 1 cm^3 sample is crushed into 10μm cubes, 0.6m^2 additional surface area is therefore generated. Presuming once again that there are an average number of 4.6 –OH groups per 100 $Å^2$ of silica surface (Iler 1979; Zhuravlev 1989), this represents ~2.76x10^{18} atoms. Since 1 cm^3 of opal weighs ~2.1 grams (Smallwood 1999), and assuming for the sake of simplicity it is 100% SiO_2, there must be ~2.1x10^{22} atoms in the sample (2.1/60.09 x 6.023x10^{23}). Therefore, by crushing the 1 cm^3 sample to 10μm cubes, the additional surface area introduced accounts for only 0.013 % of the sample. Although it could be argued that crushed opals do

not give rise to perfect little cubes, the calculations nevertheless ascertain that crushing the opal samples for NMR analysis does not contribute to a significant increase of surface area, so long as the particle size is somewhat greater than 10μm. As the NMR samples consisted of little chips that were the order of several mm^3, the additional surface area generated is practically negligible; considering the limit of sensitivity of solid-state NMR is well above 0.013% (it is difficult to quantify exactly, but it probably approaches ~0.1% or higher), any additional silanol groups created would probably not even be detected.

7.2.1.2. Thermally aged specimen

One of the Tintenbar opal samples investigated with NMR was thermally aged. This sample was the same specimen previously used in the TMA experiment by Smallwood (1999). This sample underwent heating in the TMA apparatus by ramping from room temperature to 750°C at a heating rate of 5°C per minute, followed by air cooling.

7.2.2. ^{29}Si NMR acquisition parameters

7.2.2.1. Tuning and matching procedure; MAS optimisation

All spectra were recorded on a Bruker 300 MAS NMR spectrometer equipped with xwinnmr software, located at the Department of CMF, UTS city campus. Spectral sweep width was between 14,285 and 14,368 Hz for all ^{29}Si NMR spectra recorded. Dead time (d3) was 6.2μs for all ^{29}Si NMR spectra, with a total acquisition time of less than 0.036 seconds per pulse. Dwell time for all ^{29}Si NMR spectra was 34.8 to 35.0 μs, with a pre-scan delay of 30 μs.

Tuning and matching was first achieved by maximising the intensity of the wobble curve and aligning (centring) it with reference to the standard baseline of ^{79}Br in KBr. The magic-spinning angle (54.7º) was then optimised by maximising the intensity (and number) of spinning sidebands contained in the real-time spectrum. Chemical shifts were measured relative to the ^{29}Si resonance in kaolin; spectra were calibrated and the spectral reference was recorded.

7.2.2.2. Single pulse

The ^{29}Si NMR single-pulse spectra were acquired using an irradiation frequency of 59.62 MHz, and a MAS spinning rate of 3 kHz. Receiver gain was set to 18,390. A recycle delay time (d1) of 20 seconds was used between each 90° pulse, until 256 scans were accumulated. The combined FIDs were then processed[1] by a standard exponential multiplier function (identical in all cases), followed by Fourier transformation. The phase was also corrected manually to give a flat baseline.

7.2.2.3. Proton cross polarisation

The ^{29}Si {^{1}H}NMR cross-polarisation (CP) spectra were acquired using an irradiation frequency of 59.62 MHz for the primary nucleus (^{29}Si) and 300.13 MHz for the secondary nucleus (^{1}H). MAS spinning speeds were 7 kHz. Receiver gain was between 11,585 and 13,004, depending on the sample. For the CP-NMR experiments, a contact time (p15) of between 6 ms and 10 ms was used, with a recycle delay time (d1) of 1.0 s. The tuning procedure for the broadband nucleus (^{29}Si) was repeated as above, but the proton channel was also tuned separately in the same manner. A minimum of 10,240 scans were collected for each sample. The combined FIDs were then processed by a standard exponential multiplier function (identical in all cases), followed by Fourier transformation. The phase was also corrected manually to give a flat baseline.

7.2.3. ^{27}Al NMR

The ^{27}Al NMR spectra were obtained with an operating frequency of 78.2 MHz, and a spinning rate of 7 kHz. Spectral sweep width was 46,620.047 Hz; receiver gain was between 3647 and 14,596, depending on the sample. The recycle delay time (d1) was set to 1 second and the dead time (d3) was 6.2μs for all ^{27}Al NMR spectra, with a total acquisition time of

[1] The signal is weighted slightly towards t=0 rather than T=∞. The reason for this is that at t=0 the signal intensity is at its highest point, as the signal decays rapidly thereafter. Although an exponentially decaying signal persists for an infinite time, in practice the background noise level in the receiver overwhelms the signal in the FID well before t=∞. Obviously the same noise level exists throughout the entire duration of the FID, but once the signal drops to a level well below the noise it is logical to discontinue data acquisition for that particular FID. Since there is no real contribution to the NMR spectrum beyond that point, the FID is normally truncated by reducing the acquisition time to a value approximately 3 to 4 times T_2.

11.0 ms per pulse. Dwell time for all ^{27}Al NMR spectra was 10.725 μs, with a pre-scan delay of 7.14 μs.

The tuning and matching procedure for the broadband nucleus (^{27}Al) was repeated as above using ^{79}Br in KBr. Optimisation of the magic angle was undertaken in the same manner. The chemical shifts were measured relative to the ^{27}Al resonance in $AlCl_3$; spectra were calibrated and the spectral reference was recorded. A total of 1024 FID signals were collected with a recycle delay time (d1) of 1 second. The combined FIDs were then processed by a standard exponential multiplier function (identical in all cases), followed by Fourier transformation. The phase was also corrected manually to give a flat baseline.

7.2.4. Deconvolution

Curve fitting was attempted by several methods. Deconvolution was initially performed using the generic deconvolution program incorporated within the NMR spectroscopy software. The Origin 6.1 software utility, containing more advanced deconvolution algorithms, was also attempted. However, more success was achieved using an Excel spreadsheet simply by overlaying the superposition of two or more theoretical curves (using simple mathematical functions) with an experimentally acquired spectrum. Different parameters were evaluated, such as peak position, half width and shapes (Gaussian, Lorentzian, etc). Although more time consuming, curve-fitment was more accurate using the latter procedure.

7.3. RESULTS

7.3.1. ^{29}Si NMR – single pulse

The single-pulse ^{29}Si MAS NMR spectra showed a single broad asymmetric peak centred at -111.8 ppm for opal-AG samples, and at -111.9 ppm for opal-CT samples (Figure 7-9). Full width at half maximum (FWHM) values were 9.5 ppm for all four opal-AG samples, and 6.5 ppm for the two opal-CT samples. These results agree closely with other NMR data published in the literature (de Jong *et al.* 1987; Graetsch *et al.* 1990). The S/N ratio of the Mexican opal-CT sample was observed to be lower than the Tintenbar opal-CT sample as well as the other opal-AG samples.

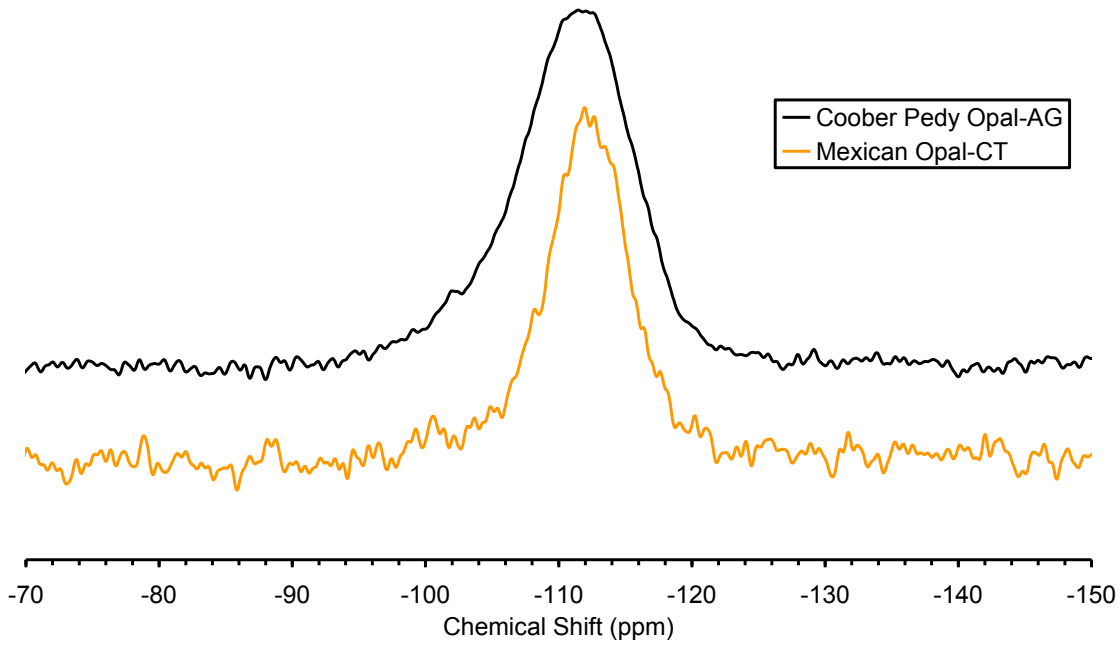

Figure 7-9: ^{29}Si NMR Bloch decay results of opal-AG from Coober Pedy (top) and Mexican opal-CT (below). The Q^4 resonance is centred at -111.8 ppm for opal-AG and -111.9 ppm for opal-CT.

7.3.1.1. Further investigation of Tintenbar sample (opal-CT)

After 256 scans were completed on the sample from Tintenbar, the spectrum showed signs of a second peak at around -102 ppm. Additional pulses were therefore acquired to improve the S/N ratio and attempt to resolve the apparent peak. After numerous scans were accumulated, the

spectrum revealed a small but distinct second peak at -102.5 ppm (Figure 7-10). The Tintenbar specimen was heated to 700°C, and analysed with NMR, and the intensity of the resonance at -102.5 ppm had substantially reduced when compared to the original un-aged sample. The spectra of the aged and un-aged Tintenbar samples are shown in Figure 7-10.

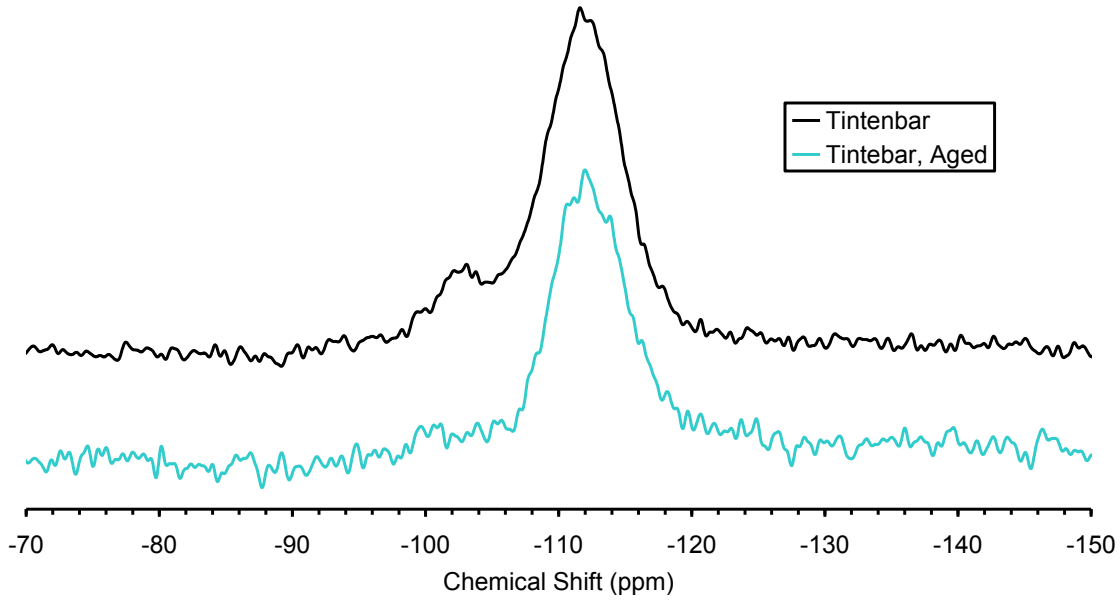

Figure 7-10: ^{29}Si NMR Bloch decay results of un-aged (top) and aged (bottom) opal from Tintenbar; the resonance present at -102.5 ppm in the un-aged sample is absent in the aged sample.

7.3.1.2. Peak deconvolution

As the NMR signals were asymmetric, an attempt was made to deconvolute some of the spectra to determine the proportions of the component peaks. Results are shown in Figures 7-11 and 7-12.

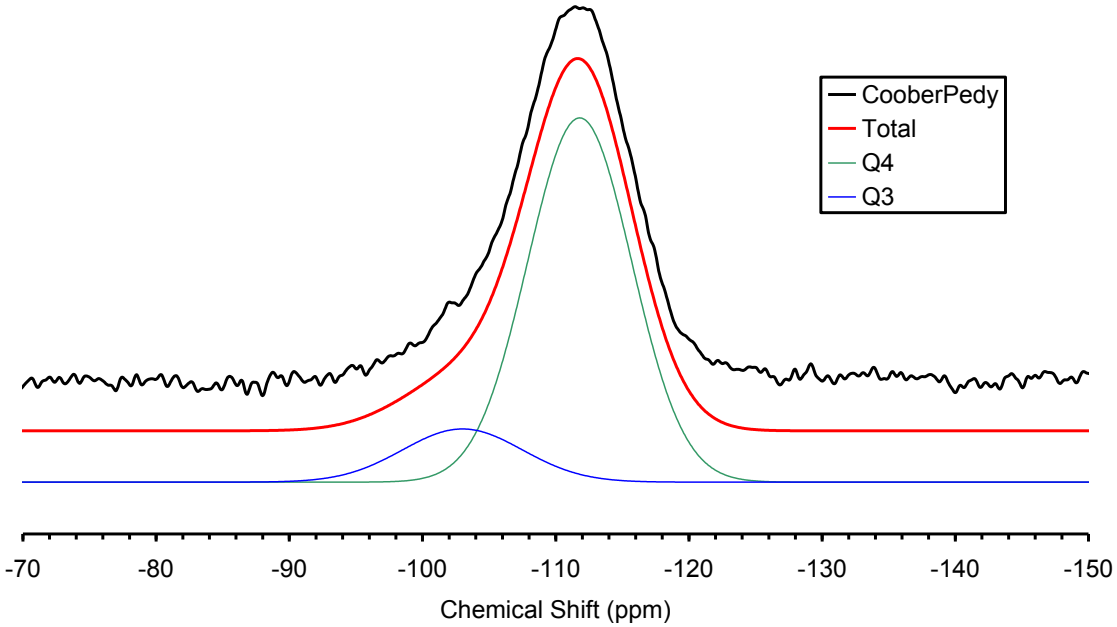

Figure 7-11: A single-pulse ^{29}Si NMR spectrum of an un-aged opal sample from Coober Pedy (top). The curve below it is a theoretical curve resulting from the superposition of the two Gaussian peaks (bottom) at -102.5 ppm and -111.9 ppm.

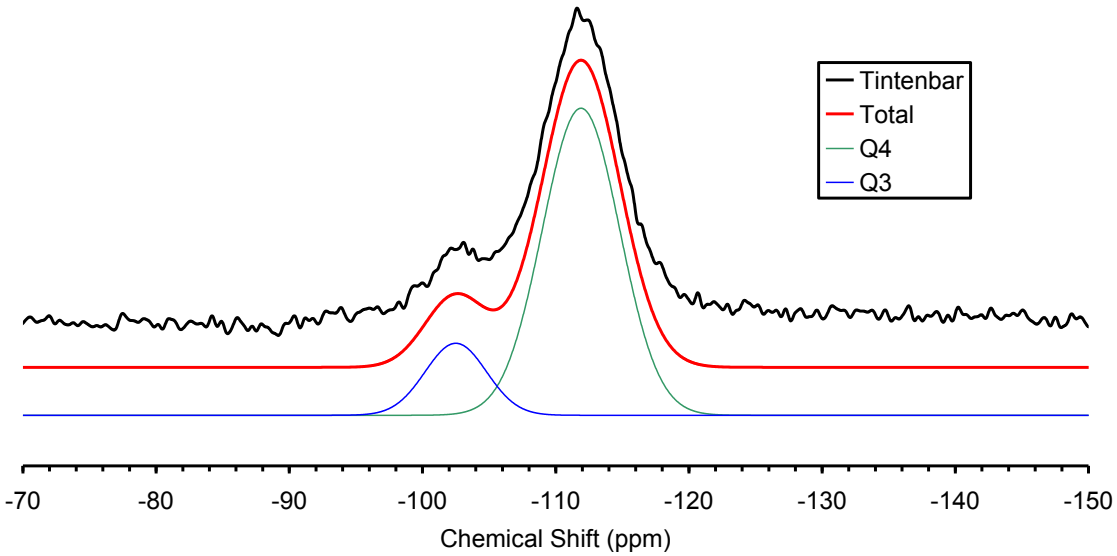

Figure 7-12: A single-pulse ^{29}Si NMR spectrum of an un-aged opal sample from Tintenbar (top). The curve below it is a theoretical curve resulting from the superposition of the two Gaussian peaks (bottom) at -102.5 ppm and -111.9 ppm.

7.3.2. ^{29}Si NMR – Proton cross-polarisation

The ^{29}Si {^{1}H} CP MAS NMR spectra of the opal-AG samples revealed a small shoulder at -102.0 ppm in addition to the primary peak, which was now centred at about -111.2 ppm. Cross-polarisation spectra of the two opal-CT samples showed the original peak at -112.2 ppm and a greatly enhanced peak at -102.5 ppm. Figure 7-13 shows the CP spectra of the opals, using a contact time of 10ms. The volcanic opal-CT samples evidently contain a greater proportion of Q^3 units than the sedimentary opal-AG samples. The Mexican opal sample again appears to have a lower signal to noise ratio (more noise) than all of the other samples. Table 7-1 demonstrates that the Q^4 chemical shifts of the opal-CT samples were 1.0 ppm more negative than those of opal-AG.

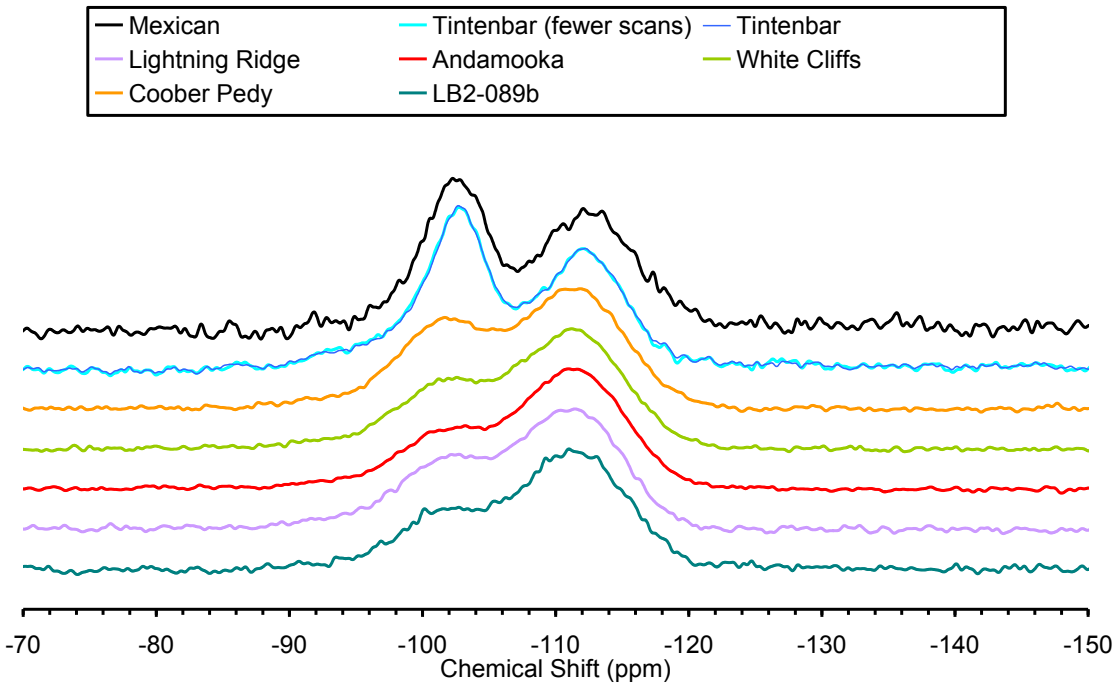

Figure 7-13: Stack plot of proton cross-polarisation ^{29}Si NMR spectra for various opals.

	Q^3	Q^4
Opal-AG	-102.0 ppm	-111.2 ppm
Opal-CT	-102.5 ppm	-112.2 ppm

Table 7-1: ^{1}H cross polarisation ^{29}Si NMR Resonance peak positions for opal-AG and opal-CT.

7.3.2.1. Reduction in contact time experiments

A small shoulder was discernible at approximately -94 ppm for these spectra, especially noticeable with the sample from Tintenbar. Therefore in an attempt to resolve this resonance, the contact time was reduced to 6ms and another spectrum was recorded from this sample. An extremely weak peak was detected at approximately -93.5 ppm (Figure 7-14).

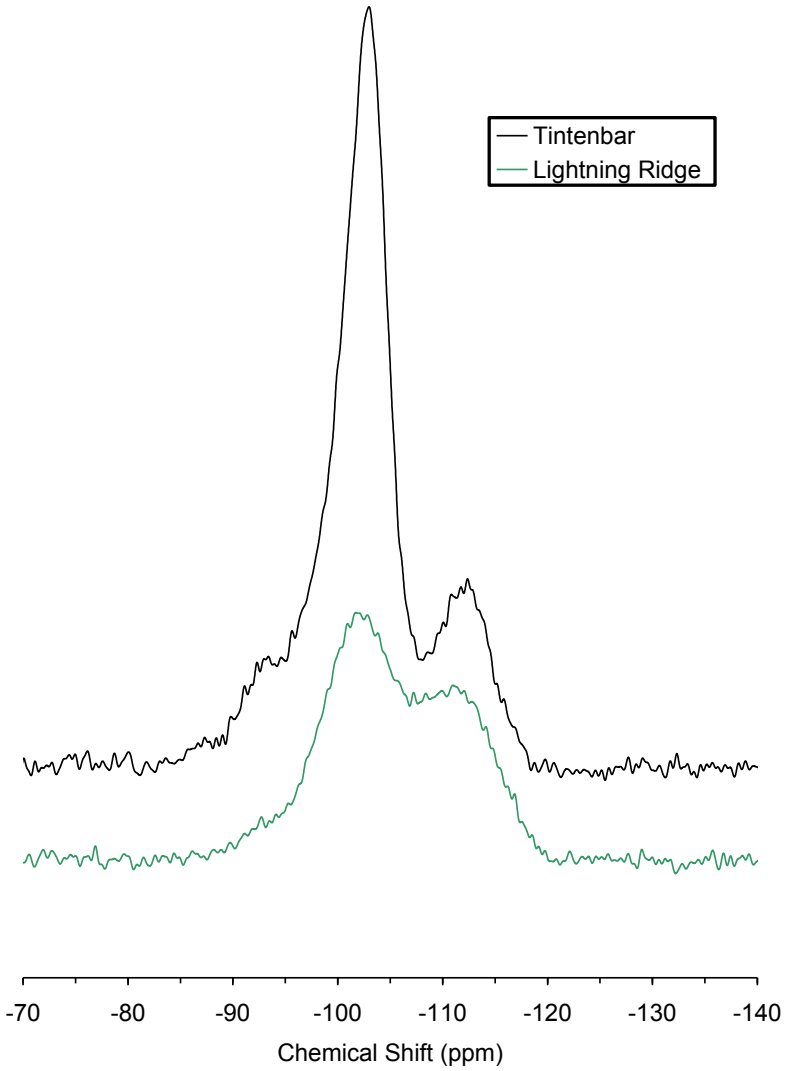

Figure 7-14: A proton cross-polarisation ^{29}Si NMR spectrum of the Tintenbar sample, obtained with a contact time of 6ms (top). A proton cross-polarisation ^{29}Si NMR spectrum of the Lightning Ridge sample, obtained with a contact time of 6ms (below). Note the shoulder that appears at -94 ppm in the spectrum of Tintenbar opal.

7.3.2.2. Peak deconvolution

The NMR results of the Andamooka sample were deconvoluted to attempt to determine the proportions of Q^4, Q^3 and Q^2 resonances compared with those of the Tintenbar sample (Figure 7-15). These could not be accurately quantified, as the technique of proton cross-polarisation intensifies the Q^3 resonance, and the exact magnitude of this enhancement is unknown.

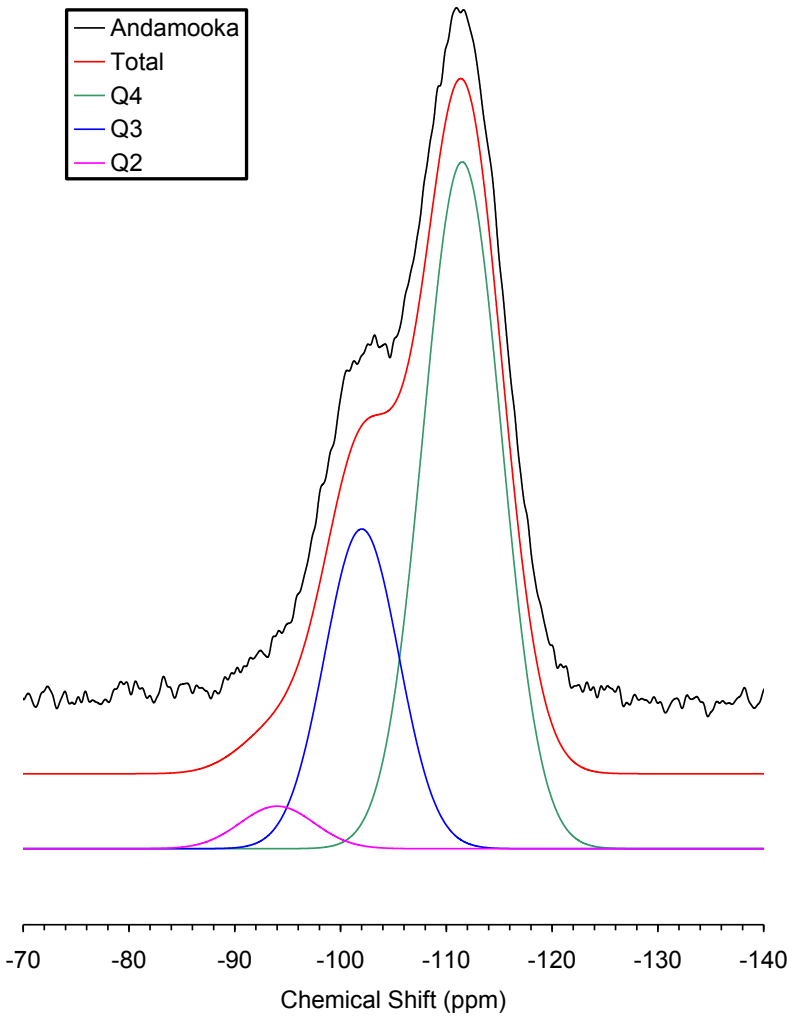

Figure 7-15: A proton cross-polarisation ^{29}Si NMR spectrum of Andamooka opal sample (top). The curve below it is a theoretical curve resulting from the superposition of the three Gaussian peaks (bottom) centred at -94.0 ppm, -102.5 ppm, and -111.5 ppm.

The signal intensity of the Q^2 resonance is approximately one-tenth of that of the Q^3 resonance in the CP ^{29}Si NMR spectrum of Tintenbar opal-CT (Figure 7-14). It follows that the Q^2 content is probably less than one-twentieth (5%) the fraction of Q^3, since the Q^2 resonance should be enhanced significantly more than the Q^3 resonance in a CP spectrum. Therefore with the opal-CT sample from Tintenbar, an approximate calculation of the proportion of Q^n configurations are as follows $Q^4 \approx 83\%$; $Q^3 \approx 16\%$; and $Q^2 \approx 1\%$. For the opal-AG samples, an estimation is that it contains half to one-quarter the ratio of Q^3 groups as opal-CT from Tintenbar. $Q^4 \approx 95\%$; $Q^3 \approx 5\%$; and $Q^2 \approx 0.25\%$.

7.3.2.3. Ageing of Tintenbar sample

Both intensities of the -102.5 and -112.2 ppm resonances are substantially decreased in the aged Tintenbar sample (Figure 7-16). The resonance at -102.5 is reduced to a greater degree than the -112.2 ppm resonance.

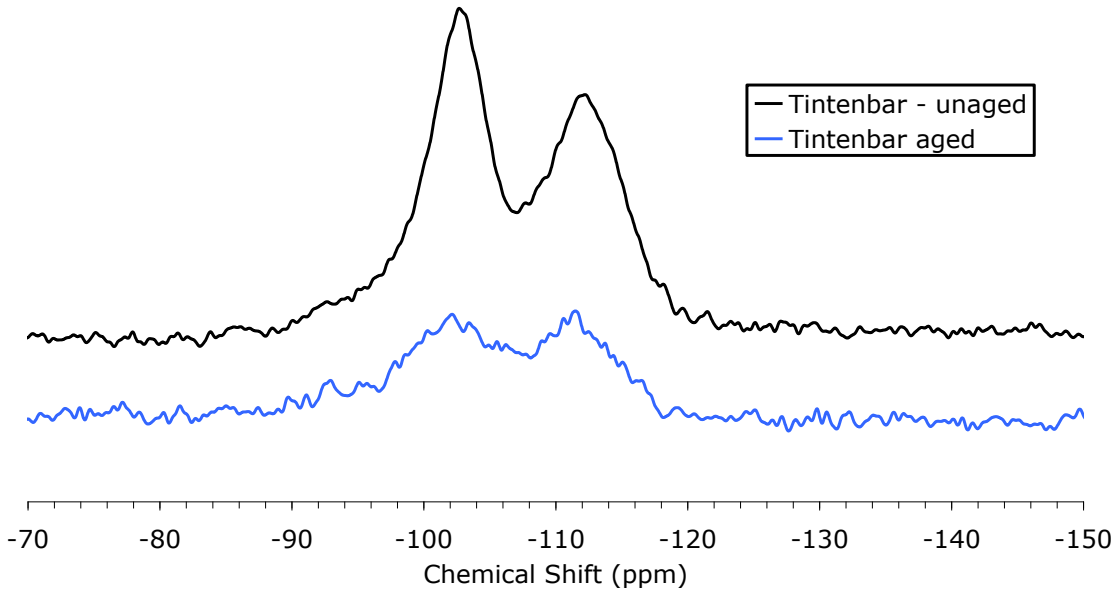

Figure 7-16: CP ^{29}Si NMR spectra of un-aged (top) and aged (bottom) opal-CT from Tintenbar. Note that both Q^3 and Q^4 resonances in the spectrum of aged opal exhibit reduced signal intensity; the Q^4 resonance is not reduced to the same extent as the Q^3 resonance.

7.3.3. ^{27}Al NMR

^{27}Al NMR was also performed on all six opal samples. Each of the spectra showed a single peak between +51.6 and +53.2 ppm (Table 7-2). No differences of any importance could be detected between the ^{27}Al NMR spectra obtained. One such spectrum can be seen in Figure 7-17.

Type of Opal and locality	^{27}Al NMR resonance (ppm)
Opal-AG, Coober Pedy	+53.2
Opal-AG, Andamooka	+51.7
Opal-AG, Lightning Ridge – translucent	+51.9
Opal-AG, Lightning Ridge – black	+52.3
Opal-CT, Tintenbar	+52.6
Opal-CT, Mexican	+51.8

Table 7-2: ^{27}Al NMR resonance positions for various types of opals and localities.

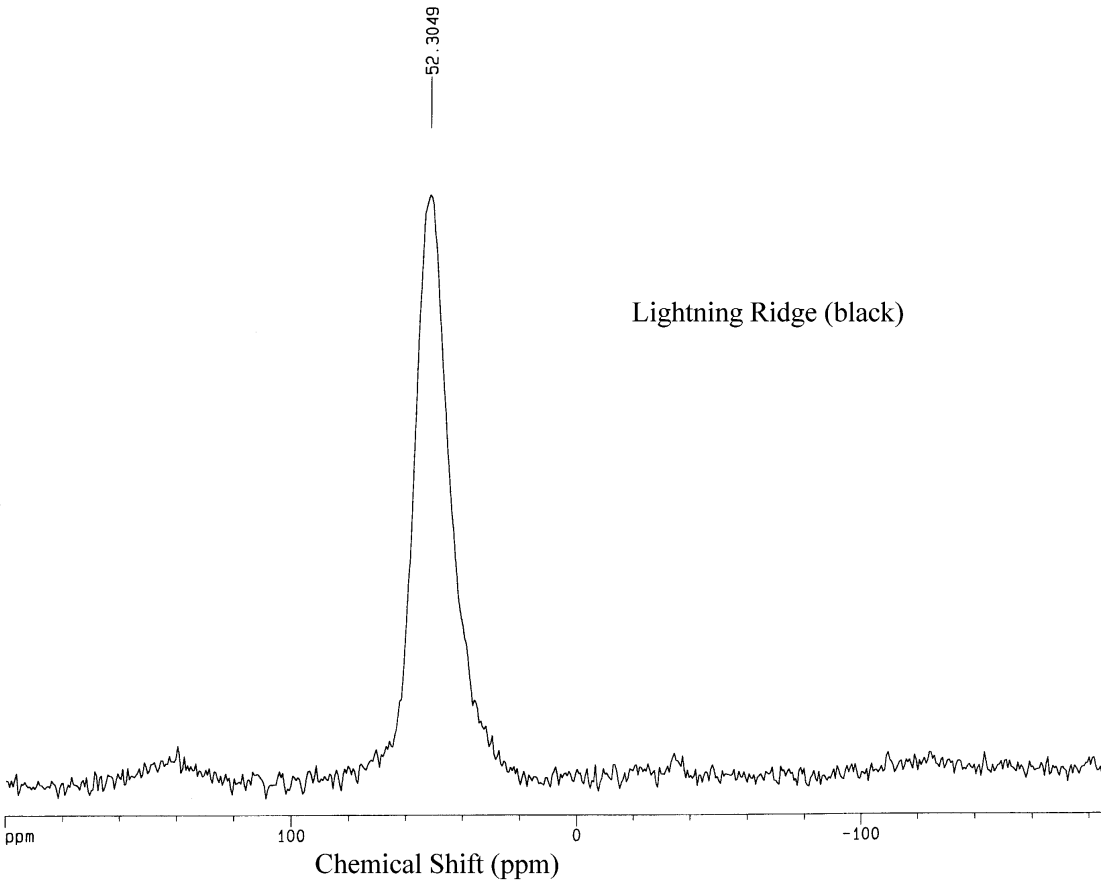

Figure 7-17: ^{27}Al NMR of opal-AG from Lightning Ridge. The small peak at 140 ppm is a spinning sideband.

7.4. DISCUSSION

7.4.1. ^{29}Si NMR - single pulse

The single broad peak at -111.8 ppm is characteristic of amorphous silica that is in the Q^4 structural arrangement. The asymmetry in the NMR spectra of opal-AG samples is most likely due to a combination of the major Q^4 resonance at -111 ppm and the lesser signal from Q^3(1OH), and perhaps Q^4(1Al), both of which occur at approximately -102 ppm (Lippmaa *et al.* 1981; Murdoch *et al.* 1985; Adams *et al.* 1991).

Part of the asymmetry observed in the Q^4 peak may be due to the asymmetry in the actual bond angle distribution, and not just from the superposition of the Q^3 and Q^4 peaks. I.e. the distribution of bond angles is not a symmetrical Gaussian function (for example if the average angle is 151º, there may still be more bonds present with an Si–O–Si angle of 141º than at 161º). This population of species would lead to a corresponding change in chemical shift (δ value), producing asymmetry in the principal Q^4 resonance. The existence of an asymmetric bond angle distribution may also imply that in addition to 6–membered rings of tetrahedra, there are 5– or 7–membered rings, with Si–O–Si angles smaller than 148 degrees (Graetsch *et al.* 1990).

The deconvoluted NMR spectrum of opal-AG from Coober Pedy (Figure 7-11) shows that the component Q^3 peak clearly has a much broader half width than the principal Q^4 peak. One explanation is that the tetrahedra giving rise to the Q^3 resonances show a broader range of bond angles than the majority of Q^4 tetrahedra. This proposition is plausible, as tetrahedra containing OH groups can only bond with three other tetrahedra and are thus able to take up more random positions in the network than their Q^4 counterparts, which bond with four other tetrahedra.

7.4.2. ^{29}Si NMR - Cross Polarisation

The CP spectra of opal-AG closely resemble those of other researchers (Adams *et al.* 1991; Graetsch *et al.* 1994). The resonance at -102.5 ppm is assigned to silicon in the Q^3(1OH) configuration, for two reasons. Firstly, the peak is absent for the sample that had been thermally aged. After heating,

silanol bonds are expected to be permanently removed from the silica network, and this is reflected in the difference between the two spectra. Secondly, the peak is significantly enhanced when the proton cross-polarisation technique is used, indicating that it is not caused by Q^3(1Al). If Al occurs as next-nearest neighbours to Si, forming Q^4(1Al) units, the ^{29}Si resonance would be expected to have a chemical shift similar to that of Q^3 units, but the Q^4(1Al) would not be enhanced in the ^{29}Si–{^{1}H} CP-MAS spectra (Adams *et al.* 1991).

The Q^3 resonance in the cross polarisation NMR spectra are most likely due to surface silanols rather than internal ones, because the surface silanols are more strongly H–bonded. Consequently, the Q^3 resonance will be enhanced to a higher degree than the internal[1] silanols, which are less H–bonded.

The degree of structural ordering affects the FWHM much more than the peak position. Therefore, since the structure is paracrystalline in the case of opal-CT, the peaks in the opal-CT spectra are narrower than the corresponding peaks in the opal-AG spectra, as they contain a smaller distribution of bond angles. This is also the reason the component peaks of the NMR spectra of opal-CT are more easily resolved than the spectra of opal-AG samples.

7.4.2.1. Q^2 resonance assignment

The weak resonance at approximately -94.0 ppm is most likely due to silicon in the Q^2(2OH) structural arrangement. Shorter contact times allow silicon atoms close to protons to give enhanced signals with respect to those further from protons (Maciel and Sindorf 1980). When the contact time was reduced from 10ms to 6ms, both the -102.5 ppm peak and the -94.0 ppm peak were significantly intensified, signifying that the nuclei attributed to these resonance peaks are in close proximity to protons. This result suggests that there are indeed geminal silanol groups contained within opal-AG and opal-CT, and they are not restricted to opal-AN, as suggested by Graetsch *et al.* (1994). The NMR spectra of opal-AG as seen by ^{29}Si NMR appears to be remarkably similar to that of a synthetic silica gel (Sindorf

[1] Within a silica sphere's interior.

and Maciel 1983), although the proportions of the various silanol groups are different. Although the concentration of these geminal hydroxyl groups must be extremely low, this result elucidates some earlier discussions on the thermal characteristics of opals, which postulated the existence of geminal hydroxyl groups within the structure (Jones and Segnit 1969).

7.4.2.2. Deconvolution of spectra

Some of the spectra were curve fitted. Generally, the spectra could be approximated very well with the superposition of three Gaussian peaks at -93.5 ppm, -102.5 ppm and -111.2 ppm. Figure 7-12 shows the fitting results of the single-pulse spectrum of a Tintenbar sample; Figure 7-15 shows the fitting results of the CP spectrum of an Andamooka sample. From the proportions of these component peaks it is clearly evident that opal-CT contains more single hydroxyl bonds than opal-AG and probably more twin hydroxyls as well. This deduction is in contrast to what is reported elsewhere (Langer and Flörke 1974; Flörke *et al.* 1991).

A curve fit was also attempted on the CP NMR spectrum of the Tintenbar sample, where the contact time was 6 ms. A reasonable fit was obtained with the three principal Q^2, Q^3, and Q^4 resonances. However, a slightly more accurate fit was achieved if a fourth peak around -98 ppm was included. This peak may be due to two different levels of shielding of a Q^3(1OH) groups, caused by varying degrees of H-bonding, such as an internal and a surface silanol, as proposed by Adams *et al.* (1991).

7.4.2.3. Bond Angles

The degree of structure order of the sample can also be inferred from the NMR signal; the broadness of the signal is due to a distribution in the average Si–O–Si bond angle per tetrahedron, and thus represents the extent of the relative localised disorder of the silica framework (de Jong *et al.* 1987). In this respect, Opal-CT obviously has more short-range order[1] than Opal-AG, because it shows a half-width of only 6.5 ppm, compared to 9.5 ppm for Opal-AG.

[1] In this respect, opal-CT has a narrower distribution of bond angles than opal-AG, localised around each appropriate nucleus.

The chemical shift of silica polymorphs correlates with the Si–O–Si bond angle (Dupree and Pettifer 1984; de Jong *et al.* 1987). The opal-AG spectra show Q^4 resonances at -111.2 ppm, while the two opal-CT spectra show their Q^4 shifted to an even higher field, at -112.2 ppm. This signifies that opal-CT has a slightly greater mean Si–O–Si angle than Opal-AG.

7.4.3. Tintenbar and Mexican opal-CT samples

The Q^3 signal in the spectra of Tintenbar and Mexican opal-CT is significantly greater than in the spectra of opal-AG (Figure 7-13). It was previously stated that well-ordered network structures exhibit inefficient nuclear relaxation when compared to those that are amorphous (7.1.2), and that this tends to reduce the sensitivity of NMR towards crystalline phases (7.1.4.5); the intense Q^3 signals in the spectra of paracrystalline opal-CT, when compared with those of amorphous opal-AG, are thus even more substantial than they first appear. This result signifies that these particular volcanic samples contain a higher proportion of chemically bound water than the sedimentary opal-AG samples. Conversely, opal-AG contains a higher proportion of molecular water than the opal-CT samples. Generally, opal-CT investigated with ^{29}Si NMR spectroscopy is found to contain less silanol groups than opal-AG; however, Graetsch *et al.* (1994) also noted that one green Bohemian opal-CT sample contained a high concentration of Q^3 units. The samples from Tintenbar and Mexico show Q^3 resonances even higher than the opal-AN analysed by Graetsch and Topalović-Dierdorf (1996); previously opal-AN was thought to contain a greater silanol water content than either opal-AG or opal-CT (2.6.2). This unusual but not unexpected result may be reflected in the formation of opal-CT in volcanic environments.

7.4.3.1. High proportion of Q^3 units

The ^{29}Si NMR bloch decay spectrum of the Tintenbar sample has a very high proportion (~19%) of Q^3 units, considering the same sample contains a total of only 6.5% water (as measured by TGA; Smallwood 1999). The 12.5% extra Q^3 units cannot be accounted for even if this resonance is partly due to Si(1Al), because the highest Al content so far detected is only 1.3% for a Lightning Ridge opal. The extraordinarily high proportion Q^3 units indicated in the NMR spectra can be explained as follows. The total

water content determined by TGA is measured in wt.%, whereas Q^n notations are in relative terms. Thus, the percentage of nuclei in the Q^3 environment is expressed in terms of the proportion of tetrahedra containing a single silanol group compared to the number of tetrahedra containing different numbers of silanol groups. I.e. for this particular sample, 19% of the nuclei have only one OH group, while the remainder are either fully interconnected tetrahedra (Q^4), or tetrahedra containing two silanols (Q^2).

The Q^3 units in question are undeniably Si–OH groups, as ^{29}Si NMR measures the bonds pertaining to nuclei (meaning that these Si-OH groups cannot be mistaken for molecular water). Moreover, this spectrum was undertaken without ^{1}H cross-polarisation, so this resonance cannot be due different silanol groups being more strongly H-bonded.

7.4.3.2. Thermal ageing experiment

The results of a thermal ageing experiment show that after ageing, the resonance at -102.5 ppm is absent (Figure 7-10). This result correlates with the previous model of dehydroxylation (Equation 3-1), resulting in significant shrinkage of the structure as measured by TMA (Smallwood 1999). As many of the surface –OH groups are driven off during thermal ageing, the structure must form new Si–O–Si linkages (Equation 3-1), although no changes were detected in the FWHM or peak position of the Q^4 resonance, which might otherwise be indicative of this reaction (to form new Si–O–Si linkages, others may need to be rearranged).

7.4.3.3. Opal-CT comparisons

The spectrum of the Mexican opal-CT sample did not exhibit the same contribution to the signal of Q^3 as the Tintenbar sample, indicating that a lesser proportion of silanol groups were contained in the Mexican opal-CT than the Tintenbar opal sample. The total water content of Tintenbar and Mexican opal-CT is 6.5 and 8.5%, respectively (Smallwood 1999), hence the high proportion of silanol groups in the Tintenbar opal becomes even more apparent. The reason for this is unclear, however the voids in some types of volcanic opal can be completely filled with interstitial silica (2.4). It is not known whether this additional silica could contain the supplementary

silanol groups observed in the ^{29}Si NMR spectroscopy results of the Tintenbar sample. Conversely, the Mexican opal could contain additional silica and this might instead reduce the internal surface area and hence lower the number of silanol groups present. Bustillo *et al.* (1993) previously reported that various types of opal-CT investigated with nitrogen adsorption analysis presented different specific surface areas, which was thought to be due to the different textures generated by their diverse genesis mechanisms. Mexican opal-CT was previously discovered by Smallwood (1999) to possess a transition temperature of 465 to 520°C, markedly higher than that of Tintenbar opal-CT (~215°C). This is clearly indicative of microstructural variations, and possibly genetic differences, between these samples.

7.4.3.4. Internal surface area of opal-CT

The N_2 adsorption results (calculated for pores with sizes between 1.7 and 300 nm), revealed that the modal size for the voids in the Tintenbar opal was only 1.7 to 1.8 nm. This indicates that the Tintenbar opal contains micropores even smaller than the limits of detection, therefore an extremely large internal surface area is inferred. The additional surface area of volcanic paracrystalline opal compared to sedimentary amorphous opal (2.4) certainly helps explain the additional silanol groups detected in the opal-CT samples, as these silanol groups primarily reside at inner surfaces. Theoretically, opal-AG is also expected to have a lower Si–OH content than a non-colloidal opal such as opal-CT, as the polymerisation of silica in a sol tends to minimise the number of uncondensed silanol groups (3.2.4).

The opal from Tintenbar thus contains a greater quantity of inner surfaces at which the additional silanol groups would reside. These voids also must be predominantly interconnected in nature. This hypothesis is supported by the SEM evidence of biogenic opal-CT, which has revealed a microstructure of lepispheres, yielding a high internal surface area (Figure 2-4).

7.4.3.5. Inferences about opal-CT structure and formation

Graetsch and Ibel (1997) used Small Angle Neutron Diffraction (SANS) to investigate precious, potch opal-A, opal-CT and opal-C and estimated

that the specific surface area of microcrystalline opal-CT is about ten times larger than in non-crystalline opal-AG, consistent with the SEM findings that opal-CT contains a very small particulate microstructure. Opal-CT of volcanic origin has been shown to contain "thin platy microcrystals" (Nagase and Akizuki 1997); the microstructure of wood opal also commonly consists of opal-CT lepispheres (Scurfield and Segnit 1984). Moreover, opal-CT lepispheres have been observed to increase in size, and the blades give way to a more "lumpy" morphology with time (Williams *et al.* 1985). Bustillo *et al.* (1993) has reported that the growth of lepispheres can increase the specific surface area considerably. Atomic-scale variations on the surfaces of silica spheres associated with these textures undoubtedly contain a much higher surface area than the smooth amorphous spheres within opal-AG.

Although these lepispheres have not yet been observed in opal from Tintenbar and Mexico with SEM, they are probably only just starting to form through the silica diagenesis mechanism. Indeed, several studies have shown that the degree of paracrystallinity of opal-CT varies according to different types of samples, and that it is better described as a continuous series extending from opal-A to opal-C (Plyusnina 1979; Williams and Crerar 1985; Williams *et al.* 1985; Elzea and Rice 1996; 2.5.2). Furthermore, the process of etching fracture surfaces with HF acid (to provide the relief necessary for SEM imaging) would also dissolve most traces of these newly forming small-scale textures.

Alternatively, the high internal surface area evident in Tintenbar opal-CT may arise as a consequence of the 'mobility via metastability' mechanism outlined below. Opal from Tintenbar exhibits the XRD patterns of opal-CT (Smallwood 1999), but shows evidence of a colloidal sphere microstructure similar to opal-AG (Tintenbar opal often displays a poc, but unfortunately it is difficult to image). Normally, crystalline materials are expected to be more dense than amorphous ones, yet opal-CT of volcanic origin is consistently found to have a lower density (2.00±0.05 g/cm^3) than sedimentary opal-AG (2.1 to 2.2 g/cm^3) (Koivula *et al.* 1983; Smallwood 1999). Opal-CT rocks in diagenetic sequences are often much more porous than the accompanying cherts consisting of quartz or chalcedony (Landmesser 1995), and the mobility by metastability mechanism yields

bodies with significantly lower densities (3.4.2). Yet the voids (between spheres) in opal-CT are often completely filled with silica and this additional silica would tend to increase the bulk density of opal-CT, not reduce it. Landmesser (1995) previously reported that the density discrepancy introduced through the action of silica diagenesis can result in the formation of tiny voids in the transformed bodies (3.4.2). Hence, this density discrepancy suggests that volcanic opal-CT has a slightly more open, porous structure than opal-AG (in relation to the silica network itself). This presumption is supported by previous TGA results (Smallwood 1999), which showed that water was removed from Tintenbar opal-CT at lower temperatures than opal-AG from all other Australian regions investigated.

7.4.3.6. Model for volcanic opal-CT precipitation

Opal-AG can first precipitate and coagulate via the mechanisms outlined previously (3.1). Since there are pore networks present within the structure of opal-AG, silica with different solubilities arises and thus transport and accumulation of silica is initiated, ultimately allowing localised phase transitions via Landmesser's mechanism (3.4.2). Hence silica is able to be transported at the surfaces of the spheres where it is transformed to opal-CT. This process does not exclude the silica from proceeding to more ordered phases such as opal-C via the diagenesis mechanism (3.4.1) at sites where silica is not able to be transported (for example, the centre of silica spheres). This transition occurs more rapidly at elevated temperatures.

Since the extent of the solution transport is a time dependent process (Williams and Crerar 1985; Landmesser 1995, 1998; 3.4.2), and as the voids of Mexican opals are known to be more completely filled than opal-AG, this suggests that the Mexican opals are geologically more ancient than other opals, such as opal-AG, which is thought to be geologically young (Darragh *et al.* 1976). This is in accordance with the silica diagenesis mechanism, which asserts that opaline silica naturally becomes more crystalline with age. The local concentration or addition of silica at sites of enhanced permeability in opal-A diatomite plays a critical role in promoting early formation of opal-CT (Cady *et al.* 1996).

7.4.3.7. S/N ratios of opal-CT samples

Curiously, the opal sample from Mexico consistently had a lower signal to noise ratio (more noise) than all of the other samples; the cause of this behaviour is conjectured below. Mexican opal is known to contain significant quantities of Fe (giving it a distinctive orange colouration), and the presence of this paramagnetic element in silicates is known to reduce lattice relaxation times significantly (7.1.2.2; 7.1.4.5). Since the presence of high amounts of Fe in Mexican opal-CT can facilitate efficient paramagnetic relaxation, it is therefore conceivable that the NMR spectra will exhibit increased linewidths due to the high abundance of this paramagnetic impurity, hence the quality of the spectra may be degraded.

On the other hand, it is feasible that this Mexican sample contains a more ordered cristobalite-tridymite stacking sequence than the Tintenbar sample, as NMR is not as sensitive to crystalline phases as amorphous ones. Langer and Flörke (1974) reported that opal from Tintenbar was not as crystalline as it should be and may have contained regions of both opal-AG and opal-CT phases. The importance of this finding supports the idea that the various silica phases are represented as a continuous series of structural order extending from opal-CT to opal-C, and also from opal-A to opal-C (Plyusnina 1979; Williams and Crerar 1985; Williams *et al.* 1985; Elzea and Rice 1996). I.e. various samples of opal-CT retain different degrees of structural order.

It was previously stated that "The ordered regions of opal-CT occur in a matrix of disordered silica, although it is unknown whether the ordered domains are anhydrous and thus can be identified as cristobalite" (2.5.2). This is clearly not the case, as the NMR spectra of Tintenbar opal indicates that the 'ordered phase' in fact contains a significant quantity of silanol groups, and furthermore, that this phase appears to be much more disordered than the NMR spectra of either tridymite or cristobalite. Since NMR is a next-nearest neighbour analytical technique, and as the Q^4 resonance of the opal-CT samples has a narrower half width than all of the opal-AG samples, these silanol groups are known to be bonded directly within the 'ordered phase'.

7.4.4. Theoretical Surface Area

An approximate[1] measure of the theoretical Si–OH content of an opal can be calculated by the following method. Firstly, knowing size of spheres, the number of spheres per cm^3 may be determined, and by simply using the equation $S.A=4\pi r^2$, an approximation of the total internal surface area can be calculated. The theoretical number of Si–OH groups can also be calculated by assuming 4.6 –OH groups for each 100 $Å^2$ of surface area for a complete monolayer coverage on silica (Iler 1979; Zhuravlev 1989). The number of atoms can be determined by using the molar fraction of silica divided by the molecular mass of SiO_2 and then multiplying by Avogadro's number. The total percentage of surface silanol bonds can then be estimated by dividing the approximate number of Si–OH groups by the number of atoms present. For spheres of 100 nm diameter arranged in an FCC lattice, the theoretical SSA amounts to 21 m^2/g, assuming a density of $2.1g/cm^3$. This represents ~0.96% surface silanols. The results obtained from nitrogen adsorption experiments show that the SSA of opals (0.25 to 2.6 m^2/g) is less than the figure calculated here, but as discussed previously some of the surface area is inaccessible to N_2 molecules (4.4.6). Also, the calculations above assume that silica has not been accumulated in solution via Landmesser's mobility by metastability mechanism.

7.4.5. ^{27}Al NMR

Dissolved Al concentration in the sol depends primarily on the solubility of aluminosilicate minerals as a function of pH and on their abundance (Hinman 1998). In natural systems, dissolution of clay minerals, zeolites, and feldspars maintains the concentrations of dissolved Al (Hinman 1998).

For all the types of opal investigated, the ^{27}Al NMR spectra display a single resonance around +52 ppm. This result ascertains that all the Al ions are all in a tetrahedral arrangement, substituting for silicon atoms within the molecular structure; thus opal is technically an aluminosilicate (de Jong *et al.* 1983; Smith *et al.* 1984). These results contrast with those of Bartoli

[1] There may also be internal silanols contained within the silica spheres and in the additional silica between the spheres, but it is difficult to determine their relative proportions and hence calculate the total number of these silanol groups. This calculation also assumes a single layer of hydroxyls is present, not multiple layers.

et al. (1990), who reported that there was little or no Al for Si substitution in Australian opals. Since these samples contain as much as 1% Al, it is not surprising that these atoms occasionally substitute for silicon; as the opals were originally polymerised from silica-rich solutions, they must have contained sufficient Al to become incorporated within the network structure. The ^{27}Al NMR results therefore support the idea that the impurities were present during the growth of the colloids (3.4.3.1), as the abundance of Al was high in all bands of opals.

Iler (1973) studied the effect of adsorbed alumina on the solubility of amorphous colloidal silica in water; it was shown that even very low concentrations of Al (equivalent to less than a monolayer coverage) drastically reduced the rates of silica dissolution and solubility. Iler proposed that the negative aluminosilicate ion sites on the surfaces of colloids are able to prevent the approach of hydroxyl ions, which are required to catalyse the dissolution of silica. Since aluminium can be adsorbed onto the surfaces of silica colloids, effectively reducing their solubility, it is reasonable to expect that these colloids can then become supersaturated, leading to precipitation. Since the results presented here show that aluminosilicate sites are in fact present within all the opals studied, and previous results have shown the composition of Al can vary from one band to another (5.3.2; Table 5-2; Table 5-5), Al may be able to control the coagulation of individual opal bands in certain samples (e.g.: samples LR2, LR5, LR7 and A2).

The presence of Al in silicate glasses reduces the tendency for non-bridging oxygen formation (i.e. the number of Q^3 and Q^4 groups will reduce). Using the technique of ^{29}Si CP NMR, silanol groups (Q^3 groups, which are essentially non-bridging oxygen atoms) were detected in these opals, despite the incorporation of approximately 1% Al within the network structure.

7.4.5.1. pH of solution

A resonance corresponding to Al ions in an octahedral configuration was not observed (the ^{27}Al NMR resonance for kaolinite appears at -19 ppm; de Jong *et al.* 1983). According to Merino *et al.* (1989), and assuming the

temperature of formation was close to 25°C, this result infers that the original pH of the sol must have been in excess of 7, which is the highest pH at which the octahedral to tetrahedral transition can take place. It is well known that if the pH of a silica sol is between 2 and 7, a true gel will form in preference to a dense coagulate (Iler 1979). Since the microstructure of opal does not have a gel-type microstructure, but instead a denser colloidal structure, these results further attest that the pH of the original solution must have been between 7 and 10.5 (at which point the silica will dissolve).

7.5. CONCLUSIONS

Opal-CT from Tintenbar and Mexico was found to have significantly more silanol bonds than Australian opal-AG. This result was explained in terms of the very fine textures associated with some types of opal-CT lepisphere microstructures, which generate large internal surface areas. Geminal silanol groups (Q^2) were also detected in opal-CT and to a lesser extent, opal-AG; these double silanol groups were previously thought to be restricted to opal-AN.

Rudimentary curve fitting of ^{29}Si NMR spectra was also attempted; this process involved superimposing the original spectrum with various theoretically-derived curves, while trialling various parameters to permit the most accurate fit. It was thus determined that the resonances were centred at -94.0 ppm, -102.5 ppm, and -111.5 ppm, and these were attributed to Q^2, Q^3 and Q^4 configurations, respectively.

The ^{27}Al NMR experiments revealed that all Al atoms were tetrahedrally coordinated (i.e. shown to be an integral part of the silica network structure) within all the opal-AG and opal-CT samples investigated. This finding also validates the pH of formation of the original solution; while the aluminium was being incorporated into the silicate network structure during the time of colloidal formation, the pH must have been at least 7.

In conclusion, this data also clarifies earlier XRD research by Elzea and Rice (1996) who stated that their curious results may be the result of several types of disorder, such as Al substitution, variable OH structural positions, etc.

8. CONCLUSIONS

Hofstadter's Law: it always takes longer than you expect,
even when you take Hofstadter's Law into account.

The presently accepted model of opal formation, sphere sedimentation from a silica sol, is a process that is only valid for homogeneous samples. It is currently rather limited and cannot adequately explain how banded samples develop. The origin of the bands has remained a mystery, and the generally accepted sphere-sedimentation model of opal-genesis (Darragh *et al.* 1966) appears inadequate to account for banded opal samples. Differences in elemental composition of each layer are likely to be due to differences in their respective mechanisms of formation. Hence, a solution containing a high level of impurities should form a more polydisperse sol, which cannot produce an ordered microstructure. To better understand the mode of formation of banded opals, the degree of homogeneity contained in each band has been assessed. Thus, the subtle differences in environmental conditions that result in potch or precious opal can be identified in this manner.

The concentration of transition and rare-earth metals were found to be dependent on the colour of the opal sample. Black and grey samples contained a higher abundance of most of these elements than white or clear samples. It is thought that the transition metal ions contribute to the base colours observed with opals. Numerous differences in the transition and rare-earth elemental profiles were also detected within banded samples that contained both light and dark layers (such as black-grey or grey-poc). As these differences were distinct and repeatable, the following model was proposed to account for the most common types of banded samples encountered. Since highly charged cations allow metastable colloids to coagulate through charge-neutralisation mechanisms, they may cause the first opal layer to precipitate. Given that this process occurs relatively rapidly, these particular colloids must accumulate in a disorderly manner, especially if they are polydisperse. As this layer contains a high abundance of transition metal ions, colour must also be generated in it. The remaining sol is hence depleted of these impurities, and therefore can yield monodisperse colloids via the Ostwald ripening mechanism. The colloids are now able to form ordered arrays if they settle slowly enough (or if salt concentration is within the right range). This layer would appear almost colourless, because it contains less transition metal ions than the previous

layer; depending upon the extent of solution transport, an opaque, translucent or transparent opal could be generated. So long as the salt concentration is within a certain range, this layer may also show a play of colour, otherwise a layer of potch opal will result.

Thermal analysis showed that various types of opals exhibited different thermal behaviour. The differences observed in the rates of dehydration, and temperatures of maximum dehydration as measured by TGA were attributed to differences in the overall porosity and interconnectivity of the opal's pore structure. The collapse of this pore structure at elevated temperatures was manifested in the thermal expansion curves, which were measured by TMA. Following an initial period of expansion, the onset of shrinkage (sintering) and its extent were dependent on the type, or origin, of the opal. The opals were observed to sinter at relatively low temperatures during thermal characterisation; this result was due to the extremely small pores (2 to 4nm) contained within the opals, measured by nitrogen adsorption experiments.

Based on results obtained by nitrogen adsorption, chemical and thermal analyses, the opaque white and clear samples appeared to have different microstructural characteristics. Opaque white samples contain a greater degree of porosity than transparent opals; the additional voids consequently scatter light internally, rendering the opal opaque. The opaque opals (white, grey black) displayed higher alkali contents than the transparent or translucent opals. The presence of salts are known to produce open gel-like structures instead of denser coagulates during the colloidal agglomeration phase. Therefore, the presence of supplementary alkali metals during colloidal aggregation may have led to a slightly more "open" void structure, causing the resulting opacity in these samples.

The mechanism for the transport of silica within the void spaces of these opals, "mobility by metastability", shows that silica may be transported from regions of higher free energy (surfaces with positive curvature) to regions of lower surface energy (where spheres are in contact, having a negative radius of curvature). The pore structure of amorphous opals is initially determined by the voids that result from any system of

close-packed spheres. The shape of these voids are modified by the amount of accumulation of silica that is transported into them from other regions. This is confirmed by the nitrogen adsorption experiments which showed that the porosity of transparent opals (whose voids are filled to a greater extent) was less than opaque opals (whose voids are filled to a lesser extent). The maximum rate of water loss measured by TGA occurred at different temperatures depending on the opal, which is indicative of pore networks with different amounts of interconnectivity, further supporting this hypothesis. The variations in microstructure for opaque and white opal samples were thus attributed to the extent of solution transport following colloidal coagulation, and the extent of this process is region-dependent.

The variation of Al between the bands in banded opal samples is insignificant, yet there is a vast difference in the aluminium concentration of different opal samples originating from the same opal mining regions. Hence, the numerous bands contained in banded opals appear to be formed at similar times. ^{27}Al NMR revealed that Al substitutes for Si within opal, suggesting that spheres may be formed first, followed by band formation. The process of charge neutralisation may then proceed, allowing separate bands of opal to be formed. If the bands were formed at significantly different times, the trace element composition of the various bands would be expected to reflect those differences.

For one unusual opal specimen (sample A2), differences in the Mg, K, Ba, and Fe concentration were observed between the various bands (for elemental profiles), unlike all other samples analysed. It was proposed that the liesegang phenomenon may be responsible for the multiple parallel bands within this particular sample. This is a periodic precipitation mechanism that occurs in many types of gel systems, resulting in pattern formation. Previously, generalised statements have been made regarding opal formation at certain mining locations, but it now appears that not all opal-AG can be categorised as being formed in the same manner.

Vicinal silanol (Q^3) groups were present in all the opals studied (with ^{29}Si NMR resonances between -102 and -102.5 ppm). The two volcanic opal-CT samples (from Tintenbar and Mexico) were found to contain

significantly more vicinal silanol groups than the sedimentary opal-AG samples from Australia. The greatest number of vicinal silanol groups was detected in Tintenbar opal-CT; while the abundance of vicinal silanol groups in Mexican opal-CT was found to be slightly less than that of Tintenbar. This result was ascribed to the differences in internal surface areas, which are possible with lepisphere type opal-CT microstructures of different origins. The subsequent transport and deposition of silica within opal-AG after its initial formation inherently reduces its porosity, thereby reducing the internal surface area; this is reflected in the lower number of vicinal silanol groups in opal-AG compared with opal-CT. Nitrogen adsorption analyses confirmed that opal-CT from Tintenbar contained a median pore size that was smaller than the opal-AG samples investigated (<17-18Å). Geminal silanol groups (Q^2) were also detected in low amounts within Tintenbar opal-CT (-93.5 ppm), and in even lesser numbers in opal-AG.

^{27}Al NMR revealed that the aluminium ions in the opal samples analysed were tetrahedrally coordinated (+51.7 to +53.2 ppm); no octahedrally coordinated aluminium was detected. This result inadvertently established the original pH of the sol during opal formation; according to the work of Merino *et al.* (1989), for temperatures of 25°C, the pH must have been in excess of 7, since that is the highest pH at which octahedral aluminium will form.

In conclusion, a range of characterisation techniques have been applied to the characterisation of Australian opal. These analytical techniques have demonstrated that they can distinguish amongst the different chemical and microstructural characteristics of various types of Australian opals. The amalgamation of results obtained from nitrogen adsorption, thermal and elemental analytical techniques has shown that different microstructural characteristics within an opal can arise directly as a consequence of the initial composition of the silica sol, and that this in turn can affect the incorporation of water into the structure. A detailed understanding of the trace element composition and microstructure of opals has thus underscored the level of complexity in their formation processes.

REFERENCES

Adams, S.J. et al. 1991 "A solid state ^{29}Si nuclear magnetic resonance study of opal and other hydrous silicas" Am. Miner., **76**, 1863-1871.

Adamson, A.W. 1990 "Physical Chemistry of Surfaces" 5th ed. John Wiley and Sons, New York.

Anderson, J.H. and Wickershiem, K.A. 1964 "Near infrared characterisation of water and hydroxyl groups on silica surfaces" Surface Science, **2**, 252-260.

Andrew, E.R. 1981 "Magic angle spinning in solid state NMR spectroscopy" Philosophical Transactions of the Royal Society of London, Series A: Mathematical, Physical and Engineering Sciences, **299**(1452), 505-520.

Astratov, V.N. 1996 "Photonic band gaps in 3D ordered fcc silica matrices" Physics Letters A, **222**, 349-353.

Baier, E. 1966 "Diffraction lattices in precious opal an example of crystallisation from supra–molecular elements" Experientia, **22**, 129-133.

Ball, R.A. 1982 "Common opal and potch opal" Aust. Gemmol. 305-310.

Ball, R.A. 1985 "Black opal: A brief review" Aust. Gemmol., 310-314.

Bamford, C.R. 1977 "Colour generation and control in glass" Elsevier Scientific Publishing Company, Amsterdam.

Banerjee, A. and Wenzel, T. 1999 "Black opal from Honduras" Eur. J. Mineral., **11**, 401-408.

Bansal, N.P. and Doremus, R.H. 1986 "Handbook of glass properties" Academic Press, Orlando.

Barnes L.C. and Townsend, I.J. 1982 "Opal, South Australia's Gemstone" Dept. Mines and Energy.

Bartoli, F. and Wilding, L.P. 1980 "Dissolution of biogenic opal as a function of its physical and chemical properties" Soil Sci. Soc. Am. J., **44**, 873-878.

Bartoli, F. et al. 1990 "Role of aluminium in the structure of Brazilian opals" Eur. J. Mineral., **2**, 611-619.

Bascom, W.D. et al. 1970 "Evidence that polywater is a colloidal silicate sol" Nature, **228**(5278), 1290-1293.

Baur, W.H. 1977 "Silicon–Oxygen bond lengths, bridging angles Si–O–Si and synthetic low tridymite" Acta Cryst., **33**, 2615-2619.

Bayliss, P. and Males, P.A. 1965 "The Mineralogical similarity of precious and common opal from Australia" Mineralogical Magazine, **35**(270), 429-431.

Behr, H.J. et al. 2000 "Cretaceous microbes - Producer of black opal at Lightning Ridge, NSW, Australia" Geological Society of Australia, Abstract **59**, 15th Australian Geological Convention, Sydney.

Benesi, H.A. and Jones, A.C. 1959 "An infrared study of the water–silica gel system" Journal of Physical Chemistry, **63**, 179-182.

Benninghoven, A. et al. 1987 "Secondary Ion Mass Spectrometry: Basic Concepts, Instrumental Aspects, Applications, and Trends" John Wiley and Sons, New York, 1987.

Bermanec, V. et al. 2004 "Nanocrystals of Tridymite in Opal Cavities" 8th International Congress on Applied Mineralogy, São Paulo, 525-527, ISBN: 85-98656-02-X.

Bezrukov, A. et al. 2001 "Spatial statistics for simulated packings of spheres" Image Anal. Stereol., **20**, 203-206.

Bogomolov, V.N. et al. 1997 "A comparative TEM study of the 3D lattice of tellurium nanoclusters fabricated by different techniques in an opal host" Phys. Solid State, **39**(11), 1869-1874.

Botz, R. and Bohrmann, G. 1991 "Low-temperature opal-CT precipitation in Antarctic deep-sea sediments: evidence from oxygen isotopes" Earth and Planetary Science Letters, **107**, 612-617.

Brown, L.D., Ray, A.S., Thomas, P.S., and Guerbois, J.P. 2002 "Thermal Characteristics of Australian Sedimentary Opals" J. Therm. Anal. Calor., **37**, 31-36.

Brown, L.D., Ray, A.S. and Thomas, P.S. 2003 "^{29}Si and ^{27}Al NMR study of amorphous and paracrystalline opals from Australia" Journal of Non-Crystalline Solids, **332**, 242-248.

Brown, L.D., Ray, A.S. and Thomas, P.S. 2004 "Elemental analysis of Australian amorphous banded opals by laser-ablation ICP-MS" Neues Jahrbuch für Mineralogie - Monatshefte, **9**, 411-424.

Brummer, S. B. et al. 1972 "Anomalous water" U.S. Nat. Tech. Inform. Serv., Govt. Rep. Announce., **72**(18), 62.

Buerger, M.J. and Shoemaker, G.L. 1972 "Thermal Effect in Opal Below Room Temperature" Proc. Nat. Acad. Sci. USA, **69**(11), 3225-3227.

Büki, A. et al. 1995 "Two dimensional chemical pattern formation in gels. Experiments and computer simulation" Physica A, **220**, 357-375.

Bustillo, M.A. et al. 1993 "Specific surface area and ultramicroporosity in polymorphs of silica" Eur. J. Mineral., **5**(6), 1195-1204.

Bustillo, M.A. 1995 "Una nueva ultraestructura de opalo CT en silcretas. Posible indicator de influencia bacteriana" Estudios Geol., **51**, 3-8.

Bustillo, M.A. and Martínez-Fríaz, J. 2003 "Green opals in hydrothermalized basalts (Tenerife Island, Spain): alteration and aging of silica pseudoglass" Journal of Non-Crystalline Solids, **323**(1-3), 27-33.

Cady, S.L. et al. 1996 "HRTEM of microcrystalline opal in chert and porcelanite from the Monterey Formation, California" Am. Miner., **81**, 1380-1395.

Carr, S.G. et al. 1979 "Andamooka opal fields: The geology of the precious stones field and the results of the subsidised mining program." Geological survey of South Australia, Report of investigations 51.

Champagnon, B. et al. 1997 "Differentiation of natural silica glasses using Raman microspectrometry" Chem. Erde., **57**(2–3), 289-296.

Chang, J. and Yortsos, Y.C, 1994 "Lamination during silica diagenesis – effects of clay content and Ostwald ripening" American Journal of Science, **294**, 137-172.

Cheng, B. et al. 1999 "More direct evidence of the FCC arrangement for artificial opal" Optics Communications, **170**(1), 41-46.

Chojcan, J. and Sachanbinski, M. 1993 "Positron Annihilation in Tektite and Hyalite" Acta Physica Polonica A, **83**(3), 267–271.

Churaev, N.V. 1999 "The DLVO theory in Russian colloid science" Advances in Colloid and Interface Science, **83**, 19-32.

Cole, S.H. and Monroe, E.A. 1967 "Electron microscope studies of the structure of opal" J. Appl. Phys., **38**(4), 1872-1873.

Cong, Xian-Dong, et al. 1993 "^{29}Si MAS NMR spectroscopic investigation of alkali silica reaction product gels" Cement and Concrete Research, **23**, 811-823.

Crerar, D.A. et al. 1981 "Growth and ripening of silica polymers in aqueous solutions" Geochimica et Cosmochimica Acta, **45**, 1259-1266.

Darragh, P.J. et al. 1966 "Origin of precious opal" Nature, **209**(5018), 13-16.

Darragh, P.J. and Sanders, J.V. 1969 "Volcanic gem opal examined by electron microscopy" Australian Gemmologist, **10**, 58.

Darragh, P.J. and Perdrix, J.L. 1975 "Notes on synthetic precious opal" Journal of Gemmology, **14**, 215-223.

Darragh, P.J. et al. 1976 "Opals" Scientific American, **234**, 84-95.

Darragh, P.J. et al. 1977 "Synthetic Opals" Australian Gemmologist, **13**(4), 109.

Davis, K.E. et al. 1989 "Disorder-to-Order: transition in settling suspensions of colloidal silica: X-Ray measurements" Science, **245**, 507-510.

Davydov, V.Y. et al. 2000 "Fabrication and structural studies of opal-III nitride nanocomposites" Nanotechnology, **11**, 291-294.

Dietzel, M. 2000 "Dissolution of silicates and the stability of polysilicic acid" Geochimica et Cosmochimica Acta, **64**(19), 3275-3281.

De Jong, B.H.W.S. et al. 1983 "Polymerization of silicate and aluminate tetrahedra in glasses, melts, and aqueous solutions – IV. Aluminium coordination in glasses and aqueous solutions and comments on the aluminium avoidance principle" Geochimica et Cosmochimica Acta. **47**, 1223-1236.

De Jong, B.H.W.S. et al. 1987 "X–ray diffraction and ^{29}Si magic–angle–spinning NMR of opals: Incoherent long– and short–range order in opal-CT" Am. Miner. **72**, 1195-1203.

De Pablo-Galán, L. et al. 1997 "Electrical properties of opal-CT" Phys. Chem. Minerals, 24, 90-101.

Deniskina, N.D. et al. 1981 "The genesis of precious opal, I: Conditions of formation of silica sols and their realization in nature" Geologiya i Geofizika, **22**(12), 87-92.

Deryagin, B. V. and Churaev, N. V, 1973 "Nature of anomalous water" Nature, **244**(5416), 430-1.

Deveson, B. 2004 "The origin of precious opal" Aust. Gemmol., **22**, 50-58.

Doremus, R.H. 1973 "Glass Science" John Wiley and Sons, New York.

Dove, P.M. and Rimstidt, J.D. 1994 "Silica water interactions" Reviews in Mineralogy, **29**, 259-308.

Dupree, E. and Pettifer, R.F. 1984 "Determination of the Si–O–Si bond angle distribution in vitreous silica by magic angle spinning NMR" Nature, **308**, 523-525.

Duran J. and Jullien, R. 1998 "Attractive forces in a granular cocktail" Physical Review Letters, **80**(16), 3547-3550.

Dwyer, F.P. and Mellor, D.P. 1934 "An X-Ray study of opals" Journal and Proceedings of the Royal Society of New South Wales, **68**, 47-50.

Eckert, H. 1988 "Water in silicate glasses: Quantification and structural studies by ^{1}H solid echo and MAS–NMR methods" J. Phys. Chem., **92**, 2055-2064.

Einstein, A. 1956 "Investigations in the theory of Brownian movement" Dover Publications, New York.

Elzea, J.M. et al. 1994 "Distinguishing well ordered opal-CT and opal-C from high temperature cristobalite by X–ray diffraction" Analytica Chimica Acta, **286**, 107-116.

Elzea, J.M. and Rice, S.B. 1996 "TEM and X–ray diffraction evidence for cristobalite and tridymite stacking sequences in opal" Clays and Clay Miner., **44**(4), 492-500.

Epova, E.I. et al. 1983 "The genesis of precious opal, II: Conditions and mechanism of formation" Geologiya I Geofizika, **24**(11), 76-83.

Erel, E. et al. 2003 "Capabilities of Laser Ablation Mass Spectrometry in the differentiation of natural and artificial opal gemstones" Anal. Chem., **75**(23), 6422-6429.

Esenli, F. et al. 2001 "Characteristics of opals from Simav, Turkey" N. Jb. Miner. Mh., **3**, 97-113.

Etchepare, J. et al. 1978 "Vibrational normal modes of SiO_2. II. Cristobalite and tridymite" J. Chem. Phys., **68**, 1531-1537.

Farnan, I. et al. 1987 "A study of the structural role of water in hydrous silica glass using cross–polarisation magic angle spinning NMR" Geochimica et Cosmochimica Acta, **51**, 2869-2873.

Field, L.D. and Sternhall, S. 1989 "Analytical NMR" John Wiley and Sons, New York.

Finsy, R. 2004 "On the critical radius in Ostwald ripening" Langmuir, **20**, 2975-2976.

Flörke, O.W. 1967 "Die modifikationen von SiO_2" Fortschr. Miner., **44**, 181-230. [German]

Flörke, O.W. 1972 "Transport and deposition of SiO_2 with H_2O under supercritical conditions" Kristall und Technik, **7**(1-3), 159-166. [German]

Flörke, O.W. 1976 "A new microcrystalline silica from Gran Canaria" Zeitschrift für Kristallographie, **143**, 156-165.

Flörke, O.W. et al. 1973 "The genesis of hyalite" N. Jb. Miner. Mh., (2), 82-89.

Flörke, O.W. et al. 1975 "Opal-CT crystals" N. Jb. Miner. Mh., (8), 369-377.

Flörke, O.W. et al. 1976 "Intergrowth and twinning in opal-CT lepispheres" Contrib. Mineral. Petrol., **58**, 235-242.

Flörke, O.W. et al. 1991 "Nomenclature of micro– and non–crystalline silica minerals, based on structure and microstructure" Neues Jahrbuch Miner. Abh., **163**(1), 19-42.

Frischat, D.H. 1975 "Ionic diffusion in oxide glasses" Trans. Tech. Publications, Switzerland.

Frischat, G.H. et al. 1989 "High–temperature thermal expansion of Libyan Desert Glass as compared to that of silica glasses and natural silicates" Geochim. Cosmochim., **53**, 2731-2733.

Frischat, G.H. et al. 2001 "Mystery of the Libyan desert glasses" Phys. Chem. Glasses, **42**(3), 179-183.

Furbish, W.J. and Schrader, E.L. 1979 "Structure of hyalite from the spruce pine pegmatite district, North Carolina" Canadian Mineralogist, **17**, 541-547.

George, J. and Varghese, G. 2002 "Formation of periodic precipitation patterns: a moving boundary problem." Chemical Physics Letters, **362**, 8-12.

Giuseppetti, G. and Veniale, F. 1969a "Relazioni tra natura dell'acqua, morfologia e struttura degli opali. Nota II" Rend. Soc. Ital. Miner. Petrol., **25**(2), 407-437. [Italian]

Giuseppetti, G. and Veniale, F. 1969b "Relazioni tra natura dell'acqua, morfologia e struttura degli opali. Nota preliminare" Rend. Soc. Ital. Miner. Petrol., **25**(2), 83-97. [Italian]

Gladden, L.F. et al. 1986 "^{29}Si MASNMR studies of the spin-lattice relaxation time and bond-angle distribution in vitreous silica" Philosophical Magazine, B**53**, 81-87.

Goldstein, J. I. et al. 1992 "Scanning Electron Microscopy and X-Ray Microanalysis." Plenum Press, New York, 2nd Edition.

Göttlicher, J. et al. 1998 "On the Microstructure of Geyserites and Hyalites, Natural Hydrous Forms of Silica" Journal of Sol–Gel Science and Technology, **13**, 85–88.

Graetsch, H. 1994 "Structural characteristics of opaline and microcrystalline silica minerals" Reviews in Mineralogy, **29**, 209-232.

Graetsch, H. and Topalović-Dierdorf, I. 1996 "MAS NMR spectra of hyalite from Gran Canaria" Chemie der Erde, **56**, 387-391.

Graetsch, H. and Ibel, K. 1997 "Small angle neutron scattering by opals" Phys. Chem. Minerals, **24**, 102-108.

Graetsch, H. et al. 1985 "The nature of water in chalcedony and opal-C from Brazilian Agate Geodes", Phys. Chem. Minerals **12**, 300-306.

Graetsch, H. et al. 1987 "Structural defects in microcrystalline silica" Phys. Chem. Minerals, **14**, 249-257.

Graetsch, H. et al. 1990 "XRD and ^{29}Si MAS–NMR study on some non–crystalline silica minerals" J. Non–Cryst. Solids, **119**, 173-180.

Graetsch, H. et al. 1994 "NMR, XRD and IR study on microcrystalline opals" Phys. Chem. Minerals, **21**, 166-175.

Greer, R.T. 1969 "Submicron structure of 'amorphous' opal" Nature, **224**, 1199-1200.

Greig, J.W. 1932 "The existence of the high–temperature form of cristobalite at room temperature and the crystallinity of opal. Nota II" J. Am. Chem. Soc., **54**, 2846-2849.

Guthrie, G.D. et al. 1995 "Modelling the X-Ray diffraction pattern of opal-CT" American Mineralogist, **80**, 869-872.

Haines, P.J. 1995 "Thermal methods of analysis: principles, applications and problems" London, Blackie Academic Professional, 1st Edition.

Hänni, H.A. 1989 "Iridescent natural glass from Mexico" J. Gemm., **21**(8), 488–495.

Harder, H. 1995 "Precious layer opal with a complex sedimentary formation as colloid chemical precipitation, sedimentation and evaporation" N. Jb. Miner. Mh., **3**, 121-126.

Heaney, P.J. 1992 "The widespread distribution of a novel silica polymorph in microcrystalline quartz varieties" Nature (London), **255**, 441-443.

Heaney, P.J. et al. 1994 "Silica. Physical Behaviour Geochemistry and Materials Applications" Reviews in Mineralogy, **29**, Mineralogical Society of America, Washington.

Hiemenz, P.C. and Rajagopalan, R. 1997 "Principles of colloid and surface chemistry" 3rd ed., Marcel Dekker, New York.

Hiern, M.N. 1967 "Coober Pedy opalfield" S. Aust., Dep. Mines, Mining Rev., **122**, 5-27.

Hinman, N.W. 1990 "Chemical factors influencing the rates and sequences of silica phase transitions: Effect of organic constituents" Geochimica et Cosmochimica Acta, **54**, 1563-1574.

Hinman, N.W. 1998 "Sequences of silica phase transitions: effects of Na, Mg, K, Al and Fe ions" Marine Geology, **147**(1–4), 13–24.

Hockey, J.A. and Pethica, B.A. 1961 "Surface hydration of silicas" Transactions– Faraday Society, **57**, 2247-2262.

Holmberg, K. 2001a "Handbook of applied surface and colloid chemistry. Volume I" John Wiley and Sons, New York.

Holmberg, K. 2001b "Handbook of applied surface and colloid chemistry. Volume II" John Wiley and Sons, New York.

Huang, W.H. and Vogler, D.L. 1972 "Dissolution of opal in water and its water content" Nature Physical Science, **235**, 157-158.

Hunt, J.M. 1950 "Infrared absorption spectra of minerals and other inorganic compounds" Anal. Chem., **22**(12), 1478-1497.

Hunter, R.J. 2001 "Foundations of colloid science" Oxford University Press, New York.

Hutton, D.R. et al. 1997 "EPR/ESR spectra of natural and synthetic opals" Australian Gemmologist, **19**, 365-367.

Iler, R.K. 1965 "Formation of precious opal" Nature, **207**(4996), 472-473.

Iler, R.K. 1973 "Effect of Adsorbed Alumina on the Solubility of Amorphous Silica in Water" Journal of Colloid and Interface Science, **43**(2), 399–408.

Iler, R.K. 1979 "The Chemistry of Silica: Solubility, Polymerisation, Colloid and Surface Properties, and Biochemistry", John Wiley and Sons, New York.

Jobbins, A. et al. 1976 "Internal structures and identification of Gilson synthetic opals" Journal of Gemmology, **15**(2) 66-75.

Jones, B. et al. 1999 "Actively growing siliceous oncoids in the Waiotapu geothermal area, North Island, New Zealand" Journal of the Geological Society, London, **156**, 89–103.

Jones, J.B. 1975 "Nomenclature and the structure of natural disordered (opaline) silica" Contrib. mineral. Petrol., **51**, 231-234.

Jones, J.B. and Segnit, E.R. 1966 "The occurrence and formation of opal at Coober Pedy and Andamooka" Aust. J. Sci, **29**(5), 129-133.

Jones, J.B. and Segnit, E.R. 1969 "Water in sphere-type opal" Min. Mag., **37**(287), 357-361.

Jones, J.B. and Segnit, E.R. 1971 "The nature of opal. I. Nomenclature and constituent phases" J. Geol. Soc. Aust., **18**(1), 57-68.

Jones, J.B. and Segnit, E.R. 1972 "Genesis of cristobalite and tridymite at low temperatures" Journal of the Geological Society of Australia, **18**(4), 419-422.

Jones, J.B. et al. 1963 "Differential thermal and X–ray analysis of opal" Nature, **198**(4886), 1191.

Jones, J.B. et al. 1964 "Structure of Opal" Nature, **204**(4962), 990-991.

Jones, J.B. et al. 1966 "Opal genesis" Nature, **210**(5043) 1353-1354.

Kahlweit, M. 1975 "Ostwald ripening of precipitates" Advances in Colloid and Interface Science, **5**, 1-35.

Kalinin, D.V. et al. 1998 "Structure of precious opal and an energy-based analysis of interaction of silica spheres during its formation: a new interpretation" Geologiya i Geofizika, **39**(7), 1019-1022.

Kano, K. 1983 "Ordering of opal-CT in diagenesis" Geochemical Journal, **17**, 87-93.

Kano, K. and Taguchi, K. 1982 "Experimental study on the ordering of opal-CT" Geochemical Journal, **16**, 33-41.

Kastner, M. and Gieskes, J.M. 1983 "Opal-A to opal-CT transformation: A kinetic study" Dev. Sedimentol., **36** (Siliceous Deposits Pac. Reg.), 211-227.

Kastner, M. et al. 1977 "Diagenesis of siliceous oozes – I. Chemical controls on the rate of opal-A to opal-CT transformation – an experiment study" Geochimica et Cosmochimica Acta, **41**, 1041-1059.

Kazantseva, L.K. et al. 1987 "Structural changes in the matrix of the precious opal effected by heating and impregnation" Geologiya I Geofizika, **39**, 44-48. [Russian-English Translation]

Keller, P.C. 1990 "Gemstones and Their Origins" Van Nostrand Reinhold, New York.

Khimicheva, N.V., Plyusnina, I.I., Isirikyan, A.A. 1991 "Sorption properties of a number of minerals from opal→quartz" Moscow University Herald, Serial **4**, Geology, 33-44. [Russian]

Klinowski, J. et al. 1982 "A re-examination of Si, Al ordering in zeolites NaX and NaY" J. Chem. Soc., Faraday Trans. 2, **78**, 1025-1050.

Koivula, J.I. et al. 1983 "Opal from Querétaro, Mexico: Occurrence and inclusions" Gems and Gemology, **19**(2), 87-96.

Krauskopf, K.B. 1956 "Dissolution and precipitation of silica at low temperatures" Geochimica et Cosmochimica Acta, Geochimica et Cosmochimica Acta, **10**, 1–26.

Kruyt, H.R. 1949 "Colloid Science. Volume II" Elsevier Scientific Publishing Company, Amsterdam.

Kulchitskaya, A.A. et al. 1995 "On the nature of water in opal" Mineralogitcheskij Zhurnal, ISSN: 0204-3548, 17(1), 56-70. [Ukrainian]

Kulchitskaya, A.A. et al. 1997 "The nature of carbon compounds in opal" Mineralogitcheskij Zhurnal, ISSN: 0204-3548, **19**(1), 18-37. [Ukrainian]

Lakhanpal, M.L. et al. 1955 "Influence of capillarity on the boiling point of water" J. Phys. Chem., Ithica, **59**, 160-161.

Landmesser, M. 1995 "Mobility by metastability: Silica transport and accumulation at low temperatures" Chem. Erde, **55**, 149-176.

Landmesser, M. 1998 " 'Mobility by metastability' in sedimentary Agate Petrology" Chem. Erde, **58**, 1-22.

Langer, K. and *Flörke, O.W.* 1974 "Near infrared absorption spectra (4000–9000cm^{-1}) of opals and the role of 'water' in these $SiO_2.nH_2O$ minerals" Fortschr. Miner., **52**(1) 17-51.

Langer, K. et al. 1979 "Measurement of the near–infrared spectra of H_2O–SiOH bearing siliceous materials at high pressures" Applied Spectroscopy, **33**(5), 495-499.

Larson, E.D. et al. 1996 "Atomic Force Microscopy Investigations on Libyan Desert Glass and Other Silica Glasses of Different Origins" Chemie der Erde, **56**(4), 423-430.

Levin, I. and Ott, E. 1933 "X–Ray study of opals, silica glass and silica gel" Zeitschrift für Kristallographie, **85**, 305-318.

Lewin, J. 1961 "The dissolution of silica from diatom walls" Geochim. Cosmochim. Acta, **21**, 182-198.

Li, D. et al. 1994 "X–ray absorption spectroscopy of silicon dioxide (SiO_2) polymorphs: The structural characterisation of opal" American Mineralogist, **79**, 622-632.

Lippmaa, E. et al. 1981 "Investigation of the structure of zeolites by solid-state high-resolution ^{29}Si NMR spectroscopy" J. Am. Chem. Soc., **103**, 4992-4996.

McDonald, R.S. 1958 "Surface functionality of amorphous silica by infrared spectroscopy" Journal of Physical Chemistry, **62**, 1168-1178.

Maciel, G.E. and Sindorf, D.W. 1980 "Silicon–29 Nuclear Magnetic Resonance study of the surface of silica gel by Cross Polarisation and Magic Angle Spinning" Journal of the American Chemical Society, **102**, 7606-7607.

Mägi, M. et al. 1984 "Solid–state high–resolution Silicon–29 chemical shifts in silicates" J. Phys. Chem., **88**, 1518-1522.

Males, P.A 1974 "Opal nobbies from Lightning Ridge" Australian Lapidary Magazine, **10**, 5-9.

McOrist, G.D. and Smallwood, A. 1995 "Trace elements in coloured opals using neutron activation analysis" J. Radioanal. Nucl. Chem., **198**(2), 5-7.

McOrist, G.D. and Smallwood, A. 1997 "Trace elements in precious and common opals using neutron activation analysis" J. Radioanal. Nucl. Chem., **223**(1-2) 9-15.

McOrist, G.D. et al. 1994 "Trace elements in Australian opals using neutron activation analysis" J. Radioanal. Nucl. Chem., **185**(2), 293-303.

McPherson, D.M. et al. 1989 "Was Libyan Desert Glass formed by a sol–gel process?" Glastechnische Berichte, **62**(8), 208-212.

Merino, E. et al. 1989 "Aqueous–chemical control of the tetrahedral–aluminium content of quartz, halloysite, and other low–temperature silicates" Clays and Clay Minerals, **37**(2), 135-142.

Míguez, H. et al. 1997 "Evidence of FCC crystallization of SiO_2 nanospheres" Langmuir, **13**, 6009-6001.

Mikhailov, G.M., et al. 1963 "The condition of water in opal" Tr. Sibirsk. Tekhnol. Inst., **36**, 29-32.

Milisenda, C.C. et al. 1994 "A new occurrence of dendritic opal in south–eastern Zambia" J. Gemm., **24**(4), 277-280.

Monroe, E.A. et al. 1969 "Stacking faults and polytypism in opal, $SiO_2.nH_20$" Acta Cryst. A **25**, 578-580.

Moxon, T.J. 1996 "The co–precipitation of Fe^{3+} and SiO_2 and its role in agate genesis" Neues Jahrbuch für Mineralogie Monatshefte, **1**, 21–36.

Murdoch, J.B. et al. 1985 "High–resolution ^{29}Si NMR study of silicate and aluminosilicate glasses: The effect of network–modifying cations" American Mineralogist, **70**, 332-343.

Murray, M. J. and Sanders, J.V. 1980 "Close–packed structures of spheres of two different sizes II. The packing densities of likely arrangements" Philosophical Magazine, **42**(6), 721-740.

Myers, D. 1999 "Surfaces, Interfaces, and Colloids. Principles and Applications" 2nd ed. John Wiley and Sons, New York.

Nagase, T. and Akizuki, M. 1997 "Texture and structure of opal-CT and opal-C in volcanic rocks" Canadian Mineralogist, **35**, 947-958.

Nassau, K. 1981 "Varied causes of colour in glass" Materials Research Society Symposia Proceedings, **61**, 427-439.

Norman, M.D. et al. 1996 "Quantitative Analysis of Trace Elements in Geological Materials by Laser Ablation ICPMS: Instrumental Operating Conditions and Calibration Values of NIST Glasses." Geostandards Newslett., **20**, 247-261.

Norman, M.D. et al. 1998 "Quantitative Analysis of Trace Element Abundances in Glasses and Minerals: A Comparison of Laser Ablation Inductively Coupled Mass Spectrometry, Solution Inductively Coupled Plasma Mass Spectrometry, Proton Microprobe and Electron Microprobe Data." J. Anal. Atom. Spectrom., **13**, 477-482.

Nukui, A. and Flörke, O.W. 1987 "Three tridymite structural modifications and cristobalite intergrown in one crystal" American Mineralogist, **72**, 167-169.

Okamoto, G. et al. 1957 "Properties of silica in water" Geochimica et Cosmochimica Acta, **12,** 123–132.

Olliver, J.G. and Townsend, I.J. 1993 "Gemstones in Australia" Australian Gemstone Industry Council, Australian Government Publishing Service, Canberra, 3-18.

Ostrooumov, M. et al. 1999 "Specres Raman des opales: aspect diagnostique et aide à la classification" Eur. J. Mineral., **11**(5), 899-908.

Pearson, G. 1985 "Role of water in cracking of opal" Aust. Gemm., **15**(12) 435-445.

Pechar, F. 1985 "Infrared reflection spectra of selected modifications of SiO_2 and Al_2O_3" Crystal Res. Tech., **20**(2), 239-246.

Pense, J. 1964 "Ein elektronenmikroskopischer Beitrag zur Optik der Edelopale" Fortschr. Miner., **41**, 166.

Philipse, A.P. 1989 "Solid opaline packings of colloidal silica spheres" Journal of Materials Science Letters, **8**, 1371-1373.

Pines, A. et al. 1973 "Proton–enhanced NMR of dilute spins in solids" Journal of Chemical Physics, **59**(2), 569-590.

Plyusnina, I.I. 1979 "Infrared spectra of opals" Soviet Physics Doklady, **24**, 322-333.

Plyusnina, I.I. et al. 1971 "Infrared spectroscopic investigation of cryptocrystalline varieties of silica" International Geology Review, **13**, 1750-1754.

Popiel, W.J. 1978 "Introduction to colloid science" Exposition Press, New York.

Prigogine, M. and Fripiat, J. J. 1971 "Anomalous water. Possible explanation of its formation and nature" Chemical Physics Letters, **12**(1), 107-9.

Pusey, P.N. et al. 1989 "Structure of hard colloidal spheres" Physical Review Letters, **63**(25), 2753-2756.

Rau, R.C. and Amaral, E.J. 1969 "Electron microscopy of precious opal" Metallography, **2**, 323-328.

Rawson, H. 1980 "Properties and applications of glass" 1st Ed., Elsevier Scientific Publishing Company, Amsterdam.

Rice, S.B. et al. 1995 "Application of Fourier transform infrared spectroscopy to silica digenesis: The opal-A to opal-CT transformation" Journal of Sedimentary Research, A**65**(4), 639-647.

Richerson, D.W. 1992 "Modern ceramic engineering. Properties, processing, and use in design" 2nd Edition, Marcel Dekker, New York.

Rintoul, M.D. and Torquato, S. 1996 "Computer simulations of dense hard-sphere systems" J. Chem. Phys., **105**(20), 9258-9265.

Roberts, G.J. and Roberts, J.P. 1966 "An oxygen tracer investigation of the diffusion of 'water' in silica glass" Physics and Chemistry of Glasses, **7**(3), 82-89.

Robertson, R.S. and Scott, D.C. 1990 "Geology of the Coober Pedy precious stones field." Geological survey of South Australia, Report of investigations 56.

Romanov S.G. et al. 1997 "Enhancement of the photonic gap of opal-based three-dimensional gratings" Appl. Phys. Lett. **70**(16), 2091-2093.

Rondeau, B. et al. 2004 "Opals from Slovakia ("Hungarian" opals): a re-assessment of the conditions of formation" Eur. J. Mineral., **16**, 789-799.

Sanders, J.V. 1964 "Colour of precious opal" Nature, **204**(4964), 1151-1153.

Sanders, J.V. 1968 "Diffraction of light by opals" Acta Cryst., A**24**, 427-434.

Sanders, J.V. 1975 "Microstructure and crystallinity of gem opals" Am. Miner., **60**, 749-757.

Sanders, J.V. 1976 "The structure of star opals" Acta Cryst., **32**, 334.

Sanders, J.V. 1980 "Close–packed structures of spheres of two different sizes I. Observations on natural opal" Philosophical Magazine, **42**(6), 705-720.

Sanders, J.V. 1985 "Structure of opals" Journal de Physique, **46**(3), 1-8.

Sanders, J.V. and Murray, M.J. 1978 "Ordered arrangements of spheres of two different sizes in opal" Nature, **275**, 201-203.

Schmetzer, K. 1984 "An investigation of the synthetic products of Gilson showing a play of colours" J. Gemm., **19**(1), 27-42.

Schmidt, M. et al. 2001 "Oxygen isotopes of marine diatoms and relations to opal-A maturation" Geochimica et Cosmochimica Acta, **65**, 201-211.

Scrivener, K.L. and Monteiro, P.J.M. 1994 "The alkali–silica reaction in a monolithic opal" J. Am. Ceram. Soc., **77**(11), 2849-2856.

Scurfield, G. 1979 "Wood petrification: An aspect of biomineralogy" Aust. J. Bot., **27**, 377-390.

Scurfield, G. and Segnit, E.R. 1984 "Petrification of wood by silica minerals" Sedimentary Geology, **39**, 149-167.

Segnit, E.R. et al. 1965 "The role of water in opal" J. Geol. Soc. Aust., **12**(2), 211-226.

Segnit, E.R. et al. 1970 "A scanning microscope study of the morphology of opal" Search, 1(6).

Serdobintseva, V.V. and Kalinin, D.V. 1998 "Potch opal and its genetic significance" Geologiya i Geofizika, **39**, 1793-1799.

Serdobintseva, V.V. et al. 1998 "Forms of colloidal silica participating in the formation of precious opal and the mechanism of silification of its gel crystals" Russian Geology and Geophysics, **39**(8), 1118-1122.

Serdobintseva, V.V. et al. 1999 "Supramolecular crystal growth in concentrated suspensions of charged monodisperse spherical silica particles" React. Kinet. Catal. Lett., **68**(2), 313-318.

Shaw, D.J. 1992 "Introduction to colloid and surface chemistry" Butterworth-Heinemann, London.

Shepherd, G.F. 1971 "The story of opal" Rocks and Minerals, **46**(6) 363-370.

Simonton, T.C. et al. 1986 "Microstructure and mechanical properties of synthetic opal: A chemically bonded ceramic" J. Mater. Res., **1**(5), 667-674.

Sinclair, R.N. et al. 1992 "Inelastic neutron scattering studies of amorphous network solids" Journal of Non–Crystalline Solids, **150**, 219–230.

Sindorf, D.W. and Maciel, G.E. 1983 "^{29}Si NMR study of dehydrated/rehydrated silica gel using cross polarisation and magic–angle spinning" Journal of the American Chemical Society, **105**, 1487-1493.

Smallwood, A.G. 1997 "A new era for opal nomenclature" Australian Gemmologist, **19**, 486-496.

Smallwood, A.G. 1999 "Chemical and physical evaluation of Australian precious opal" M.Sc. Thesis, University of Technology, Sydney.

Smallwood, A.G. et al. 1997 "Characterisation of sedimentary opals by Fourier transform Raman spectroscopy" Spectrochim. Acta Part A, **53**, 2341-2345.

Smith, A.L. 1960 "Infrared Spectra - Structure correlations for organosilicon compounds" Spectrochimica Acta, **16**, 87-105.

Smith, D.K. 1998 "Opal, cristobalite, and tridymite: Noncrystallinity versus crystallinity, nomenclature of the silica minerals and bibliography" Powder Diffraction **13**(1), 2-19.

Smith, J.V. and Steele, I.M. 1984 "Chemical substitution in silica polymorphs" Neues Jahrbuch für Mineralogie - Monatshefte, **3**, 137-144.

Smith, J.V. et al. 1984 "NMR of albite–microcline series" Nature, **309**, 140–142.

Sosnowska, I. et al. 1997 "Structure and dynamics of the opal silica–water system" Physica B 234-236, 455-457.

Spencer, R.J. et al. 1992 "Opal from Querétaro, Mexico: Fluid inclusion study" Gems and Gemology, **28**(1) 28-34.

Steefel, C.I. and Van Cappellen, P. 1990 "A new kinetic approach to modeling water–rock interaction: The role of nucleation, precursors, and Ostwald ripening" Geochimica et Cosmochimica Acta, **54**, 2657-2677.

Stern, K.H. et al. 1954 "The liesegang phenomenon" Chemistry Reviews, **54**, 79-99.

Stevens Kalceff, M.A. et al. 1997 "Cathodoluminescence microanalysis of natural hydrated amorphous SiO_2; opal" Phys. Chem. Miner., **24**, 131-138.

Sultan, R.F. 2002 "Propagating fronts in periodic precipitation systems with redissolution." Physical Chemistry Chemical Physics, **4**(8), 1253-1261.

Taijing, L. et al. 1995 "Nanometre scale textures in agate and Beltane opal" Mineralogical Magazine, **59**, 103-109.

Taliaferro, N.L. 1935 "Some properties of opal" Am. J. Sci., **30**, 450-474.

Temniskova-Topalova, D.N. et al. 1990 "Electron paramagnetic resonance of diatom opal from three Bulgarian deposits" Doklady Bolgarskoi Akademii Nauk, **43**(5), 45-48.

Thomas, J.M. et al. 1983 "The evaluation of non-equivalent tetrahedral sites from ^{29}Si NMR chemical shifts in zeolites and related aluminosilicates" Chemical Physics Letters, **102**, 158-162.

Thomas, P.S. 1997 "Characterisation of Sedimentary Opals by Fourier transform Raman spectroscopy" Spectrochim. Acta Part A, **53**, 2341-2345.

Thompson, W.K. 1965 "An infrared study of water adsorbed on silica" Proc. Brit. Ceram. Soc., **5**, 143-151.

Torquato, S. et al. 2000 "Is random close packing of spheres well defined?" Physical Review Letters, **84**(10), 2064-2067.

Tsunekawa, S. et al. 1997 "Characterisation of precious opals: AFM and SEM observations, photonic band gap, and incorporation of CdS nano–particles" Microporous Materials, 8, 275-282.

Vaidyan, V.K. et al. 1981 "On the theory of periodic precipitation" Journal of Crystal growth, **54**, 239-242.

Van Steveninck, J. et al. 1991 "Anomalous properties of water in macromolecular gels" Biochimica et Biophysica Acta, **1115**(2), 96-100.

Veniale, F. 1972 "Thermo-hygrometric analyses of the dehydration processes in opal, hydro-chrysotile, sepiolite, and palygorskite." Rendiconti della Societa Italiana di Mineralogia e Petrologia, 28(1), 339-350. [Italian]

Visscher, W.M. and Bolsterli, M. 1972 "Random packing of equal and unequal spheres in two and three dimensions" Nature, **239**, 504-507.

Vlasov, Y.A. et al. 1997 "Existence of photonic pseudogap for visible light in synthetic opals" Physics Review B, **55**(20), 357-360.

Volf, M.B. 1984 "Glass Science and Technology; Volume 7, Chemical Approach to Glass" Elsevier Science, New York, 303-386.

Vosel, S.V. and Kalinin, D.V. 1999 "Thermodynamic analysis of formation of crystal-like precious-opal structures" Russian Geology and Geophysics, **40**(4), 592-598.

Warne, S.St.J. 1970 "The detection and identification of the silica minerals quartz, chalcedony, agate and opal, by differential thermal analysis" J. Inst. Fuel., **43**, 240-242.

Webb, J.A. and Finlayson, B.L. 1984 "Allophane and opals speleothems from granite caves in south-east Queensland", Australian Journal of Earth Science, **31**, 341-349.

Webb, J.A. and Finlayson, B.L. 1987 "Incorporation of Al, Mg, and water in opal-A: Evidence from speleothems", Am. Mineral. **72**, 1204-1210.

Wilding, L.P. 1967 "Accessibility and properties of occluded carbon in biogenetic opal" Soil Science, **103**(1), 56-61.

Williams, L.A. and Crerar, D.A. 1985 "Silica diagenesis, II. General Mechanisms" Journal of Sedimentary Petrology, **55**(3), 312-321.

Williams, L.A. et al. 1985 "Silica diagenesis, I. Solubility controls" Journal of Sedimentary Petrology, **55**(3), 301-311.

Woodcock, L.V. 1997 "Entropy difference between face-centred cubic and hexagonal close-packed crystal structures" Nature, **39**, 141-143.

Yoshida, A. 1987 "Structures of Anomalous Cristobalites Contained in Ioujima Opals" Kyushu Kogyo Gijutsu Shikensho Hokoku, **39**, 2491-2498.

Yuliya, S. and Khristova, J. 1992 "Fluid inclusions in opal siliceous rocks from Svetoslav village, district of Haskavo" Review of the Bulgarian Geological Society, **53**(3), 59-66. [Bulgarian]

Zabelin, B.A. 1968 "Influence of heat-treatment on the structure and the sorption activity of natural silica gels" Zhurnal Prikladnoi Khimii (Russian Journal of Applied Chemistry), **41**(2) 259-266. [Russian-English translation]

Zakhidov, A.A. et al. 2001 "Three-dimensionally periodic conductive nanostructures: network versus cermet topologies for metallic PBG" Synthetic Materials, **116**, 419-426.

Zarubin, D.P. 2001 "The two-component bands at about 4500 and 800 cm^{-1} in infrared spectra of hydroxyl containing silicas. Interpretation in terms of Fermi resonance." Journal of Non-Crystalline Solids, **286**, 80-88.

Zhuravlev, L.T. 1989 "Structurally bound water and surface characterisation of amorphous silica" Pure and Appl. Chem., **61**(11), 1969–1976.